Astronomy Reports, Vol. 48, No. 2, 2004, pp. 103–107. Translated from Astronomicheskiĭ Zhurnal, Vol. 81, No. 2, 2004, pp. 124–128.

Galactic Parameters Derived from Open-Cluster Data

T. P. Gerasimenko

Astronomical Observatory, Ural State University, Yekaterinburg, Russia

Received September 20, 2001; in final form, July 26, 2003

Abstract—The components U_0 and V_0 of the solar motion and the Oort constant A_0 are determined using the data of a homogeneous open-cluster catalog with corrected distance moduli. The results are based on a sample of 146 open clusters with known radial velocities located in the Galactic plane ($b < 7°$) within 4 kpc of the Sun. The solar Galactocentric distance R_0 is determined using two kinematic methods. The following results are obtained: $A_0 = 17.0 \pm 0.9$ km/s kpc, $U_0 = 10.5 \pm 1.0$ km/s, $V_0 = 11.5 \pm 1.1$ km/s, $R_0 = 8.3 \pm 0.3$ pc. © *2004 MAIK "Nauka/Interperiodica"*.

1. INTRODUCTION

One of the traditional areas of kinematic studies is the determination of the main Galactic parameters required to construct theoretical equilibrium models: the gradient of the angular velocity (the Oort constant A_O), the Oort constant B_0, and the principal scale parameter—the distance of the Sun from the Galactic center, R_O. These parameters are difficult to measure, first and foremost, because of the presence of local group motions, which hinder selection of a model to describe the motion of these objects and degrade the accuracy of the derived parameters. These parameters should be determined by comparing results obtained for various methods using trustworthy, homogeneous data sets. One such data set is our continuously updated, uniform catalog of photometric parameters for 425 open clusters, which have been redetermined using published UBV, $uvbyj$, and DDO photometric data [1]. (Hereafter, we refer to this as the Uniform Catalog.) The large size of the open-cluster sample, uniformity of the parameter estimates, which were obtained using a single technique, and availability of radial-velocity data for a large number of the clusters make this catalog a useful tool for the analysis of the structure of the Galaxy and the kinematics of disk objects. In the current paper, we use only the radial velocities and, therefore, do not estimate the Oort constant B_0.

2. CLUSTER SAMPLE

Radial velocities are available for 205 of the 425 clusters listed in the Uniform Catalog. We adopted the radial velocities from sources listed in [2–11]. We corrected the distance moduli of the clusters by subtracting the mean difference between the distance-modulus estimates from the Uniform Catalog and those determined using Hipparcos trigonometric parallaxes [12]; the distance scale changed by -0.153^m, independent of the cluster age. The clusters span a fairly wide age interval. Clusters in different age groups are known to have different motions. Analysis of the rotation of the open-cluster subsystem revealed a small group among the young clusters whose motion differs from that of the cluster sample as a whole [13]. To ensure uniformity, we excluded these objects from the sample of young open clusters when deriving final estimates of the Galactic parameters. We introduced weights to allow for variations in the quality of the initial data.

3. ANALYSIS METHODS

3.1. Components of the Solar Motion and the Oort Constant A_0

We determined the components of the solar motion with respect to the centroid of the open clusters and the Oort constant A_0 by solving the following system of equations:

$$V_r' = V_r + U_0 \cos l \cos b + V_0 \sin l \cos b + W_0 \sin b = -2A_0(R - R_0) \sin l \cos b, \quad (1)$$

where V_r is the observed radial velocity; U_0, V_0, and W_0 are the components of the solar motion (the X, Y, and Z axes point toward the Galactic center, in the direction of the Galactic rotation, and toward the North Galactic Pole, respectively); l and b are Galactic coordinates; and R and R_0 are the Galactocentric distances of the cluster and the Sun, respectively, so that

$$R = [(R_0)^2 + (r \cos b)^2 - 2R_0 r \cos l \cos b]^{1/2}. \quad (2)$$

1063-7729/04/4802-0103$26.00

Some previous determinations of the solar Galactocentric distance

No.	Reference	Year	R_0, kpc	Objects
1	Weaver [14]	1954	8.2	Open clusters, Cepheids
2	Feast and Shuttleworth [15]	1965	9.9±0.9	B stars, open clusters, Cepheids
3	Barkhatova and Gerasimenko [16, 17]	1973, 1985	8.2±0.5	Open clusters
4	Merrifield [18]	1992	7.9±0.8	HI
5	Reid [19]	1993	8.0±0.5	
6	Feast and Whitelock [20]	1997	8.5	Cepheids
7	Olling and Merrifield [21]	1998	7.1±0.4	Cepheids
8	Metzger *et al.* [22]	1998	7.66±0.32	Cepheids
9	Glushkova *et al.* [23]	1999	7.4±0.3	Open clusters, Cepheids, supergiants
10	McNamara *et al.* [24]	2000	7.9±0.3	RR Lyr, Miras
11	Gerasimenko (this paper)	2003	8.2±0.3	Open clusters

In the calculations, we weighted Eqs. (1) in accordance with the errors in both the radial velocity and the heliocentric distance: $P = (\sigma_r^2 + \sigma_{V_r}^2)^{-1/2}$, where σ_r^2 and $\sigma_{V_r}^2$ are the errors in the distance and radial velocity, respectively.

3.2. Solar Galactocentric Distance

The question of the correct value of the scale parameter R_0 remains open, and available estimates range from 6 to 10 kpc (see table). Moreover, some estimates show a decreasing trend [23]. Reid [19] compiled a list of $R_\odot$ estimates dating from the 1970s onward and plotted R as a function of date. It is evident from his plot that, on average, $R_\odot$ decreased until the early 1990s, then began to increase. However, the mean R_0 remains near 8.0 kpc. The table gives a short list of $R_\odot$ determinations, including some early estimates of this parameter.

Several kinematic methods for determining the Galactic scale parameter are known. Almost all require that the input data be selected in accordance with stringent criteria and assume that the objects studied move in circular orbits in the Galactic plane. In this paper, we use two methods.

METHOD OF WEAVER

This method for estimating the Galactic scale parameter $R_\odot$, suggested by Weaver [14] in the 1950s, is used relatively rarely [16, 17], probably due to the fairly severe restrictions that must be imposed on the initial sample in terms of the locations of the sample objects in the Galactic plane relative to the Sun. As a result, only a few of all clusters with known radial velocities can be used in these analyses. Weaver himself used 13 clusters, while Barkhatova and Gerasimenko used 19 [16] and 21 [17] clusters. Here, we estimate $R_\odot$ by applying Weaver's method to 28 clusters. The objects used to determine $R_\odot$ must satisfy the following criteria.

(1) They must be fairly distant, $r > 1$ kpc.

(2) They must be located in the ring $0.5 < |R - R_0| < 1.5$ kpc.

(3) Their orbits must be close to circular.

(4) The dependence of V_r' on $C(R, R_0)$, defined below by formula (6), must be nonlinear.

We found a total of 28 clusters meeting these criteria. Figure 1 shows their distribution.

We can see four groups of clusters located in two (inner and outer) critical domains in Fig. 1. The inner clusters make up two groups located closer to the Galactic center (a total of 20 clusters), while the outer clusters comprise two groups located farther from the center (a total of eight clusters). All the clusters have ages $\log T < 8.0$ (where T is in years). We assume the clusters move in circular orbits in the Galactic plane. We varied the preliminary $R_\odot$ distances (denoted R_0^*) from 6 to 11 kpc. The angular-velocity gradient, $\omega'(R_0)$, is negative in all domains. It can easily be shown that, if $R_0^* > R_0$ (which corresponds to the outer critical domain), $|\omega'(R_\odot^*)| < |\omega'(R_\odot)|$. When $R_0^* < R_0$ (the inner critical domain), $|\omega'(R_\odot^*)| > |\omega'(R_\odot)|$. The two monotonic functions have different slopes and, therefore, intersect. The point of intersection corresponds to the true value of R_0.

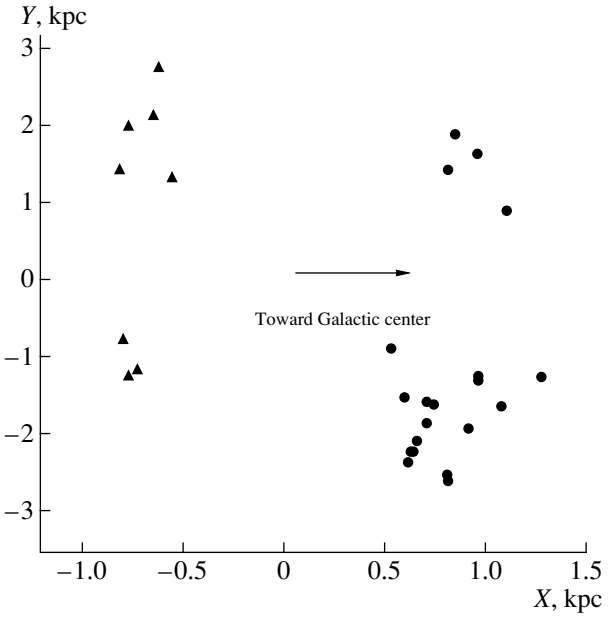

Fig. 1. Location of clusters used for Weaver's method projected onto the Galactic plane.

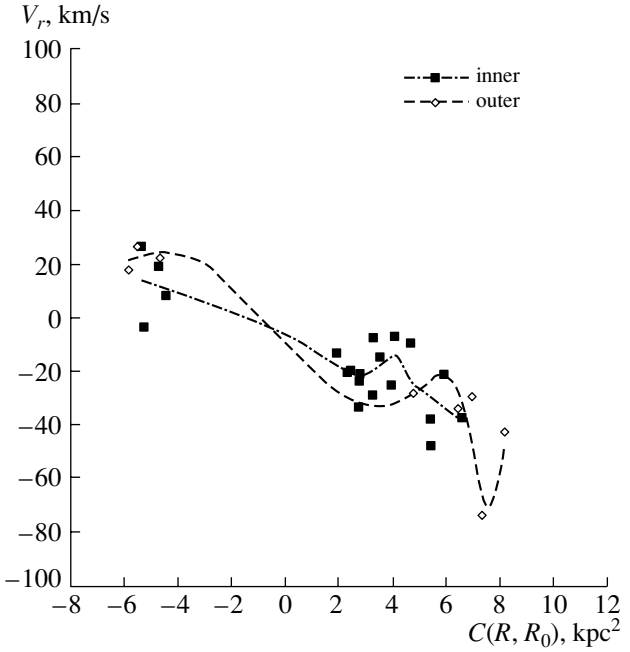

Fig. 2. Dependence of cluster radial velocities $V_r^{'}$ on the parameter $C(R, R_0)$.

For objects located in the domain $|R - R_0| <$ 1 kpc, the angular velocity $\omega(R)$ depends linearly on the Galactocentric distance and can be represented by the first term of the expansion

$$\omega(R) = \omega(R_0) + (R - R_0)\omega^{'}(R_0). \qquad (3)$$

It follows that

$$V_r^{'} = R_0(R - R_0)\omega^{'}(R_0)\sin l\cos b. \qquad (4)$$

The main relation used in Weaver's method is

$$\omega^{'}(R_{\rm O}) = V_r^{'}/C(R, R_0), \qquad (5)$$

where

$$C(R, R_0) = R_0(R - R_0)\sin l\cos b. \qquad (6)$$

Figure 2 shows the relationship between $C(R, R_0)$ and $V_r^{'}$. It is evident that the selected clusters fully satisfy the condition specified by Weaver—the relationship between the two quantities is nonlinear.

Figure 3 illustrates the behavior of the functions $\omega^{'}(R_{\rm O})$ studied here for the inner and outer domains. The intersection of the two curves yields the true value of the Galactic scale parameter. We estimated the error in the resulting R_0 value by propagating the corresponding errors in the input quantities [25].

METHOD OF FOKKER

This method is based on an analysis of the dependence of the residual radial velocity on the scale parameter R_0 [26]. The residual velocity is equal to $\Delta V = V_{obs} - V_{mod}$, where V_{obs} is the observed radial velocity corrected for the Sun's motion toward the apex (or $V_r^{'}$) and V_{mod} is the model radial velocity calculated using the formula

$$V_{mod} = -2A_0(R - R_0)\sin l\cos b. \qquad (7)$$

The clusters used must meet the following conditions:

(1) $|R - R_0| < 1$ kpc, where $\omega(R)$ depends linearly on R;

(2) $1.5 < r < 3$ kpc.

We calculated a weight for each cluster using the formula

$$P = 1 - 2/\sqrt{\pi}\int_0^u e^{-t^2}dt, \qquad (8)$$

where $2/\sqrt{\pi}\int_0^u e^{-t^2}dt$ is the error function, $u = \Delta V/\alpha$, and α is a scale parameter.

We varied R_0 from 5 to 11 kpc and calculated for each R_0 the weighted average of $\langle\Delta V^2\rangle = \Sigma\Delta V_i^2 P_i/\Sigma P_i$. Figure 4 plots $\langle\Delta V_2\rangle$ as a function of R_0. The minimum of this function yields the most likely value of R_0. The main drawback of this method is the difficulty of determining the error in the resulting R_0 value.

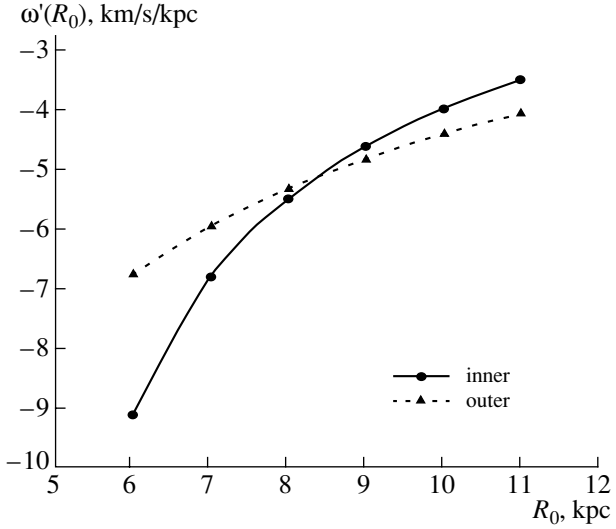

Fig. 3. Dependence of the angular-velocity gradient $\omega'(R_0)$ on the scale parameter R_0.

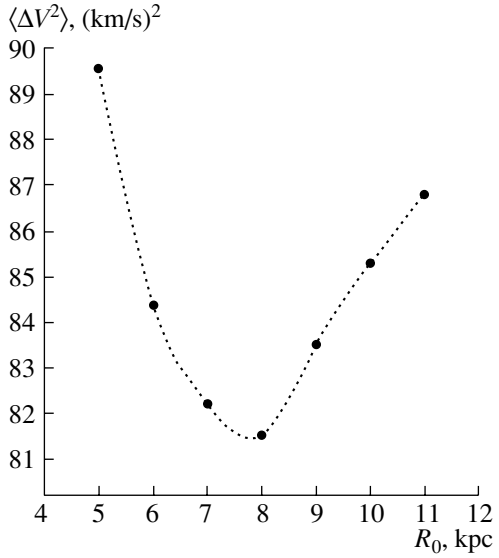

Fig. 4. Dependence of the weighted mean squared residual radial velocity on the scale parameter R_0.

4. RESULTS

We calculated the components of the solar motion using clusters distributed about the Sun fairly uniformly in the Galactic plane ($b < 7.2°$) within heliocentric distances $r = 4$ kpc and with $|R - R_0| < 1$ kpc. We used the same sample as the one employed to estimate the components of the solar motion to determine the Oort constant.

Our final estimate of the components of the solar motion is based on a sample consisting of 149 open clusters. A least-squares solution of Eqs. (1) yielded the velocity components $U_0 = 10.5 \pm 1.0$ km/s and $V_0 = 11.5 \pm 1.1$ km/s; we assumed that W_0 is known and equal to 8.2 km/s [13]. We used these values to correct the observed radial velocities for the solar motion. Note that the adopted W_0 value has little effect on the components U_0 and V_0. We found the Galactic-rotation rate at the solar Galactocentric distance to be $A_0 = 17.5 \pm 0.9$ km/s kpc.

Weaver's method yields a scale parameter of 8.3 ± 0.3 kpc. We determined the error by propagating the errors in the corresponding input quantities [25]. Applying the same method to the data of the catalog described by Dambis [27] yields the same result, $R_0 = 8.3 \pm 0.3$ kpc. Estimating R_0 by applying Fokker's method to 34 clusters meeting the corresponding conditions yields $R_0 = 8.0$ kpc.

ACKNOWLEDGMENTS

This work was supported by the Russian Foundation for Basic Research (project code no. 00-02-16217) and the State Research and Technology Program "Astronomy."

REFERENCES

1. A. V. Loktin, T. P. Gerasimenko, and L. K. Malisheva, Astron. Astrophys. Trans. **20**, 605 (2001).
2. E. H. Geyer, Astron. Astrophys., Suppl. Ser. **62**, 301 (1985).
3. J. Hron, Astron. Astrophys., Suppl. Ser. **60**, 355 (1985).
4. L. M. Cameron, Mon. Not. R. Astron. Soc. **224**, 822 (1987).
5. D. A. Klinglesmith and J. M. Hollis, Astrophys. J., Suppl. Ser. **64**, 127 (1987).
6. Garsia, Astrophys. Space Sci. **148**, 163 (1988).
7. D. Gaisler, Publ. Astron. Soc. Pac. **100**, 338 (1988).
8. D. Leisawitz, Astrophys. J., Suppl. Ser. **70**, 731 (1989).
9. T. Liu, Astron. J. **98**, 626 (1989).
10. E. D. Fril, Publ. Astron. Soc. Pac. **101**, 1105 (1989).
11. J.-C. Mermilliod, Astron. Astrophys. **237**, 61 (1990).
12. A. V. Loktin and G. V. Beshenov, Pis'ma Astron. Zh. **27**, 450 (2001) [Astron. Lett. **27**, 386 (2001)].
13. T. P. Gerasimenko, Astron. Zh. **75**, 840 (1998) [Astron. Rep. **42**, 742 (1998)].
14. H. P. Weaver, Astrophys. J. **59** (10), 375 (1954).
15. M. W. Feast and M. Shuttleworth, Mon. Not. R. Astron. Soc. **130**, 245 (1965).
16. K. A. Barkhatova and T. P. Gerasimenko, Astron. Tsirk., No. 743, 3 (1973).
17. K. A. Barkhatova and T. P. Gerasimenko, Byull. Abastuman. Astrofiz. Obs., No. 59, 169 (1985).
18. M. R. Merrifield, Astron. J. **103** (5), 1552 (1992).
19. J. M. Reid, Ann. Rev. Astron. Astrophys. **31**, 345 (1993).
20. M. Feast and P. Whitelock, Mon. Not. R. Astron. Soc. **291**, 683 (1997).

21. R. P. Olling and M. R. Merrifield, Mon. Not. R. Astron. Soc. **297**, 943 (1998).
22. M. R. Metzger, J. A. R. Carwell, and P. L. Schechter, Astron. J. **115**, 635 (1998).
23. E. V. Glushkova, A. K. Dambis, and A. S. Rastorguev, Astron. Astrophys. Trans. **18**, 349 (1999).
24. D. H. McNamara, J. B. Madsen, J. Barness, and B. F. Ericksen, Publ. Astron. Soc. Pac. **112**, 202 (2000).
25. D. Hudson, *Statistics. Lectures on Elementary Statistics and Probability* (Geneva, 1964; Mir, Moscow, 1970).
26. Fokker, Bull. Astron. Inst. Netherlands **20**, 29 (1968).
27. A. K. Dambis, Pis'ma Astron. Zh. **25**, 10 (1999) [Astron. Lett. **25**, 7 (1999)].

Translated by A. Dambis

Astronomy Reports, Vol. 48, No. 2, 2004, pp. 108–111. Translated from Astronomicheskiĭ Zhurnal, Vol. 81, No. 2, 2004, pp. 129–133.

Dynamical Evolution of Gaseous Clouds in the Atmospheres of Wolf–Rayet Stars

N. A. Kudryashova

St. Petersburg State University (Petrodvorets Branch), Universitetskiĭ pr. 2, Petrodvorets, 198904 Russia

Received March 8, 2002; in final form, August 8, 2003

Abstract—We have computed the dynamical evolution of homogeneous, spherical gaseous condensations in the atmosphere of a Wolf–Rayet star. The physical conditions in the condensations vary substantially in the course of their motion in the stellar wind, which should result in variations in the observed spectrum of the star. The condensations also move at velocities of up to 1000 km/s relative to the surrounding stellar wind. Variations of the physical conditions in these condensations should be taken into account in models of the stellar winds of Wolf–Rayet stars. © *2004 MAIK "Nauka/Interperiodica"*.

1. INTRODUCTION

The suggestion that individual condensations (clouds) occur in the expanding atmospheres of Wolf–Rayet stars (WR) [1] is based on specific features observed in spectra of the eclipsing binary WR+OBV 444 Cyg. A model with an expanding atmosphere containing clouds was developed in [2] to explain the simultaneous presence of lines with appreciably different ionization potentials in the spectra of WR stars. It was suggested that the gas that flows from the star contains clouds of various sizes. The narrow small peaks observed in the spectra of some early-type stars, which shift along the profiles of broad emission lines, were explained in [3, 4] as the radiation of gaseous clouds moving through a more rarefied medium.

Later, Brown *et al.* [5] attempted to derive the physical parameters of the clouds from variability of the emission-line profiles in the spectra of WR stars. Such variability was also calculated theoretically for early-type stars, assuming a stochastic ensemble of clouds in the atmosphere [6]. Modeling of the spectral features due to the clouds did not taken into account the dynamical interactions of the clouds with the surrounding medium. It was assumed that the clouds do not move relative to the surrounding gas and that their density, temperature, and, hence, emitted radiation remain constant. The models are obviously not self-consistent under these assumptions.

If the velocities of a cloud and the surrounding gas flowing from the star are the same, the physical conditions in the cloud cannot remain the same as they were when it formed, since both the temperature and density in the surrounding gas vary. The pressure and temperature in the cloud also vary, as was pointed out in [7]. Taking into account variations of the pressure in the cloud that result in its expansion (or contraction), the cloud should move relative to the surrounding gas with a velocity that can reach $\sim$1000 km/s. When the volume of a gaseous cloud with constant mass varies, so must its temperature. In addition, the temperature of the cloud should be affected by the external medium, which should heat the cloud, since it will usually have a higher temperature. Thus, a gas condensation should be substantially nonsteady-state, with its radiation also varying with time.

Here, we estimate the impact of these factors on the dynamical evolution of gaseous clouds in the atmospheres of WR stars. In the absence of a theory of cloud formation, we have used a simple phenomenological model with homogeneous, spherical clouds. A detailed solution for the gas dynamical interaction between real clouds and the surrounding gas and, accordingly, for the influence of the cloud radiation on the observed spectrum of the star can be obtained only after the cloud-formation mechanism has been determined, so that the correct initial conditions for the computations can be specified.

2. THE CLOUD MODEL AND FORMULATION OF THE PROBLEM

Let a homogeneous spherical condensation have a radius of $R_c(r)$ and a constant mass of M_c. The radius of the condensation is then

$$R_c(r) = \left(\frac{3M_c}{4\pi\rho_c(r)}\right)^{\frac{1}{3}}, \qquad (1)$$

where r is the distance from the center of the star and $\rho_c(r)$ is the density of the condensation.

1063-7729/04/4802-0108$26.00

The condensation is also described by its pressure $P_c(r)$ and temperature $T_c(r)$. The heating of the condensation by the hot external medium and the star's radiation, and also radiative energy losses, lead to nonadiabaticity of the variations in the physical conditions in the condensation. It is impossible to take this effect into account rigorously, since we do not have complete information about the internal composition of the cloud. Let us represent the pressure inside the condensation by the polytropic dependence

$$P_c(r) = K{\rho_c}^n, \tag{2}$$

with the index $1 \le n < 5/3$. This form of the equation of state simplifies the problem dramatically and makes it possible to partially take radiation processes into account. The equation describes an adiabatic process when $n = 5/3$.

At the time of its formation, a cloud should be in a state of equilibrium; the pressure in the condensation $P_c(r)$ should be equal to the pressure in the surrounding gas $P_w(r)$. Further, this approximation remains valid if the condensation has time to adjust to variable external conditions.

The parameters of the wind, labeled with the index w, are related as follows:

$$P_w(r) = \frac{k}{\mu_w m_H}\rho_w(r)T_w(r). \tag{3}$$

The continuity condition for the homogeneous component of the wind implies that

$$\rho_w(r) = \dot{M}\frac{1}{4\pi r^2 v_w(r)}, \tag{4}$$

where $\dot{M}$ is the mass-loss rate of the star and $v_w(r)$ is the velocity of the outflow as a function of the distance from the center of the star.

We adopt a parametric law for $v_w(r)$, which can be written in the generally adopted form [8]

$$v_w(r) = v_0 + (v_\infty - v_0)\left(1 - \frac{R_\star}{r}\right)^\beta.$$

Here, v_0 is the wind velocity near the boundary of the photosphere; v_∞, the terminal velocity of the wind; $R_\star$, the distance from the center of the star to the lower boundary of the wind; and β, a parameter describing the degree of acceleration of the material. When the outflow of gas from hot stars is considered, it is generally assumed that $\beta \simeq 1$.

We obtain from the pressure-equality condition $P_c(r) = P_w(r)$ and Eqs. (2) and (3) the equality

$$\rho_c(r) = \rho_c(r_0)\left(\frac{P_w(r)}{P_w(r_0)}\right)^{\frac{1}{n}},$$

Model parameters independent of the presence of a condensation

$M_\star$	$10M_\odot$
$R_\star$	$3R_\odot$
$L_\star$	$10^5 L_\odot$
$\dot{M}$	$10^{-5}M_\odot$/year
T_w	40×10^3 K
v_∞	2000 km/s
v_0	400 km/s
β	1
τ	0–1

which, if T_w does not depend on r, yields

$$\rho_c(r) = \rho_c(r_0)\left(\frac{r_0^2 v_w(r_0)}{r^2 v_w(r)}\right)^{\frac{1}{n}}. \tag{5}$$

3. EQUATION OF MOTION OF A CONDENSATION

A condensation in the stellar wind is affected by the force of gravity, the radiation pressure, and the gas-pressure gradient. When calculating the velocity of the condensation, the resistance of the gas constituting the wind should also be taken into account.

The turbulent resistance of the medium is proportional to the square of the relative velocity of the condensation, $v_c(r) - v_w(r)$. The corresponding term in the equation of motion should be positive for a negative relative velocity of the condensation. To take into account the absorption of the stellar radiation in the medium, we introduce the factor $\tau \le 1$ in the term describing the radiation pressure.

The equation of motion of the condensation can then be written in the form

$$v_c\frac{dv_c}{dr} = -\frac{1}{\rho_c}\frac{dP_w}{dr} - \frac{GM_\star}{r^2}$$
$$- \frac{c_x}{2M_c}\rho_w \pi {R_c}^2 [v_c - v_w(r)]^2 \frac{|v_c - v_w(r)|}{(v_c - v_w(r))}$$
$$+ \frac{\tau L_\star}{4\pi r^2 M_c}\pi {R_c}^2 \frac{1}{c},$$

where $M_\star$ is the mass of the star and c_x is the coefficient of turbulent resistance; we will adopt $c_x = 1$. The last term is associated with the radiation pressure of a star with luminosity $L_\star$.

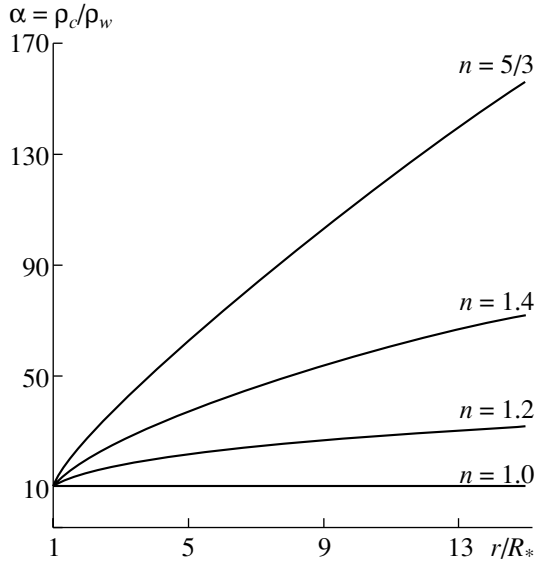

Fig. 1. Variation of the ratio of the densities of the condensation and surrounding gas $\alpha = \dfrac{\rho_c(r)}{\rho_w(r)}$ with distance from the center of the star as a function of n. The curves were obtained for an initial density $\rho_0 = 10\rho_w(r_0)$ and condensation radius $R_0 = 10^{-3}R_\star$.

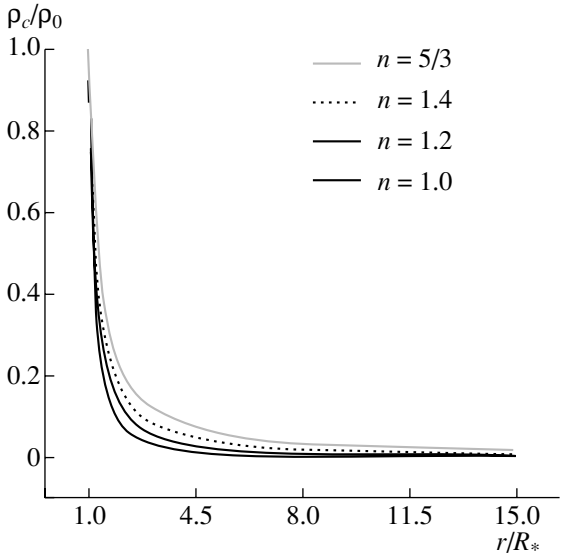

Fig. 2. Variation of the density of the condensation with distance from the center of the star as a function of n. The curves were obtained for an initial density $\rho_0 = 10\rho_w(r_0)$ and condensation radius $R_0 = 10^{-3}R_\star$.

Using the obtained relations (1) and (3)–(5), we transform the equation of motion as follows:

$$v_c\frac{dv_c}{dr} = A_1\left[\frac{2}{r} + \frac{1}{v_w(r)}\frac{dv_w(r)}{dr}\right]\left(r^2v_w(r)\right)^{\frac{1-n}{n}} - A_2\frac{1}{r^2} - A_3\left(r^2v_w(r)\right)^{\frac{2-3n}{3n}} \times [v_c(r) - v_w(r)]^2\frac{|v_c(r) - v_w(r)|}{(v_c(r) - v_w(r))} + A_4\left(r^2v_w(r)\right)^{\frac{2-3n}{3n}}v_w(r), \quad (6)$$

where the factors A_1, A_2, A_3, and A_4 depend on the parameters of the star, the initial conditions, and physical constants.

Thus, computing the evolution of the condensation reduces to solving (6) with the initial conditions r_0, $\rho(r_0) = \rho_0$, $R_c(r_0) = R_0$, and $v_c(r_0) = v_w(r_0)$. These initial conditions are specified so that a condensation with radius R_0 and density ρ_0 is initially located a distance r_0 from the center of the star and is at rest relative to the moving medium.

The numerical solution of (6) also requires that external parameters that are independent of the presence of the condensation be specified: v_∞, v_0, β, $R_\star$, $L_\star$, $M_\star$, $\dot{M}$, T_w, and τ.

4. CALCULATIONS AND RESULTS

The table presents selected values of the external parameters that are characteristic of Wolf–Rayet stars.

Equation (6) was solved numerically for a broad range of initial densities and condensation radii. We did not consider condensations with initial radii exceeding $10^{-2}R_\star$, since they should substantially affect the state of the surrounding medium, making the problem much more complicated. Solutions were obtained for various initial distances of the condensation from the center of the star. We restrict the computational domain to the zone between the surface of the star and $15R_\star$.

Independent of the initial density of the cloud, the ratio of the densities of the condensation and surrounding gas $\alpha = \rho_c(r)/\rho_w(r)$ increases as the condensation moves in the medium, whose density decreases outwards. This is due to the chosen polytropic form of the equation of state for the condensation with polytrope index $n \geq 1$. α remains constant when $n = 1$. Figure 1 presents the variation of α with distance from the center of the star for various n.

The density of the cloud itself decreases substantially (by an order of magnitude) relative to its initial value. The radius of the cloud increases as it moves into the more rarefied outer layers of the atmosphere. Figures 2 and 3 present the variations of the condensation density and radius as a function of n. We can see that both parameters vary especially strongly at small distances from the stellar surface. This is due to

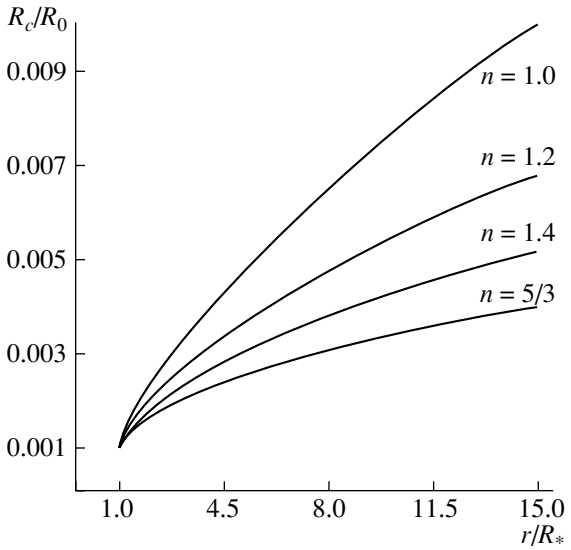

Fig. 3. Variation of the radius of the condensation with distance from the center of the star as a function of n. The curves were obtained for an initial density $\rho_0 = 10\rho_w(r_0)$ and condensation radius $R_0 = 10^{-3}R_\star$.

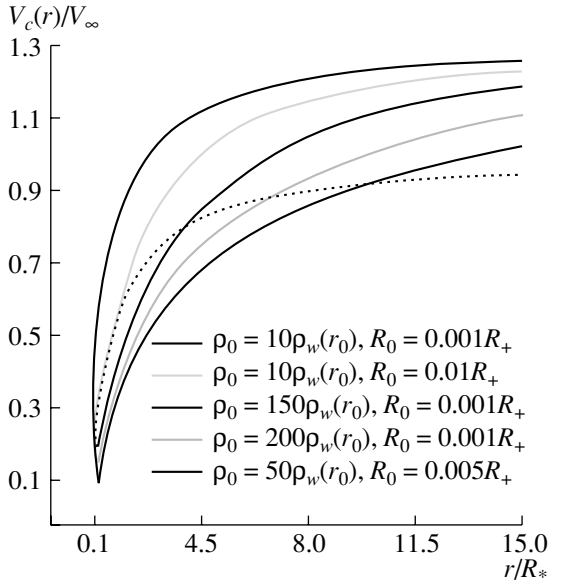

Fig. 4. Velocities of clouds as a function of distance from the center of the star. Each curve is marked with the corresponding initial radius and density of the cloud. All curves were calculated with $n = 1.2$. The dotted curve indicates the dependence between the cloud velocity and distance for the homogeneous component of the wind.

the law for variations of the velocity of the homogeneous wind $v_w(r)$ and, accordingly, its density, which undergo their strongest variations in this region of the atmosphere.

To illustrate this, Fig. 4 presents examples of the computed dependences of the condensation velocity $v_c(r)$. The general form of these curves is consistent with the results of [7]. The velocity of a condensation can be both higher and lower than the velocity of the homogeneous stellar wind. Note that the velocity of a cloud relative to the surrounding gas can reach substantial values.

The influence of the polytropic index n (2) in the dependence of the velocity of the condensation on distance from the center of the star is small. This dependence is basically specified by the initial radius and density of the cloud.

5. CONCLUSIONS

We have considered a model with homogeneous, spherical condensations and a polytropic equation of state. The physical conditions in the condensations vary substantially as they move in an accelerated medium with non-constant density and pressure. The density and radius of the condensation vary by several orders of magnitude compared to their initial values. The variations of the physical conditions in the condensation affect its parameters and should be taken into account in stellar-wind models and calculations of spectra. The condensations can move with substantial velocities relative to the surrounding gaseous flows. Thus, the clouds cannot be treated like static formations with constant characteristics that are at rest relative to the expanding atmosphere of the star.

These results can be considered a first step toward clarifying the mechanisms that give rise to the formation of inhomogeneities in the atmospheres of hot stars.

ACKNOWLEDGMENTS

The author is grateful to V. G. Gorbatskiĭ for useful comments. This work was supported by the Russian Foundation for Basic Research (project code 01-02-16858).

REFERENCES

1. A. M. Cherepashchuk, Kh. F. Khaliullin, and J. A. Eaton, Astrophys. J. **281**, 774 (1984).
2. I. I. Antokhin, A. F. Kholtygin, and A. M. Cherepashchyuk, Astron. Zh. **65**, 558 (1988) [Sov. Astron. **32**, 285 (1988)].
3. A. F. J. Moffat, S. Lépine, R. N. Henriksen, and C. Robert, Astrophys. Space Sci. **216**, 55 (1994).
4. T. Eversberg, S. Lépine, and A. F. J. Moffat, Astrophys. J. **494**, 799 (1998).
5. J. C. Brown, L. L. Richardson, I. Antochin, *et al.*, Astron. Astrophys. **295**, 725 (1995).
6. N. A. Kudryasheva and A. F. Kholtygin, Astron. Zh. **78**, 1 (2001) [Astron. Rep. **45**, 287 (2001)].
7. J. C. Howk, J. P. Cassinelli, J. E. Bjorkman, and H. J. G. L. M. Lamers, Astrophys. J. **534**, 348 (2000).
8. H. J. G. L. M. Lamers and J. P. Cassinelli, *Introduction to Stellar Winds* (Cambridge Univ. Press, Cambridge, 1999), p. 9.

Translated by K. Maslennikov

Astronomy Reports, Vol. 48, No. 2, 2004, pp. 112–120. Translated from Astronomicheskiĭ Zhurnal, Vol. 81, No. 2, 2004, pp. 134–142.

Axially Symmetrical Models of the Products of a Conservative Merger of a Binary White Dwarf with Similar-Mass Components

D. P. Savokhin

Astronomical Observatory, Ural State University, Yekaterinburg, Russia

Received June 28, 2003; in final form, August 8, 2003

Abstract—The possibility of a conservative merger of a binary white dwarf whose components have similar masses is studied. Axially symmetrical models for single, rapidly rotating white dwarfs that are possible products of such mergers are constructed and their physical characteristics investigated. The merger products must be turbulent, and the viscosity of the electron gas is not sufficient to support the observed luminosities of massive, bright white dwarfs. The amount of dissipative energy and the timescale for its release are estimated. © *2004 MAIK "Nauka/Interperiodica"*.

1. INTRODUCTION

The recent discovery of close binary white dwarfs [1] has stimulated numerous theoretical studies of the evolution of these systems. This is related, first and foremost, to the possibility of explaining observations of type Ia supernovas in old elliptical galaxies (whose stars have masses lower than $\sim 0.8 M_\odot$) as being associated with mergers of the components of close binary white dwarfs [2–4]. The origin of the recently discovered massive and very bright white dwarfs PG 0136+251, PG 1658+441, and GD 50 [5] with masses of 1.2, 1.3, and $1.2 M_\odot$ and luminosities $L = (6.7, 1.2, 9.7) \times 10^{-2} L_\odot$, respectively, also must be explained. This may be possible in a scenario with the merger of two low-mass dwarfs. Mergers of degenerate stars have also been considered as a possible origin for gamma-ray bursts (see, e.g., [6]).

The merger of the components of a binary white dwarf is accompanied by a number of complex physical processes: the radiation of gravitational waves, formation of a common envelope, accretion of matter, formation of a massive disk (torus), viscous transport of angular momentum in the merger product, release of the energy of viscous friction, nuclear burning of helium, carbon, and oxygen, and other processes. All of these play equally important roles. The process of coalescence and the properties of the merger product and its further evolution depend most strongly on the component-mass ratio before coalescence [7]. Only two dynamical computations of mergers of two white dwarfs have been carried out [5, 8] and have provided models for this process for a narrow range of parameters of the binary systems. Due to the complexity of the accompanying phenomena, mergers are often studied in another way: a steady-state model is computed for a merged configuration whose parameters (mass, angular momentum, energy) are close to those of the initial binary system. This paper is one such study.

In our paper [7], we focused on conservative mergers of binary components with mass ratios of $q = (0.35 - 0.55)$. However, according to population synthesis studies [1, 9], most binary white dwarfs should have components with similar masses. Therefore, the main channel for the formation of the progenitors of type Ia supernovas is mergers of carbon–oxygen white dwarfs with mass ratios q close to unity. Here, we turn our attention to binary white dwarfs with such mass ratios, $q = (1 - 0.6)$.

We have computed axially symmetric models for zero-temperature, strongly distorted, steady-state, rapidly differentially rotating white dwarfs for four rotation laws. The temperature corrections are small, even for very hot white dwarfs with $T \sim 10^8$ K [10], and can be neglected (they cannot be neglected in studies of the dynamics of coalescence accompanied by the formation of shock waves and carbon burning at the dwarf surface, when the temperature can rise to $\sim 10^9$ K). We found the total energy and angular momentum of a semidetached white-dwarf binary based on computations of models of the internal structure of the white dwarfs and a standard binary model with two point masses, assuming the rotation of the dwarfs to be synchronous with their orbital motion. By comparing the total energy and angular momentum of a single, massive, differentially rotating white dwarf with the energy and momentum of a semidetached white-dwarf binary with similar total mass, we can identify those binary systems that can produce single, massive, rapidly rotating dwarfs during their coalescence.

1063-7729/04/4802-0112$26.00

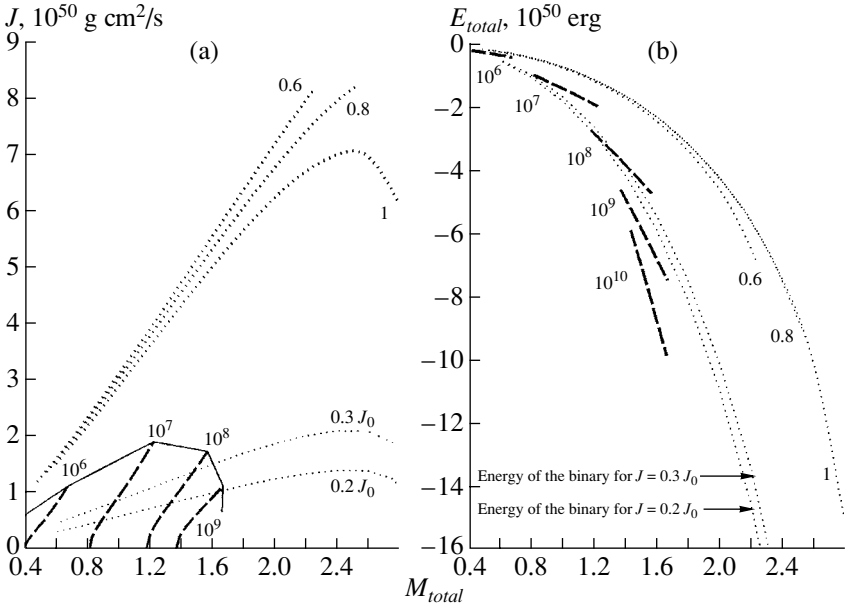

Fig. 1. (a) Angular momenta and (b) total energies of binary white dwarfs (dotted curves) and massive single white dwarfs (dashed curves) obeying rotation law (1) as a function of the mass of the system or dwarf. The numbers next to the dashed curves indicate the component-mass ratios q for the binary systems; the numbers by the dotted curves label the maximum density in the models (in g/cm^3). The dotted curves with the labels "0.3 J_0" and "0.2 J_0" show the momenta of binaries with $q = 1$ after the loss of 70% and 80% of their initial momentum J_0 via gravitational-wave radiation. The energy of these systems after the loss of these fractions of their initial momenta are shown by the two lower dotted curves at the right side of the plot.

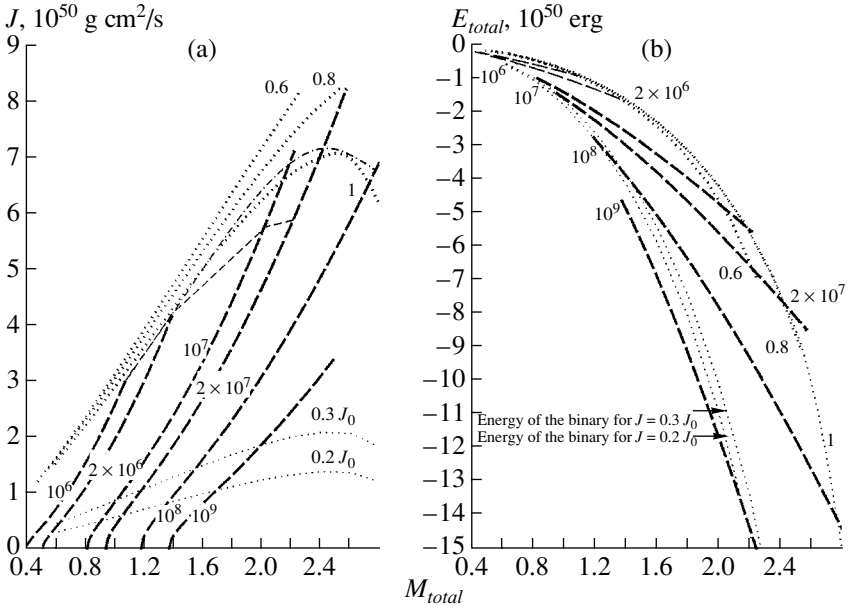

Fig. 2. Same as Fig. 1 for single dwarfs obeying rotation law (2). The dash–dot curve represents the upper boundary of the region of binary systems whose conservative mergers can produce single dwarfs obeying law (2). The thin dashed curve shows models of single dwarfs with the same total energy as that of semidetached binaries with component-mass ratios $q = 0.6$.

2. FORMULATION OF THE PROBLEM AND COMPUTATIONAL METHOD

We computed models for axially symmetric, strongly flattened white dwarfs in a state of stationary rapid rotation having the same angular momenta and total energy as contact or semidetached white-dwarf binaries with the same total masses. A rigorous mathematical formulation of this problem for such degenerate configurations and the method used in the computations are presented in detail in [7, 11]. Here,

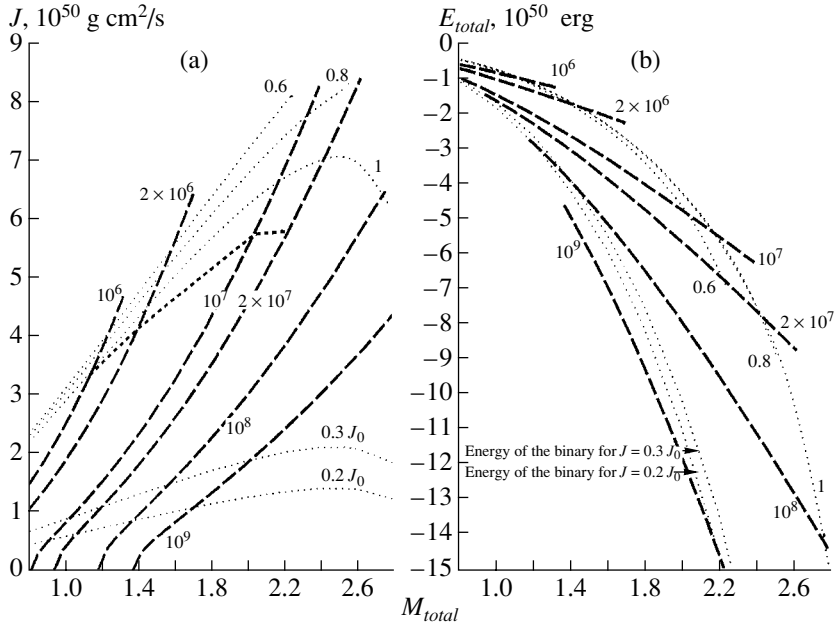

Fig. 3. Same as Fig. 1 for white dwarfs obeying rotation law (3). In this case, the dash–dot curve coincides with the dotted curve for $q = 1$. This curve and the thin dashed curve have the same meaning as the corresponding curves in Fig. 2 (see the text).

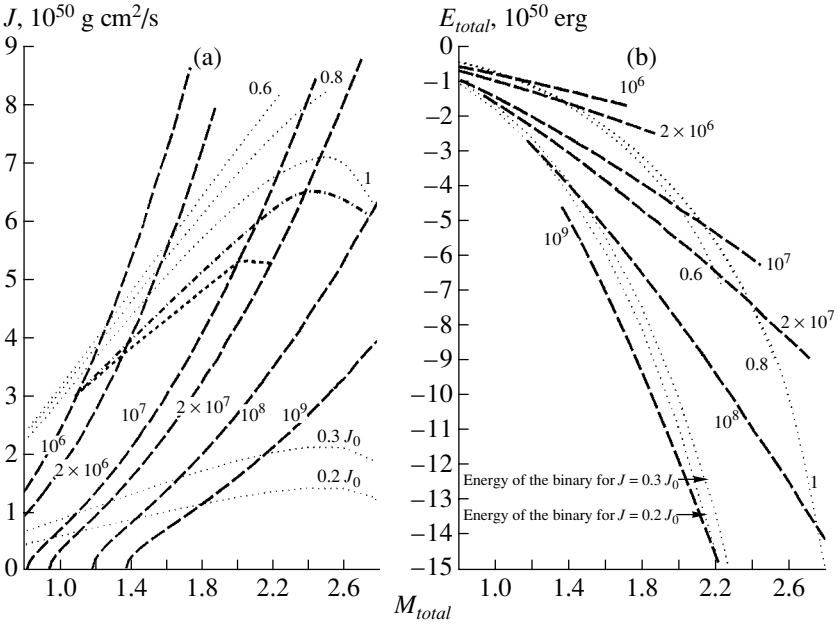

Fig. 4. Same as Fig. 1 for single white dwarfs obeying rotation law (4).

we are interested in the properties of dwarfs obeying cylindrical rotation laws:

$$\Psi(\overline{\omega}) \sim -\overline{\omega}, \tag{1}$$

$$\Psi(\overline{\omega}) \sim -\overline{\omega}^{0.4}, \tag{2}$$

$$\Psi(\overline{\omega}) \sim -\ln(\overline{\omega}), \tag{3}$$

$$\Psi(\overline{\omega}) \sim 1/\overline{\omega}, \tag{4}$$

where Ψ is the potential of the centrifugal forces, which is related to the angular velocity $\Omega(\overline{\omega})$ as

$$\Psi(\overline{\omega}) = -\int \Omega^2(\overline{\omega})\omega d\overline{\omega}, \tag{5}$$

where ϖ is the distance to the rotational axis. Law (3) corresponds to rotation for which the linear velocity inside the star is constant, while law (4) corresponds to rotation for which the angular velocity depends on the distance in a way similar to Keplerian rotation.

The accuracy of the computations was monitored using a virial test [7, 11]. For all the computed models, $VT \sim 10^{-4}$–10^{-5}.

3. MODELS OF THE WHITE-DWARF MERGER PRODUCTS

The white-dwarf models obeying rotation law (1) differ from those obeying laws (2)–(4) in the concentration of their specific angular momenta predominantly in outer layers, close to the equator. Therefore, as the angular momentum is increased, there comes a time when the effective acceleration at the equator becomes positive (this is qualitatively similar to rigid-body rotation). The solid broken curve in Fig. 1a roughly bounds from above the region containing models having $g_{eff} < 0$ that do not lose matter from their equator. In this case, the maximum possible angular momentum of the computed configurations is much lower than that of the binary system (Fig. 1a). Thus, it is not possible to produce a merged object that obeys law (1) or rotates according to a law with a centrifugal potential that decreases with distance from the rotational axis more slowly than (1) via the completely conservative coalescence of the components of a semidetached binary.

The white-dwarf models obeying rotation law (2) can be the products of conservative mergers of two white dwarfs with total masses of $1.6M_\odot < M_{total} < 2.8M_\odot$ (Fig. 2), if the merger occurs on the dynamical timescale (see below). The range of q in this case depends on M_{total}, and attains its largest value of $\sim$0.9–1 for $M_{total} = \sim(2.0$–$2.4)M_\odot$. In Fig. 2a, binaries producing white dwarfs obeying rotation law (2) as a result of conservative mergers are located in a narrow region bounded from above by the dash–dot curve and from below by the dotted curve corresponding to binaries with $q = 1$. Binaries outside this region can form single dwarfs if the merger is not conservative.

It is possible to compute white-dwarf models obeying law (3) and having masses, angular momenta, and total energies similar to those for semidetached white-dwarf binaries if q is in the narrow range $\sim$0.98–1 and the total mass is $M_{total} > \sim 1.1M_\odot$ (Fig. 3). If $q < 0.98$, single dwarfs with total masses and momenta similar to those of the corresponding binaries have higher total energies than those for the corresponding pair of white dwarfs (Fig. 3b), and their formation is energetically unfavorable. Thus, the formation of a merged dwarf from a binary with $q < 0.98$ is possible only in the nonconservative case.

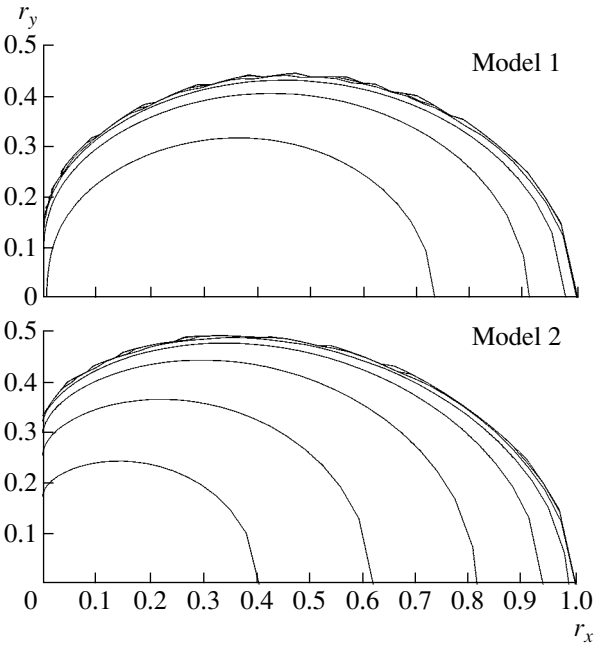

Fig. 5. Density distribution in two selected models. The density at two neighboring constant-density surfaces differs by a factor of ten. The properties of the models are given in Table 1.

Single white dwarfs obeying rotation law (4) and having masses and angular momenta similar to semidetached white-dwarf binaries have higher total energy (Fig. 4). Therefore, a completely conservative scenario for the formation of merger products obeying law (4) is not possible. Note that rotation law (4) has the highest central concentration of the specific angular momentum. Therefore, white dwarfs with masses and angular momenta similar to the binaries form toroidal configurations in which the space close to the rotational axis is not filled with matter.

The structure of a massive, differentially rotating white dwarf that can be produced by a conservative merger (if it occurs on a dynamical timescale) is shown in Fig. 5 (model 1). The properties of this model are given in Table 1.

4. THE COALESCENCE OF COMPONENTS

The process of coalescence depends on the component-mass ratio and the total mass of the system (Fig. 6).

Let us first consider the case $M_1 = M_2$. The approach of the components due to the radiation of gravitational waves turns a detached binary into a contact system. Since gravitational-wave radiation remains the only mechanism for the loss of angular

Table 1. Models of massive, differentially rotating dwarfs

Model	Rotation law	$M, M_\odot$	R_e, 10^9 cm	J, 10^{50} g cm^2/s	E_{total}, 10^{50} erg	$\rho_{\max}$, g/cm^3	L_{visc}, $L_\odot$	ε
1	2	2.1747	1.0645	6.8557	−5.362	1.01×10^7	0.06	0.0625
2	2	2.1747	0.2950	2.1071	−15.967	1.08×10^9	12.75	0.3025

Note: The columns present the model number, rotation-law number, mass M, equatorial radius R_e, angular momentum J, total energy E_{total}, maximum density $\rho_{\max}$, dissipative luminosity L_{visc}, and ratio of polar and equatorial radii ε. The models were computed using a grid with $(r, \theta) = 100 \times 80$ nodes and had virial tests with $VT \simeq 10^{-5}$–10^{-6}.

momentum (the magnetic stellar wind may play an important role, but we do not consider this mechanism here), the subsequent merger of the components will proceed, as before, on a timescale that is much longer than the dynamical timescale, $\tau_{dyn} \sim p_{orb} \sim$ 20 s, and is equal to the timescale for the loss of angular momentum via gravitational-wave radiation, τ_{gr}, which is $\sim 10^3$ yr for such systems [12]. During this time, the binary will initially have a dumbbell shape, then form a dwarf with a binary core and common envelope. The two cores will continue to approach one another due to the radiation of gravitational waves, which carry away most of the angular momentum and energy over a time of $\sim 10^3$ yr. It is possible that, at some point, the cores will merge into a single axially symmetric object. If the angular momentum of the system is $\sim 30\%$ of the initial momentum of the binary J_0 at the moment of coalescence (Figs. 1a, 2a, 3a, 4a), the merged, axially symmetric object will have the structure shown in Fig. 5 (model 2). The maximum density in such axially symmetric merger products (model 2 in Table 1) is very close to the density for which pulsational carbon burning can be initiated ($\sim 2 \times 10^9$ g/cm^3 [13]); this density can be attained as more angular momentum is lost.

Thus, the merger of binary components with equal masses occurs on long timescales, is determined by the radiation of gravitational waves, and is fundamentally nonconservative. We shall label this merger regime the gravitational-wave regime.

In contrast, computations of the merger dynamics carried out for $q = 0.75$ [8] and $q = 0.66$ [5] show that the coalescence of components with unequal or very different masses proceeds on the dynamical timescale. Since τ_{dyn} is very short, the binary does not have time to lose momentum, mass, or energy. Thus, the merger is conservative. It is convenient to label this the dynamically conservative regime. The dynamically conservative merger regime is possible due to the formation of a massive disk that is in contact with the primary. The total orbital angular momentum of the system is transferred to this disk.

An efficient, stable disk can exist only if it is located inside the inner critical surface of the primary. In the case of semidetached systems, the dimensions of the primary and its inner critical surface gradually become more similar as q increases from 0.75 to 1. Thus, the space available for the disk is diminished. On the other hand, the inner Lagrangian point (L_1) approaches the rotational axis of the system, so that the specific angular momentum of the matter lost by the secondary through the inner Lagrangian point is decreased. Analytical ballistic estimates show that the radius of the disk, which is determined by the angular momentum at L_1, very rapidly decreases as q approaches unity and becomes much smaller than the radius of the primary. As a consequence, the stream of matter from the inner Lagrangian point must impact the surface of the primary. The dynamical computations of [8] confirm this conclusion. Hence, the disk does not form when q becomes large enough. Thus, there must exist some q_{cr} above which the dynamically conservative merger regime does not occur. The value of q_{cr} is between 0.75 and 1. When $q > q_{cr}$, the coalescence must occur in the gravitational-wave regime. In Fig. 6, q_{cr} is represented by the line corresponding to binaries with $q = 0.95$. The precise value of q_{cr} must be determined via dynamical computations of the mergers. When $0.35 < q < 0.55$, the merger occurs in the dynamically conservative regime, with an intermediate stage with the formation of a massive torus [7]. The value $q = \sim 0.35$ is the lower limit for the dynamically conservative merger regime [7, 8]. When $q < 0.35$, the merger is again determined by the radiation of gravitational waves [8].

The merger of binaries with $q < 1$ will depend on the value of q_{cr}. If the critical component-mass ratio is indeed > 0.9, the dynamically conservative merger regime is possible for binaries with $0.9 < q < q_{cr}$; the mergers result in the formation of dwarfs obeying either rotation law (2) (Fig. 5; Table 1, model 1) or a law close to (2). In Fig. 6, the region occupied by such dwarfs is bounded from above by the curve $q = q_{cr} = 0.95$ and from below by the dash–dot curve. The merger of a binary with a component-

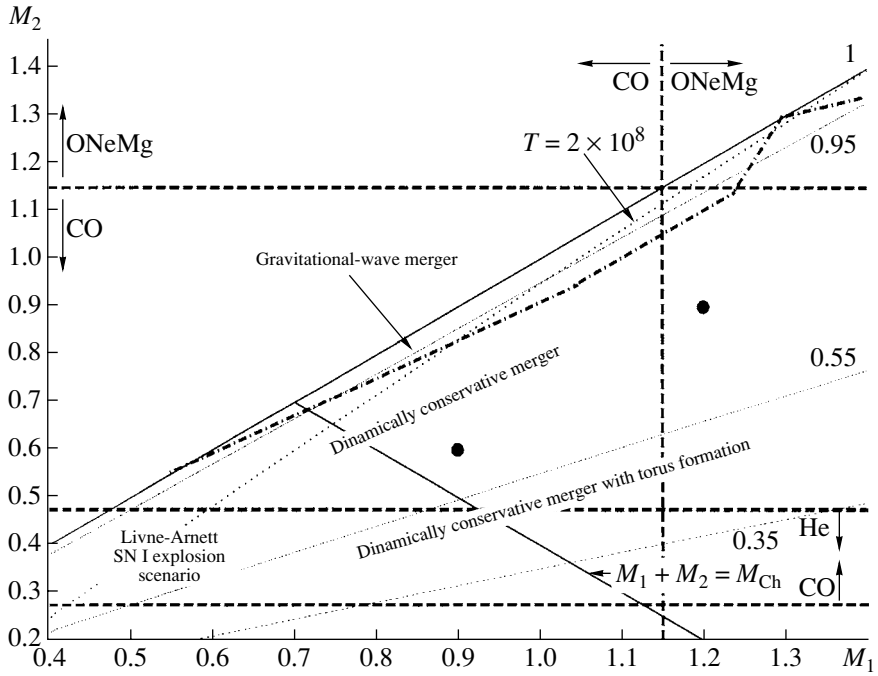

Fig. 6. Regions of various merger regimes in the plane of the masses M_1 and M_2 of the primary and secondary components of the binary white dwarfs. The dotted curve shows the positions of binaries in which the difference of the surface potentials is sufficient to heat matter to temperatures of 2×10^8 K. The dash–dot curve bounds from below the region of binaries for which conservative mergers are possible on the dynamical timescale. The dashed lines mark the boundaries between helium, carbon–oxygen, and oxygen–neon–magnesium dwarfs. The filled circles show the positions of binary systems for which the dynamics of the disruption of their less massive components were computed in [4] (right circle) and [5] (left circle).

mass ratio $q_{cr} < q < 1$ will proceed as follows. First, the components approach one another due to the radiation of gravitational waves to form a semidetached system on the timescale τ_{gr}. Next, unstable mass transfer will begin and a low-mass ($M_{env} \sim 0.01$–$0.001 M_\odot$) hot envelope with a temperature of $\sim 10^6$ K and luminosity $L \sim L_{Edd}$ will form around the primary [12]. This envelope tends to slow the process of accretion by the primary so that it extends over $\sim 10^4$ yr, but the timescale τ_{gr} is shorter, and the components continue to approach on the gravitational-wave radiation timescale [12]. As in the case of equal component masses, the merged configuration should initially have the shape of a dumbbell for $\sim 10^3$ yr, then evolve into a dwarf with a binary core surrounded by a common envelope.

The dynamically conservative coalescence of components resulting in the formation of a white dwarf obeying rotation laws (1)–(4) is not possible if $q < 0.9$.

Mergers of low-mass binaries ($M_1, M_2 < 0.5 M_\odot$) containing CO and He dwarfs are of considerable interest in relation to the new mechanism for type I supernovas recently suggested in [14, 15]. As was shown in [14, 15], the release of a small amount of energy at the bottom of the helium envelope of a hybrid white dwarf can produce a full-scale explosion of the star. This mechanism is efficient for a wide range of white dwarf masses, from at least $0.7 M_\odot$ to $1.1 M_\odot$, and has several advantages over other mechanisms. In the merger of a binary with $q < q_{cr}$, the maximum temperature in the merger product is attained at the boundary between the matter of the more massive component and the freshly accreted matter of the less massive star [5, 8]. This is due to two main factors: the formation of a shock at the surface of the primary at the place where the matter falls in from the secondary and viscous heating of the differentially rotating layers of the star. When the motion of the matter becomes turbulent, the viscosity can increase by several orders of magnitude. It is possible that these factors can lead to a substantial release of energy at the bottom of the helium envelope formed by the matter accreted from the less massive helium or hybrid component of the binary, thereby triggering the explosion of the merger product as a type I supernova. This possibility must be confirmed by dynamical computations of the mergers of low-mass components.

5. DISSIPATIVE LUMINOSITY OF THE MERGER PRODUCTS

Differential rotation results in the release of energy due to viscous friction. The amount of energy released

Table 2. Dissipative luminosities of differentially rotating white dwarfs

Model	Rotation law	$M, M_\odot$	$J, 10^{50}$ g cm^2/s	$L_{visc}, L_\odot$	$\rho_{\max}$, g/cm^3	$R_e, 10^9$ cm	ε
A	3	1.20	3.70	0.002	1.07×10^6	1.59	0.19
B	3	1.20	0.26	0.013	9.70×10^7	0.44	0.96
C	4	1.20	1.83	0.042	5.03×10^6	0.92	0.00
D	4	1.20	0.17	0.039	1.03×10^8	0.43	0.96

Note: The columns indicate the model designation, rotation law, mass M, angular momentum J, dissipative luminosity L_{visc}, maximum density $\rho_{\max}$, equatorial radius R_e, and ratio of polar and equatorial radii ε. The models were computed using a grid with $(r, \theta) = 50 \times 40$ nodes and had virial tests with $VT \sim 10^{-4}$–10^{-5}.

in the total volume of the star per unit time is [5]

$$L_{visc} = \frac{1}{2} \int \left(r \frac{d\Omega}{dr} \right)^2 \eta(r) dV, \qquad (6)$$

where η is the viscosity coefficient. We shall call this quantity the dissipative luminosity. The dissipative luminosity is, thus, determined by two factors: the rotation curve and the viscosity of the stellar material. We computed the dissipative luminosity for models 1 and 2 in Tables 1 and 2 assuming that η is the molecular viscosity of the electron gas, which is determined by the relations [5]

$$\eta_e = \begin{cases} 1.2 \times 10^{-5} \rho^{5/3} \text{ g cm}^{-1} \text{ s}^{-1} \\ \rho < 2 \times 10^6 \text{ g cm}^{-3} \\ 0.19 \rho \text{ g cm}^{-1} \text{ s}^{-1} \\ \rho > 2 \times 10^6 \text{ g cm}^{-3}. \end{cases} \qquad (7)$$

The high observed luminosities of the three known bright white dwarfs PG 0136+251, PG 1658+441, and GD 50 cannot be explained by the nuclear burning of carbon in their central regions or by hydrogen or helium burning at their surface layers because of their low temperatures (the observed surface temperatures are $\sim (30$–$40) \times 10^3$ K) and the high thermal conductivity of the electron gas that supports the virtually isothermal structure of the dwarf. The only possible means to support the high luminosities of these dwarfs is via the radiation of dissipative energy. Thus, the discovery of bright, massive white dwarfs, first, provides evidence for mergers of binary white dwarfs and, second, suggests that the merger products rotate differentially.

The dissipative luminosity of the white-dwarf models increases along the sequence of rotation laws (1)–(4) (with the remaining conditions being the same). In the case of the merger products of binaries with component-mass ratios considerably lower than q_{cr} displaying rigid-body rotation at their centers and quasi-keplerian rotation in their massive envelopes (as for the merger product obtained in [8]), the dissipative luminosity of the rigid-body core is zero. Therefore, models obeying law (4) will have the largest dissipative luminosity among models obeying the five different rotation laws. If we assume that the viscosity is determined by the molecular viscosity of the electron gas alone, it is possible to estimate the ability of the electron gas to support the high luminosity of the white dwarfs. For this purpose, we computed four white-dwarf models with masses $1.2 M_\odot$ and found their dissipative luminosities.

A comparison of the computed L_{visc} values with the observed luminosities of bright white dwarfs of similar mass (Table 2, see also the Introduction) shows that, if the viscosity is solely due to the electron gas and the white dwarf obeys rotation law (3), the dissipative luminosity is a factor of five to ten lower than is observed. The dissipative luminosities of models obeying the quasi-keplerian law (4) are consistent with the observed luminosities, but, as we have pointed out above, the conservative formation of objects obeying this law is not possible (nevertheless, models C and D in Table 2 display the maximum dissipative power of the electron gas). Thus, we can conclude that the viscosity of the material comprising the observed bright white dwarfs is higher than we have assumed, e.g., due to turbulence. A sufficient condition for the stability of the gas against turbulence is [16, 17]

$$\text{Ri} > 1/4, \qquad (8)$$

where Ri is the Richardson number, computed from the relation

$$\text{Ri} = \left(\frac{g_{eff}}{u_s} \right)^2 \left(1 - \frac{\gamma}{\Gamma} \right) \Big/ \left(r \frac{d\Omega}{dr} \right)^2, \qquad (9)$$

where g_{eff} is the effective acceleration of the matter, u_s is the sound speed, $\gamma = (d \ln P / d \ln \rho)$, and $\Gamma = 5/3$. Violation of (8) does not ensure turbulence of the

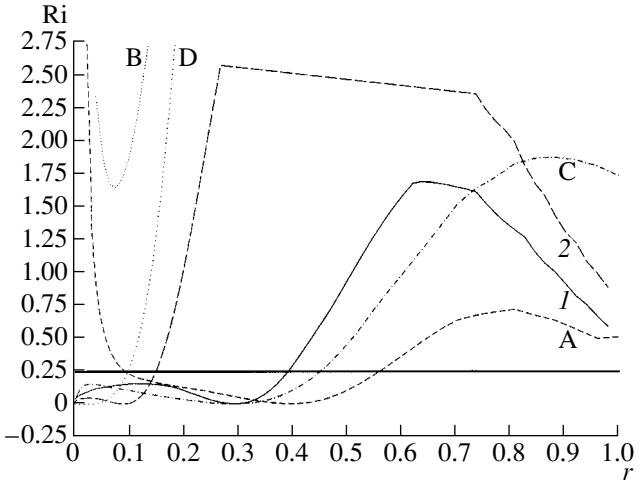

Fig. 7. Behavior of the Richardson number in the equatorial planes of six selected models (labeled by letters and numbers) as a function of the radial coordinate (in units of the equatorial radius).

flow but is a good indicator of the presence of turbulence. Figure 7 shows the behavior of the Richardson number for the models shown in Tables 1 and 2. It is clear that a considerable fraction (and, for models 1 A and C, the bulk) of the mass of the models must be in a state of turbulent motion.

It is possible to obtain a crude estimate for the timescale for the release of dissipative energy, τ_{diss}, from an estimate of the energy itself, E_{diss}, derived from the angular-velocity dispersion $\Delta\Omega$:

$$E_{diss} \sim \frac{1}{2} M R^2 (\Delta\Omega)^2. \qquad (10)$$

If $\Delta\Omega \sim \Omega_{surf} = 2\pi/P$, where P is the rotational period of the massive white dwarf, then

$$E_{diss} \sim 2\pi^2 M R^2 / P^2.$$

When $M \sim M_\odot$, $R \sim 0.01 R_\odot$, and $P \sim 20$ s, this relation gives $E_{diss} \sim 5 \times 10^{49}$ erg. For an observed luminosity of $L \sim 0.05 L_\odot$, the time required for the release of this energy is $\tau_{diss} \sim 3 \times 10^{17}$ s $\sim 10^{10}$ yr. This implies that a large number of merger products should be observed. In fact, three such white dwarfs have been discovered within ~ 40 pc of the Earth [5].

6. CONCLUSIONS

There exist two qualitatively different regimes for the merging of the components of white-dwarf binaries: a gravitational-wave regime and a dynamically conservative regime.

Binaries with component-mass ratios equal to or very close to unity merge in the gravitational-wave regime. The merger occurs on the timescale for the radiation of gravitational waves, $\sim 10^3$ yr, during which gravitational waves carry away nearly all the angular momentum. As a result, a white dwarf with a density sufficient for the ignition of carbon may form.

Binary white dwarfs with component-mass ratios lower than some q_{cr} merge in the dynamically conservative regime. The value of q_{cr} is in the range 0.75–1 and must be determined via dynamical computations of the coalescence process. The result of a merger in this regime is a dwarf surrounded by a massive disk that accumulates the total angular momentum of the binary. The maximum densities in such dwarfs are not sufficient for the ignition of carbon.

If $q_{cr} > 0.9$, the conservation laws do not rule out the formation of axially symmetric, differentially rotating white dwarfs from binaries with component-mass ratios $0.9 < q < q_{cr}$. The angular velocities in such dwarfs vary with the distance $\overline{\omega}$ to the rotational axis as $\Omega \sim \overline{\omega}^{-\alpha}$, $\alpha \sim 0.8$. An example of such a dwarf is shown in Fig. 5 (model 1), and its properties are listed in Table 1.

The viscosity of the electron gas is not sufficient to support the observed luminosities of massive, bright white dwarfs such as PG 0136+251, PG 1658+441, and GD 50. The main contribution to the total viscosity is apparently provided by the turbulent viscosity. The turbulence of the merger products is confirmed by estimates of the critical Richardson number. The amount of dissipative energy in the star due to differential rotation may be $\sim 10^{49}$ erg; this is sufficient to support a dwarf in a hot state with the observed luminosities for $\sim 10^{10}$ yr.

REFERENCES

1. G. Nelemans, L. R. Yungelson, S. F. Portegies Zwart, *et al.*, Astron. Astrophys. **365**, 491 (2001).
2. I. Iben and A. V. Tutukov, Astrophys. J. **282**, 615 (1984).
3. I. Iben and A. V. Tutukov, Astrophys. J., Suppl. Ser. **54**, 335 (1984).
4. A. G. Masevich and A. V. Tutukov, *Stellar Evolution: Theory and Observations* (Nauka, Moscow, 1988) [in Russian].
5. L. Segretain, G. Chabrier, and R. Mochkovitch, Astrophys. J. **481**, 355 (1997).
6. C. L. Frier, S. E. Woosley, M. Herant, *et al.*, Astrophys. J. **520**, 650 (1999).
7. D. P. Savokhin and E. I. Staritsyn, Astron. Zh. **79**, 534 (2002) [Astron. Rep. **46**, 481 (2002)].
8. W. Benz, R. L. Bowers, A. G. Cameron, *et al.*, Astrophys. J. **348**, 647 (1990).
9. G. Nelemans, F. Verbunt, L. R. Yungelson, *et al.*, Astron. Astrophys. **360**, 1011 (2000).
10. G. S. Bisnovatyĭ–Kogan, *Physical Aspects of the Theory of Stellar Evolution* (Nauka, Moscow, 1989) [in Russian].

11. A. G. Aksenov and S. I. Blinnikov, Astron. Astrophys. **290**, 674 (1994).
12. I. Hachisu, Y. Eriguchi, and K. Nomoto, Astrophys. J. **308**, 161 (1986).
13. N. V. Dunina-Barkovskaya, V. S. Imshennik, and S. I. Blinnikov, Pis'ma Astron. Zh. **27** (6), 412 (2001) [Astron. Lett. **27**, 353 (2001)].
14. E. Livne, Astrophys. J. **354**, L53 (1990).
15. E. Livne and D. Arnett, Astrophys. J. **452**, 62 (1995).
16. R. Mochkovitch and M. Livio, Astron. Astrophys. **209**, 111 (1989).
17. R. Mochkovitch and M. Livio, Astron. Astrophys. **236**, 378 (1990).

Translated by L. Yungel'son

Astronomy Reports, Vol. 48, No. 2, 2004, pp. 121–135. Translated from Astronomicheskiĭ Zhurnal, Vol. 81, No. 2, 2004, pp. 143–158.

Thermal Cyclotron Radiation by Isolated Magnetic White Dwarfs and Constraints on the Parameters of Their Coronas

V. V. Zheleznyakov, S. A. Koryagin*, and A. V. Serber

Institute of Applied Physics, Russian Academy of Sciences, ul. Ul'yanova 46, Nizhni Novgorod, 603600 Russia
**E-mail: koryagin@appl.sci-nnov.ru*

Received April 22, 2003; in final form, August 8, 2003

Abstract—An efficient method for the detection and estimation of the parameters of the coronas of isolated white dwarfs possessing magnetic fields of about 10^7 G is tested. This method is based on the detection of thermal radiation of the coronal plasma at harmonics of the electron gyrofrequency, which is manifest as a polarized infrared excess. The Stokes parameters for the thermal cyclotron radiation from the hot corona of a white dwarf with a dipolar magnetic field are calculated. A new upper limit for the electron density, 10^{10} cm^{-3}, in a corona with a temperature of $\gtrsim 10^6$ K is found for the white dwarf G99-47 (WD 0553+053). This limit is a factor of 40 lower than the value derived earlier from ROSAT X-ray observations. Recommendations for subsequent infrared observations of isolated magnetic white dwarfs aimed at detecting their coronas or deriving better constraints on their parameters are presented.

1. INTRODUCTION

Hot outer envelopes—coronas—exist in almost all types of stars. The most well known are the coronas of main-sequence stars. At the same time, it is unclear if coronas are present in isolated white dwarfs. Coronal X-ray emission has been reliably detected from only one isolated white dwarf, KPD 0005+5106 [1, 2]. This nonmagnetic white dwarf possesses a very hot photosphere with an effective temperature of $T_{\rm eff} = 1.2 \times 10^5$ K. The coronal temperature in KPD 0005+5106 was estimated to be about 2.6×10^5 K, only a factor of two greater than $T_{\rm eff}$. It is believed that the coronal plasma is heated by shock waves formed in supersonic plasma flow from the stellar surface [1, 3].

Along with KPD 0005+5106, about one hundred very hot ($T_{\rm eff} \gtrsim 2.5 \times 10^4$ K) isolated white dwarfs have been detected in the X-ray [4], but this radiation originates in their photospheres [5, 6]. In cooler objects ($T_{\rm eff} \lesssim 2.5 \times 10^4$ K), the X rays from deep photospheric layers are absorbed by the upper layers and do not escape from the star. Therefore, detecting X-ray radiation from these stars would provide unambiguous evidence for the presence of coronal envelopes in their atmospheres.

The theoretical calculations of [7, 8] show that a quite powerful flux of Alfven waves (of the order of 10^{10} erg cm^{-2}s^{-1}) is generated in the convective layers of relatively cool white dwarfs with strong magnetic fields ($T_{\rm eff} \sim 2 \times 10^4$ K, $B \gtrsim 10^4$ G), and this flux reaches the upper layers of the photosphere. The absorption of the Alfven waves can support the high temperature of coronas.

In their analysis of archival data of the *Einstein* Observatory for the five nearest cool, isolated, magnetic white dwarfs, Arnaud *et al.* [9] found with high (99%) probability that G99-47 (WD 0553+053) is a source of X rays with energies of 0.2–3.5 keV. The radiation flux derived from the archival data corresponds to an X-ray luminosity of 4.1×10^{27} erg/s and a coronal electron density of $n_{\rm e0} = 2.4 \times 10^{12}$ cm^{-3}. This last estimate was derived assuming that the observed X-ray flux is due to bremsstrahlung in a corona with low optical depth and temperature $T_{\rm cor} \simeq 10^7$ K. However subsequent observations of G99-47 by the ROSAT satellite did not confirm the *Einstein* data and provided only an upper limit for the luminosity of 1.03×10^{26} erg/s at 0.1–2.5 keV. Such a luminosity corresponds to an electron density of 4.6×10^{11} cm^{-3} in a corona with a temperature of 10^7 K [10].

Therefore, the available X-ray observations do not answer the question of whether isolated white dwarfs possess coronas. In particular, the sensitivity of modern X-ray detectors is sufficient to detect X-ray bremsstrahlung only from very dense coronas with electron densities several orders of magnitude greater than the density in the solar corona.

However, we can approach the problem of detecting the coronas of isolated white dwarfs in a completely different way. Due to the presence of magnetic fields of the order of several tens of millions of

Gauss in some white dwarfs (in particular, in G99-47) [11], emission features can be formed at harmonics of the electron gyrofrequency in the optical and infrared spectrum of a magnetic white dwarf surrounded by a hot corona with a sufficiently high particle density [12–14]. Cyclotron features can be observed even when the coronal electron density is substantially less than is required for the detection of X rays. For example, according to [14], a corona with an electron density of 2.4×10^{10} cm^{-3} and a temperature of 10^7 K would double the luminosity of G99-47 at wavelengths 4–8 μm, corresponding to the electron gyrofrequency for the magnetic field of this star. This shows that searching for cyclotron radiation in the infrared could be a very efficient and sensitive method for detecting the coronas of isolated white dwarfs possessing magnetic fields of about 10^7 G.

The cyclotron emission by a corona with low optical depth was calculated analytically in [15, 16]. The aim was to explain the polarization of the optical continua of strongly magnetized ($B \gtrsim 10^8$ G) white dwarfs.[1] Ingham *et al.* [16] considered thermal cyclotron radiation by a corona with low optical depth in local thermodynamic equilibrium (LTE), when the electron velocity distribution in the entire corona is an isotropic Maxwellian distribution with a constant temperature. The assumption of LTE is applicable only within a limited range of conditions and is often not satisfied by magnetic white dwarfs.

It was noted as early as in [16], and later in [12], that the characteristic lifetime of an electron in excited Landau levels in a magnetic white dwarf provided by cyclotron radiation,

$$t_c = 3mc^3/4e^2\omega_B^2,$$

is considerably shorter than the mean free time between successive collisions of the electron, $\nu_{\rm eff}^{-1}$. Here and below, m is the electron mass; $e > 0$, the elementary charge; c, the speed of light; and $\omega_B = eB/mc$, the electron gyrofrequency. If $\nu_{\rm eff} t_c \ll 1$, the system is not in LTE, and the distribution of electrons over the Landau levels is formed for the most part by radiation at the cyclotron frequency, with collisions resulting only in small adjustments. The acceptability of the assumption of LTE ($\nu_{\rm eff} t_c \gg 1$) is obviously violated in the upper layers of an isothermal corona with a barometric density profile [see (1)]. In this case, the intensity of the cyclotron radiation and the electron distribution over the Landau levels must be calculated in a self-consistent way.

[1] The continuum polarization is usually thought to be associated with the difference between the absorption coefficients (dichroism) of normal waves in the photospheres of the magnetic white dwarfs [17, 18].

The electron distribution over the Landau levels formed by spontaneous and induced radiative transitions at the first (fundamental) cyclotron harmonic, as well as by collisions, was found analytically in [13, 19, 20]. Expressions for the radiative power and the absorption coefficients of the normal waves at all the cyclotron harmonics used in our work were obtained in [20].

Note that the electron distribution in the velocity along the magnetic field, which is less affected by radiative processes, is taken to be specified both in [13, 19, 20] and in our analysis. In other words, some external source supports a constant longitudinal (along the magnetic field) electron temperature. The energy of this source is transformed into cyclotron emission from the white-dwarf corona. Analysis of particular mechanisms for field-aligned heating of electrons is beyond the scope of this paper.

The Stokes parameters for coronal thermal cyclotron emission are calculated below for the particular case of the isolated magnetic white dwarf G99-47. The results of these detailed calculations are compared with photometric observations of G99-47 in the infrared [21, 22]. As a result, we obtained an upper limit for the electron density in the corona of this white dwarf corresponding to a minimum value for the coronal kinetic temperature of $T_{\rm cor} \simeq 10^6$ K. This new upper limit is more than a factor of 40 lower than the value derived earlier from X-ray observations [10].

2. FORMULATION OF THE PROBLEM AND CALCULATION METHOD

G99-47 is a typical cool, magnetic white dwarf with a hydrogen photosphere. Only the Balmer Hα absorption line is observed in its optical spectrum [23]. The effective temperature $T_{\rm eff}$ determining the bolometric luminosity of the star is estimated to be 5790 ± 110 K [22, 24, 25]. The free-fall acceleration at the stellar surface is $g = (1.44–1.74) \times 10^8$ cm/s^2. G99-47 is located quite close to the Sun (at a distance of 8 pc [26]) and has been observed at various wavelengths from the radio [27] to the X-ray [9, 10].

The stellar magnetic field results in the Zeeman splitting of the Hα line, as well as polarization of the optical continuum of the order of 1% [28]. In a simple approximation, the magnetic field of G99-47 can be represented by a dipole located at the center of the star and producing a field $B_{\rm p} = 2.5 \times 10^7$ G at the magnetic poles [29]. The dipole axis is tilted by $\Theta_{\rm obs} = 120°$ to the direction toward the Earth. A more complex model of the magnetic field in the form of a dipole shifted from the stellar center was used in [28]. The best agreement between the observed and calculated polarizations of the radiation was achieved

when the dipole was shifted from the stellar center by about $0.14R_*$ (where $R_* = 10^9$ cm is the radius of the star) and inclined by $\Theta_{\rm obs} = 100^\circ \pm 5^\circ$ to the direction toward the Earth. Here, we calculate the cyclotron radiation of the corona for an arbitrary angle $\Theta_{\rm obs}$ and assume that the stellar magnetic field is produced by a dipole at the stellar center with $B_{\rm p} = 2.5 \times 10^7$ G.

Further, we assume that the corona is composed of fully ionized hydrogen plasma uniformly covering the entire surface of the white dwarf and that the field-aligned temperature of the electrons $T_{\rm cor}$ is constant throughout the corona. The distribution of the electron density in height z will then be described by the barometric formula

$$n_{\rm e} = n_{\rm e0} \exp(-z/H_{\rm cor}), \qquad (1)$$

where $n_{\rm e0}$ is the density at the base of the corona,

$$H_{\rm cor} = \frac{2k_{\rm B}T_{\rm cor}}{m_{\rm p}g} = 1.65 \times 10^6 \left(\frac{T_{\rm cor}}{10^6\ {\rm K}}\right) \times \left(\frac{g}{10^8\ {\rm cm/s^2}}\right)^{-1} {\rm cm}$$

is the scale height of the isothermal corona, $k_{\rm B}$ is the Boltzmann constant, $m_{\rm p}$ is the proton mass, and $g = 10^8$ cm/s^2 is the free-fall acceleration. Note that $H_{\rm cor}$ is considerably less than the distance

$$l_B \simeq \sqrt{2}\beta_{T_{\rm cor}} L_B = 6.12 \times 10^6 \left(\frac{T_{\rm cor}}{10^6\ {\rm K}}\right)^{1/2} \times \left(\frac{R_*}{10^9\ {\rm cm}}\right) {\rm cm}$$

at which the change in the electron gyrofrequency due to the vertical nonuniformity of the magnetic field is comparable to the Doppler width of the cyclotron line (here and below, $\beta_{T_{\rm cor}} = \sqrt{k_{\rm B}T_{\rm cor}/mc^2}$ is the ratio of the thermal velocity of the electrons to the speed of light c and $L_B \simeq R_*/3$ is the characteristic spatial scale of the stellar dipolar magnetic field). [2] Accordingly, we shall take into account only nonuniformity of the magnetic field over the stellar surface, neglecting its variation with height of the corona (or, more precisely, along any ray inside the corona).

We shall assume that no radiation is incident at the upper boundary of the corona and that the lower boundary is irradiated by unpolarized radiation from the photosphere, whose spectral intensity is given by a Planck law with temperature $T_{\rm eff} = 5700$ K:

$$B^*_\omega(\omega; T_{\rm eff}) = \frac{\hbar\omega^3/4\pi^3c^2}{\exp(\hbar\omega/k_{\rm B}T_{\rm eff}) - 1},$$

where $\hbar$ is Planck's constant.

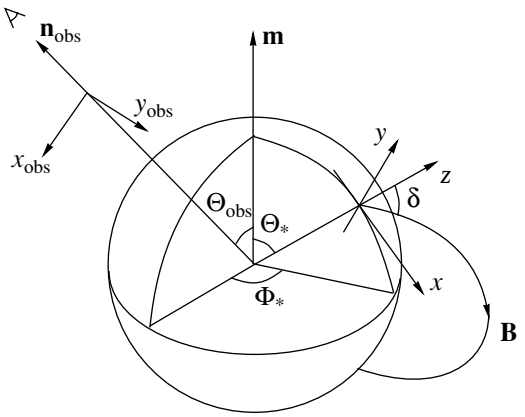

Fig. 1. Coordinate systems used to calculate the coronal cyclotron radiation.

In the adopted model, the observed coronal cyclotron radiation is determined by the six parameters $B_{\rm p}$, g, $T_{\rm eff}$, $n_{\rm e0}$, $T_{\rm cor}$, and $\Theta_{\rm obs}$ and is described by the well-known Stokes parameters F, Q, U, and V. Here, F is the spectral density of the energy flux of the radiation received, and the ratios $V/F = \zeta_{\rm c}$ and $\sqrt{Q^2+U^2}/F = \zeta_{\rm l}$ are the degrees of circular and linear polarization, respectively. In general, Q and U depend on the choice of coordinate system in the plane of the sky. They also determine the orientation of the polarization ellipse with respect to the axes of this system. As follows from the symmetry of this system, the axes of the polarization ellipse are directed along and across the projection of the stellar magnetic dipole onto the plane of the sky. Consequently, it is convenient to use the plane-of-the-sky Cartesian coordinate system $x_{\rm obs}, y_{\rm obs}$ shown in Fig. 1. The $x_{\rm obs}$ axis is directed opposite to the projection of the stellar magnetic dipole onto the plane of the sky; the basis vector $\mathbf{y}^\circ_{\rm obs} = [\mathbf{n}_{\rm obs}, \mathbf{x}^\circ_{\rm obs}]$ forms a right-handed system with the unit vector $\mathbf{n}_{\rm obs}$ directed toward the observer and the basis vector $\mathbf{x}^\circ_{\rm obs}$. In this system, $U = 0$ and the degree of linear polarization is $\zeta_{\rm l} = |Q|/F$. If Q is positive and negative, the major axis of the polarization ellipse is directed along and perpendicular to the projection of the stellar magnetic dipole onto the plane of the sky. According to the definition of the Stokes parameters [32, 33], positive values of V correspond to right-hand circular polarization, when the electric-field vector rotates in the counterclock-

[2] The quantity l_B is of the order of the thickness of the so-called gyroresonant layer in a fairly large region of plasma (whose size is much greater than l_B). The gyroresonant layer is responsible for the cyclotron radiation and absorption of photons with frequency ω propagating at the angle α with respect to the direction of the magnetic field, whose characteristic scale for nonuniformity is L_B (for more details, see, for example, [30] and [31, § 19.3]).

wise direction if the observer looks at the source of radiation.

The position of a point on the stellar surface can be described in the spherical coordinate system shown in Fig. 1. The magnetic latitude Θ_* is measured from the north magnetic pole, and the longitude Φ_* is measured from the plane specified by the stellar magnetic dipole $\mathfrak{m}$ and the line of sight $\mathbf{n}_{\rm obs}$.

The coronal cyclotron radiation at frequency ω is formed in narrow regions of latitude on the stellar surface (in regions of efficient radiation), where one of the harmonics $s\omega_B$ of the local gyrofrequency

$$\omega_B = \omega_{B_{\rm p}}\sqrt{1+3\cos^2\Theta_*}/2$$

is close to ω (here, $\omega_{B_{\rm p}} = eB_{\rm p}/mc$ is the electron gyrofrequency at the magnetic pole). Inside a region of efficient radiation, there is a resonant interaction between the photons and thermal electrons, whose normalized momentum along the magnetic field has the magnitude

$$\frac{p_{||}}{\sqrt{2}mc\beta_{T_{\rm cor}}} \equiv \xi = \frac{\omega - s\omega_B}{\sqrt{2}\beta_{T_{\rm cor}}\omega\cos\alpha_{\rm obs}} \qquad (2)$$

less than on the order of unity. Here,

$$\cos\alpha_{\rm obs} = \frac{(3\cos^2\Theta_* - 1)\cos\Theta_{\rm obs} + 3\cos\Theta_*\sin\Theta_*\cos\Phi_*\sin\Theta_{\rm obs}}{\sqrt{1+3\cos^2\Theta_*}}, \qquad (3)$$

$\alpha_{\rm obs}$ is the angle between the direction of the local magnetic field and the direction of propagation of the radiation (the line of sight $\mathbf{n}_{\rm obs}$). Beyond the region of efficient radiation, the speed of the resonant electrons is substantially greater than the thermal speed, and the optical depth of the corona at a fixed frequency tends to zero.

If the frequency ω is in the interval $s\omega_{B_{\rm p}}/2 \lesssim \omega \lesssim s\omega_{B_{\rm p}}$, there are two regions of efficient radiation at the sth harmonic, which are located in the northern and southern hemispheres symmetrically about the magnetic equator and have the characteristic size in latitude $\Delta\Theta_* \sim \beta_{T_{\rm cor}} \ll 1$. As the frequency ω decreases, these two regions shift toward the equator and merge at $\omega = s\omega_{B_{\rm p}}/2$. The magnetic field has a minimum at the equator and varies more slowly with latitude, so that the characteristic width of the equatorial region of efficient radiation increases to $\Delta\Theta_* \sim \sqrt{\beta_{T_{\rm cor}}}$. As ω continues to decrease, this region shrinks near the equator and disappears when the frequency ω is less than $s\omega_{B_{\rm p}}/2$ by about $\beta_{T_{\rm cor}}s\omega_{B_{\rm p}}$, which is the Doppler width of the cyclotron line at the sth harmonic. As ω increases, the regions of efficient radiation shift toward the magnetic poles and, at $\omega = s\omega_{B_{\rm p}}$, they shrink near the poles to spots with a characteristic size in latitude $\Delta\Theta_* \sim \sqrt{\beta_{T_{\rm cor}}}$. When the difference $\omega - s\omega_{B_{\rm p}}$ becomes a factor of a few greater than $\beta_{T_{\rm cor}}s\omega_{B_{\rm p}}$, the spots disappear.

If $\Delta\Theta_* \ll 1$, the regions of efficient radiation of different harmonics s do not intersect: they are separated by extensive regions of the stellar surface where the corona is transparent to radiation at the frequency ω. This enables us to represent the excess observed radiation flux with respect to the photospheric continuum $F - F_{\rm ph}$ and the Stokes parameters Q and V in the form

$$\frac{F-F_{\rm ph}}{F_{\rm ph}} = \sum_{s=1}^{s_{\max}}\int\limits_{\cos\vartheta_{\rm obs}>0}\frac{I_{s1}^{\rm out}+I_{s2}^{\rm out}-B_\omega^*}{\pi B_\omega^*} \times\cos\vartheta_{\rm obs}{\rm d}\Phi_*{\rm d}\cos\Theta_*, \qquad (4)$$

$$\frac{Q}{F_{\rm ph}} = \sum_{s=1}^{s_{\max}}\int\limits_{\cos\vartheta_{\rm obs}>0}\frac{I_{s1}^{\rm out}-I_{s2}^{\rm out}}{\pi B_\omega^*} \times(e_{sx}e_{sx}^* - e_{sy}e_{sy}^*)\cos\vartheta_{\rm obs}{\rm d}\Phi_*{\rm d}\cos\Theta_*,$$

$$\frac{V}{F_{\rm ph}} = \sum_{s=1}^{s_{\max}}\int\limits_{\cos\vartheta_{\rm obs}>0} i\frac{I_{s1}^{\rm out}-I_{s2}^{\rm out}}{\pi B_\omega^*} \times(e_{sx}e_{sy}^* - e_{sx}^*e_{sy})\cos\vartheta_{\rm obs}{\rm d}\Phi_*{\rm d}\cos\Theta_*.$$

Here, $I_{s1}^{\rm out}$ and $I_{s2}^{\rm out}$ are the intensities of the extraordinary and ordinary radiation at the sth harmonic outgoing from the corona, and the summation over s is limited to the harmonic $s_{\max}$, above which the coronal cyclotron radiation is negligible.

The integration in (4) is carried out over the entire observable surface of the star, which is defined by the condition that

$$\cos\vartheta_{\rm obs} = \cos\Theta_*\cos\Theta_{\rm obs} + \sin\Theta_*\cos\Phi_*\sin\Theta_{\rm obs} \qquad (5)$$

be positive ($\vartheta_{\rm obs}$ is the angle between the line of sight $\mathbf{n}_{\rm obs}$ and the normal vector $\mathbf{z}^\circ$ to the stellar surface at the point of integration). Strictly speaking, integrals (4) for fixed s are calculated not only over the regions of efficient radiation at the sth harmonic but also over the corresponding regions for other harmonics; however, this does not change the results appreciably, since the integrands in (4) fall to zero very rapidly with

increasing distance of the point of integration from the regions of efficient radiation at the sth harmonic. The integrals are equal to zero when the region of effective radiation at the sth harmonic is essentially absent (i.e., when the frequency ω is greater than $s\omega_{B_\mathrm{p}}$ or less than $s\omega_{B_\mathrm{p}}/2$ by several $\beta_{T_\mathrm{cor}} s\omega_{B_\mathrm{p}}$).

The coefficients

$$e_{sx} = \frac{h_y + iK_{s1}h_x}{\sqrt{(1+K_{s1}^2)(h_x^2+h_y^2)}}, \qquad (6)$$

$$e_{sy} = \frac{iK_{s1}h_y - h_x}{\sqrt{(1+K_{s1}^2)(h_x^2+h_y^2)}}$$

in (4) represent the components of the unit vector $\mathbf{e}_s = e_{sx}\mathbf{x}^\circ_\mathrm{obs} + e_{sy}\mathbf{y}^\circ_\mathrm{obs}$ of the polarization of the extraordinary wave at the sth harmonic, where

$$h_x = \frac{3\cos\Theta_*\sin\Theta_*\cos\Phi_*\cos\Theta_\mathrm{obs} + (1-3\cos^2\Theta_*)\sin\Theta_\mathrm{obs}}{\sqrt{1+3\cos^2\Theta_*}}, \quad h_y = \frac{3\cos\Theta_*\sin\Theta_*\sin\Phi_*}{\sqrt{1+3\cos^2\Theta_*}} \qquad (7)$$

are the components of the unit vector $\mathbf{h} = h_x\mathbf{x}^\circ_\mathrm{obs} + h_y\mathbf{y}^\circ_\mathrm{obs} + \cos\alpha_\mathrm{obs}\mathbf{n}_\mathrm{obs}$ along the magnetic field at the point (Θ_*, Φ_*) in the coordinate system of the observer. The coefficient

$$K_{s1} = \frac{2s\cos\alpha_\mathrm{obs}}{\sin^2\alpha_\mathrm{obs} + \sqrt{\sin^4\alpha_\mathrm{obs} + 4s^2\cos^2\alpha_\mathrm{obs}}} \qquad (8)$$

gives the ratio of the amplitudes $E_{||}$ and $E_\perp$ of the electric field in the extraordinary wave along and across the projection of the magnetic field onto the plane of the sky: $|E_{||}/E_\perp| = |K_{s1}|$ [31, § 5.2]. The polarization vector of the ordinary wave, $e^*_{sy}\mathbf{x}^\circ_\mathrm{obs} - e^*_{sx}\mathbf{y}^\circ_\mathrm{obs}$, is orthogonal to the polarization vector $\mathbf{e}_s$ of the extraordinary wave, so that the difference of the wave intensities I^out_{s1} and I^out_{s2} appears in the expressions for Q and V in (4). The asterisks in the superscripts of the components e_{sx} and e_{sy} in (4) and the subsequent expressions denote complex conjugation, and i is the imaginary unity.

Using (6) and (7), we can write explicit expressions for the factors $e_{sx}e^*_{sx} - e_{sy}e^*_{sy}$ and $i(e_{sx}e^*_{sy} - e^*_{sx}e_{sy})$ in (4) in terms of the quantities h_x and h_y:

$$e_{sx}e^*_{sx} - e_{sy}e^*_{sy} = \frac{(1-K_{s1}^2)(h_y^2-h_x^2)}{(1+K_{s1}^2)(h_x^2+h_y^2)},$$

$$i(e_{sx}e^*_{sy} - e^*_{sx}e_{sy}) = \frac{2K_{s1}}{1+K_{s1}^2}.$$

To calculate the intensities I^out_{s1} and I^out_{s2} of the radiation leaving the corona at the point (Θ_*, Φ_*), we approximate the corona by a plane-parallel plasma layer in a uniform magnetic field whose absolute value $B = B_\mathrm{p}\sqrt{1+3\cos^2\Theta_*}/2$ and inclination to the vertical z axis

$$\delta = \arccos\left(\frac{2\cos\Theta_*}{\sqrt{1+3\cos^2\Theta_*}}\right)$$

coincide with the corresponding values for the stellar dipole field at this point (Fig. 1). The direction of the vector $\mathbf{n}_\mathrm{obs}$ at the point (Θ_*, Φ_*) is described by the same angles, α_obs and ϑ_obs [see (3) and (5)].

If $\eta_{sl}(\tau, \xi, \mathbf{n}_\mathrm{obs})$ is the radiative power and $\chi_{sl}(\tau, \xi, \mathbf{n}_\mathrm{obs})$ is the absorption coefficient of the normal wave l at the sth harmonic in the direction $\mathbf{n}_\mathrm{obs}$,[3] then

$$I^\mathrm{out}_{sl} = \frac{B^*_\omega(T_\mathrm{eff})\exp(-\tau_{sl}(\tau_0))}{2} + \int_0^{\tau_{sl}(\tau_0)} S_s\exp(-\tau_{sl})\mathrm{d}\tau_{sl}, \qquad (9)$$

where $S_s(\tau, \xi) = \eta_{sl}(\tau, \xi, \mathbf{n})/\chi_{sl}(\tau, \xi, \mathbf{n})$ and

$$\tau_{sl}(\tau, \xi, \mathbf{n}_\mathrm{obs}) = \int_{z(\tau)}^{+\infty} \frac{\chi_{sl}\mathrm{d}z}{\cos\vartheta_\mathrm{obs}} = \int_0^\tau \frac{\chi_{sl}(\tau', \xi, \mathbf{n}_\mathrm{obs})}{\cos\vartheta_\mathrm{obs}}\left|\frac{\mathrm{d}z}{\mathrm{d}\tau'}\right|\mathrm{d}\tau' \qquad (10)$$

are the corresponding source function and optical depth,

$$\tau(z) = \frac{4\sqrt{2}\pi^2e^2}{3mc\beta_{T_\mathrm{cor}}\omega_B}\int_z^{+\infty} n_\mathrm{e}\mathrm{d}z = 1.14\times10^3\left(\frac{n_\mathrm{e}(z)}{10^{10}\ \mathrm{cm}^{-3}}\right)\left(\frac{B}{10^7\ \mathrm{G}}\right)^{-1} \qquad (11)$$

[3] Here and below, the subscripts $l = 1$ and $l = 2$ denote quantities characterizing the extraordinary and ordinary waves, respectively. The quantity ξ, defined by (2), will be used as a frequency variable: $\omega = s\omega_B/(1-\sqrt{2}\beta_{T_\mathrm{cor}}\xi\cos\alpha_\mathrm{obs})$.

$$\times \left(\frac{g}{10^8\ \mathrm{cm/s^2}}\right)^{-1} \left(\frac{T_{\mathrm{cor}}}{10^6\ \mathrm{K}}\right)^{1/2}$$

is the characteristic optical depth to the extraordinary wave at the first harmonic, which is used to specify the height z of a point in the corona, and $\tau_0 = \tau(z=0)$ is the corresponding optical depth of the entire corona.

The radiative-transport coefficients η_{sl} and χ_{sl} depend on the electron distribution over the Landau levels, which is determined by the radiation at the first cyclotron harmonic and Coulomb collisions. These quantities were found in [19], taking into account only collisions and the radiation of the extraordinary wave at the first cyclotron harmonic.

The formulas of [19] can easily be generalized to the case when the effect of the ordinary wave of the first cyclotron harmonic on the electron distribution is also taken into consideration [20, 34]:

$$S_s(\tau,\xi) = \frac{\hbar\omega^3}{8\pi^3c^2}\sum_{k=0}^{s}\frac{\bar{q}^{s-k}p^k}{k!\prod_{r=k}^{s}(\bar{\epsilon}+r)} \Bigg/ \sum_{k=0}^{s}\frac{(1+\bar{q})^{s-k}(1+p)^k - \bar{q}^{s-k}p^k}{k!\prod_{r=k}^{s}(\bar{\epsilon}+r)}, \tag{12}$$

$$\chi_{sl}(\tau,\xi,\mathbf{n})\left|\frac{\mathrm{d}z}{\mathrm{d}\tau}\right| = \phi(\xi)\frac{3(1+K_{sl}\cos\alpha)^2}{4(1+K_{sl}^2)\,|\cos\alpha|}\left(\frac{s^2\hbar\omega_B\sin^2\alpha}{2mc^2}\right)^{s-1}\sum_{k=0}^{s}\frac{(1+\bar{q})^{s-k}(1+p)^k - \bar{q}^{s-k}p^k}{\bar{\epsilon}^{-1}k!\prod_{r=k}^{s}(\bar{\epsilon}+r)}. \tag{13}$$

Here, $\phi(\xi) = \exp(-\xi^2)/\sqrt{\pi}$ is the Doppler profile of the cyclotron line;

$$\bar{q}(\tau,\xi) = \frac{2\pi^2c^2\oint_{4\pi}\left[\Psi_{11}(\alpha)I_{11}(\tau,\xi,\mathbf{n}) + \varpi(\xi)\Psi_{12}(\alpha)I_{12}(\tau,\xi,\mathbf{n})\right]\mathrm{d}\mathbf{n}}{\hbar\omega_B^3\,(1+\varpi(\xi))} \tag{14}$$

is the mean number of photons near the first cyclotron harmonic characterized by the same normalized momentum ξ; the functions

$$\Psi_{11}(\alpha) = \frac{3\left(1+\cos^2\alpha\right)}{4},$$

$$\Psi_{12}(\alpha) = \frac{24\sin^4\alpha\left(1+2\cos^2\alpha\right)^2}{(147\pi-448)\left(1+\cos^2\alpha\right)^3}$$

are the normalized (to unity) directivity diagrams for radiation by an electron of the extraordinary and ordinary waves at the first cyclotron harmonic in a rarefied plasma; the parameter

$$\varpi(\xi) = \frac{(147\pi-448)\,\beta_{T_{\mathrm{cor}}}^2}{16\pi\,|w(\xi)|^2}$$

represents the ratio of the powers of spontaneous radiation by an electron in the ordinary and extraordinary waves at the first cyclotron harmonic, where $w(\xi)$ is the Kramp function [35, formula (7.1.3)];

$$p(T_{\mathrm{cor}}) = \frac{1}{\exp(\hbar\omega_B/k_{\mathrm{B}}T_{\mathrm{cor}})-1}$$

is the equilibrium number of photons in one normal wave at the first cyclotron harmonic at the temperature T_{cor};

$$\bar{\epsilon}(\tau) = \frac{\epsilon(\tau)}{1+\varpi(\xi)}$$

is the normalized thermalization parameter, where $\epsilon = \nu_{\mathrm{eff}}t_{\mathrm{c}}$;

$$\nu_{\mathrm{eff}} = \frac{8\sqrt{\pi}(\sqrt{2}+1)e^4n_{\mathrm{e}}L}{15m^{1/2}\,(k_{\mathrm{B}}T_{\mathrm{cor}})^{3/2}} \tag{15}$$

is the effective rate of Coulomb collisions, which characterizes the rate at which the field-aligned and transverse electron temperatures are equalized and is determined by both electron–ion and electron–electron collisions; and $L = \ln(r_B/\lambda_{\mathrm{B}})$ is the Coulomb logarithm, where $r_B = v_T/\omega_B$ is the Larmor radius and $\lambda_{\mathrm{B}} = \hbar/mv_T$ is the de Broglie wavelength for an electron with the characteristic thermal velocity $v_T = \sqrt{k_{\mathrm{B}}T_{\mathrm{cor}}/m}$.[4]

The parameter K_{s1} in (13) is determined by (8), and $K_{s2} = -1/K_{s1}$. The factor $3(1+K_{12}\cos\alpha)^2/[4\times(1+K_{12}^2)|\cos\alpha|]$ in the coefficient (13) is formally zero for the ordinary wave at the first cyclotron harmonic ($s=1$, $l=2$). In this case, this factor must be replaced by the more accurate expression $\varpi(\xi)\Psi_{12}(\alpha)/|\cos\alpha|$ [19, 38].

The distribution (14) for the mean number of photons $\bar{q}(\tau,\xi)$ determining the source functions (12) and the absorption coefficients (13) can be found from the solution of the system of integro-differential transfer equations [34] for the intensities $I_{11}(\tau,\xi,\mathbf{n})$ and

[4] Note that expression (15) for the collision rate is valid only when $T_{\mathrm{cor}} \gtrsim 10^5$ K. The collision rate changes radically in the photospheres of cool magnetic white dwarfs [31, 36, 37].

$I_{12}(\tau,\xi,\mathbf{n})$:

$$\cos\vartheta\frac{\partial I_{11}(\tau,\xi,\mathbf{n})}{\partial\tau}=\frac{\phi(\xi)\Psi_{11}(\alpha)}{|\cos\alpha|}\times\left(I_{11}(\tau,\xi,\mathbf{n})-S_1(\tau,\xi)\right), \quad (16)$$

$$\cos\vartheta\frac{\partial I_{12}(\tau,\xi,\mathbf{n})}{\partial\tau}=\frac{\phi(\xi)\varpi(\xi)\Psi_{12}(\alpha)}{|\cos\alpha|}\times\left(I_{12}(\tau,\xi,\mathbf{n})-S_1(\tau,\xi)\right)$$

taking into account resonant cyclotron scattering at the first harmonic.

The transfer equations (16) are solved in the interval $0\le\tau\le\tau_0$ with the boundary conditions

$$I_{1l}(\tau=0,\xi,\cos\vartheta<0)=0,$$
$$I_{1l}(\tau=\tau_0,\xi,\cos\vartheta>0)=B^*_\omega(\omega_B;T_{\rm eff})/2.$$

The first boundary condition indicates that there is no radiation incident at the upper boundary of the corona. The second boundary condition corresponds to irradiation of the lower boundary of the corona by photospheric blackbody radiation with temperature $T_{\rm eff}$.

A numerical solution of system of equations (16) was obtained using the method of Feautrier with variable Eddington factors, as is described in [39, 40].[5] The optical depth τ was covered using an approximately logarithmic grid containing about 80 nodes per decade of optical depth at the center of the cyclotron line (at $\xi=0$). A special grid whose density increased near the directions $\mathbf{n}$ perpendicular to the magnetic field or the normal vector to the layer was developed for the numerical integration over the solid angle in (16). This enabled us to take into account the sharp angular variations in the radiation intensity near these directions.

The intensities of the outgoing radiation $I^{\rm out}_{s1}$ and $I^{\rm out}_{s2}$ in (4) were calculated using (9). The numerical method enables us to integrate exactly the piecewise-linear functions S_s of the optical depth τ_{sl} (this is analogous to integrating using the trapezoid formula in the case when the integrands have exponential weights).

The numerical integration over the stellar surface in (4) for the required Stokes parameters was carried out successively over the variables $\cos\Theta_*$ (outer) and Φ_* (inner) using the adaptive procedure [41], which automatically increases the density of the integration grid near the regions of efficient radiation at the specified frequency ω and minimizes the number of calculations of the integrands far from these regions. The total number of grid nodes in the integration over $\cos\Theta_*$ and Φ_* was usually a few tens of thousand if $s\omega_{B_{\rm p}}/2<\omega<s\omega_{B_{\rm p}}$ and decreased to a few hundred when the star was observed from the pole, when the integrands in (4) do not depend on the longitude Φ_*.

Concluding our consideration of the computational methods used, we note that the expressions for the Stokes parameters Q and V in (4) assume that the radiation leaving the corona represents a superposition of incoherent extraordinary and ordinary waves. This approximation is valid if pairs of extraordinary and ordinary waves emitted from different optical depths acquire substantially different phase differences along their trajectories to the top of the corona (due to the different indices of refraction for the normal waves). If the optical depth of the corona at the frequency ω is much less than unity, then this condition is satisfied when the phase difference

$$\theta=\frac{\omega}{c}\int\limits_0^\infty(n_2-n_1)\mathrm{d}z=3.32\left(\frac{n_{\rm e0}}{10^{10}\ \mathrm{cm}^{-3}}\right) \quad (17)$$
$$\times\left(\frac{T_{\rm cor}}{10^6\ \mathrm{K}}\right)\left(\frac{B}{10^7\ \mathrm{G}}\right)^{-1}\left(\frac{g}{10^8\ \mathrm{cm/s^2}}\right)^{-1}$$
$$\times\begin{cases}1.88\beta_{T_{\rm cor}}^{-1}\,\mathrm{Im}\,w(\xi), & \text{if } s=1,\ \ \alpha_{\rm obs}=0\\ 3/(s^2-1), & \text{if } s\ge2,\ \ \alpha_{\rm obs}=0,\end{cases}$$

acquired by the normal waves at the height of the corona is much greater than unity. In (17), n_1 and n_2 are the indices of refraction for the extraordinary and ordinary waves [31, § 5.2] and $\mathrm{Im}\,w(\xi)\sim1$ is the imaginary part of the Kramp function [35, formula (7.1.3)]. We can see that the condition $\theta\gg1$ is easily satisfied in the region of parameters $T_{\rm cor}\ge10^6$ K and $n_{\rm e0}\ge10^{10}\ \mathrm{cm}^{-3}$ for harmonics $s\ge2$ that are not very high. It follows from (11) and (17) that, at the first harmonic, the phase difference $\theta\gtrsim1$ only when $\tau_0\gtrsim1$. If the optical depth of the corona at the frequency ω is high, the normal waves must acquire a phase difference much greater than unity at a distance corresponding to an optical depth of the order of unity [42]. This requirement is satisfied for the second and higher harmonics but not the first harmonic [38, 43, § 5.3.1].

Nevertheless, the radiation of an optically thick corona at the first harmonic is approximately the same as the radiation of the mutually-incoherent normal waves. This is due, first, to the considerable difference between the absorption coefficients of the normal waves at the first harmonic and, second, to the fact that the polarization of the radiation of a single electron nearly coincides with the polarization of one of the normal waves (namely, the extraordinary wave). In this case, the radiation flux with extraordinary polarization leaving the corona is formed by electrons

[5] The software for the numerical calculations carried out for this work was prepared by S.A. Koryagin.

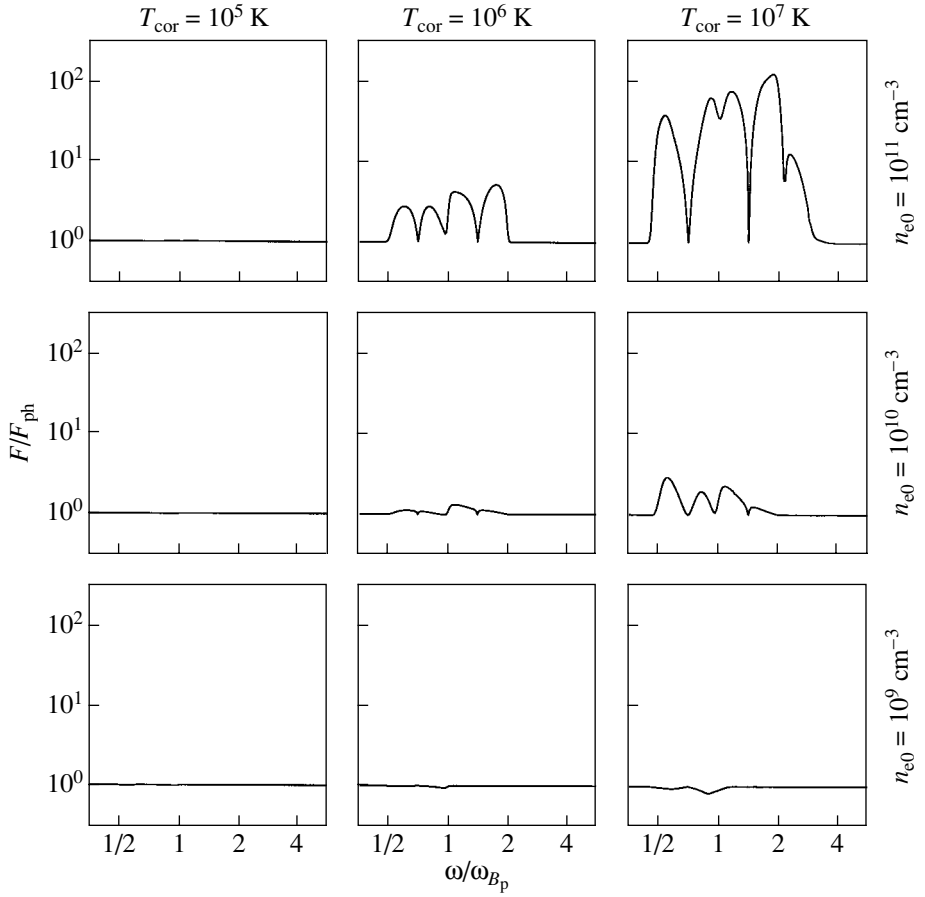

Fig. 2. Spectral flux density F of the coronal cyclotron radiation of G99-47 calculated for a pole-on orientation of the star ($\Theta_{obs} = 0^\circ$). The coronal temperatures are $T_{cor} = 10^5$, 10^6, and 10^7 K for the plots in the left, central, and right columns, respectively. The electron densities are $n_{e0} = 10^9$, 10^{10}, and 10^{11} cm^{-3} for the plots in the bottom, middle, and top rows, respectively.

located in its upper part, at optical depths $\tau \lesssim 1$. The contribution of these electrons to the radiation of the ordinary polarization is small. The radiation flux of the ordinary polarization is formed by other electrons, located at substantially larger depths $1 \ll \tau \lesssim \beta_{T_{cor}}^{-2}$. Their extraordinary radiation is absorbed by upper layers of the corona and does not contribute appreciably to the outgoing radiation with extraordinary polarization. Since the radiation of the two groups of electrons is uncorrelated, the extraordinary and ordinary waves in the radiation leaving the corona are incoherent.

3. DISCUSSION OF THE CALCULATED SPECTRA

Let us follow the variations in the frequency spectra of the flux and polarization of the coronal cyclotron radiation as functions of T_{cor} and n_{e0}. Consider our numerical results corresponding to the case where the white dwarf G99-47 is observed from the north pole ($\Theta_{obs} = 0^\circ$), the temperatures $T_{cor} = 10^5, 10^6$, and 10^7 K, and densities $n_{e0} = 10^9, 10^{10}$, and 10^{11} cm^{-3} (Figs. 2 and 3).

We can see in Fig. 2 that the flux of coronal cyclotron radiation appreciably exceeds the photospheric continuum for $T_{cor} = 10^6$ and 10^7 K and $n_{e0} = 10^{10}$ and 10^{11} cm^{-3}. The first and second cyclotron harmonics, corresponding to frequencies $\omega_{B_p}/2 < \omega < \omega_{B_p}$ and $\omega_{B_p} < \omega < 2\omega_{B_p}$, are clearly visible in the radiation spectrum. When $T_{cor} = 10^7$ K and $n_{e0} = 10^{11}$ cm^{-3}, the third harmonic at frequencies $3\omega_{B_p}/2 < \omega < 3\omega_{B_p}$ also becomes visible.

The presence of these harmonics in the integrated spectrum of the star is explained by Fig. 4, which shows the regions of the T_{cor}–n_{e0} plane where the

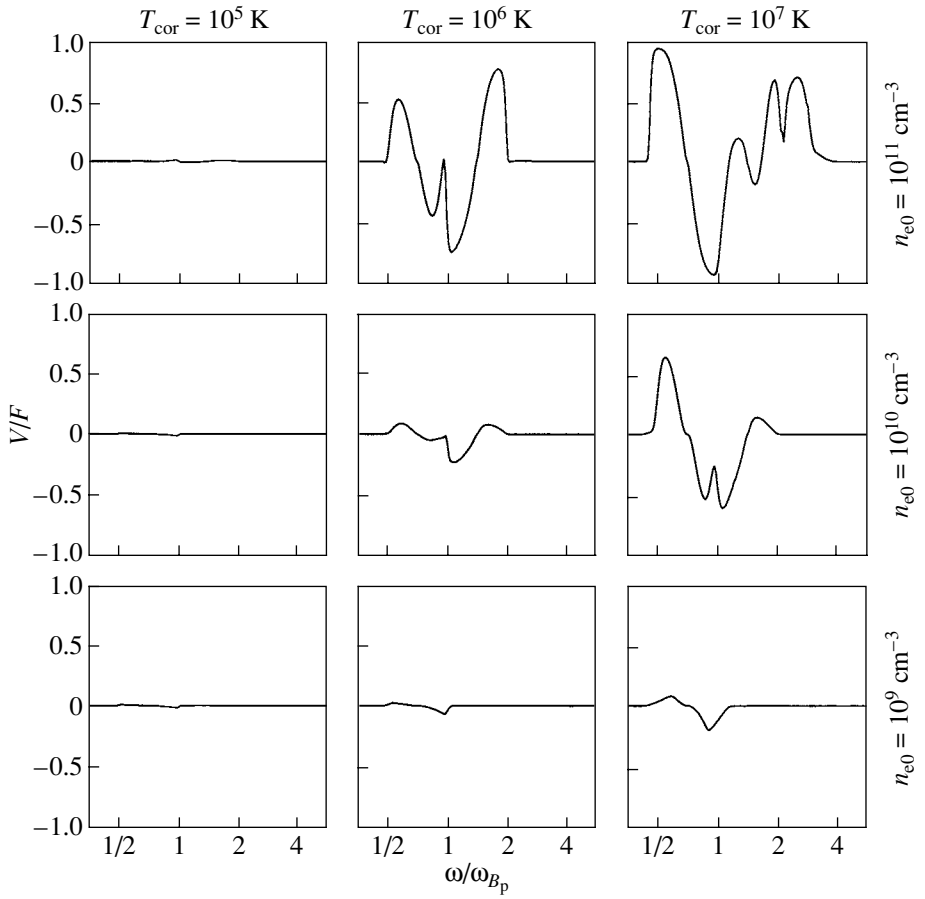

Fig. 3. Degree of circular polarization $\zeta_c = V/F$ of the coronal cyclotron radiation of G99-47 calculated for the same conditions as in Fig. 2.

weighted-mean optical depths of the corona

$$\langle\tau_{sl}\rangle = \frac{\oint\limits_{\cos\vartheta>0} \cos\vartheta\,|\cos\alpha|\,\tau_{sl}(\tau_0, \xi=0, \mathbf{n})\mathrm{d}\mathbf{n}}{\oint\limits_{\cos\vartheta>0} \cos\vartheta\,|\cos\alpha|\,\mathrm{d}\mathbf{n}} \quad (18)$$

are equal to unity at the stellar pole.[6] In the parameter region located above a line $\langle\tau_{sl}\rangle = 1$, the optical depth of the corona becomes high for the normal wave l at the sth harmonic. As can easily be seen, when $T_{cor} = 10^6$ K and $n_{e0} = 10^{11}$ cm^{-3}, and $T_{cor} = 10^7$ K and $n_{e0} = 10^{10}$ cm^{-3}, the optical depth of the corona to the extraordinary wave at the second cyclotron harmonic is $\langle\tau_{21}\rangle \sim 1$. Therefore, the second harmonic is observable in the coronal radiation in the case of these parameters, as well as at the higher values of $T_{cor} = 10^7$ K and $n_{e0} = 10^{11}$ cm^{-3}. In this last case, the optical depth of the corona to the extraordinary wave at the third harmonic $\langle\tau_{31}\rangle$ is close to unity, so that this component of the cyclotron radiation becomes appreciable in the integrated radiation of the star.

Note that the coronal cyclotron radiation in the case $T_{cor} = 10^7$ K and $n_{e0} = 10^{11}$ cm^{-3} increases the bolometric luminosity of the star by an appreciable factor. To support the powerful cyclotron radiation, a nonradiative energy-transport mechanism would have to exist in the white dwarf's photosphere, to provide a flux of energy to the corona exceeding the radiative flux from the photosphere. This essentially excludes the existence of coronas with such parameters.

When there are only two cyclotron harmonics in the spectrum (and the third harmonic is absent), the ordinary wave dominates in the first harmonic and the extraordinary wave in the second harmonic. This follows from the polarization of the radiation calculated for $T_{cor} = 10^6$ K and $n_{e0} = 10^{11}$ cm^{-3}, $T_{cor} = 10^6$ K and $n_{e0} = 10^{10}$ cm^{-3}, and $T_{cor} = 10^7$ K and $n_{e0} = 10^{10}$ cm^{-3} (Fig. 3). The region of efficient radiation of the first harmonic at frequencies $\omega_{B_p}/2 \lesssim$

[6] To simplify the calculations, it is assumed in (18) that $\bar{q} = p$ at any height in the corona [see (10), (13)].

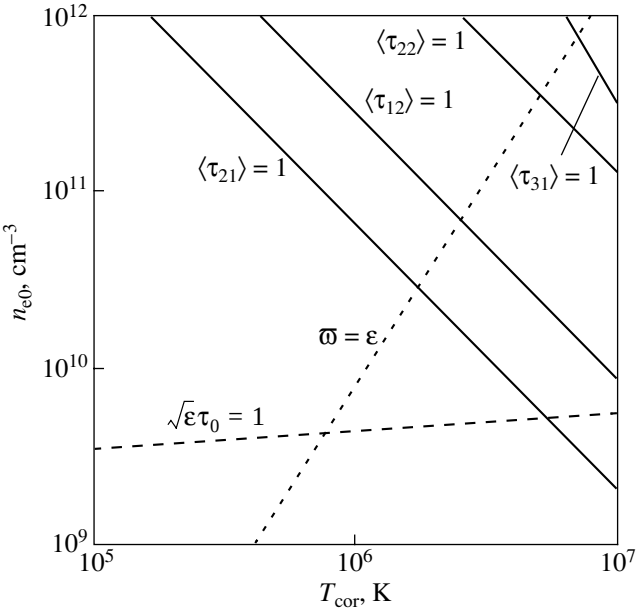

Fig. 4. Separation of the T_{cor}–n_{e0} parameter plane into characteristic regions with various conditions for the transport of cyclotron radiation in the corona of G99-47 for $B = 2.5 \times 10^7$ G and $\delta = 0$. To the right of the dotted line $\varpi = \epsilon$, the parameter $\varpi(\xi = 0)$ is greater than $\epsilon(\tau_0)$, so that the conversion of normal waves via cyclotron scattering is appreciable over the entire height of the corona. The mean optical depths of the corona (18) exceed unity above the solid straight lines $\langle\tau_{sl}\rangle = 1$. The optical depth of the corona to the extraordinary wave at the first harmonic, $\langle\tau_{11}\rangle$, exceeds unity for all values of T_{cor} and n_{e0} plotted in the figure. The thermalization length of the radiation of the extraordinary wave at the first cyclotron harmonic is less than the height of the corona in the region above the dashed line $\sqrt{\epsilon(\tau_0)}\tau_0 = 1$.

$\omega \lesssim \omega_{B_p}/\sqrt{2}$ is located near the equator, where, in general, the magnetic field is directed away from the observer. Right-hand circular polarization ($V > 0$) at these frequencies corresponds to the ordinary wave. At higher frequencies $\omega_{B_p}/\sqrt{2} \lesssim \omega \lesssim \omega_{B_p}$, the region of efficient radiation shifts toward the pole, where the magnetic field is directed toward the observer. The direction of rotation of the electric-field vector in the normal wave changes, reversing the sign of the circular polarization of the coronal radiation near the frequency $\omega_{B_p}/\sqrt{2}$. The same arguments for the frequency range $\omega_{B_p} \lesssim \omega \lesssim 2\omega_{B_p}$, corresponding to the second cyclotron harmonic, clarify the dominance of the extraordinary wave in this case.

To explain the dominance of the ordinary wave in the coronal radiation at the first harmonic, we must carry out a special analysis of the transfer equations taking into account thermalization and mutual conversion of the normal waves during cyclotron scattering. The line $\varpi = \epsilon$ (where the efficiencies of the above processes are comparable) goes through the considered range of T_{cor} and n_{e0} in the T_{cor}–n_{e0} plane (Fig. 4). Accordingly, we limit our discussion here to a few remarks. The coronal optical depth to the extraordinary wave at the first harmonic $\langle\tau_{11}\rangle = 3\tau_0/\sqrt{\pi}$ is substantially greater than unity for all combinations of T_{cor} and n_{e0} considered above [see (11)]. When $\epsilon \ll 1$ and $\varpi \ll 1$, the source function at the top of the corona is substantially less than in the deeper layers and the characteristic spatial scale for variations in the source function is considerably greater than the distance corresponding to unit optical depth to the extraordinary radiation [19, 44]. Therefore, the extraordinary radiation is formed in upper coronal layers, where the source function is relatively small. For the parameter combinations $T_{cor} = 10^6$ K and $n_{e0} = 10^{11}$ cm^{-3}, $T_{cor} = 10^6$ K and $n_{e0} = 10^{10}$ cm^{-3}, and $T_{cor} = 10^7$ K and $n_{e0} = 10^{10}$ cm^{-3}, the optical depth of the corona to the ordinary radiation is $\langle\tau_{12}\rangle \lesssim 1$. As a result, the ordinary radiation is formed primarily in central regions of the corona, where the source function is greater. The ratio of the intensities of the normal waves at the first harmonic depends on the degree of scattering of the extraordinary radiation in the upper layers of the corona and the transparency of the corona to the ordinary radiation. As follows from the calculated frequency profiles of the polarization, the scattering of the extraordinary wave is very strong.

On the contrary, the dominant contribution of the extraordinary wave at the second cyclotron harmonic can be explained very simply. The corresponding optical depths of the corona to the extraordinary and ordinary waves, $\langle\tau_{21}\rangle$ and $\langle\tau_{22}\rangle$, are less than or of the order of unity. However, the optical depth to the

extraordinary wave, $\langle\tau_{21}\rangle$, is greater (Fig. 4), and so it dominates in the coronal radiation.

Let us specially note the flux and polarization of the radiation at the temperature $T_{\rm cor} = 10^6$ K and the minimum density $n_{\rm e0} = 10^9$ cm^{-3} for which the calculations were performed. In this case, the radiation flux differs only slightly from the photospheric continuum, and the presence of the corona can be detected only from variations in the polarization of the radiation in the range $\omega_{B_{\rm p}}/2 < \omega < \omega_{B_{\rm p}}$, corresponding to the first cyclotron harmonic. The dominance of the ordinary wave in this case is due to the fact that the photospheric radiation of the ordinary polarization passes through the corona virtually unchanged ($I_{12}^{\rm out} \approx B_\omega^*(T_{\rm eff})/2$). On the other hand, the intensity of the outgoing radiation in the extraordinary wave drops below $B_\omega^*(T_{\rm eff})/2$ (primarily due to scattering). As a result, the intensity of the ordinary radiation will be greater than the intensity of the extraordinary radiation.

At lower densities $n_{\rm e0}$ (for which calculations were not carried out), the corona behaves like a scattering layer, and so the observed radiation flux should be lower than the photospheric flux. However, this cannot result in the formation of a prominent absorption feature in the observed spectrum, since radiation at the given frequency ω is efficiently scattered only in a very small region of the corona (within the narrow latitude interval $\Delta\Theta_* \sim \beta_{T_{\rm cor}} \ll 1$). The relative variation in the stellar radiation flux should be about $\beta_{T_{\rm cor}}$, which is virtually undetectable.

At low temperatures $T_{\rm cor} \lesssim 10^5$ K, the corona also affects the observed radiation flux only slightly. Even at the maximum possible intensity of the coronal emission $B_\omega^*(T_{\rm cor})$ (inside the region of efficient radiation), its relative contribution to the observed radiation flux from the entire star,

$$\frac{\beta_{T_{\rm cor}} B_\omega^*(T_{\rm cor})}{B_\omega^*(T_{\rm eff})} \sim \left(\frac{T_{\rm cor}}{5\times10^5\ {\rm K}}\right)^{3/2},$$

becomes negligible when $T_{\rm cor} \lesssim 10^5$ K.

Concluding this section, we note that the force due to the pressure of the cyclotron radiation in the very dense coronas of magnetic white dwarfs can be comparable to or even greater than the gravitational force [34]. In this case, the height profile of the electron density in the corona will differ from the barometric profile (1). In the corona of G99-47, the radiation-pressure force will exceed the gravitational force only when $n_{\rm e0} > 5\times10^{11}$ cm^{-3} and $T_{\rm cor} > 10^7$ K (i.e., beyond the parameter region presented in Figs. 2 and 3). However, in other white dwarfs with stronger magnetic fields, the cyclotron-radiation pressure will be comparable to the gravitational force for lower electron densities and temperatures in the corona. This should be taken into account when studying white-dwarf coronas whose cyclotron radiation at the first harmonic is in the optical.

4. UPPER LIMIT FOR THE CORONAL ELECTRON DENSITY OF G99-47

Let us compare our calculations with the results of photometric observations of the white dwarf G99-47 in the infrared. The above analysis shows that the coronal cyclotron radiation can be observed only as broadband emission features in the infrared radiation of the white dwarf, with the maximum excess over the photospheric continuum being in the wavelength interval $\lambda = (0.5{-}2.0)\times 2\pi c/\omega_{B_{\rm p}} = 2.14{-}8.57$ μm, corresponding to the first and second cyclotron harmonics. Consequently, the emission of the corona should increase the observed brightness of G99-47 in the K, L, L', and M photometric bands (with the effective wavelengths $\lambda \simeq 2.2$, 3.5, 3.8, and 4.8 μm, respectively [45]) and increase the color indices of these bands with respect to bands with smaller effective wavelengths, such as V (0.55 μm), J (1.2 μm), or H (1.6 μm).

According to the catalog [46], G99-47 has been observed several times in the J, H, and K [21, 22, 24, 47–50] infrared photometric bands and once in the L and L' bands [21].[7] The B, V, R, I, J, H, and K observations of [22, 24] revealed no peculiarity in the K magnitude of G99-47 compared to other white dwarfs with approximately the same photospheric temperature, 5700 K. The $(B-V)$–$(V-K)$ and $(V-I)$–$(V-K)$ diagrams for white dwarfs with hydrogen photospheres resemble narrow strips whose half-widths in $B-V$, $V-I$, and $V-K$ are approximately 0.05^m, 0.05^m, and 0.12^m; i.e., they approximately coincide with the errors [24, Fig. 13]. The white dwarf G99-47 is located nearly in the centers of these diagrams; i.e., no excess infrared radiation in the K band is observed. This means that the flux of the coronal cyclotron radiation at the second harmonic in this band is much less than the photospheric flux. Consequently, there is no appreciable cyclotron radiation in the shorter-wavelength J and H bands containing the third and higher cyclotron harmonics.

Let us compare the observed $J-K$, $J-L$, and $J-L'$ color indices from [21, 22] with our calculations. The J and K, L, L' bands have fairly similar wavelengths, so that the corresponding color indices

[7] The aim of the observations of [21] in the J, H, K, L, and L' bands was to search for a low-mass, cool companion (planet) near G99-47. The blackbody radiation of such a companion should increase the observed infrared flux from G99-47.

Observed and theoretical color indices for the white dwarf G99-47

Data source	Model parameters			Color indices		
	T_{cor}, K	n_{e0}, cm^{-3}	Θ_{obs}, deg	$J-K$	$J-L$	$J-L'$
Observations [21, 22]	–	–	–	$0\overset{m}{.}20$–$0\overset{m}{.}40$	$0\overset{m}{.}16$–$0\overset{m}{.}58$	$0\overset{m}{.}11$–$0\overset{m}{.}63$
Model without corona	–	0	–	$0\overset{m}{.}34$	$0\overset{m}{.}51$	$0\overset{m}{.}53$
Model with corona	10^6	10^{10}	0, 180	$0\overset{m}{.}36$	$0\overset{m}{.}73$	$0\overset{m}{.}81$
Model with corona	10^6	10^{10}	30, 150	$0\overset{m}{.}37$	$0\overset{m}{.}68$	$0\overset{m}{.}78$
Model with corona	10^6	10^{10}	60, 120	$0\overset{m}{.}37$	$0\overset{m}{.}7$	$0\overset{m}{.}78$
Model with corona	10^6	10^{10}	90	$0\overset{m}{.}37$	$0\overset{m}{.}67$	$0\overset{m}{.}82$

The row of observed color indices presents the lower and upper boundaries for these quantities. The $J-K$ values measured in [22] are given in the CIT photometric system, and $J-L$ and $J-L'$ values obtained in [21], in the IRTF system. The calculated color indices are presented in the Johnson–Glass photometric system [45]. The small discrepancies in the definitions of the color indices in the different photometric systems are not important for our analysis. The column of Θ_{obs} presents the two values Θ_{obs1} and $\Theta_{obs2} = 180^\circ - \Theta_{obs1}$ at which the same color indices are observed. The observations at Θ_{obs1} and Θ_{obs2} correspond to opposite directions of the line of sight with respect to the stellar magnetic dipole.

are less sensitive to the particular form of the spectrum of the photospheric continuum than are the color indices for photometric bands with larger wavelength differences.[8] The coronal cyclotron radiation can change the flux in the K, L, and L' bands but does not affect the flux in the J band, since it corresponds to the very weak third and fourth cyclotron harmonics. The transmission coefficients for the J, K, L, and L' filters and the constants required to calculate the color indices in the Johnson–Glass photometric system were taken from [45]. The $J-K$, $J-L$, and $J-L'$ color indices calculated for G99-47 without a corona (i.e., for a blackbody spectrum with temperature 5700 K) proved to be within the confidence intervals of their observed values (first and second rows in the table). Therefore, the radiation of G99-47 in the K, L, and L' bands could be formed solely by the photosphere (without a corona). Therefore, the available observational data enable us to derive only upper limits on the coronal electron density n_{e0} for various temperatures T_{cor},[9] i.e., to draw a line in the T_{cor}–n_{e0} plane above which the calculated $J-K$, $J-L$, and $J-L'$ color indices fall outside the confidence intervals for the observations. Such a detailed analysis is beyond the scope of the present work, and we present the upper limit n_{e0} only for the characteristic coronal temperature $T_{cor} \simeq 10^6$ K. In the case of higher temperatures T_{cor}, the upper limit on n_{e0} should be less.

Comparison of the calculations and observational data shows that the electron density in the corona of G99-47 does not exceed $n_{e0} = 10^{10}$ cm^{-3} if the temperature is $T_{cor} = 10^6$ K (see the table). Cyclotron radiation of the corona with the above parameters results in $J-L$ and $J-L'$ being outside the confidence intervals for the observed values for any observation angle Θ_{obs}. This conclusion is also valid for $\Theta_{obs} = 120^\circ$, which is in best agreement with the polarization of the radiation in the Zeeman-split Hα line [28, 29]. As the temperature T_{cor} increases, the coronal cyclotron radiation increases. Therefore, at higher temperatures ($T_{cor} > 10^6$ K), the coronal electron density n_{e0} cannot exceed the limit 10^{10} cm^{-3} established for $T_{cor} = 10^6$ K (in fact, n_{e0} should be even lower).

The frequency dependences of the flux and polarization of the coronal cyclotron radiation for $\Theta_{obs} = 120^\circ$, $T_{cor} = 10^6$ K, and $n_{e0} = 10^{10}$ cm^{-3} are presented in Fig. 5. For comparison, the frequency dependences of these quantities for $\Theta_{obs} = 0^\circ$ and $\Theta_{obs} = 90^\circ$ are also shown. The frequency spectra of the radiation flux for $\Theta_{obs} = 120^\circ$ and $\Theta_{obs} = 90^\circ$ possess well-defined maxima at frequencies slightly above $\omega_{B_p}/2$ at the first harmonic and slightly above

[8] We did not use $H-K$, $H-L$, and $H-L'$, although the H band is closer to the K, L, and L' bands, because the H photometric data for G99-47 presented in [21, 22] differ from each other by 0.52^m. This discrepancy appears to be due to a misprint in [21], since it is stated there that the H observations of G99-47 in [21] are in agreement with the earlier data of [48], which coincide with [22] within 5%.

[9] With fixed B_p, g, T_{eff}, and Θ_{obs}, the flux of the coronal cyclotron radiation depends on only two parameters: T_{cor} and n_{e0}.

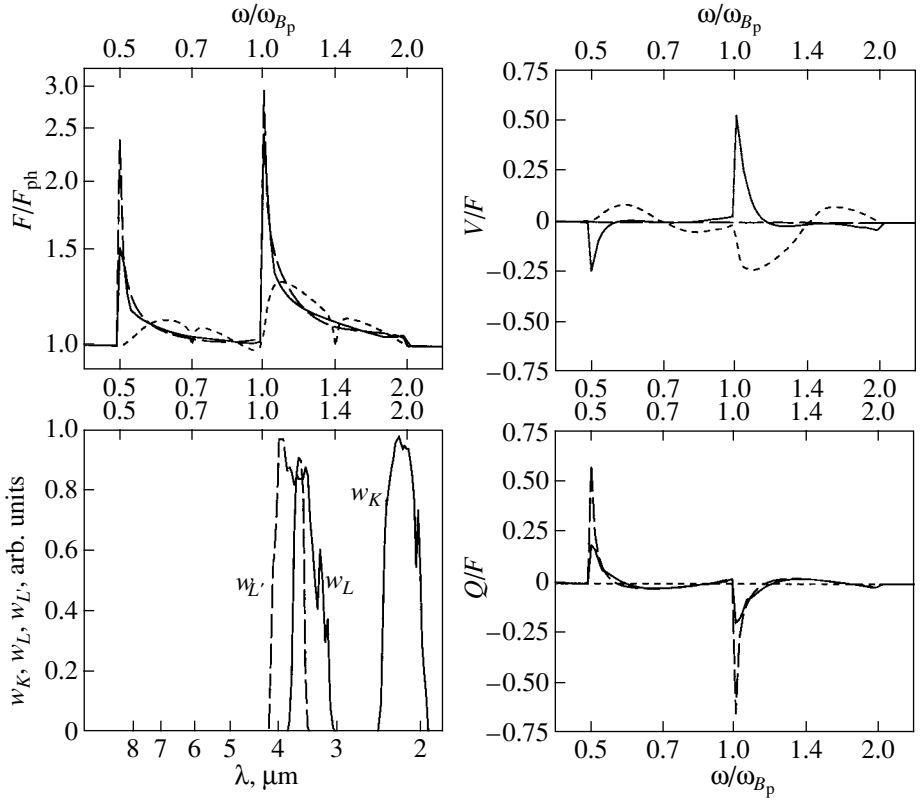

Fig. 5. The spectral flux density F and degrees of circular and linear polarization ($\zeta_c = V/F$ and $\zeta_l = |Q|/F$) of the coronal radiation of G99-47 calculated for observation angles $\Theta_{obs} = 120°$ (solid curves), $\Theta_{obs} = 0°$ (dotted curves), and $\Theta_{obs} = 90°$ (dashed curves). The coronal temperature is $T_{cor} = 10^6$ K and the electron density is $n_{e0} = 10^{10}$ cm^{-3}. The transmission coefficients w_K, w_L, and $w_{L'}$ for the K, L, and L' filters [45] are presented in the bottom left panel whose upper and lower horizontal axes, refer, respectively, to the wavelengths and the ratios ω/ω_{B_p} (also used in other panels of this figure), along the upper axis.

ω_{B_p} at the second harmonic. The radiation at these frequencies is formed near the equator, where the magnetic field is minimum and the region of efficient radiation is substantially broader. The planes of the linear polarization, defined by the sign of the ratio Q/F, coincide at the boundaries of the frequency range $\omega_{B_p}/2 < \omega < \omega_{B_p}$ of the first cyclotron harmonic. This feature of the linear polarization is due to the axial symmetry of the stellar dipole magnetic field [16]. The magnetic field is directed along the same line (but in opposite directions) at the equator and the pole, where the radiation at the frequencies $\omega_{B_p}/2$ and ω_{B_p} is formed. In addition, the radiation of the ordinary wave, whose polarization ellipse is stretched along the projection of the magnetic field onto the plane of the sky, dominates at the first harmonic. As a result, the plane of linear polarization of the coronal radiation goes through the same axis x_{obs} in the plane of the sky at frequencies slightly above $\omega_{B_p}/2$ and slightly below ω_{B_p}. Such polarization corresponds to positive Q/F, as is demonstrated in Fig. 5. The same relation for the planes of linear polarization occurs in the range $\omega_{B_p} < \omega < 2\omega_{B_p}$ of the second cyclotron harmonic, where the radiation of the extraordinary wave dominates.

Our new upper limit $n_{e0} = 10^{10}$ cm^{-3} on the electron density in the corona of the white dwarf G99-47 for the temperature $T_{cor} \geq 10^6$ K is more than a factor of 40 lower than the value derived in [10] from ROSAT X-ray observations. Therefore, the detection of coronas of isolated magnetic white dwarfs via their cyclotron radiation has high sensitivity currently unattainable with X-ray observations. Since the X-ray bremsstrahlung flux is proportional to n_{e0}^2, the sensitivity of these measurements must be enhanced by a factor of $40^2 \sim 2000$ to be comparable to our method based on analyzing the coronal cyclotron radiation.

Our upper limit n_{e0} can be further decreased using polarization observations of G99-47 at 4–8 μm, corresponding to the first cyclotron harmonic.[10] The

[10] Most polarization observations of white dwarfs have been carried out only in the optical [51].

degree of polarization of the radiation at these wavelengths could be several percent in the case of a corona with $T_{cor} = 10^6$ K and $n_{e0} = 10^9$ cm^{-3}.

Note that radiation from the photosphere of an isolated magnetic white dwarf is polarized due to the dichroism of normal waves in a magnetized plasma [17, 18]. A characteristic feature of the polarization associated with the presence of the corona is the change in the sign of the circular polarization near the frequency $\omega_{B_p}/\sqrt{2}$. Both the linear and circular polarization of the coronal radiation decrease sharply to zero below $\omega_{B_p}/2$ (where cyclotron radiation is absent) and above ω_{B_p} if the corona is transparent to cyclotron radiation at the second harmonic.

The choice of the magnetic white dwarf G99-47 for our study was dictated, first, by the reported detection of coronal X-ray radiation by the *Einstein* satellite (which was not confirmed later) and, second, by the fact that this star was observed precisely in the region of the infrared where, in principle, coronal cyclotron radiation could be detected. Upper limits on the coronal electron densities of other magnetic white dwarfs—G99-37 (WD 0548−001, $B_p = 2 \times 10^7$ G, $T_{eff} = 6400$ K) and G195-19 (WD 0912+536, $B_p = 10^8$ G, $T_{eff} = 8000$ K) [11]—can be determined in the same way using their infrared photometry [22, 52]. We will do this in a separate paper.

In conclusion, we note that it would be desirable to carry out photometric and polarization observations of the unique magnetic white dwarf GD 356 (WD 1639+537, $B_p = 1.3 \times 10^7$ G, $T_{eff} = 7500$ K) in the range 4–16 μm, corresponding to the first and second cyclotron harmonics (for example, using the SIRTF (Spitzer Space Telescope) satellite). The Hα and Hβ lines in the optical spectrum of this star are observed in emission rather than absorption, as for other white dwarfs [53]. This suggests an enhanced temperature in the upper layers of its photosphere and the probable presence of a chromosphere [54] and corona in this object.

ACKNOWLEDGMENTS

This work was supported by the Russian Foundation for Basic Research (project code 02-02-16236), the President of the Russian Federation Program of Support of Young Russian Scientists and Leading Scientific Schools of the Russian Federation (project nos. NSh-1744.2003.2 and MK-2161.2003.02), the program "Nonstationary Phenomena in Astronomy" of the Presidium of the Russian Academy of Sciences, and the Federal Science and Technology Program in Astronomy (project no. 40.022.1.1.1103).

REFERENCES

1. T. A. Fleming, K. Werner, and M. A. Barstow, Astrophys. J. **416**, L79 (1993).
2. I. J. O'Dwyer, Y.-H. Chu, R. A. Gruendl, *et al.*, Astron. J. **125**, 2239 (2003).
3. E. M. Sion and R. A. Downes, Astrophys. J. **396**, L79 (1992).
4. T. A. Fleming, S. L. Snowden, E. Pfeffermann, *et al.*, Astron. Astrophys. **316**, 147 (1996).
5. H. L. Shipman, Astrophys. J. **206**, L67 (1976).
6. C. Martin, G. Basri, M. Lampton, and S. M. Kahn, Astrophys. J. **261**, L81 (1982).
7. Z. E. Musielak, Astrophys. J. **322**, 234 (1987).
8. Z. E. Musielak and J. M. Fontenla, Astrophys. J. **346**, 435 (1989).
9. K. A. Arnaud, V. V. Zheleznyakov, and V. Trimble, Publ. Astron. Soc. Pac. **104**, 239 (1992).
10. R. Cavallo, K. A. Arnaud, and V. Trimble, J. Astrophys. Astron. **14**, 141 (1993).
11. D. T. Wickramasinghe and L. Ferrario, Publ. Astron. Soc. Pac. **112**, 873 (2000).
12. V. V. Zheleznyakov, Astrophys. Space Sci. **97**, 229 (1983).
13. V. V. Zheleznyakov and A. A. Litvinchuk, Astrophys. Space Sci. **105**, 73 (1984).
14. V. V. Zheleznyakov and A. V. Serber, Adv. Space Res. **16**, 77 (1995).
15. V. N. Sazonov and V. V. Chernomordik, Astrophys. Space Sci. **32**, 355 (1975).
16. W. H. Ingham, K. Brecher, and I. Wasserman, Astrophys. J. **207**, 518 (1976).
17. J. C. Kemp, Astrophys. J. **162**, 169 (1970).
18. J. C. Kemp, Astrophys. J. **213**, 794 (1977).
19. A. V. Serber, Astron. Zh. **67**, 582 (1990) [Sov. Astron. **34**, 291 (1990)].
20. A. V. Serber, Izv. Vyssh. Uchebn. Zaved., Ser. Radiofiz. **42**, 1035 (1999) [Radiophys. Quant. Electron. **42**, 911 (1999)].
21. C. Krishna Kumar, Publ. Astron. Soc. Pac. **97**, 294 (1985).
22. P. Bergeron, S. K. Leggett, and M. Ruiz, Astrophys. J., Suppl. Ser. **133**, 413 (2001).
23. F. Wesemael, J. L. Greenstein, J. Liebert, *et al.*, Publ. Astron. Soc. Pac. **105**, 761 (1993).
24. P. Bergeron, M. T. Ruiz, and S. K. Leggett, Astrophys. J., Suppl. Ser. **108**, 339 (1997).
25. S. K. Leggett, M. T. Ruiz, and P. Bergeron, Astrophys. J. **497**, 294 (1998).
26. G. P. McCook and E. M. Sion, Astrophys. J., Suppl. Ser. **121**, 1 (1999).
27. V. A. Hughes, P. A. Feldman, and A. Woodsworth, Astrophys. J. **170**, L125 (1971).
28. A. Putney and S. Jordan, Astrophys. J. **449**, 863 (1995).
29. D. T. Wickramasinghe and B. Martin, Mon. Not. R. Astron. Soc. **188**, 165 (1979).
30. V. V. Zheleznyakov, Itogi Nauki Tekhn., Ser. Astron. **22**, 135 (1983) [Sov. Sci. Rev. Astrophys. Space Phys. Rev. **3**, 157 (1984)].

31. V. V. Zheleznyakov, *Radiation in Astrophysical Plasmas* (Kluwer, Dordrecht, 1996; Yanus-K, Moscow, 1997).
32. Standard Definitions of Terms for Radio Wave Propagation, IEEE Trans. Antennas Propag. **17**, 270 (1969).
33. J. P. Hamaker and J. D. Bregman, Astron. Astrophys., Suppl. Ser. **117**, 161 (1996).
34. V. V. Zheleznyakov, S. A. Koryagin, and A. V. Serber, Pis'ma Astron. Zh. **25**, 522 (1999) [Astron. Lett. **25**, 445 (1999)].
35. M. Abramowitz and I. A. Stegun, *Handbook of Mathematical Functions*, Ed. by M. Abramowitz and I. A. Stegun (Dover, New York, 1965, 1971; Nauka, Moscow, 1979).
36. V. V. Zheleznyakov, S. A. Koryagin, and A. V. Serber, Pis'ma Astron. Zh. **25**, 513 (1999) [Astron. Lett. **25**, 437 (1999)].
37. S. A. Koryagin, Zh. Éksp. Teor. Fiz. **117**, 853 (2000) [JETP **90**, 741 (2000)].
38. V. V. Zheleznyakov, Astrofizika **16**, 539 (1980) [Astrophysics **16**, 316 (1981)].
39. D. Michalas, *Stellar Atmospheres* (Freeman, San Francisco, 1978; Mir, Moscow, 1982).
40. D. Mihalas, J. Comp. Phys. **57**, 1 (1985).
41. G. Forsythe, M. Malcolm, and C. Moler, *Computer Methods for Mathematical Computations* (Prentice-Hall, Englewood Cliffs, 1977; Mir, Moscow, 1980).
42. Yu. N. Gnedin and G. G. Pavlov, Zh. Éksp. Teor. Fiz. **65**, 1806 (1973).
43. A. I. Akhiezer, I. A. Akhiezer, R. V. Polovin, *et al.*, *Plasma Electrodynamics* (Nauka, Moscow, 1974; Pergamon, Oxford, 1975).
44. V. V. Zheleznyakov and A. V. Serber, Astron. Zh. **70**, 1002 (1993) [Astron. Rep. **37**, 507 (1993)].
45. M. S. Bessell and J. M. Brett, Publ. Astron. Soc. Pac. **100**, 1134 (1988).
46. D. Y. Gezari, P. S. Pitts, and M. Schmitz, *Catalog of Infrared Observations* (Centre de Données Astronomiques de Strasbourg, 1999); http://cdsweb.u-strasbg.fr/viz-bin/VizieR?-source=II/225.
47. J. Mould and J. Liebert, Astrophys. J. **226**, L29 (1978).
48. D. T. Wickramasinghe, D. A. Allen, and M. S. Bessell, Mon. Not. R. Astron. Soc. **198**, 473 (1982).
49. R. G. Probst, Astrophys. J., Suppl. Ser. **53**, 335 (1983).
50. S. K. Leggett, Astron. Astrophys. **208**, 141 (1989).
51. S. C. West, Astrophys. J. **345**, 511 (1989).
52. C. Krishna Kumar, Astron. J. **94**, 158 (1987).
53. J. L. Greenstein and J. K. McCarthy, Astrophys. J. **289**, 732 (1985).
54. L. Ferrario, D. T. Wickramasinghe, J. Liebert, *et al.*, Mon. Not. R. Astron. Soc. **289**, 105 (1997).

Translated by Yu. Dumin

Astronomy Reports, Vol. 48, No. 2, 2004, pp. 136–144. Translated from Astronomicheskiĭ Zhurnal, Vol. 81, No. 2, 2004, pp. 159–167.

Two Scales for the Frequency Dependence of the Scattering of Pulsar Radio Emission

A. D. Kuz'min and B. Ya. Losovsky

Pushchino Radio Astronomy Observatory, Astro Space Center, Lebedev Institute of Physics, Russian Academy of Sciences, Pushchino, Moscow oblast, 142290 Russia

Received May 20, 2003; in final form, August 8, 2003

Abstract—We have measured the pulse broadening by scattering at 40, 60, and 111 MHz for the pulsars PSR B0809+74, B0950+08, B1919+21, and B2303+30. The frequency dependence of the scatter-broadening parameter is analyzed based on these measurements and data from the literature. The dependence obtained purely from the literature data is not consistent with the theory, and the scattering magnitudes differs considerably from the data of the catalog of 706 pulsars of Taylor *et al*. A two-component model for the frequency dependence of the scattering of the pulsar radio emission in the interstellar medium is proposed. Allowing for the presence of two scattering scales removes both inconsistencies between the observational data for these four pulsars and differences between the observed and theoretical frequency dependences for the scattering, as well as the need to invoke anomalous scattering magnitudes. The data of the catalog of Taylor *et al*. need to be corrected for the difference in the scattering magnitudes in the two branches of the frequency dependence. © *2004 MAIK "Nauka/Interperiodica"*.

1. INTRODUCTION

The frequency dependence of the scattering of pulsar radio emission is an important characteristic that can identify appropriate models for the scattering interstellar medium. However, this dependence has been studied only for individual pulsars, and the available sparse data are quite contradictory.

The standard theory predicts the frequency dependence $\tau_{sc}(\nu) \propto \nu^{\gamma}$, where $\gamma = -4$ for a normal distribution of the inhomogeneities of the interstellar medium and $\gamma = -4.4$ for a Kolmogorov model [1]. Based on their observations of the pulsar PSR B0833−45 at four frequencies from 300 to 1410 MHz, Komesaroff *et al*. [2] found the shape of the observed profiles to be consistent with frequency dependence for the scatter broadening of the pulses $\tau_{sc} \propto \nu^{-4}$. Measurements of the frequency dependence of the scatter broadening for the Crab pulsar by Rankin *et al*. [3] and Kuzmin and Losovsky [4] yielded the index for the frequency dependence $\gamma \simeq -4$. The measurements for this same pulsar of Kuzmin *et al*. [5] over a very broad frequency interval, from 40 to 2228 MHz, yielded $\tau_{sc} \propto \nu^{-3.8\pm0.2}$. Based on an analysis of their measurements and other published data for nine pulsars, Kuz'min *et al*. [6] determined the mean value $\gamma = -3.0 \pm 0.7$. From measurements of giant pulses of the millisecond pulsar PSR B1937+21 and published data, Kuz'min and Losovskiĭ [7] derived the frequency dependence $\tau_{sc} \propto \nu^{-4}$.

Thus, the above results show that the index in the frequency dependence γ is approximately -4, corresponding to a spectrum with a normal distribution of inhomogeneities. However, based on measurements of the frequency dependence of the decorrelation bandwidth $\Delta\nu_d(\nu)$ for five pulsars, Cordes *et al*. [8] found the mean value $\gamma = -4.45 \pm 0.3$ and concluded that the frequency dependence does not agree with a normal inhomogeneity distribution and is instead consistent with a Kolmogorov spectrum, for which $\gamma = -4.4$. This spectral index γ is adopted in the catalog of 706 pulsars of Taylor *et al*. [9], which contains the most complete data on pulsar scattering.

In addition, for a number of pulsars having many published measurements of the decorrelation bandwidth and pulse scatter broadening, the frequency dependence of the scattering differs considerably from the theoretical expectations. In particular, the published data for PSR B0809+74, PSR B0950+08, PSR B1919+21, and PSR B2303+30 indicate $\gamma = -2.7 \pm 0.7$, -2.0 ± 0.4, -1.8 ± 0.5, and -5.8 ± 2.9, respectively.

These observational results demonstrate that the scatter broadening for these pulsars at 1 GHz differs from the value given in the catalog of Taylor *et al*. [9] by more than an order of magnitude.

Thus, the question of the frequency dependence of the pulse scattering, and, consequently, of the distribution of inhomogeneities of the interstellar medium, remains unsolved. The most complete and widely used list of magnitudes of scatter broadening τ_{sc} is the

1063-7729/04/4802-0136$26.00

Table 1. Observation conditions and measurement results

PSR	DM, pc cm^{-3}	ν, MHz	$\Delta t_{\rm DM}$, ms	Res, ms	τ, ms	N	τ_{sc}, ms	$\delta\tau_{sc}$, ms
B0809+74	5.751	40	0.93	0.82	1.0	14	5.0	1.0
		60	0.25	0.82	1.0	2	0.6	0.4
B0950+08	2.7	40	0.45	0.205	0.3	10	1.0	0.7
		40	0.45	0.409	0.5	22	1.0	0.7
B1919+21	12.43	40	1.9	1.228	1.5	10	15	3.5
		60	0.56	1.228	1.5	10	4.5	3.0
		111	0.09	0.409	0.5	2	0.6	0.4
B2303+30	49.9	40	129	2.56	3.0	2	360	100
		111	5.9	2.56	3.0	8	13	3

Note: DM is the dispersion measure; ν, the observing frequency; $\Delta t_{\rm DM}$, the dispersion broadening; Res, the data sampling interval; τ, the time constant for the postdetector filter; τ_{sc}, the measured pulse scatter broadening; $\delta\tau_{sc}$, the corresponding error; and N, the number of measurements.

catalog of Taylor *et al.* [9], which is based on selective single measurements and the frequency dependence $\tau_{sc} \propto \nu^{-4.4}$ and, therefore, requires refinement and experimental verification.

We have measured the pulse scatter broadening for PSR B0809+74, PSR B0950+08, PSR B1919+21, and PSR B2303+30 at 40, 60, and 111 MHz, expanding considerably the frequency range of these data. Based on our measurements and literature data, we have analyzed the frequency dependences of this parameter and propose a two-scale model for the frequency dependence of the scattering. The model removes the inconsistencies indicated above and enables us to determine the parameters for scattering of the pulsar radio emission in the interstellar medium more precisely.

2. MEASUREMENTS AND REDUCTION

The measurements were carried out at three frequencies (40, 60, and 111 MHz) on the Large Phased Array and decameter radio telescopes of the Pushchino Radio Astronomy Observatory (Astro Space Center, Lebedev Physics Institute, Russian Academy of Sciences) from April 2002 to June 2003. Linear polarization was received. We used a 128-channel receiver with channel bandwidth $\Delta f =$ 1.25 kHz. For PSR B2303+30, a 128-channel receiver with the channel bandwidth $\Delta f = 20$ kHz was used.

The conditions for the observations are summarized in Table 1, where DM is the dispersion measure, ν is the observing frequency, $\Delta t_{\rm DM}$ is the dispersion broadening, Res is the data sampling interval, τ is the time constant for the postdetector filter of the receiver, and N is the number of measurements.

The observations were carried out in an individual-pulse recording regime, with subsequent analysis of the integrated pulse for the entire observing session and of the strongest individual pulses.

The scatter-broadening magnitude was determined by matching the observed pulsar pulse with a model-scattered template representing the intrinsic pulse of the pulsar. The template was specified using a pulse consisting of several Gaussian components that best fit the shape of the intrinsic pulsar pulse. The template pulse was model-scattered by convolving it with a truncated exponential function,

$$G(t) = \begin{cases} \exp(-t/\tau_{sc}) & \text{for } \ t \geq 0 \\ 0 & \text{for } \ t < 0, \end{cases} \quad (1)$$

representing scattering in a thin screen. The pulse was also dispersion-broadened over the channel bandwidth of the receiver, $\Delta f = 1.25$ or 20 kHz, and broadened with the time constant of the postdetector filter of the receiver. A least-squares fit to the observed pulsar pulse was found using the resulting model-scattered pulse. The magnitude of the scatter broadening, τ_{sc}, and the amplitudes, positions, and widths of the Gaussian components were found, as well as the time delay of the template pulse. Figure 1 shows samples of recordings and the processed pulses.

To eliminate the effect of the intrinsic shape of the initial pulsar pulse, we measured τ_{sc} at several frequencies. The value of τ_{sc} at 102 MHz for PSR B0950+08 was taken from Kuzmin *et al.* [5].

Table 2. Literature data on scattering measurements

PSR	ν, GHz	τ_{sc}, ms	$\delta\tau_{sc}$, ms	$\Delta\nu_d$, kHz	$\delta\Delta\nu_d$, kHz	References
B0809+74	0.063			8.5	5	Shitov [10]
	0.102			2.2	0.5	Kuz'min *et al.* [5]
	0.105			130	130	Shitov [10]
	0.15			1200		Rickett [11]
	0.408			2000		Lyne and Smith [12]
	0.43			4000		Lyne and Smith [13]
B0950+08	0.050			30		Phillips and Clegg [14]
	0.063			97	22	Shitov [10]
	0.102	0.05	0.02			Kuz'min *et al.* [5]
	0.102			2.8	0.7	Kuz'min *et al.* [5]
				200	50	
	0.105			210	50	Shitov [10]
	0.320			792		Cordes *et al.* [8]
				1188		
	0.430			20000		Lyne and Smith [12]
	0.430			1089		Cordes *et al.* [8]
	0.436			2000		Johnston *et al.* [15]
B1919+21	0.102			3.8		Kondratiev *et al.* [16]
				8.6		
				25		
				30		
				51		
	0.102			2	0.5	Kuz'min *et al.* [5]
				4	1	
				7	2	
	0.105			6.4	0.9	Shitov [10]
	0.320			800		Rickett [17]
	0.320			7.4		Cordes *et al.* [8]
				19		
				20		
				25		
				54		
	0.335			730		Roberts and Ables [18]
	0.410			2400		
	0.410			3000		Rickett [11]
	0.430			393		Boriakoff [19]
	0.430			900		Smith and Wright [13]
	0.430			100		Lyne and Smith [12]
	0.430			99		Cordes *et al.* [8]
				105		
				119		
				129		
				149		
				347		
B2303+30	0.160	9.9	3.6			Alurkar *et al.* [20]
	0.410			87		Armstrong *et al.* [21]
	0.410			190		Wolszczan [22]
	0.430			0.77		Cordes *et al.* [8]
				1.7		
				4.3		

Notes: ν is the frequency; τ_{sc}, the pulse scatter broadening; $\delta\tau_{sc}$, the corresponding error; $\Delta\nu_d$, the decorrelation bandwidth; and $\delta\Delta\nu_d$, the corresponding error.

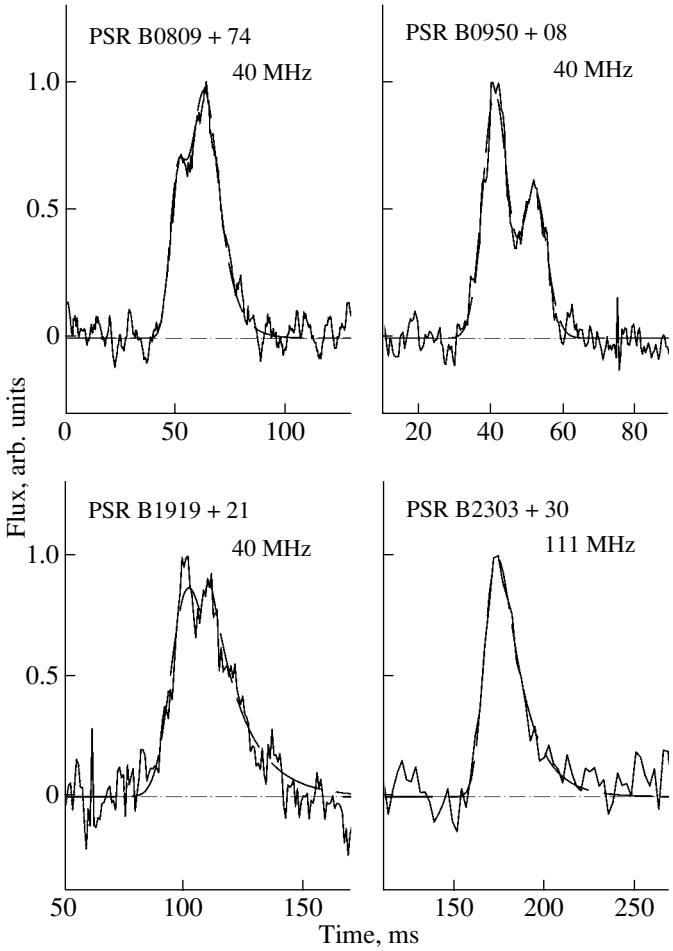

Fig. 1. Sample recordings and processed data. The solid curve shows the observed pulse, and the dashed curve, the model-scattered template.

3. RESULTS

Our results are listed in the last columns of Table 1, where τ_{sc} is the measured pulse scatter broadening and $\delta\tau_{sc}$ is the corresponding error in τ_{sc}.

We used data from the literature to analyze the frequency dependences of this parameter, summarized in Table 2. To reduce the data to a unified system and compare them with the data of Taylor *et al.* [9], we recalculated the literature values for the decorrelation bandwidth $\Delta\nu_d$ to the pulse scatter broadening τ_{sc} using the relationship used in [9], $2\pi\tau_{sc}\Delta\nu_d = 1.53$.

4. ANALYSIS

PSR B0950+08

The pulsar showing the largest inconsistencies of the available scattering data and their frequency dependence is PSR B0950+08. In particular, measurements of the decorrelation bandwidth [8, 10, 12, 14] (Fig. 2a) yield an index for the frequency dependence of the scattering $\Delta\nu_d(\nu) \propto \nu^{-\gamma}$ of $\gamma = -2.0 \pm 0.4$ instead of the theoretical value $\gamma = -4$ to -4.4 and the value adopted by Taylor *et al.* [9], $\gamma = -4.4$. The pulse scatter broadening extrapolated from the observational data at 1 GHz, $\log\tau_{sc} = -7.77$, is three orders of magnitude lower than the catalog value ($\log\tau_{sc} = -10.84$). The measurements of Phillips and Clegg [14] at 50 MHz and of Shitov [10] at 63 and 105 MHz indicate that the scattering is an order of magnitude smaller than for other nearby pulsars.

To explain this anomaly, Phillips and Clegg [14] proposed that the fluctuations of the electron density along the line of sight are an order of magnitude smaller toward PSR B0950+08 than toward any other pulsar. They suggest that the anomalously small value of $\gamma = -1.8$ derived by comparing their data with the results of Cordes *et al.* [8] is due to the fact that the receiver bandwidth in the 320 and 430 MHz measurements of [8] was considerably narrower than the decorrelation bandwidth corresponding to the data of Phillips and Clegg [14] with $\gamma =$

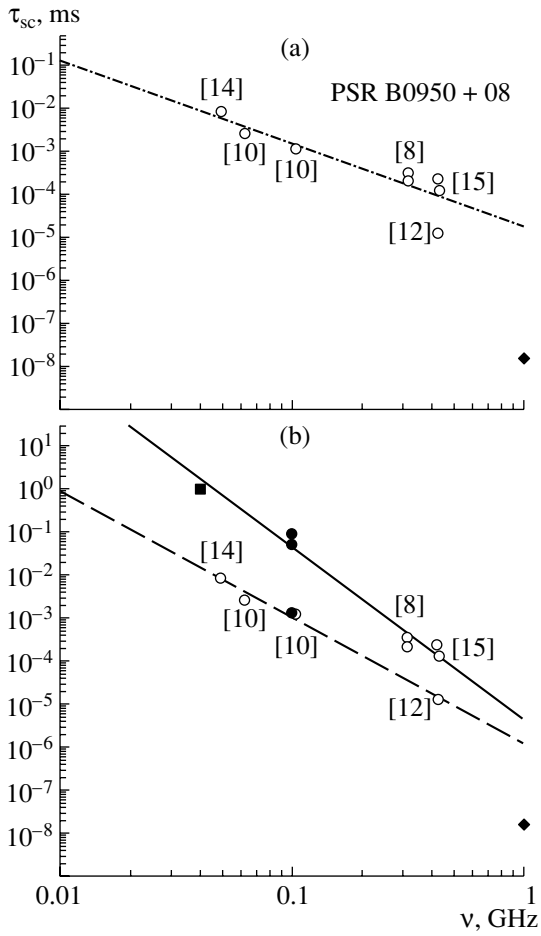

Fig. 2. Frequency dependence of the pulse scatter broadening for PSR B0950+08 (a) purely from previously published data and (b) from our measurements together with the published data. The filled diamond shows the value from the catalog of Taylor *et al.* [9], and the filled squares, our own results. The filled circles in the lower panel show the microstructure measurements of Kuzmin *et al.* [5].

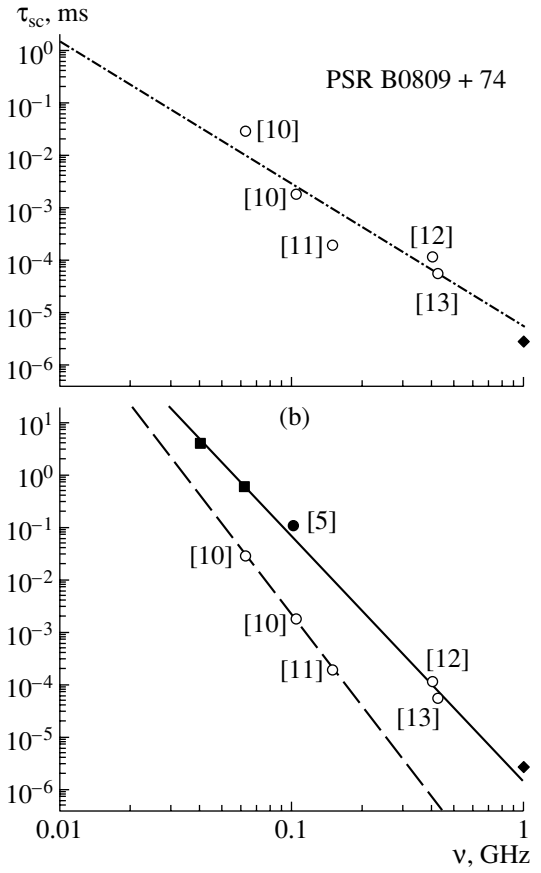

Fig. 3. Same as Fig. 2 for PSR B0809+74.

−4.4; this means that Cordes *et al.* [8] did not measure the actual decorrelation bandwidth. However, the data of [8] have been confirmed by the measurements of Johnston *et al.* [15]. Moreover, following the argument of Phillips and Clegg [14], it is also possible that the frequency resolution of the receiver used by Phillips and Clegg [14] was considerably lower than the decorrelation bandwidth corresponding to the data of Cordes *et al.* [8] with $\gamma = -4.4$, so that Phillips and Clegg [14] likewise did not measure the actual decorrelation bandwidth.

We propose a different approach that removes the above inconsistencies, the anomalous frequency dependence of the scattering, and the need to invoke anomalously small fluctuations of the electron density of the interstellar medium toward this pulsar. We suppose that all the quoted measurements have been carried out correctly but are related to two different branches in the frequency dependence of scattering in the interstellar medium. The basis for this approach is as follows.

Popov and Soglasnov [23] have found two characteristic frequency scales for the decorrelation bandwidth of PSR B0329+54. Kondratiev *et al.* [16] have reported the presence of more than one characteristic scale for the decorrelation bandwidth of PSR B0329+54, PSR 1508+55, PSR 1919+21, and PSR 1641−45. Based on measurements of the pulse microstructure at 102 MHz, Kuzmin *et al.* [5] have detected two scales in the decorrelation bandwidth of PSR B0950+08, $\Delta\nu_{d1} = 200 \pm 50$ kHz and $\Delta\nu_{d2} = 2.8 \pm 0.5$ kHz.

Cordes *et al.* [8] have proposed a two-component model for the scattering interstellar medium: a uniform medium with a characteristic scale $H \geq 0.5$ kpc and local condensations in compact areas with characteristic scales $H \leq 100$ pc. The existence of two types of inhomogeneities in the interstellar medium is also noted by Smirnova *et al.* [24].

Our measurements of pulse scatter broadening at the very low frequency of 40 MHz, the microstructure measurements at 102 MHz of [5] ($\Delta\nu_1 = 2.8$ kHz and $\tau_{sc} = 50$ μs), the data of Cordes *et al.* [8], and

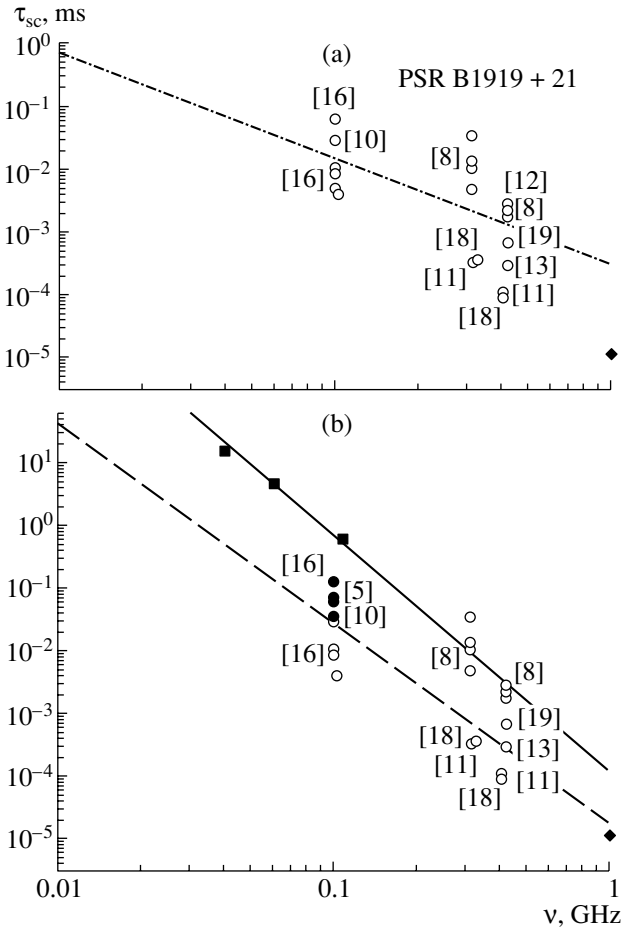

Fig. 4. Same as Fig. 2 for PSR B1919+21.

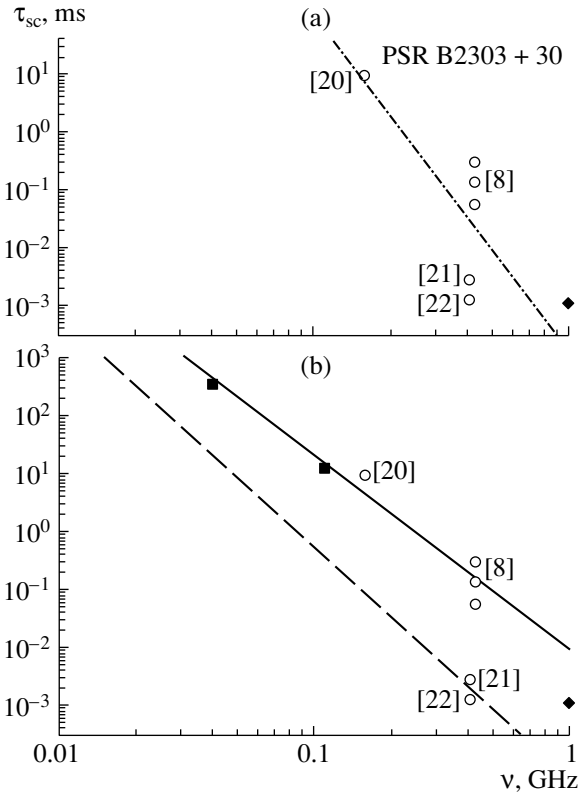

Fig. 5. Same as Fig. 2 for PSR B2303+30.

the data of Johnston *et al.* [15] constitute the upper branch of the frequency dependence, $\tau_{sc}(\nu) \propto \nu^{\gamma}$ with $\gamma = -4.0 \pm 0.3$ (Fig. 2b), which agrees with the theoretical relationship for $\gamma = -4$. The lower branch of this dependence is formed by the data of Phillips and Clegg [14], Shitov [10], Kuzmin *et al.* [5] ($\Delta\nu_2 =$ 200 kHz), and Lyne and Smith [12] with $\gamma = -3.0 \pm 0.2$. The difference from the theoretical value $\gamma = -4$ is probably due to the stated uncertainty in the data of Lyne and Smith [12].

Extrapolation of the upper branch of the frequency dependence to 1 GHz, the frequency adopted by Taylor *et al.* [9], yields $\log \tau_{sc}^{1\,\mathrm{GHz}}\,[\mathrm{s}] = -8.2$, consistent with the scattering data for other pulsars [25]; this removes the need to invoke an anomalous scattering magnitude. The difference of two and a half orders of magnitude between this value and the value of Taylor *et al.* [9] ($\log \tau_{sc}^{1\,\mathrm{GHz}}\,[\mathrm{s}] = -10.84$), which is based only on the 50-MHz observations of Phillips and Clegg [14] and a very long extrapolation to 1 GHz with $\gamma = -4.4$, demonstrates the need to correct the catalog data.

PSR B0809+74

There are also considerable inconsistencies in the available data on the scattering of PSR B0809+74 and its frequency dependence. For instance, measurements of the decorrelation bandwidth [10–13] (Fig. 3a) indicate the index of the frequency dependence of the scattering $\Delta\nu_d(\nu) \propto \nu^{-\gamma}$ to be $\gamma = -2.7 \pm 0.7$.

Our measurements and the 102-MHz microstructure measurements of [5] also reveal a second scale in the frequency dependence of the scattering. The upper branch of the frequency dependence $\tau_{sc}(\nu) \propto \nu^{\gamma}$ with $\gamma = -4.6 \pm 0.2$ (Fig. 3b), which is consistent with the theoretical value $\gamma = -4$, is formed by our measurements at the very low frequency 40 MHz, the microstructure measurements of [5], and the data of [12, 13]. The lower branch of this dependence is formed by the data of Rickett [11] and Shitov [10] with $\gamma = -5.7 \pm 0.3$. The difference from the theoretical value of $\gamma = -4$ could be due to the availability of a small number of measurements in a fairly narrow frequency range.

The extrapolation of the upper branch of the frequency dependence to 1 GHz, the frequency adopted by Taylor *et al.* [9], yields $\log \tau_{sc}^{1\,\mathrm{GHz}} = -8.67$, consistent with the catalog data.

Table 3. Summary of the frequency dependence of the scattering

PSR	γ	$\delta\gamma$	$\log \tau^{0.1}$ (s)	$\log \tau^{1.0}$ (s)	Reference
B0809+74	−4.7 UP	0.2	−4.11 UP	−8.81 UP	This work
	−5.7 LW	0.3	−5.67 LW	−11.35 LW	This work
	−2.7	0.7	−5.55	−8.27	Literature data
	−4.4		−4.14	−8.54	Taylor *et al.* [9]
B0950+08	−4.0 UP	0.3	−4.35 UP	−8.35 UP	This work
	−3.0 LW	0.2	−5.99 LW	−8.94 LW	This work
	−2.0	0.4	−5.82	−7.77	Literature data
	−4.4		−6.44	−10.84	Taylor *et al.* [9]
B1919+21	−3.8 UP	0.2	−3.15 UP	−6.95 UP	This work
	−3.5 LW	0.4	−4.54 LW	−8.05 LW	This work
	−1.8	0.5	−4.84	−6.56	Literature data
	−4.4		−3.59	−7.99	Taylor *et al.* [9]
B2303+30	−3.6 UP	0.6	−1.54 UP	−5.15 UP	This work
	−[4] LW		−3.27 LW	−7.27 LW	This work
	−5.8	2.9	−0.93	−6.77	Literature data
	−4.4		−1.55	−5.95	Taylor *et al.* [9]

Notes: γ is the spectral index of the frequency dependence; $\delta\gamma$, the error in γ; $\log \tau^{0.1\,\mathrm{GHz}}$, the logarithm of the pulse scatter broadening at 0.1 GHz; and $\log \tau^{1\,\mathrm{GHz}}$, the logarithm of the pulse scatter broadening at 1 GHz for the upper (UP) and lower (LW) branches of the frequency dependences $\tau_{sc}(\nu)$.

PSR B1919+21

The index for the frequency dependence of the scattering $\Delta\nu_d(\nu) \propto \nu^{-\gamma}$ for this pulsar from previous measurements of the decorrelation bandwidth [8, 10, 11, 13, 16–19] (Fig. 4a) is $\gamma = -1.8 \pm 0.5$. Extrapolation of this dependence to the catalog frequency $\nu =$ 1 GHz recalculating $\Delta\nu$ to τ_{sc} using $2\pi\tau_{sc}\Delta\nu = 1.53$ yields $\log \tau_{sc}^{1\,\mathrm{GHz}} = -6.58$; this differs from the catalog value, $\log \tau_{sc}^{1\ \mathrm{GHz}} = -7.99$, by one and a half orders of magnitude.

Our measurements at 40, 60, and 111 MHz show the presence of a second scattering scale and its frequency dependence (Fig. 4b). The upper branch, which includes our measurements and those of Cordes *et al.* [8], displays the frequency dependence $\gamma = -3.8 \pm 0.2$, matching the expected theoretical value $\gamma = -4$ to 4.4 within the errors. The scatter broadening, $\log \tau_{sc}^{0.1\,\mathrm{GHz}} = -3.15$, is consistent with the broadening obtained from the statistical dependence of Kuz'min and Losovskiĭ [7], $\tau_{sc}(\mathrm{DM}) = 40(\mathrm{DM}/100)^{2.1}$ $\log \tau_{sc}^{0.1\,\mathrm{GHz}} = -3.3$. The lower branch, which includes the measurements of [5, 10, 11, 13, 16–19], displays the frequency dependence $\gamma = -3.5 \pm 0.4$, and the scatter broadening, $\log \tau_{sc}^{1\,\mathrm{GHz}} = -7.86$, is consistent with the catalog values.

PSR B2303+30

There are also considerable inconsistencies in the available data on the scattering of PSR B2303+30 and its frequency dependence. Published measurements of the decorrelation bandwidth [8, 20, 21, 28] yield the index of the frequency dependence of the scattering $\gamma = -5.8 \pm 2.9$. In Fig. 5a, the pulse scatter broadening extrapolated from the observational data, $\log \tau_{sc}^{1\,\mathrm{GHz}} = -6.77$, is almost an order of magnitude lower than the catalog value [9], $\log \tau_{sc}^{1\,\mathrm{GHz}} = -5.95$.

Our measurements also reveal the presence of a second scale in the frequency dependence of the scattering. The upper branch with $\gamma = -3.6 \pm 0.6$ (Fig. 5b), which agrees with the theoretical dependence $\gamma = -4$, is formed by our measurements at

111 MHz and the measurements of [8, 20]. The lower branch of this relation is formed by the data of [21, 22].

Extrapolation of the upper branch of the frequency dependence to the frequency of 1 GHz adopted in [9] yields $\log \tau_{sc}^{1\,\mathrm{GHz}} = -5.15$, almost an order of magnitude greater than the value in [9], likewise indicating the need to correct the catalog data.

5. DISCUSSION

Table 3 summarizes the results of our analysis of the frequency dependence of the scattering of pulsar pulses based on our own measurements and data from the literature. This table lists the following parameters derived from least-squares fits of the data: the index of the frequency dependence of the pulse scatter broadening γ, logarithm of the pulse scatter broadening at 0.1 GHz $\log \tau^{0.1\,\mathrm{GHz}}$, and logarithm of the pulse scatter broadening at 1 GHz for the upper (UP) and lower (LW) branches of the frequency dependences $\tau_{sc}(\nu)$, $\log \tau^{1\,\mathrm{GHz}}$. Due to the limited amount of data, we adopted $\gamma = -4$ for the lower scattering branch for PSR B2303+30. The table also lists analogous parameters derived from published data and the scatter broadening values presented in [9].

For all four pulsars studied, allowing for the presence of two scattering scales removes inconsistencies between the observational data and the discrepancy between the frequency dependence of the scattering and the theoretical expectations, as well as the need to invoke anomalous scattering magnitudes.

The average index in the frequency dependence of the scattering for the upper branches of the four pulsars studied (which include a greater number of measurements over a broader frequency band) is $\gamma = -4.0 \pm 0.5$, in agreement with the theoretical expectation for a normal distribution of inhomogeneities.

Note that the difference between the scattering magnitudes on the upper and lower branches is nearly the same for all the pulsars—about one and a half orders of magnitude.

6. CONCLUSIONS

We have measured the scatter broadening of the pulses of PSR B0809+74, PSR B0950+08, PSR B1919+21, and PSR B2303+30 at 40, 60, and 111 MHz.

Based on these measurements and data from the literature, we have analyzed the frequency dependences of this parameter. We propose a two-component model for the frequency dependence of the scattering of the pulsar radio emission in the interstellar medium.

Allowing for two scattering scales removes inconsistencies in the observational data for these pulsars and also the discrepancy of the frequency dependence of the scattering with theoretical expectations.

The index in the frequency dependence of the scattering $\tau_{sc}(\nu) \propto \nu^{\gamma}$ for the four pulsars studied, $\gamma \cong -4.0$, is in agreement with the theory if the inhomogeneities obey a normal distribution.

The scattering data in the catalog of 706 pulsars of Taylor *et al.* [9] require corrections for the difference in the scattering magnitudes in the two branches of the frequency dependence.

ACKNOWLEDGMENTS

The authors are grateful to V.V. Ivanova, K.A. Lapaev, and A.S. Aleksandrov for their software and technical support of the observations; to A.A. Ershov and V.A. Samodurov for the data reduction software; and to V.I. Shishov for useful discussions. The authors thank L.B. Potapova for help with preparation of the manuscript. This work was partially supported by the Russian Foundation for Basic Research (project code 01-02-16326).

REFERENCES

1. R. N. Manchester and J. H. Taylor, *Pulsars* (Freeman, San Francisco, 1977; Mir, Moscow, 1980).
2. M. M. Komesaroff, P. A. Hamilton, and J. G. Ables, Aust. J. Phys. **25**, 759 (1972).
3. J. M. Rankin, J. M. Comella, H. D. Craft, *et al.*, Astrophys. J. **162**, 707 (1970).
4. A. D. Kuzmin and B. Ya. Losovsky, Astron. Astrophys. Trans. **18**, 179 (1999).
5. A. D. Kuzmin, P. A. Hamilton, Yu. P. Shitov, *et al.*, Mon. Not. R. Astron. Soc. **344**, 1187 (2003).
6. A. D. Kuz'min, V. A. Izvekova, V. M. Malofeev, *et al.*, Pis'ma Astron. Zh. **14**, 120 (1988) [Sov. Astron. Lett. **14**, 58 (1988)].
7. A. D. Kuz'min and B. Ya. Losovsky, Pis'ma Astron. Zh. **28**, 1 (2002) [Astron. Lett. **28**, 21 (2002)].
8. J. M. Cordes, J. M. Weisberg, and V. Boriakoff, Astrophys. J. **288**, 221 (1985).
9. J. H. Taylor, R. N. Manchester, A. G. Lynn, *et al.*, *Catalog of 706 Pulsars* (1995, unpublished).
10. Yu. P. Shitov, Astron. Zh. **49**, 470 (1972) [Sov. Astron. **16**, 383 (1972)].
11. B. J. Rickett, Mon. Not. R. Astron. Soc. **150**, 67 (1970).
12. A. G. Lyne and F. G. Smith, Nature **298**, 825 (1982).
13. F. G. Smith and N. C. Write, Mon. Not. R. Astron. Soc. **214**, 97 (1985).
14. J. A. Phillips and A. W. Clegg, Nature **60**, 137 (1992).
15. S. Johnston, L. Nicastro, and B. Koribalsky, Mon. Not. R. Astron. Soc. **297**, 108 (1998).
16. V. I. Kondratiev, M. V. Popov, V. A. Soglasnov, *et al.*, Astrophys. Space Sci. **278**, 43 (2001).

17. B. J. Rickett, Ann. Rev. Astron. Astrophys. **15**, 479 (1977).
18. J. A. Roberts and J. G. Ables, Mon. Not. R. Astron. Soc. **201**, 1119 (1982).
19. V. Boriakoff, Ph. D. Thesis (Cornell Univ., 1973).
20. S. K. Alurkar, O. B. Slee, and A. D. Borba, Aust. J. Phys. **39**, 433 (1986).
21. J. W. Armstrong, J. M. Cordes, and B. Rickett, Nature **292**, 561 (1981).
22. A. Wolszczan, Acta Astron. **27**, 127 (1977).
23. M. V. Popov and V. A. Soglasnov, Astron. Zh. **61**, 727 (1984) [Sov. Astron. **28**, 424 (1984)].
24. T. V. Smirnova, V. I. Shishov, and D. R. Stinebring, Astron. Zh. **75**, 866 (1998) [Astron. Rep. **42**, 766 (1998)].
25. A. D. Kuz'min and B. Ya. Losovskiĭ, Astron. Zh. **76**, 338 (1999) [Astron. Rep. **43**, 288 (1999)].

Translated by G. Rudnitskiĭ

Astronomy Reports, Vol. 48, No. 2, 2004, pp. 145–152. Translated from Astronomicheskiĭ Zhurnal, Vol. 81, No. 2, 2004, pp. 168–175.

Coronal Mass Ejections and Eruptive Prominences: Mutual Spatial Arrangement

A. V. Lozhechkin and B. P. Filippov

Institute of Terrestrial Magnetism, Ionosphere, and Radiowave Propagation, Russian Academy of Sciences, Troitsk, Moscow oblast, 142090 Russia

Received July 10, 2003; in final form, August 8, 2003

Abstract—The mutual spatial arrangement of coronal mass ejections and eruptive prominences on the Sun is considered. These phenomena occur on different scales and are observed at different heights above the solar surface. In spite of the presumed causal connection between them, they are often widely separated in position angle at epochs of solar minimum. This means that the motion of a prominence in the corona is not strictly radial and has an appreciable component along the surface. This behavior can be explained in a model of a filament as a magnetic flux rope in equilibrium in the coronal magnetic field. The initial trajectory of the filament is determined by the structure of the global field. © *2004 MAIK "Nauka/Interperiodica"*.

1. INTRODUCTION

The conditions for observing solar-activity phenomena usually make it impossible to observe the development of a single process continuously, from its origin in the lower layers of the atmosphere to its transition into an interplanetary disturbance. This is largely the case for eruptive prominences. Hα observations of the onset of the activation of a filament (prominence) frequently end very soon due to the departure of this line from the filter band due to the Doppler effect, the decrease of the emission due to the decrease in the density of expanding material, and the ionization of hydrogen due to heating of the prominence plasma. The subsequent evolution can sometimes be observed in the ultraviolet or radio, but the fate of a prominence usually becomes visible only when it reaches the lower boundary of the field of view of a spaceborne coronagraph ($\sim 2R_\odot$) and becomes visible in white light as a coronal mass ejection (CME). A typical CME consists of three parts: a bright core that is the remnant of an eruptive prominence; a large, dark, lower-density surrounding cavity; and an outer, rather diffuse envelope having the projected shape of a closed loop with its legs fixed on the Sun [1, 2]. However, detailed comparisons of the positions of filaments on the disk that have suddenly disappeared and CMEs reveal certain problems in explaining CMEs as continuations of filament eruptions in the upper corona. The heliolatitudes of the disappeared filaments and subsequent coronal ejections sometimes differ by tens of degrees [3–5]. If the two phenomena are causally connected, this raises the question of why they are so widely separated in latitude (position angle).

In this paper, we study the mutual spatial arrangement of a number of eruptive prominences and CMEs at an epoch of solar minimum and compare the results with a model that enables us to interpret phenomena observed at various levels of the solar atmosphere as parts of a single process associated with the evolution of a magnetic-flux rope in the coronal magnetic field.

2. DATA USED IN THE ANALYSIS

Studies of statistical connections between coronal ejections and other forms of activity have shown that, among phenomena observed in the lower layers of the solar atmosphere, CMEs are most closely associated with eruptive prominences [6–9]. However, some analyses have shown the correlation between eruptions and coronal mass ejections to be weak (10–30%) [10, 11]. Such low correlations are probably due to the fact that the authors also include into eruptive prominences the thermal disappearance of filaments [12], sprays and surgers, and the activation of filaments with finite motion [13]. Recent studies distinguishing between eruptive and activated or between radially and tangential moving prominences confirm the presence of high correlations between the two phenomena (at the 83–94% level) [14–16].

We have proceeded from the assumption that a "genuine" eruption of a prominence, with all or most of a filament departing from equilibrium and accelerating upward to a large height in the corona, always produces a coronal ejection. We are interested in the path of a prominence up until the moment when it becomes a bright CME core.

Figures 1–3 show the development of an eruptive phenomenon on October 19, 1997, as an example.

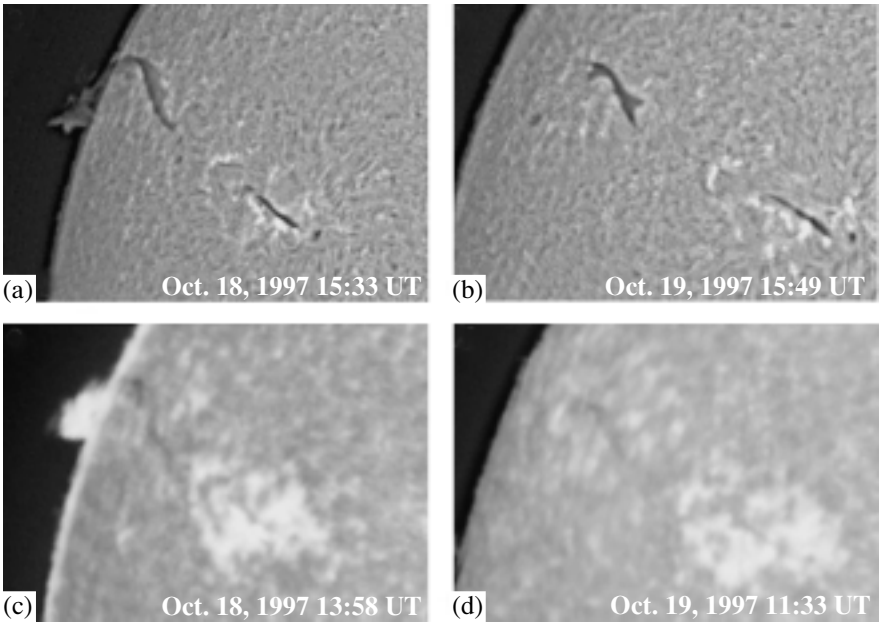

Fig. 1. (a, b) Hα filtergrams of the Sun obtained at Big Bear Observatory and (c, d) Meudon Observatory spectroheliograms in the K3 Ca line.

In the filtergrams of October 18, a large filament is visible as a bulging prominence at the eastern limb of the Sun (Fig. 1). The eruption of part of the filament (prominence) was observed in the ultraviolet by the EIT telescope on SOHO and the Nobeyama radioheliograph. The dark prominence above the limb vanished from the EIT images between 1:26 UT and 1:55 UT on October 19. By 2:25 UT, some of the dark filament on the disk also disappeared and the rest became low-contrast. In snapshots taken from 2:46 UT until 3:26 UT, a bright node moving eastward above the limb is visible. It is obvious that this is material from the prominence, heated during the eruption and so evolving from absorption of the ultraviolet radiation to emission [17]. The path of the prominence is shown in Fig. 2 as a chain of dark and bright nodes above the prominence. These nodes trace the positions of the eruptive prominence at different times. This image was obtained by combining a snapshot at 1:26 UT with a series of time-difference images taken from 2:46 UT to 3:26 UT. The path of the prominence deviates by more than 30° southward from the radial direction, shown in Fig. 2 by the white dashed line. After 6 UT, arches of emission appear above the place where the filament was located, which increase in size until 12 UT and then slowly fade. In filtergrams taken on October 19 (Fig. 1), we can see that the filament did not decay completely but reduced its length to less than half its initial value. There is also no prominence above the limb visible in the Meudon Observatory spectroheliograms (Fig. 1d).

Figure 3 shows a sequence of snapshots made by the C2 LASCO coronagraph on board the SOHO spacecraft, illustrating the development of a coronal ejection that followed the eruption of a prominence. There were some overlapping streamers at the eastern limb, which filled the region within ±30° of the equator. Some disturbance crossed the C2 field of view along the streamers from 5 UT to 6 UT but did not upset the ray structure. This feature probably had a wave nature. The first signs of the development of a CME appear about 8 UT as an inflation of the feet of the streamers at the edge of the occulting disk. The ejection encompasses the entire system of streamers, though it does not destroy them completely after its transit. As a whole, it is arranged symmetrically about the equatorial plane and is moving along this plane.

The eruption pattern observed on October 19, 1997, is typical of activity minimum. At such epochs, the filaments are mainly concentrated at middle latitudes, and it is natural that eruptions are initiated from these regions. Coronal structures are clustered about the equator. Unfortunately, the motions of prominences can only rarely be traced to the boundary of the field of view of the spaceborne coronagraph; therefore, we had to compare the coordinates of the beginnings of eruptions (prominences, disappeared filaments) and those of CMEs at distances of $\geq 2R_\odot$. We have analyzed a set of SOHO observations of CMEs for 1996–1998 together with observations of disappearing filaments and eruptive prominences. The latter were taken from the catalog of solar events presented by the NOAA at http://www.sec.noaa.gov/ftpmenu/indices/events.html.

We have selected only events that can confidently be associated with CMEs, where the CME can be considered to be a continuation of the eruption of a specific filament in time and space (table).

We have compared the distributions of eruptive prominences and CMEs about the solar magnetic equator, since it is likely that only electromagnetic forces can control the motions of plasma structures tangent to the solar surface. We have taken the neutral line on maps of the magnetic field of the source surface calculated and published monthly in the Solar Geophysical Data as the solar magnetic equator. Unfortunately, although we know a CME's position angle, we can say nothing about its heliographic longitude. The neutral line is a fairly sinuous curve, and we cannot readily tell at what angular distance from this line the CME appeared. Therefore, we have plotted on the map a segment with the given latitude and a scatter in heliographic longitude of 90° (±45° with respect to the limb). If CMEs are separated from the limb by more than 45°, they are likely to be halo-type CMEs, which we did not consider. We then found the mean distance of the given segment from the neutral line after integrating using the method of trapezoids. We adopted this quantity for the distance of the CME from the magnetic equator. In the table, the letters B and A before a time denote that the event began before or after this time. A minus sign before the CME's distance from the magnetic equator indicates that the prominence and CME were located on opposite sides of the equator. The notation EPL denotes an eruptive prominence observed above the limb, and DFS, the disappearance of a filament on the solar disk.

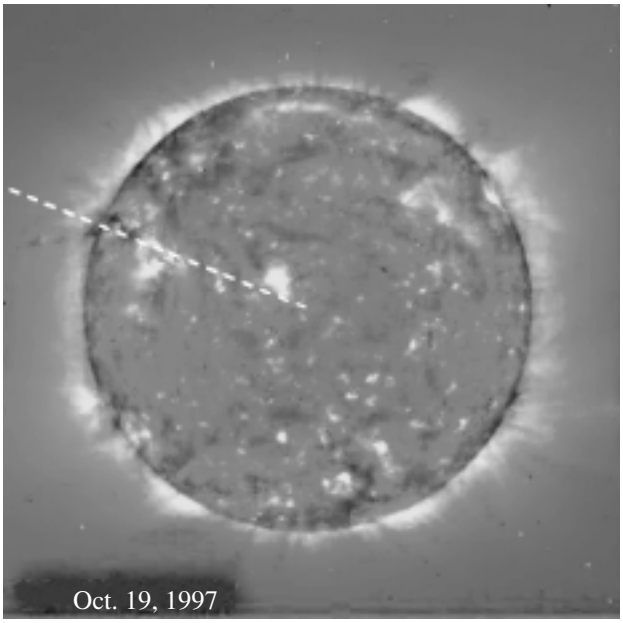

Fig. 2. Composite image combined from a snapshot at 1:26 UT in the 195-Å ultraviolet band of the SOHO EIT telescope and several time-difference images in the same line obtained between 2:46 and 3:26 UT. A chain of dark and bright nodes above the prominence transferred from the time-difference images traces the path of the eruptive prominence. The path deviates more than 30° southward from the radial direction, shown with the white dashed line (we have used data from the joint ESA–NASA project SOHO).

3. RESULTS

In 1996–1997, prominences disappeared, on average, at an angular distance of 25° from the magnetic equator, with a dispersion of 19°, and CMEs appeared, on average, 15° from the equator, with a dispersion of 15°. The positions of 81% of CMEs are closer to the magnetic equator than are those of the disappearing filaments. The distributions are shown as histograms in Figs. 4a and 4b. The distribution of prominences peaks at 20°–29°, whereas the maximum of the CME distribution is at 0°–9°. It can be shown that CMEs and disappearances of filaments could differ in position angle by as much as 70°, with the difference being most often between 16° and 33°. Thus, the positional relationship is such that eruptions of prominences take place fairly far from the plane of the magnetic equator, while CMEs tend to concentrate toward this plane. Therefore, if a CME indeed represents a further development of an eruptive prominence, the latter would have to have traveled a long distance along the solar limb rather than rise radially.

Figures 4c and 4d present data for 1998. Prominences disappeared, on average, 33° from the magnetic equator, with a dispersion of 23°, while CMEs appeared, on average, 37° from the equator, with a dispersion of 25°. The picture for CMEs is very "blurred," and we can see that, in many cases, the eruption proceeded nearly radially.

4. DISCUSSION AND COMPARISON WITH THE MODEL

The distributions we have obtained are consistent with the results of other studies [3–5, 16], though ours are based on a different sample and are plotted as functions of the angular distance from the magnetic equator, not as functions of heliolatitude. The plane of the magnetic equator virtually coincides with the plane of the heliographic equator during solar minimum, the two differ during the phase of increasing activity, and they can be perpendicular near solar maximum. The situation near solar minimum is suitable for analyses of the development of eruptive processes in space, because it is close to axisymmetric

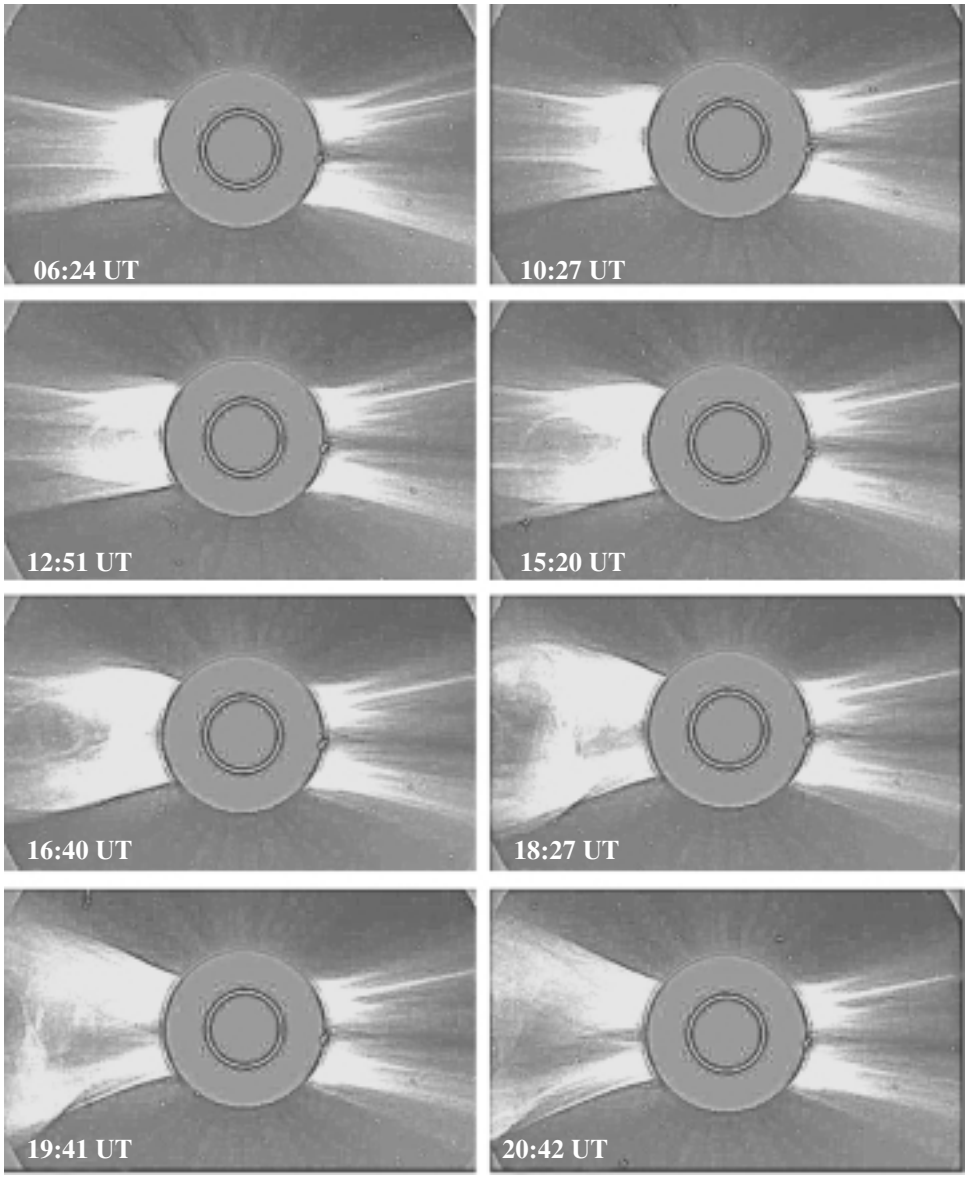

Fig. 3. Sequence of images from the SOHO C2 LASCO coronagraph illustrating the development of a coronal ejection that followed the eruption of a prominence (we have used data from the joint ESA–NASA project SOHO).

with the axis perpendicular to the line of sight, which is convenient for observations. We can see that the paths of plasma structures at the beginning and end of the eruption can differ widely. Because of this, the coordinates of the "source" (filament) and coronal ejection can also differ by tens of degrees, not only in latitude, as we have established here, but also in longitude. This is very important for estimating the geoeffectiveness of CMEs.

According to classical concepts, a quiescent prominence is located above a polarity-inversion line of the photospheric magnetic field. The mean theoretical pattern of the global solar magnetic field at activity minimum assumes the presence of three polarity-inversion lines in the photosphere and a dipole character for the field in the upper corona (Fig. 5). Thus, the third harmonic (octupole) of the expansion of the magnetic-field potential in spherical functions dominates at the photospheric surface, while the first harmonic (dipole) [18] dominates at a distance of about one solar radius. Filaments and prominences "select" mainly middle-latitude neutral lines, whereas coronal phenomena (streamers, CMEs) are clustered toward the neutral line of the dipole field, near the equator. If the equilibrium and motion of a prominence is determined by electromagnetic forces, the global magnetic field will determine the path of a prominence in the corona. We have

Angular distance of CMEs and eruptive prominences from the magnetic equator

	CME			EP				
Date	Time (UT)	Position angle, deg	Distance from magnetic equator, deg	Beginning (UT)	End (UT)	Type of event	Coordinates	Distance from magnetic equator, deg
Oct. 19, 1996	17:39	156	83	B16:08	B17:00	DSF	S19E55	42
Dec. 8, 1996	18:30	87	17	B15:48	B16:09	DSF	N41E46	60
Dec. 12, 1996	14:30	94	25	A07:35	B07:58	DSF	S22E10	3
Dec. 19, 1996	16:30	269	−10	B16:33	B17:13	DSF	N02W34	23
Dec. 23, 1996	13:38	284	35	20:11	20:48	EPL	S13W67	37
Jan. 10, 1997	10:04	85	−8	B05:15	10:15	DSF	N21E15	13
May 31, 1997	18:39	280	−5	B12:02	13:49	DSF	N43W90	40
July 30, 1997	19:32	95	−7	B16:35	16:50	DSF	N45E21	25
Sept. 29, 1997	15:47	75	−10	B12:54	14:59	DSF	N22E90	23
Sept. 29, 1997	18:31	78	−13	A14:47	14:57	EPL	N23E90	25
Oct. 13, 1997	11:52	265	−3	B10:00	10:26	EPL	S34W29	30
Oct. 21, 1997	01:27	108	30	A23:49	B00:56	DSF	S33E59	32
Nov. 10, 1997	12:02	257	22	B07:30	07:58	DSF	N30W70	23
Nov. 12, 1997	04:33	270	8	A23:56	03:01	DSF	N25W39	25
Dec. 9, 1997	12:27	253	20	11:50	11:54	EPL	S27W90	17
Dec. 27, 1997	00:34	279	7	B23:52	01:16	EPL	N35W90	18
Feb. 15, 1998	10:27	322	28	B03:50	B07:35	DSF	N33E23	62
Feb. 23, 1998	23:27	86	−10	20:58	21:55	DSF	N28E11	28
March 1, 1998	20:13	268	−8	18:59	00:00	EPL	S26W86	20
March 6, 1998	01:19	256	20	B17:26	A18:34	EPL	S52W90	60
March 28, 1998	22:42	326	52	18:26	20:38	DSF	N19W26	5
March 31, 1998	13:17	97	38	A11:02	11:29	DSF	S27E51	50
Apr. 28, 1998	23:43	63	7	18:51	B19:14	DSF	S24E31	12
May 9, 1998	15:18	228	40	15:20	16:08	EPL	S22W90	43
May 28, 1998	22:31	140	45	19:06	19:24	EPL	N20W90	10
May 29, 1998	22:31	281	2	18:32	18:52	EPL	S26W50	27
June 5, 1998	07:03	205	79	A05:48	06:40	DSF	S41W18	65
June 15, 1998	14:55	195	30	B11:09	11:24	DSF	S71E01	73
June 15, 1998	17:27	106	33	16:55	17:37	EPL	S18E90	35
Oct. 26, 1998	21:37	288	32	17:10	17:39	EPL	N23W90	47
Nov. 9, 1998	01:26	80	32	23:18	23:30	DSF	N24E25	2
Nov. 10, 1998	22:18	106	3	15:20	16:08	EPL	S22W90	27

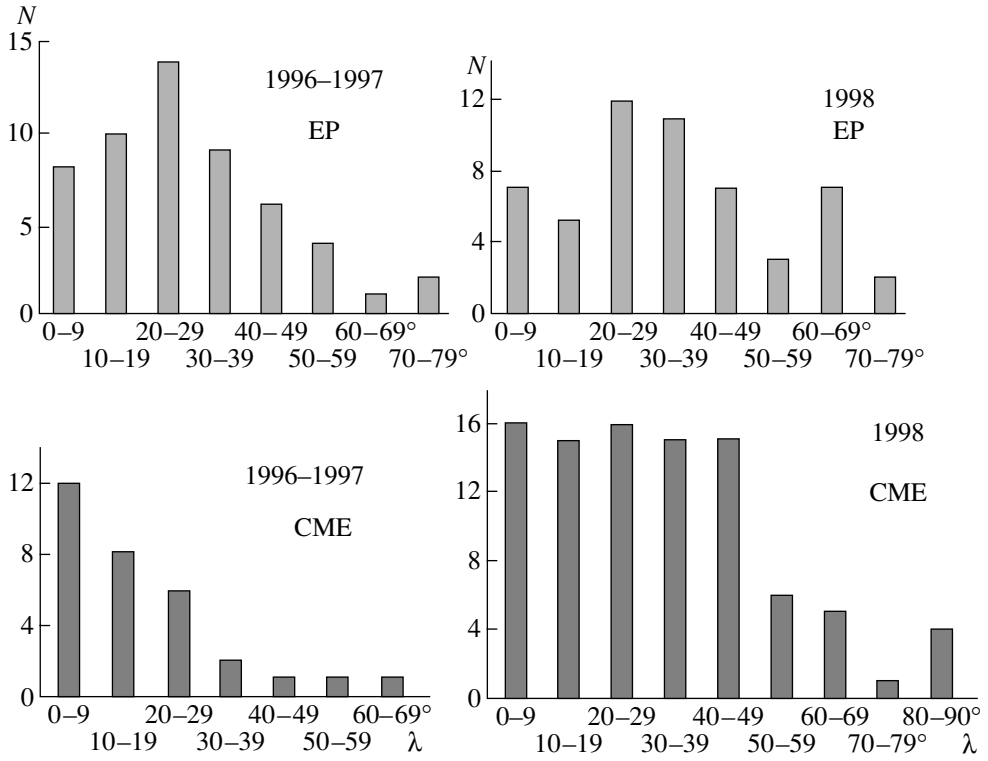

Fig. 4. Histograms of the numbers N of eruptive prominences (EPs) and CMEs as functions of the angular distance λ from the solar magnetic equator in 1996–1997 and 1998.

developed an axisymmetric model for the eruption of a filament represented by a toroidal magnetic-flux rope [19, 20]. In a cylindrical coordinate system (ρ, φ, z) with its origin at the center of the Sun and its z axis aligned with the rotational axis, the equations of motion of a segment of a torus with unit length are

$$m\frac{d^2\rho}{dt^2} = \frac{I}{c}(B_z^{(ex)} + B_z^{(m)} + B_z^{(I)}) - mgR_\odot^2\frac{\rho}{(\rho^2+z^2)^{3/2}}, \quad (1)$$

$$m\frac{d^2z}{dt^2} = -\frac{I}{c}(B_\rho^{(ex)} + B_\rho^{(m)}) - mgR_\odot^2\frac{z}{(\rho^2+z^2)^{3/2}}, \quad (2)$$

where $B^{(ex)}$ is the magnetic field created by subphotospheric sources and currents in the region of the solar wind, $B^{(m)}$ is the field of induction currents in the photosphere that hinder the coronal-current field from penetrating into the Sun, $B^{(I)}$ is a field created by a current flowing along the axis of a ring, M is the mass per unit length of the filament, and g is the gravitational acceleration at the photosphere level.

Solving (1)–(2) with zero left-hand sides for various currents I, we can derive the final equilibrium position of a filament. For specified coronal magnetic fields for the subphotospheric sources in the range 1–10 G, a filament in the corona at a height of about 10–30 Mm can be in equilibrium if the current strengths are 10^{10}–10^{11} A. For typical densities of $\approx 10^5 \mathrm{g\,cm^{-1}}$, the prominence mass in this model does not appreciably affect the final equilibrium position in the lower corona, since the gravitational force is more than an order of magnitude weaker than the electromagnetic forces acting on the filament. Two equilibrium points on the curve representing the locus of equilibrium points of the filament correspond to each current. One lies higher and one lower than some critical point; a unique solution of (1)–(2) corresponds to the current I_c at this point. No equilibrium in the corona is possible for currents greater than I_c. Only the lower equilibrium position is stable; if the critical current is exceeded, a "catastrophe" (i.e., eruption of the filament) occurs.

Having reached the critical point after a slow evolution due to the changing external field or its own current, the filament loses stability and erupts. The behavior of a filament can be studied by numerically solving the equations of motion (1)–(2) jointly with the induction equation

$$\Phi = \Phi_{ex} + \frac{LI}{c} = \text{const}, \quad (3)$$

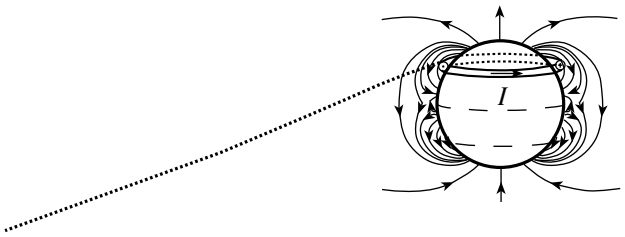

Fig. 5. Lines of force of the global solar magnetic field adopted in the model. The dashed lines show the polarity-inversion lines at the photospheric surface, and the heavy dashed line, the path of a filament during its eruption.

where L is the self-induction of the current ring.

The path of the filament during the eruption is shown by the heavy dashed line in Fig. 5. The path is initially close to the equilibrium curve, then deviates from it, presumably because inertial forces begin to exert their influence. Due to its inertia, the filament crosses the equatorial plane and continues along virtually a straight line at a small angle ($\approx 20°$) to the equatorial plane. The calculated path of the filament is very similar to the behavior of the prominence and ejection of October 19, 1997, described above. It is also probably typical of all eruptive phenomena at activity minimum. The angular distributions of a collection of such phenomena at low heights and distances beyond two solar radii will be similar to those shown in Figs. 4a and 4b.

5. CONCLUSIONS

Based on LASCO SOHO observations in 1996–1998 and SEC NOAA data for the same period, we have studied the mutual spatial arrangements of a number of CMEs and nearly contemporaneous filament disappearances and prominence eruptions. All the events were plotted on maps of the magnetic field at the source surface presented in the Solar Geophysical Data. In 1996–1997, during solar minimum, the distributions of the angular distances of CMEs and prominences from the zero line differ drastically: CMEs appear appreciably closer to the magnetic equator than the locations where filaments disappear. If we consider coronal ejections to be continuations of prominence eruptions, these distributions provide evidence for nonradial and nonrectilinear motions of prominences in the corona. Such behavior of eruptive prominences can be explained in a model with a magnetic-flux rope in equilibrium with the coronal magnetic field. The global magnetic field not only determines the sites where the prominences can appear (above large-scale polarity-inversion lines) but also controls their motion in the corona during the eruption. The evolution for a plasma clump determined by the complex magnetic field of the corona can be, at first glance, unexpected. Instead of displaying purely radial (i.e., only vertical at a given point) and rectilinear motion, the plasma can move a considerable distance along the solar surface. If, in addition, the main phase of acceleration is hidden from the observer, phenomena in the lower and upper corona could appear to be essentially unrelated, whereas they actually represent the development of a single phenomenon.

ACKNOWLEDGMENTS

This work was supported by the Russian Foundation for Basic Research (project nos. 03-02-17736, 03-02-06044) and the Federal Scientific and Technological Program in Astronomy.

REFERENCES

1. F. Crifo, J. P. Picat, and M. Cailloux, Sol. Phys. **83**, 143 (1983).
2. D. G. Sime, R. M. MacQueen, and A. J. Hundhausen, J. Geophys. Res. **89**, 2113 (1984).
3. D. F. Webb, in *IAU Coll. No. 167: New Perspectives on Solar Prominences*, Ed. by D. Webb, D. Rust, and B. Schmieder (Astron. Soc. Pacific, San Francisco, 1998); ASP Conf. Ser. **150**, 463 (1998).
4. E. W. Cliver and D. F. Webb, in *IAU Coll. No. 167: New Perspectives on Solar Prominences*, Ed. by D. Webb, D. Rust, and B. Schmieder (Astron. Soc. Pacific, San Francisco, 1998); ASP Conf. Ser. **150**, 479 (1998).
5. N. Gopalswamy, Y. Hanaoka, and H. S. Hudson, Adv. Space Res. **25**, 1851 (2000).
6. R. H. Munro and A. J. Hundhausen, Sol. Phys. **108**, 383 (1987).
7. N. R. Sheeley, Jr., R. A. Howard, M. J. Koomen, and D. J. Michels, Astrophys. J. **272**, 349 (1983).
8. D. F. Webb and A. J. Hundhausen, Sol. Phys. **108**, 383 (1987).
9. O. C. St. Cyr and D. F. Webb, Sol. Phys. **136**, 379 (1991).
10. H. Wang and P. Goode, in *Synoptic Solar Physics*, Ed. by K. S. Balasubramanian, J. W. Harvey, and D. M. Rabin (Astron. Soc. Pacific, San Francisco, 1998); ASP Conf. Ser. **140**, 497 (1998).
11. G. Yang and Y. Wang, in *Proc. COSPAR Colloq., Ser. 14: Magnetic Activity and Space Environment*, Ed. by H. N. Wang and R. L. Xu (Pergamon, Boston, 2002), p. 113.
12. Z. Mouradian, I. Soru-Escaut, and S. Pojoga, Sol. Phys. **158**, 269 (1995).
13. M. M. Molodenskiĭ, B. P. Filippov, and N. S. Shylova, Astron. Zh. **69**, 181 (1992) [Sov. Astron. **36**, 92 (1992)].
14. H. R. Gilbert, T. E. Holzer, J. T. Burkepile, and A. J. Hundhausen, Astrophys. J. **537**, 503 (2000).
15. K. Hori and J. L. Culhane, Astron. Astrophys. **382**, 666 (2002).

16. N. Gopalswamy, M. Shimojo, W. Lu, *et al.*, Astrophys. J. **586**, 562 (2003).
17. B. Filippov and S. Koutchmy, Sol. Phys. **208**, 283 (2002).
18. S. Bravo, G. A. Stewart, and X. Blanco-Cano, Sol. Phys. **179**, 223 (1998).
19. B. P. Filippov, N. Gopalswamy, and A. V. Lozhechkin, Sol. Phys. **203**, 119 (2001).
20. B. P. Filippov, N. Gopalsvamy, and A. V. Lozhechkin, Astron. Zh. **79**, 462 (2002) [Astron. Rep. **46**, 417 (2002)].

Translated by G. Rudnitskiĭ

Astronomy Reports, Vol. 48, No. 2, 2004, pp. 153–160. Translated from Astronomicheskiĭ Zhurnal, Vol. 81, No. 2, 2004, pp. 176–183.

Differential Rotation and Meridional Circulation near the Boundaries of the Solar Convection Zone

L. L. Kitchatinov

Institute for Solar–Terrestrial Physics, Siberian Division, Russian Academy of Sciences, P.O. Box 4026, Irkutsk, 664033 Russia

Received May 8, 2003; in final form, August 8, 2003

Abstract—Although the theory of differential rotation is in satisfactory agreement with helioseismological data for the deep convection zone, there are considerable discrepancies near the solar surface. This disagreement can be eliminated if the anisotropy of turbulent convection is taken into account together with the effects of nonuniformity of the medium, on which the most recent models for differential rotation are based. The model for the differential rotation of the convection envelope is supplemented by computations for the transition layer between nonuniform and rigid-body rotation in the upper layers of the solar radiative zone. These are the first computations of differential rotation for the entire volume of the Sun.

1. INTRODUCTION

Starting from the pioneering work of Lebedinskiĭ [1], the nonuniform rotation of the Sun has been explained by the interaction between rotation and convection. As was found in [1], if the convective turbulence possesses anisotropy in a specific direction, random turbulent motions produce a regular angular-momentum flux due to the Coriolis force, which disrupts the uniformity of the rotation. This phenomenon was later called the Λ effect [2].

The main problem in the theory of differential rotation is that the Coriolis number,

$$\Omega^* = 2\tau\Omega, \qquad (1)$$

determining the intensity of the interaction between convection and rotation is not small for the Sun and most similar stars. In (1), τ is the characteristic time for convective motions, and Ω, the angular velocity. Therefore, the corresponding theory must be nonlinear in the Coriolis number. Weakly nonlinear effects were studied in [3, 4], and full nonlinear expressions for the convective angular-momentum fluxes were found in [5, 6]. In addition, it was established that not only anisotropy but also nonuniformity of the turbulent medium results in the Λ effect [7, 8]. The nonuniformity of the density is most important in this connection [9]. Its contribution to the Λ effect is substantially greater than the contribution from anisotropy at large Coriolis numbers, in particular, for the value $\Omega^* \simeq 6$ that is typical for the Sun [10] (Fig. 1). This seems to be associated with the fact that rotation can change the anisotropy of the turbulence but has virtually no effect on nonuniformity.

The ratio of the contributions of nonuniformity and anisotropy indicated above is favorable for constructing models of differential rotation. The anisotropy of the convective turbulence has been studied little, and if it were substantial, this would require an additional free parameter in the models. On the contrary, the nonuniformity is well understood. The stratification of stellar convection zones is very close to adiabatic. Therefore, the model [11] based on nonuniformity actually does not contain any free parameters. Nevertheless, it is in reasonable agreement with helioseismological data on the rotation of the convection zone, and the predictions of differential stellar rotation [12, 13] are confirmed by observations [14, 15].

On the other hand, a detailed comparison of model computations with available data shows discrepancies near the boundaries of the solar convection zone. Helioseismology predicts an acceleration of the rotation with increasing depth near the solar surface [16, 17], while the theoretical model [11] exhibits the opposite behavior. In addition, the calculated meridional flow changes its direction near the surface, so that the surface flow is directed toward the equator, while observations reveal a flow from the equator toward the poles in the solar photosphere [18]. As we will demonstrate below, these discrepancies can be removed by taking the anisotropy of the convective motions into account. The reason is that the Coriolis number (1) decreases near the solar surface. For giant convection in deep layers of the convection zone, $\Omega^* \simeq 6$, and anisotropy can be neglected (Fig. 1). However, $\Omega^* \simeq 0.5$ in the surface layers of supergranules, and the angular-momentum fluxes arising due to the anisotropy of the convective motions must

1063-7729/04/4802-0153$26.00

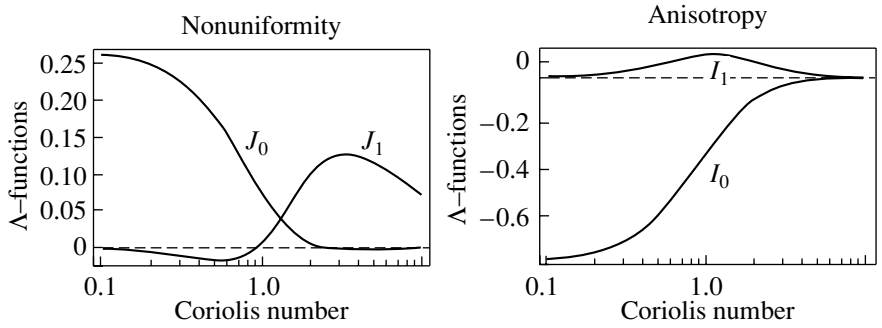

Fig. 1. Comparison of the contributions from nonuniformity of the medium and anisotropy of the turbulence to the angular-momentum fluxes. The effect of nonuniformity is dominant for large Coriolis numbers.

be taken into account. As will be shown below, this approach enables us to attain agreement with the observed radial nonuniformity of the rotation and the surface meridional flows.

There is a thin transition layer (from differential to rigid-body rotation) beneath the convection envelope [16, 17]. This transition seems to be governed by the magnetic field of the radiative zone [19, 20]. In previous studies, the base of the convection zone was the lower boundary for calculations of the differential rotation. We will supplement the differential-rotation model with an analysis of the transition layer and compute the differential rotation in the entire volume of the Sun.

2. CONVECTIVE ANGULAR-MOMENTUM FLUXES: COMPARING THE CONTRIBUTIONS FROM NONUNIFORMITY AND ANISOTROPY

Turbulent motions can redistribute the angular momentum between various spatial regions, resulting in nonuniformity of the rotation. The angular-momentum fluxes in the meridional ($-r\sin\vartheta R_{\vartheta\phi}$) and radial ($-r\sin\vartheta R_{r\phi}$) directions are proportional to the off-diagonal components of the Reynolds stress tensor:

$$R_{ij} = -\rho\langle u_i u_j\rangle, \qquad (2)$$

where the angular braces denote averaging over the ensemble of turbulent fluctuations, $\mathbf{u}$ is the fluctuational velocity, and r, ϑ, ϕ are the usual spherical coordinates. It is important for the theory of differential rotation that, along with the contributions from turbulent viscosity R^ν, the Reynolds stresses for a rotating medium include nondissipative components R^Λ, which are proportional to the angular velocity $\mathbf{\Omega}$ rather than its spatial derivatives:

$$R_{ij} = R^\nu_{ij} + R^\Lambda_{ij} = \rho\mathcal{N}_{ijkl}\frac{\partial V_k}{\partial r_l} \qquad (3)$$

$$- \rho\nu_T\Omega_k n_l\Big(U\left(n_i\varepsilon_{jkl} + n_j\varepsilon_{ikl}\right)$$
$$- H\frac{(\mathbf{n}\cdot\mathbf{\Omega})}{\Omega^2}\left(\Omega_i\varepsilon_{jkl} + \Omega_j\varepsilon_{ikl}\right)\Big).$$

Here, $\mathcal{N}$ is the effective viscosity tensor; $\mathbf{V}$, the large-scale velocity; U and H, the dimensionless angular-momentum fluxes in the radial direction and along the axis of rotation, respectively; and $\mathbf{n}$, the radial unit vector. The presence of nondissipative terms in (3) is called the Λ effect, as discussed in the Introduction. Let us write the nondissipative components of the Reynolds stresses that are sources of differential rotation:

$$R^\Lambda_{r\phi} = -\rho\nu_T\Omega\sin\vartheta\left(U - H\cos^2\vartheta\right), \qquad (4)$$
$$R^\Lambda_{\vartheta\phi} = -\rho\nu_T\Omega H\cos\vartheta\sin^2\vartheta.$$

If $H > 0$, the meridional angular-momentum flux is directed toward the equator, and we expect a decrease in the angular velocity with latitude. When $H < 0$, the opposite behavior should be observed. When $U - H\cos^2\vartheta > 0$, angular momentum is transported from the bottom to the surface of the convection zone, resulting in a decrease of the rotational velocity with depth.

The presence of the vector $\mathbf{n}$ in (3) indicates that the existence of a special direction is necessary for the Λ effect to appear. This direction can be provided by either the nonuniformity of the medium or the anisotropy of the turbulence.

The contribution of nonuniformity was analyzed in detail in [8]. The following expressions were obtained for the quantities U and H in (4):

$$U = \left(\frac{\ell}{H_\rho}\right)^2 J_0\left(\Omega^*\right), \quad H = \left(\frac{\ell}{H_\rho}\right)^2 J_1\left(\Omega^*\right), \qquad (5)$$

where ℓ is the correlation length of the turbulent motions and $H_\rho = -\rho/(d\rho/dr)$ is the density scale height. The correlation length is commonly assumed to be proportional to the pressure scale height: $\ell =$

$\alpha_{\rm MLT}H_{\rm p}$. Since $H_\rho = \gamma H_{\rm p}$ in a convection zone with almost adiabatic nonuniformity (where γ is the adiabatic index), it can easily be shown that $\ell/H_\rho = \alpha_{\rm MLT}/\gamma$ in (5). The dependence on the Coriolis number (1) in (5) is given by the functions

$$J_0(\Omega^*) = \frac{1}{2\Omega^{*4}}\left(9 - \frac{2\Omega^{*2}}{1+\Omega^{*2}} - \frac{\Omega^{*2}+9}{\Omega^*}\arctan\Omega^*\right), \tag{6}$$

$$J_1(\Omega^*) = \frac{1}{2\Omega^{*4}}\left(45 + \Omega^{*2} - \frac{4\Omega^{*2}}{1+\Omega^{*2}} + \frac{\Omega^{*4} - 12\Omega^{*2} - 45}{\Omega^*}\arctan\Omega^*\right).$$

If the anisotropy of the turbulence is taken into account, we obtain a contribution to the Λ effect (4) that is additive in the nonuniformity. This can be written in the form [6]

$$U = a\left(\frac{\ell}{H_\rho}\right)^2 I_0(\Omega^*), \quad H = a\left(\frac{\ell}{H_\rho}\right)^2 I_1(\Omega^*). \tag{7}$$

The ratio ℓ/H_ρ was introduced here to simplify the comparison with the contribution from nonuniformity. The dimensionless anisotropy parameter a is not completely free and must satisfy the inequality

$$1 - \frac{\gamma}{\alpha_{\rm MLT}} \le a \le 2\left(\frac{\gamma}{\alpha_{\rm MLT}} + 1\right), \tag{8}$$

which follows from the condition that the spectral functions [21] for the vertical and horizontal components of the fluctuational velocities be positive. In the case $\alpha_{\rm MLT} = \gamma$ (for which all subsequent computations will be done), it follows from (8) that $0 \le a \le 4$. The functions of the Coriolis number in (7) have the form

$$I_0(\Omega^*) = -\frac{3}{4\Omega^{*4}}\left(1 + \frac{2}{1+\Omega^{*2}} + \frac{\Omega^{*2}-3}{\Omega^*}\arctan\Omega^*\right), \tag{9}$$

$$I_1(\Omega^*) = \frac{3}{4\Omega^{*4}}\left(-15 + \frac{2\Omega^{*2}}{1+\Omega^{*2}} + \frac{3\Omega^{*2}+15}{\Omega^*}\arctan\Omega^*\right).$$

Figure 1 compares the contributions from the nonuniformity and anisotropy. At large Coriolis numbers, the contribution of the nonuniformity (namely, the corresponding angular-momentum flux H (7) along the axis of rotation) is dominant. Precisely large Coriolis numbers are typical for the large-scale convection in the Sun and most cool stars. As a result, differential-rotation models based on the Λ effect due to nonuniformity are satisfactory. On the other hand, there is small-scale convection near the solar surface, where the Coriolis numbers are not so large. Consequently, anisotropy must be taken into account to explain the surface features of differential rotation.

3. THE MODEL

3.1. Differential Rotation in the Convection Zone

We shall consider global flows in the convective envelope of a star, whose spatial scales are considerably greater than the correlation length for turbulent motions. These flows will be described by the gasdynamical equations for the mean fields, which can be derived by averaging over the ensemble of turbulent fluctuations. Let us assume that the average characteristics of the star are time independent and axially symmetric with respect to the axis of rotation. Such a mean axially-symmetric state can be modeled by the joint solution of the three basic equations for the angular velocity, meridional circulation, and specific entropy.

The velocity $\mathbf{V}$ of the large-scale, axially-symmetric flow can be written as

$$\mathbf{V} = \left(\frac{1}{\rho r^2\sin\vartheta}\frac{\partial\Psi}{\partial\vartheta}, \frac{-1}{\rho r\sin\vartheta}\frac{\partial\Psi}{\partial r}, r\sin\vartheta\Omega\right), \tag{10}$$

where Ψ is the flow function. The flow (10) satisfies the Reynolds equation

$$\rho(\mathbf{V}\cdot\nabla)\mathbf{V} = \nabla\cdot R - \nabla P + \rho\mathbf{g}, \tag{11}$$

where R is the Reynolds stress tensor (3) and $\mathbf{g}$ is the free-fall acceleration.

The model equations are cumbersome, and we will not write them in explicit form but will describe the "recipe" used to derive them fairly completely. In addition, the physical meaning of the model will be discussed in detail. This will enable us to clarify the reasons for previous discrepancies with observations, as well as to show the means for their removal.

The azimuthal component (11) leads to the equation of continuity for the angular-momentum fluxes, which determines the angular-velocity distribution in the convection envelope:

$$\frac{1}{r^2}\frac{\partial(r^3R_{r\phi})}{\partial r} + \frac{1}{\sin^2\vartheta}\frac{\partial(\sin^2\vartheta R_{\vartheta\phi})}{\partial\vartheta} + \frac{1}{\sin^2\vartheta}\frac{\partial(\sin^2\vartheta\Omega)}{\partial\vartheta}\frac{\partial\Psi}{\partial r} - \frac{1}{r^2}\frac{\partial(r^2\Omega)}{\partial r}\frac{\partial\Psi}{\partial\vartheta} = 0. \tag{12}$$

We can seen that, along with the Reynolds stresses, meridional circulation can also transport angular momentum and, therefore, produce nonuniformity of the rotation. The most convenient form of the equation

for the meridional flow follows from the azimuthal component of the curl of (11):

$$\mathcal{D}(\Psi) = \sin\vartheta r\frac{\partial\Omega^2}{\partial z} - \frac{g}{c_{\rm p}r}\frac{\partial S}{\partial\vartheta}, \qquad (13)$$

where $\partial/\partial z = \cos\vartheta\partial/\partial r - r^{-1}\sin\vartheta\partial/\partial\vartheta$ is the spatial derivative along the axis of rotation and $S = c_v ln\,(P/\rho^\gamma)$ is the specific entropy of a perfect gas ($c_{\rm p}$ and c_v are the specific heat capacities at constant pressure and density, respectively). The left-hand side of this equation describes the deceleration of the meridional circulation due to turbulent viscosity:

$$\mathcal{D}(\Psi) = -\varepsilon_{\phi mi}\frac{\partial}{\partial r_m}\left(\frac{1}{\rho}\frac{\partial}{\partial r_j}\rho\mathcal{N}_{ijkl}\frac{\partial V_k}{\partial r_l}\right). \qquad (14)$$

An expression for the effective viscosity tensor $\mathcal{N}$ derived from (3) and (14) taking into account its dependence on the rotational velocity can be found in [22] and will not be presented here.

The right-hand side of (13) contains two sources of meridional flows. The first is the nonpotential part of the centrifugal force (with the potential component balanced by the pressure). When the angular velocity decreases with distance to the equator, a flow toward the pole forms at the surface and a flow toward the equator near the bottom of the convection zone. This "centrifugal circulation" is very sensitive to the local direction of the transport of angular momentum. For small Coriolis numbers, i.e., near the surface, the angular-momentum flux H (5) due to nonuniformity is directed toward the pole (Fig. 1). As a result, the meridional circulation in the model of [11] changes its direction near the surface. Our analysis takes into account the contribution of the anisotropy (7). As will be shown below, if the anisotropy parameter a is sufficiently large, the flux H remains positive at any depth and the meridional flow at the surface is directed toward the poles, in agreement with observations. The vertical fluxes U from (5) and (7) are insignificant. Therefore, for simplicity, we shall assume that $U = 0$. The second source of meridional flow is the latitude dependence of the specific entropy, which results in so-called baroclinic circulation. If the convective heat flux depends on the latitude (for example, increases with latitude), hotter material at high latitudes will flow upward toward the surface, while the relatively cool fluid near the equator will flow downward toward the bottom, resulting in a meridional stream toward the equator near the surface.

Comparing the three terms in (13) in order of magnitude, we can see that both terms on the right-hand side are much greater than the left-hand side. For example, the ratio of the centrifugal force to the viscous force is the Taylor number $Ta = 4\Omega^2R^4/\nu_T$, which is $Ta \sim 10^7$ in the Sun. Consequently, the two sources of meridional circulation almost compensate each other in most of the convection zone. It is obvious that deviations from rotation with constant angular velocity on cylindrical surfaces [23] are possible only if the thermodynamics of the situation is taken into account in an appropriate way [11, 24]. Another important fact is that the mutual compensation of the two terms on the right-hand side of (13) (the Taylor–Proudman balance) is inconsistent with the standard boundary conditions for zero-surface external forces. As a result, boundary layers of thickness $\ell \sim RTa^{-1/4}$ [13] are formed near the boundaries where the meridional circulation is concentrated.

The entropy distribution is determined by the heat-transfer equation

$$\mathrm{div}\left(\mathbf{F}^{\rm conv} + \mathbf{F}^{\rm rad}\right) + \rho T\mathbf{V}\cdot\boldsymbol{\nabla}S = 0. \qquad (15)$$

In the convection zone, we can use the Kramers formula for the opacity, $\kappa = c_\kappa\rho T^{-7/2}$ ($c_\kappa = 2.04\times10^{24}$ in cgs units), to determine the radiative heat flux:

$$\mathbf{F}^{\rm rad} = -\frac{16\sigma T^3}{3\kappa\rho}\boldsymbol{\nabla}T. \qquad (16)$$

The convective heat flux depends on the latitude because of the anisotropy of the effective thermal diffusivity χ due to rotation:

$$F_i^{\rm conv} = -\rho T\chi_{ij}\frac{\partial S}{\partial r_j}, \qquad (17)$$

$$\chi_{ij} = \chi_T\left(\phi(\Omega^*)\delta_{ij} + \phi_{||}(\Omega^*)\frac{\Omega_i\Omega_j}{\Omega^2}\right).$$

The functions ϕ and $\phi_{||}$ of the Coriolis number are designated here using the same notation as in [22], where they were written in explicit form. The quantities ν_T and χ_T are the viscosity and thermal diffusivity of the so-called initial turbulence, which is the turbulence that would occur for a nearly superadiabatic distribution without rotation. The corresponding transfer coefficients can be described by the relations for a nonrotating medium

$$\nu_T = -\frac{\tau\ell^2 g}{15c_{\rm p}}\frac{\partial S}{\partial r}, \quad \chi_T = 5\nu_T/4, \qquad (18)$$

which close the set of model equations.

To avoid considering a surface layer with a very high degree of nonuniformity, the outer boundary of the model region was located at $r_e = 0.95\ R_\odot$. The standard boundary conditions [11] were applied. The surface density of the external forces was taken to be zero ($R_{r\phi} = R_{r\vartheta} = 0$). We assumed that the meridional flow did not penetrate into the stably stratified radiative zone; i.e., the radial velocity was zero at the

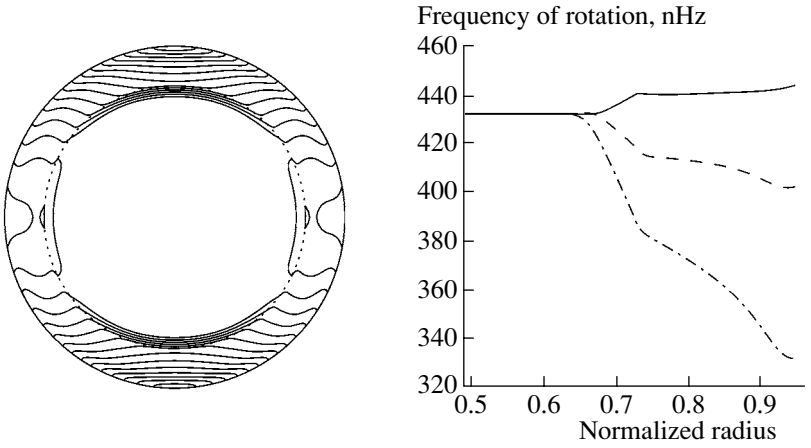

Fig. 2. Computed angular-velocity contours (left panel) and dependences of the angular velocity on depth (right panel) at the equator (solid), latitude 45° (dashed), and the poles (dot–dashed) in the absence of anisotropy ($a = 0$). The dotted curve in the left panel shows the base of the convection zone.

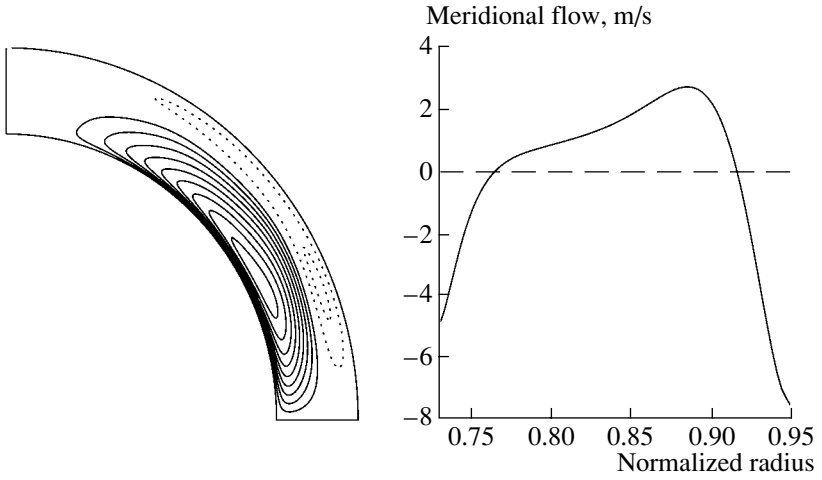

Fig. 3. Stream lines of the meridional flow (left panel) and dependence of the meridional velocity on the normalized radius at latitude 45° in the absence of anisotropy ($a = 0$). Negative velocities correspond to flows toward the equator. Solid and dotted stream lines show circulation in the counterclockwise and clockwise directions, respectively.

boundaries of the convection envelope. A constant heat flux $F_r = L_\odot/(4\pi r_i^2)$ flows into the convective zone through the lower boundary, while the outer boundary emits blackbody radiation.

The presence of the aforementioned boundary layers requires that the numerical methods used have high resolution. As a result, the commonly used relaxation method of [11, 25] with an explicit finite-difference (in time) numerical scheme is not convenient. We used the matrix sweep method in radius and expansion in Legendre polynomials in latitude to obtain the stationary solutions. This method is stable due to the presence of viscosity and heat conductivity. Because of the nonlinearity of the equations under consideration, an iterative procedure must be used.

3.2. Transition Layer

Solving for the differential rotation in the convective envelope gives us the boundary conditions at the surface of the radiative zone required to describe the transition to rigid-body rotation in deep layers of the Sun. The physical conditions in this region differ considerably from those in the convection zone, and its treatment represents a separate problem. The small thickness of the transition layer between the zones of differential and rigid-body rotation is probably associated with the (relict) poloidal field [20, 26].

The distributions of the angular velocity and toroidal field B satisfy the equations

$$\frac{\rho\nu}{\sin^3\vartheta}\frac{\partial}{\partial\vartheta}\sin^3\vartheta\frac{\partial\Omega}{\partial\vartheta} + \frac{1}{r^2}\frac{\partial}{\partial r}r^4\rho\nu\frac{\partial\Omega}{\partial r} \qquad (19)$$

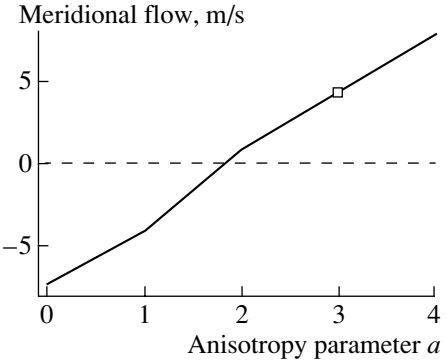

Fig. 4. Dependence of the amplitude of the meridional flow at the surface on the anisotropy parameter a (8). Positive velocities denote flows toward the poles. The point corresponding to Figs. 5 and 6 is marked.

$$= \frac{1}{4\pi r^2 \sin^3\vartheta}\left(r\frac{\partial A}{\partial r}\frac{\partial(\sin\vartheta B)}{\partial\vartheta} - \sin\vartheta\frac{\partial A}{\partial\vartheta}\frac{\partial(rB)}{\partial r}\right),$$

$$\eta\frac{\partial}{\partial\vartheta}\frac{1}{\sin\vartheta}\frac{\partial(\sin\vartheta B)}{\partial\vartheta} + r\frac{\partial}{\partial r}\eta\frac{\partial(rB)}{\partial r}$$

$$= r\left(\frac{\partial\Omega}{\partial\vartheta}\frac{\partial A}{\partial r} - \frac{\partial\Omega}{\partial r}\frac{\partial A}{\partial\vartheta}\right),$$

where ν and η are the microscopic ordinary and magnetic viscosities, respectively, and A is the potential of the poloidal field:

$$\mathbf{B} = \left(\frac{1}{r^2\sin\vartheta}\frac{\partial A}{\partial\vartheta}, \frac{-1}{r\sin\vartheta}\frac{\partial A}{\partial r}, B(r,\vartheta)\right). \qquad (20)$$

We will represent the dipolar poloidal field in the same way as in [26]:

$$A = B_0\frac{r^2}{2}\left(1 - \frac{r}{r_i}\right)^q \sin^2\vartheta, \qquad (21)$$

where B_0 is the amplitude of this field and q is a parameter determining the degre of concentration of the field toward the stellar center. In our computations, $B_0 = 0.1$ G and $q = 5$.

A joint consideration of the transition layer and differential rotation in the convection envelope enables us to determine the angular-velocity distribution in the entire volume of the Sun and compare the results obtained with helioseismological data in more detail.

4. RESULTS AND DISCUSSION

The characteristics of the global flows when the anisotropy of the turbulence is neglected are shown in Figs. 2 and 3. In general, these results are in agreement with helioseismological data on the rotation of inner layers of the Sun. There is a so-called equatorial acceleration in the entire volume of the convection zone: the angular velocity increases from the poles toward the equator. The amplitude of this acceleration decreases slightly with depth. A thin transition layer between the zones of differential and rigid-body rotation is localized beneath the convection zone. The rotation is almost uniform within most of the radiative zone.

However, there are substantial disagreements with the observational data near the outer surface. First of all, we see a change in the direction of the meridional circulation at small depths such that the flow at the surface is directed toward the equator. The observations show a flow toward the poles [18]. In addition, the calculated velocity of the rotation at low latitudes decreases with depth near the surface, whereas helioseismological data show the opposite tendency [17].

These disagreements are very likely associated with the anisotropy of the turbulence, which was not included. We can see in Fig. 1 that the contribution of the anisotropy to the development of nonuniform rotation is small for large Coriolis numbers. The Coriolis number is substantially greater than unity in most of the convection zone, so that anisotropy is not important. However, this situation changes near the surface. The Coriolis numbers for supergranules are $\Omega^* \simeq 0.5$, so that the anisotropy can be important. The problem is that solar convection has not been studied sufficiently well to be certain of its anisotropy. Thus, we must elucidate whether we can choose a value of the anisotropy parameter from the interval (8) that eliminates the inadequacies of the theoretical model.

The dependence of the amplitude of the computed meridional flow at the surface on the anisotropy parameter is shown in Fig. 4. The flow changes direction when a becomes sufficiently large, and the disagreement with the observed circulation disappears. As a increases, the thickness of the surface layer with clockwise circulation (Fig. 3) decreases, and this layer disappears completely near $a = 2$. The entire convection zone is encompassed by counterclockwise circulation when $a > 2$. In addition, as a increases, the deceleration of the rotation with depth near the surface is replaced by acceleration, and the latitude nonuniformity of the angular velocity decreases slightly. The best agreement with the available data is obtained when $a \simeq 3$.

The differential rotation and meridional circulation computed taking into account the anisotropy of the turbulence are shown in Figs. 5 and 6, which were obtained for $a = 3$. The characteristic radial velocities for the initial turbulence exceed the horizontal velocities only slightly for this value of the anisotropy parameter: $\langle u_r^2\rangle/\langle u_\vartheta^2\rangle = \langle u_r^2\rangle/\langle u_\phi^2\rangle = 12/11$.

Thus, it is not necessary to revise the theory of global solar circulation to obtain agreement with the

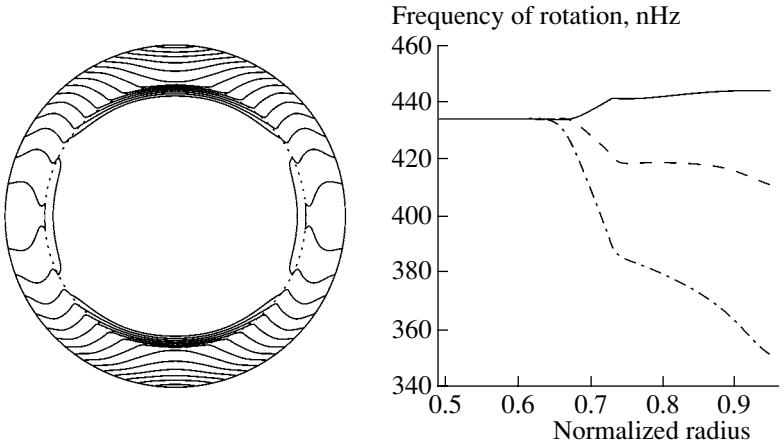

Fig. 5. Computed angular-velocity contours (left panel) and dependences of the angular velocity on depth for the equator (solid), latitude 45° (dashed), and the poles (dot–dashed) for the anisotropy parameter $a = 3$. The base of the convective zone is shown by the dotted curve in the left panel.

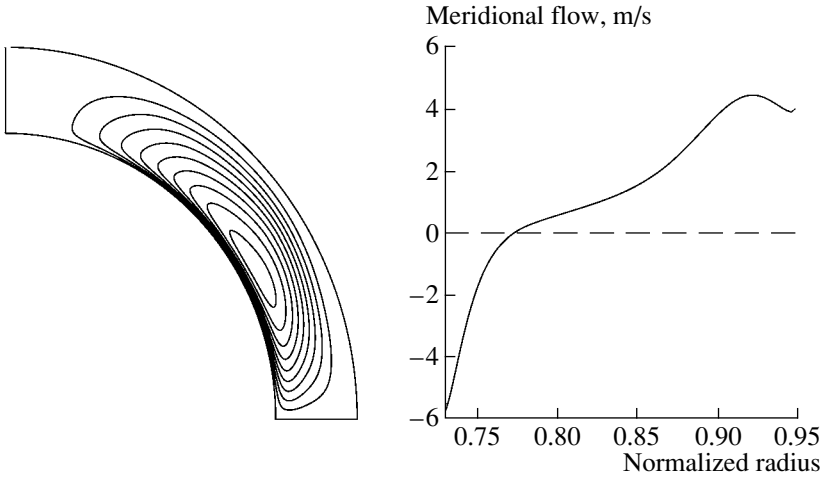

Fig. 6. Stream lines of the meridional flow (left panel) and dependence of the meridional velocity on the normalized radius at latitude 45° for the anisotropy parameter $a = 3$. Negative velocities correspond to flows directed toward the equator.

observations. It is sufficient to take into account the anisotropy of the convective turbulence together with the effects of nonuniformity.

Note that including the effects of anisotropy leaves theoretical predictions for the differential rotation of stars virtually unchanged [13]. In the same way as in the Sun, anisotropy can substantially affect meridional flows near the surface and fine features in the distribution of the angular velocity of giants and slowly rotating solar-type stars, but it is impossible to accurately estimate such peculiarities from observations of such stars. In principle, Doppler–Zeeman imaging [27] provides high resolution measurements for rapidly rotating stars; however, in this case, the Coriolis number (1) is large at all depths, so that anisotropy is negligible.

ACKNOWLEDGMENTS

This work was supported by the Russian Foundation for Basic Research (project nos. 02-02-16044 and 02-02-39027) and INTAS (project no. 2001-0550).

REFERENCES

1. A. I. Lebedinskiĭ, Astron. Zh. **18**, 10 (1941).
2. G. Rüdiger, *Differential Rotation and Stellar Convection* (Akademie, Berlin, 1989).
3. B. R. Durney and H. C. Spruit, Astrophys. J. **234**, 1067 (1979).
4. G. Rüdiger, Geophys. Astrophys. Fluid Dyn. **25**, 213 (1983).
5. L. L. Kitchatinov, Geophys. Astrophys. Fluid Dyn. **35**, 93 (1986).

6. L. L. Kitchatinov, Astron. Zh. **64**, 135 (1987) [Sov. Astron. **31**, 68 (1987)].
7. L. L. Kitchatinov, Geophys. Astrophys. Fluid Dyn. **38**, 273 (1987).
8. L. L. Kitchatinov and G. Rüdiger, Astron. Astrophys. **276**, 96 (1993).
9. L. L. Kichatinov, Pis'ma Astron. Zh. **12**, 410 (1986) [Sov. Astron. Lett. **12**, 172 (1986)].
10. B. R. Durney and J. Latour, Geophys. Astrophys. Fluid Dyn. **9**, 241 (1978).
11. L. L. Kitchatinov and G. Rüdiger, Astron. Astrophys. **299**, 446 (1995).
12. L. L. Kichatinov and G. Rüdiger, Pis'ma Astron. Zh. **23**, 838 (1997) [Astron. Lett. **23**, 731 (1997)].
13. L. L. Kitchatinov and G. Rüdiger, Astron. Astrophys. **344**, 911 (1999).
14. J. R. Barnes, A. C. Cameron, D. J. James, and J.-F. Donati, Mon. Not. R. Astron. Soc. **314**, 162 (2000).
15. J.-F. Donati, M. Mengel, B. D. Carter, *et al.*, Mon. Not. R. Astron. Soc. **316**, 699 (2000).
16. P. R. Wilson, D. Burtonclay, and Y. Li, Astrophys. J. **489**, 395 (1997).
17. J. Schou, H. M. Antia, S. Basu, *et al.*, Astrophys. J. **505**, 390 (1998).
18. R. W. Komm, R. F. Howard, and J. W. Harvey, Sol. Phys. **147**, 207 (1993).
19. L. L. Kichatinov and G. Rüdiger, Pis'ma Astron. Zh. **22**, 312 (1996) [Astron. Lett. **22**, 279 (1996)].
20. K. B. MacGregor and P. Charbonneau, Astrophys. J. **519**, 911 (1999).
21. A. Monin and A. M. Yaglom, *Statistical Hydromechanics* (Nauka, Moscow, 1967), Part 2 [in Russian].
22. L. L. Kitchatinov, V. V. Pipin, and G. Rüdiger, Astron. Nachr. **315**, 157 (1994).
23. P. A. Gilman and J. Miller, Astrophys. J., Suppl. Ser. **61**, 585 (1986).
24. B. R. Durney, Astrophys. J. **338**, 509 (1989).
25. G. Rüdiger, M. Küker, and K. L. Chan, Astron. Astrophys. **399**, 743 (2003).
26. G. Rüdiger and L. L. Kitchatinov, Astron. Nachr. **318**, 273 (1997).
27. J.-F. Donati and A. C. Cameron, Mon. Not. R. Astron. Soc. **291**, 1 (1997).

Translated by Yu. Dumin

Astronomy Reports, Vol. 48, No. 2, 2004, pp. 161–169. Translated from Astronomicheskiĭ Zhurnal, Vol. 81, No. 2, 2004, pp. 184–192.

Spectral–Correlational and Kinetic Models for the Motion of the Earth

Yu. G. Markov and I. N. Sinitsyn

Moscow State Aviation Institute, Moscow, Russia
Institute of Informatics Problems, Moscow, Russia

Received May 12, 2003; in final form, August 8, 2003

Abstract—We consider linear and nonlinear spectral–correlational and kinetic models for fluctuations in the motion of the Earth based on the Fokker–Planck–Kolmogorov and Pugachev equations. Particular attention is paid to Gaussian linear and nonlinear (statistically linearized) models. The results of analytical statistical modeling are presented. © *2004 MAIK "Nauka/Interperiodica".*

1. INTRODUCTION

Spectral methods for analyzing measurements of the motion of the Earth have been widely used in modern astronomy (see, for example, [1–5]). Linear and nonlinear, analytical, dynamical, stochastic models for the motion of the deformable Earth based on celestial mechanics have been developed in [6–8]. The general dynamical theory of one- and multi-dimensional distributions based on the equations of Fokker–Planck–Kolmogorov (for Gaussian perturbations) and Pugachev (for non-Gaussian perturbations) is set out in [9, 10].

The current paper continues the work of [7, 9, 10] and is dedicated to the construction of (i) spectral–correlational and (ii) one- and multi-dimensional kinetic models for the motion of the deformable Earth based both directly on the Fokker–Planck–Kolmogorov and Pugachev equations and on parametrized versions of these equations. The paper has seven sections. The Introduction presents a brief survey of works in this area and the formulation of the two problems considered. In Section 2, we derive the kinetic equations for the nonlinear theory of fluctuations of the motion of the Earth. Section 3 is concerned with parametrized, one- and multi-dimensional versions of the kinetic equations, concentrating on a normal (Gaussian) approximation for these equations. Section 4 contains linear and statistically linearized, spectral–correlational models for fluctuations of the Earth's motion. In Section 5, we present linear and statistically linearized kinetic models for the fluctuations. Section 6 is concerned with stochastic and analytical modeling of fluctuations of the Earth's motion and a discussion of the results obtained. We present our main conclusions in the final section.

2. KINETIC EQUATIONS FOR THE NONLINEAR THEORY OF FLUCTUATIONS OF THE MOTION OF THE EARTH

Let us first introduce the following notation and assumptions.

(1) We denote the state vector by $\mathbf{Y} = [Y_1 Y_2 Y_3]^T$, where $Y_1 = p_t$, $Y_2 = q_t$, $Y_3 = \delta r_t$, $\delta r_t = r_t - r_*$ (r_* is the axial-rotation velocity of the Earth), and p_t, q_t, and r_t are projections of the instantaneous angular-rotational velocity of the Earth on the associated axes [5, 11, 12].

(2) We will assume that, over a day, $T_* = 2\pi r_*^{-1}$, the axial and centrifugal moments of the inertia tensor $\mathcal{J} = \{J_{ij}\}$ $(i, j = p, q, r)$ of the deformable Earth $A = J_{pp}$, $B = J_{qq}$, $C = J_{rr}$, $J_{pq} = J_{qp}$, $J_{qr} = J_{rq}$, and $J_{rp} = J_{pr}$ can be written in the form

$$J_{ij} = J_{ij}^* + J'_{ij,1}\sin r_* t + J''_{ij,1}\cos r_* t + J'_{ij,2}\sin 2r_* t + J''_{ij,2}\cos 2r_* t,$$

with the harmonics 3, 4, ... being negligible. Here, a star denotes constant components of the moments of inertia and single or double primes denote the amplitudes of harmonics.

(3) We will call the following dimensionless differences of the axial moments of inertia averaged over a day, $T_* = 2\pi r_*^{-1}$, effective daily humps:

$$u_1 = \langle (C - B)A^{*-1}\cos\varphi\rangle,$$
$$u_2 = \langle (C - A)B^{*-1}\sin\varphi\rangle,$$
$$u_3 = \langle (B - A)C^{*-1}\sin 2\varphi\rangle,$$

where $\langle \ldots \rangle$ denotes averaging ($\varphi = r_* t$), with $u_1 \sim u_2$; $u_3 \ll u_{1,2}$.

(4) We will call the following dimensionless magnitudes of the centrifugal moments of inertia averaged

over a day, $T_* = 2\pi r_*^{-1}$, effective daily bulges:

$$u_4 = \langle J_{qr} A^{*-1} \rangle, \quad u_5 = \langle J_{qr} C^{*-1} \sin\varphi \rangle,$$
$$u_6 = \langle J_{qr} A^{*-1} \cos 2\varphi \rangle, \quad u_7 = \langle J_{qr} B^{*-1} \sin 2\varphi \rangle,$$
$$u_8 = \langle J_{pr} B^{*-1} \rangle, \quad u_9 = \langle J_{pr} C^{*-1} \cos\varphi \rangle,$$
$$u_{10} = \langle J_{pr} B^{*-1} \cos 2\varphi \rangle, \quad u_{11} = \langle J_{pr} A^{*-1} \sin 2\varphi \rangle,$$
$$u_{12} = \langle J_{pq} C^{*-1} \rangle, \quad u_{13} = \langle J_{pq} A^{*-1} \sin\varphi \rangle,$$
$$u_{14} = \langle J_{pq} B^{*-1} \cos\varphi \rangle, \quad u_{15} = \langle J_{pq} C^{*-1} \cos 2\varphi \rangle,$$

with $u_{4\ldots7} \sim u_3$, $u_{8\ldots11} \ll u_{4\ldots7}$, and $u_{12\ldots15} \ll u_{8\ldots11}$.

(5) We will include only the moments of the gravitational force of the Sun relative to the associated axes [5, 11, 12]. The amplitude of the gravitational moment of the Moon exceeds that of the Sun by a factor of two to three; however, due to the substantial difference between the eigen and forcing frequencies, the Moon's influence leads to monthly oscillations with amplitudes that are a factor of 15 to 20 lower than the amplitude of yearly oscillations. Essentially no oscillations of the pole with a monthly period are detected [13].

(6) We will take into consideration the external, linear, fluctuational–dissipative moments of forces $M_1^{\text{fd}} = V_{1t} - D_1 p_t$, $M_2^{\text{fd}} = V_{2t} - D_2 q_t$, and $M_3^{\text{fd}} = V_{3t} - D_3 \delta r_t$, where V_{1t}, V_{2t}, and V_{3t} are the specific external fluctuational moments of the forces, which are uncorrelated Gaussian (normal) white noise with the intensities $\nu_i = \nu_i(t)$ $(i = 1, 2, 3)$, and $D_{1,2,3}$ are the specific coefficients of the moments of the dissipative forces.

Adopting assumptions (1)–(6), the equations of motion of the Earth acquire the form [5, 9, 10]

$$\dot{p}_t + N_* q_t = \mathcal{P}_1 + V_{1t}, \quad p_{t_0} = p_0, \tag{1}$$
$$\dot{q}_t - N_* p_t = \mathcal{Q}_1 + V_{2t}, \quad q_{t_0} = q_0, \tag{2}$$
$$\delta\dot{r}_t = \mathcal{R}_1 + V_{3t}, \quad \delta r_{t_0} = r_0 - r_*, \tag{3}$$

where

$$\mathcal{P}_1 = \mathcal{P}_1(t, p_t, q_t, \delta r_t, \mathbf{u}) = 3u_1 b\omega_*^2 \cos\omega_* t - \frac{3}{2}u_4\omega_*^2(1 - 3b_1^2\cos^2\omega_* t) - \frac{3}{2}u_6\omega_*^2(1 - b_1^2\cos^2\omega_* t) - \frac{3}{2}u_{11}\omega_*^2(1 - b_1^2\cos^2\omega_* t) + \frac{3}{2}u_{13}\omega_*^2 b\cos\omega_* t - u_4(r_* + \delta r_t)^2 - D_1 p_t, \tag{4}$$

$$\mathcal{Q}_1 = \mathcal{Q}_1(t, p_t, q_t, \delta r_t, \mathbf{u}) = -3u_2 b\omega_*^2\cos\omega_* t + \frac{3}{2}u_7\omega_*^2(1 - b_1^2\cos^2\omega_* t) + \frac{3}{2}u_8\omega_*^2(1 - 3b_1^2\cos^2\omega_* t) - \frac{3}{2}u_{10}\omega_*^2(1 - b_1^2\cos^2\omega_* t) - 3u_{14}b\omega_*^2\cos\omega_* t + u_8(r_* + \delta r_t)^2 - D_2 q_t, \tag{5}$$

$$\mathcal{R}_1 = \mathcal{R}_1(t, p_t, q_t, \delta r_t, \mathbf{u}) = \frac{3}{2}u_3\omega_*^2(1 - b_1^2\cos^2\omega_* t) - \frac{3}{2}u_5 b\omega_*^2\cos\omega_* t + 3u_9 b\omega_*^2\cos\omega_* t + 3u_{15}\omega_*^2(1 - b_1^2\cos^2\omega_* t) - D_3\delta r_t. \tag{6}$$

In (1)–(6), $N_* = (C^* - B^*)A^{*-1}\omega_*$ is the Chandler frequency; the parameters $u_{1\ldots3}$ and $u_{4\ldots15}$ are determined by assumptions 3 and 4 above; ω_* ($r_* = 365\omega_*$) corresponds to the yearly period; b and b_1 ($0,4 \le b \le (4/3)\pi^{-1}$) with $b_1 \approx b$ are known parameters [12, 13]; and the functions $\mathcal{P}_1$, $\mathcal{Q}_1$, and $\mathcal{R}_1$ are written with accuracy to squared terms and derivatives with respect to $\mathbf{u} = [u_1, \ldots, u_{15}]^T$, p_t, q_t, δr_t, and the daily averaged rates of the variations in the axial and centrifugal moments of inertia.

Equations (1)–(3) can be compactly written in the vector form

$$\dot{\mathbf{Y}} = a(Y, t) + \mathbf{V}, \quad Y(t_0) = Y_0, \tag{7}$$

where

$$Y = [p_t q_t \delta r_t]^T, \quad Y_0 = [p_0 q_0 \delta r_0]^T, \quad \mathbf{V} = [V_{1t} V_{2t} V_{3t}]^T,$$

$$a = a(Y, t) = [a_1 a_2 a_3]^T, \tag{8}$$
$$a_1 = -D_1 p_t - N_* q_t + \mathcal{P}_{10} + \mathcal{P}_{11}\cos\omega_* t + \mathcal{P}_{12}\cos 2\omega_* t - u_4[(r_* + \delta r_t)^2 - r_*^2],$$
$$a_2 = -D_2 q_t + N_* p_t + \mathcal{Q}_{10} + \mathcal{Q}_{11}\cos\omega_* t + \mathcal{Q}_{12}\cos 2\omega_* t + u_8[(r_* + \delta r_t)^2 - r_*^2],$$
$$a_3 = -D_3\delta r_t + \mathcal{R}_{10} + \mathcal{R}_{11}\cos\omega_* t + \mathcal{R}_{12}\cos 2\omega_* t;$$

$$\mathcal{P}_{10} = -\frac{3}{2}u_4\omega_*^2\left(1 - \frac{3}{2}b_1^2\right) - \frac{3}{2}u_6\omega_*^2\left(1 - \frac{b_1}{2}\right) - \frac{3}{2}u_{11}\omega_*^2\left(1 - \frac{b_1^2}{2}\right) - u_4 r_*^2, \tag{9}$$
$$\mathcal{Q}_{10} = \frac{3}{2}u_7\omega_*^2\left(1 - \frac{b_1}{2}\right) + \frac{3}{2}u_8\omega_*^2\left(1 - \frac{3b_1^2}{2}\right) - \frac{3}{2}u_{10}\omega_*^2\left(1 - \frac{b_1^2}{2}\right) + u_8 r_*^2,$$
$$\mathcal{R}_{10} = \frac{3}{2}u_3\omega_*^2\left(1 - \frac{b_1^2}{2}\right) + 3u_{15}\omega_*^2\left(1 - \frac{b_1^2}{2}\right),$$

$$\mathcal{P}_{11} = 3u_1 b\omega_*^2 + \frac{3}{2}u_{13}b\omega_*^2, \tag{10}$$
$$\mathcal{Q}_{11} = -3u_2 b\omega_*^2 - 3u_{14}b\omega_*^2,$$
$$\mathcal{R}_{11} = -\frac{3}{2}u_5 b\omega_*^2 + 3u_9 b\omega_*^2,$$

$$\mathcal{P}_{12} = \frac{9}{4}u_4 b_1^2\omega_*^2 + \frac{3}{4}u_6 b_1^2\omega_*^2 + \frac{3}{4}u_{11}b_1^2\omega_*^2, \tag{11}$$

$$\mathcal{Q}_{12} = -\frac{3}{4}u_7 b_1^2\omega_*^2 - \frac{9}{4}u_8 b_1^2\omega_*^2 + \frac{3}{4}u_{10} b_1^2\omega_*^2,$$
$$\mathcal{R}_{12} = -\frac{3}{4}u_3 b_1^2\omega_*^2 - \frac{3}{2}u_{15} b_1^2\omega_*^2.$$

Equations (7) are linear in p_t and q_t and quadratic in δr_t. Sources of perturbations include, first, additive, regular components with the coefficients $\mathcal{P}_{10}$, $\mathcal{Q}_{10}$, $\mathcal{R}_{10}$, $\mathcal{P}_{11}$, $\mathcal{Q}_{11}$, $\mathcal{R}_{11}$, $\mathcal{P}_{12}$, $\mathcal{Q}_{12}$, and $\mathcal{R}_{12}$ and, second, the additive irregular (fluctuational) components V_{1t}, V_{2t}, and V_{3t}. The parameters $\mathbf{u}$ appear linearly and, in contrast to [6, 18], are taken to be known and not random.

Let us turn to the derivation of kinetic equations for the nonlinear theory of the fluctuations applied to (7). We denote $f_1 = f_1(y;t)$ and $f_n = f_n(y_1,\ldots,y_n;t_1,\ldots,t_n)$ to be the one- and n-dimensional densities, $(n = 2,3,\ldots)$, and $g_1 = g_1(\lambda;t)$ and $g_n = g_n(\lambda_1,\ldots,\lambda_n;t_1,\ldots,t_n)$ to be the corresponding characteristic functions. As applied to the nonlinear, stochastic differential equation (7) for Gaussian density perturbations, f_1 and f_n are determined by partial-differential equations called the Fokker–Planck–Kolmogorov equations. These equations together with their initial conditions have the form [14, 15]

$$\frac{\partial f_1}{\partial t} = -\frac{\partial^T}{\partial y}(af_1) + \frac{1}{2}\mathrm{tr}\left[\frac{\partial}{\partial y}\frac{\partial^T}{\partial y}(\nu f_1)\right], \qquad (12)$$
$$f_1(y;t_0) = f_0(y);$$

$$\frac{\partial f}{\partial t} = -\frac{\partial}{\partial y}(af) + \frac{1}{2}\mathrm{tr}\left[\frac{\partial}{\partial y}\frac{\partial^T}{\partial y}(\nu f)\right], \qquad (13)$$
$$f(y;\tau|\eta;\tau) = \delta(y-\eta);$$

$$f_n(y_1,\ldots,y_n;t_1,\ldots,t_n) = f_1(y_1;t_1) \qquad (14)$$
$$\times f(y_2;t_2|y_1;t_1)\times\cdots\times f(y_n;t_n|y_{n-1};t_{n-1}),$$

$$f_n(y_1,\ldots,y_{n-1},y_n;t_1,\ldots,t_{n-1},t_{n-1})$$
$$= f_{n-1}(y_1,\ldots,y_{n-1};t_1,\ldots,t_{n-1})$$
$$\times\,\delta(y_n - y_{n-1}),$$
$$y_0 = [p_0 q_0 \delta r_0]^T, \quad y_n = [p_{t_n} q_{t_n} \delta r_{t_n}]^T$$
$$(n = 2,3,\ldots).$$

Here, $f = f(y;t|\eta;\tau)$ is called the transition density.

Due to the polynomial character of the nonlinear functions $a = a(Y,t)$, the Pugachev equations for the characteristic functions g_1 and g_n can be written as a system of partial-differential equations in operator form [14, 15]:

$$\frac{\partial g_1}{\partial t} = \left[i\lambda^T a\left(\frac{\partial}{\partial i\lambda}, t\right) - \frac{1}{2}\lambda^T\nu\lambda\right]g_1, \qquad (15)$$
$$g_1(\lambda;t_0) = g_0(\lambda) \quad (i^2 = -1);$$

$$\frac{\partial g_n}{\partial t_n} = \left[i\lambda_n^T a\left(\frac{\partial}{\partial i\lambda_n}, t_n\right) - \frac{1}{2}\lambda_n^T\nu\lambda_n\right]g_n, \qquad (16)$$
$$g_n(\lambda_1,\ldots,\lambda_n;t_1,\ldots,t_{n-1},t_{n-1}) = g_{n-1}$$
$$\times\,(\lambda_1,\ldots,\lambda_{n-2},\lambda_{n-1}+\lambda_n;t_1,\ldots,t_{n-1}),$$

where $\lambda_0 = [\lambda_{p_0}\lambda_{q_0}\lambda_{\delta r_0}]^T$ and $\lambda_n = [\lambda_{p_n}\lambda_{q_n}\lambda_{\delta r_n}]^T$. The notation $((\partial/\partial i\lambda), t)$ indicates that the variable y in the polynomial is to be replaced by the differentiation operator $\partial/\partial i\lambda$.

The kinetic equations (12) and (13) lie at the basis of the nonlinear theory for fluctuations of the Earth's motion. This is a system of related partial-differential equations with their corresponding initial conditions. Currently, direct methods for the numerical analysis of these equations can be realized only on supercomputers.

3. PARAMETRIZATION OF THE KINETIC EQUATIONS FOR FLUCTUATIONS OF THE EARTH'S MOTION

Via parametrization of the one- and n-dimensional distributions using the consistent orthogonal expansions of [14, 15], we can represent the one-dimensional $(n = 1)$ and multi-dimensional $(n > 1)$ models in the form

$$f_1(y;t) \approx w_1 y'(y)\left[1 + \sum_{l=3}^{n_*}\sum_{|\mu|=l} c_{\mu t}p_\mu(y)\right], \qquad (17)$$

$$f_n(y_1,\ldots,y_n;t_1,\ldots,t_n) \approx w_n y'(y_1,\ldots,y_n) \qquad (18)$$
$$\times\left[1 + \sum_{l=3}^{n_*}\sum_{|\mu_1|+\cdots+|\mu_n|=l} c_{\mu_1,\ldots,\mu_n}\right.$$
$$\left.\times\, p_{\mu_1,\ldots,\mu_n}(y_1,\ldots,y_n)\right].$$

Here, $w_n\mathrm{st} = w_n y'(y_1,\ldots,y_n)$ is the known standard consistent density series for $(n \geq 1)$ having the same first- and second-order moments as f_n, as a consequence of which the $w_n y'$ depend on the following parameters: the mathematical expectation m_t, covariation matrix K_t, and the covariation function $K(t',t'')$ of the vector $\mathbf{Y}$ for $t',t'' = t_1,\ldots,t_n$. $\{p_\mu(y), q_\mu(y)\}$ are the known system of orthogonal polynomials, and $\{p_{\mu_1,\ldots,\mu_n}(y_1,\ldots,y_n),\ q_{\mu_1,\ldots,\mu_n}(y_1,\ldots,y_n)\}$ are the known consistent series of orthogonal polynomials. We have for the parameters m_t, K_t, $c_{\mu t}$, $K(t',t'')$, and $c_{\mu_1\mu_2},\ldots\ldots,c_{\mu_1,\ldots,\mu_n}$ in (17) and (18) a system of ordinary differential equations, which, in general, are nonlinear in m_t, K_t, and the coefficients of the consistent orthogonal expansions.

In particular, in a Gaussian approximation (the normal approximation of [14, 15]), the two-dimensional, nonlinear, kinetic model is described by the equations

$$f_1 = f_1(y, m_t, K_t; t) = [(2\pi)^3 |K_t|]^{-1/2} \times \exp\{-(y - m_t)^T K_t^{-1}(y - m_t)\}, \quad (19)$$

$$g_1(\lambda; t) = \exp\left\{ i\lambda^T m_t - \frac{1}{2}\lambda^T K_t \lambda \right\};$$

$$\dot{m}_t = M_N a(Y, t), \qquad m_{t_0} = m_0, \quad (20)$$

$$\dot{K}_t = M_N[a(Y,t)(Y^T - m_t^T) + (Y - m_t)a(Y,t)^T] + \nu, \qquad K_{t_0} = K_0; \quad (21)$$

$$f_2 = f_2 \times (y_1, y_2, m_{t_1}, m_{t_2}, K_{t_1}, K_{t_2}, K(t_1, t_2); t_1, t_2) = [(2\pi)^2 |\bar{K}_2|]^{-1/2} \times \exp\left\{ -\frac{1}{2}(\bar{y}_2^T - \bar{m}_2^T)\bar{K}_2^{-1}(\bar{y}_2 - \bar{m}_2) \right\}, \quad (22)$$

$$g_{t_1,t_2}(\bar{\lambda}) = \exp\left\{ i\bar{\lambda}^T \bar{m}_2 - \frac{1}{2}\bar{\lambda}^T \bar{K}_2 \bar{\lambda} \right\};$$

$$\bar{y}_2 = [y_{t_1}^T y_{t_2}^T]^T, \quad \bar{m}_2 = [m_{t_1}^T m_{t_2}^T]^T, \quad \bar{\lambda} = [\lambda_1^T \lambda_2^T]^T,$$

$$\bar{K}_2 = \begin{bmatrix} K(t_1,t_1) & K(t_1,t_2) \\ K(t_2,t_1) & K(t_2,t_2) \end{bmatrix},$$

$$\frac{\partial K(t_1,t_2)}{\partial t_2} = M_N[(Y_{t_1} - m_{t_1})a(Y_{t_2}, t_2)^T], \quad K(t_1,t_1) = K(t_1), \quad (23)$$

where a subscript N by the sign of the mathematical expectation indicates that it is calculated for the equivalent normal (Gaussian) distribution (19) or (22) with the unknown parameters m_t, K_t, and $K(t_1, t_2)$. Knowing the one- and two-dimensional normal (Gaussian) distributions, the old distributions f_n and g_n $(n > 2)$ are calculated in the normal approximation.

We will construct spectral–correlational models for the motion of the Earth based on equations (19)–(23).

4. LINEAR AND LINEARIZED SPECTRAL–CORRELATIONAL MODELS FOR FLUCTUATIONS OF THE EARTH'S MOTION

If we statistically linearize the nonlinear functions $u_{4,8}[(r_* + \delta r_t)^2 - r_*^2]$, setting

$$r_t^2 \approx (m_t^{\delta r})^2 + D_t^{\delta r} + 2r_* m_t^{\delta r} + 2(r_* + m_t^{\delta r})\delta r_t^0,$$

Eqs. (7) take the following form for the mathematical expectations $m_t^{p,q,\delta r}$:

$$\dot{m}_t^p = -D_1 m_t^p - N_* m_t^q - u_4[(m_t^{\delta r})^2 + D_t^{\delta r} + 2r_* m_t^{\delta r}] + \mathcal{P}_{10} + \mathcal{P}_{11}\cos\omega_* t + \mathcal{P}_{12}\cos 2\omega_* t, \qquad m_{t_0}^p = m_0^p, \quad (24)$$

$$\dot{m}_t^q = -D_2 m_t^q + N_* m_t^p + u_8[(m_t^{\delta r})^2 + D_t^{\delta r} + 2r_* m_t^{\delta r}] + \mathcal{Q}_{10} + \mathcal{Q}_{11}\cos\omega_* t + \mathcal{Q}_{12}\cos 2\omega_* t, \qquad m_{t_0}^q = m_0^q,$$

$$\dot{m}_t^{\delta r} = -D_3 m_t^{\delta r} + \mathcal{R}_{10} + \mathcal{R}_{11}\cos\omega_* t + \mathcal{R}_{12}\cos 2\omega_* t, \qquad m_{t_0}^{\delta r} = m_0^{\delta r};$$

and for the centered components p_t^0, q_t^0, and δr_t^0,

$$\dot{p}_t^0 = -D_1 p_t^0 - N_* q_t^0 - 2u_4(r_* + m_t^{\delta r})\delta r_t^0 + V_{1t}, \quad p_{t_0}^0 = p_0^0 \quad (25)$$

$$\dot{q}_t^0 = -D_2 q_t^0 + N_* p_t^0 + 2u_8(r_* + m_t^{\delta r})\delta r_t^0 + V_{2t}, \quad q_{t_0}^0 = q_0^0$$

$$\delta\dot{r}_t^0 = -D_3 \delta r_t^0 + V_{3t}, \quad \delta r_{t_0}^0 = \delta r_0^0.$$

Equations (24) are nonlinear in $m_t^{p,q,\delta r}$, while Eqs. (25) are linear in p_t^0, q_t^0, and δr_t^0. Equations (24) and (25) form a joint system of stochastic differential equations determining the mathematical expectation of the processes $m_t^{p,q,\delta r}$ and the centered fluctuational components p_t^0, q_t^0, and δr_t^0. Using the numerical methods of statistical modeling [15], we obtain estimates of the mathematical expectations, the spectral–correlational characteristics, and the one- and multi-dimensional distributions p_t^0, q_t^0, and δr_t^0 (see Section 6).

Due to the linearity of Eqs. (25), we have the following equations for the covariation matrix K_t and the covariation-function matrix $K_{t_1 t_2}$ [14, 15]:

$$\dot{K}_t = a_1 K_t + K_t a_1^T + \nu, \quad K_{t_0} = K_0, \quad (26)$$

$$\frac{\partial K_{t_1 t_2}}{\partial t_2} = K_{t_1 t_2} a_1(t_2)^T, \quad K_{t_1 t_2} = K_{t_1} \quad \text{at} \quad t_1 < t_2 \quad (27)$$

with $t_2 < t_1$, $K_{t_1 t_2} = K_{t_2 t_1}^T$. Here, the matrix a_1 of coefficients of (25) is

$$a_1 = a_1(t, m_t^{\delta r}) = \begin{bmatrix} -D_1 & -N_* & -2u_4(r_* + m_t^{\delta r}) \\ N_* & -D_2 & 2u_8(r_* + m_t^{\delta r}) \\ 0 & 0 & -D_3 \end{bmatrix},$$

$$\nu = \nu(t) = \begin{bmatrix} \nu_1(t) & 0 & 0 \\ 0 & \nu_2(t) & 0 \\ 0 & 0 & \nu_3(t) \end{bmatrix}.$$

Using (26) and (27), we arrive at the following expressions for the dispersion $D_t^{p,q,\delta r}$ and the covariations $K_t^{pq,q\delta r,p\delta r}$:

$$\begin{aligned} \dot{D}_t^p &= -2\,(D_1 D_t^p + N_* K_t^{pq}) \\ &\quad + 2u_4(r_* + m_t^{\delta r})K_t^{pr} + \nu_1, \\ \dot{D}_t^q &= 2\,(-D_2 D_t^q + N_* K_t^{pq}) \\ &\quad + 2u_8(r_* + m_t^{\delta r})K_t^{qr} + \nu_2, \\ \dot{D}_t^{\delta r} &= -2D_3 D_t^{\delta r} + \nu_3, \end{aligned} \tag{28}$$

$$\begin{aligned} \dot{K}_t^{pq} &= -(D_1 + D_2)K_t^{pq} + N_*(D_t^p - D_t^q) \\ &\quad - 2u_4(r_* + m_t^{\delta r})K_t^{q\delta r} + 2u_8(r_* + m_t^{\delta r})K_t^{p\delta r}, \\ \dot{K}_t^{p\delta r} &= -(D_1 + D_3)K_t^{p\delta r} - N_* K_t^{q\delta r} \\ &\quad - 2u_4(r_* + m_t^{\delta r})D_t^{\delta r}, \\ \dot{K}_t^{q\delta r} &= N_* K_t^{p\delta r} - (D_2 + D_3)K_t^{q\delta r} \\ &\quad + 2u_8(r_* + m_t^{\delta r})D_t^{\delta r}, \end{aligned} \tag{29}$$

and with $t_1 < t_2$ for the covariation functions K_{t_1,t_2}^{ij} $(i, j = p, q, \delta r)$,

$$\begin{aligned} \frac{\partial K_{t_1t_2}^{pp}}{\partial t_2} &= -D_1 K_{t_1t_2}^{pp} - N_* K_{t_1t_2}^{pq} \\ &\quad - 2u_4(r_* + m_{t_2}^{\delta r})K_{t_1t_2}^{p\delta r}, \\ \frac{\partial K_{t_1t_2}^{pq}}{\partial t_2} &= -D_2 K_{t_1t_2}^{pq} + N_* K_{t_1t_2}^{pp} \\ &\quad + 2u_8(r_* + m_{t_2}^{\delta r})K_{t_1t_2}^{p\delta r}, \\ \frac{\partial K_{t_1t_2}^{p\delta r}}{\partial t_2} &= -D_3 K_{t_1t_2}^{p\delta r}, \quad \frac{\partial K_{t_1t_2}^{q\delta r}}{\partial t_2} = -D_3 K_{t_1t_2}^{q\delta r}, \\ \frac{\partial K_{t_1t_2}^{\delta r\delta r}}{\partial t_2} &= -D_3 K_{t_1t_2}^{\delta r\delta r}, \\ \frac{\partial K_{t_1t_2}^{qp}}{\partial t_2} &= -D_1 K_{t_1t_2}^{qp} - N_* K_{t_1t_2}^{qq} \\ &\quad - 2u_4(r_* + m_{t_2}^{\delta r})K_{t_1t_2}^{q\delta r}, \\ \frac{\partial K_{t_1t_2}^{qq}}{\partial t_2} &= -D_2 K_{t_1t_2}^{qq} + N_* K_{t_1t_2}^{qp} \\ &\quad + 2u_8(r_* + m_{t_2}^{\delta r})K_{t_1t_2}^{q\delta r}, \\ \frac{\partial K_{t_1t_2}^{\delta rp}}{\partial t_2} &= -D_1 K_{t_1t_2}^{\delta rp} - N_* K_{t_1t_2}^{\delta rq} \\ &\quad - 2u_4(r_* + m_{t_2}^{\delta r})K_{t_1t_2}^{\delta r\delta r}, \\ \frac{\partial K_{t_1t_2}^{\delta rq}}{\partial t_2} &= -D_2 K_{t_1t_2}^{\delta rq} + N_* K_{t_1t_2}^{\delta rp} \\ &\quad + 2u_8(r_* + m_{t_2}^{\delta r})K_{t_1t_2}^{\delta r\delta r}; \end{aligned} \tag{30}$$

for the initial conditions

$$K_{t_1t_2}^{ii} = D_{t_1}^i, \quad K_{t_1t_2}^{ij} = K_{t_1}^{ij} (i, j = p, q, \delta r).$$

For covariationally stationary processes involving p_t^0, q_t^0, and δr_t^0 (i.e., processes for which the covariation functions p_t^0, q_t^0, δr_t^0 depend only on the time difference $t_2 - t_1 = \tau$), we can use the following expressions for the covariation functions and the spectral and mutual-spectral densities:

$$k^{p,q,\delta r}(\tau) = K_{t,t+\tau}^{p,q,\delta r} = \int_{-\infty}^{\infty} s^{p,q,\delta r}(\omega) e^{i\omega\tau} d\omega; \tag{31}$$

$$s^{p,q,\delta r}(\omega) = \frac{1}{2\pi} \int_{-\infty}^{\infty} k^{p,q,\delta r}(\tau) e^{-i\omega\tau} d\tau. \tag{32}$$

In the linear theory of the fluctuations [8], the terms $u_{4,8}[(r_* + \delta r_t)^2 - r_*^2]$ are neglected in (7). Equation (7) then breaks up into two independent linear systems of stochastic equations for the motion of the Earth's pole $\bar{Y} = [p_t q_t]^T$ and δr_t. Equations (28)–(30) for the mathematical expections and covariation characteristics simplify when terms containing the coefficients u_4 and u_8 are neglected.

Linear correlational models for the fluctuations of the Earth's motion can be obtained in accordance with [14, 15] based on knowledge of the weighting functions and intensities of white noise. In particular, the following formulas are valid for the mathematical expectations, covariation functions, and spectral densities:

$$\bar{m}_t = \tilde{w}(t - t_0)\bar{m}_0 + \int_{t_0}^{t} \tilde{w}(t - \tau)\alpha_0(\tau) d\tau; \tag{33}$$

$$\begin{aligned} \bar{K}_{t_1t_2} &= \tilde{w}(t_1 - t_0)\bar{K}_0 \tilde{w}(t_2 - t_0)^* \\ &\quad + \int_{t_0}^{\min(t_1,t_2)} \tilde{w}(t_1 - \tau)\bar{\nu}(\tau)\tilde{w}(t_2 - \tau)^* d\tau; \end{aligned} \tag{34}$$

$$m^{\delta r} = \tilde{w}^{\delta r}(t - t_0)m_0^{\delta r} + \int_{t_0}^{t} \tilde{w}^{\delta r}(t - \tau)\alpha_0'(\tau) d\tau; \tag{35}$$

$$K_{t_1t_2}^{\delta r} = \tilde{w}^{\delta r}(t_1 - t_0)\tilde{w}^{\delta r}(t_2 - t_0)D_0^{\delta r} \tag{36}$$

$$+\int_{t_0}^{\min(t_1,t_2)}\tilde{w}^{\delta r}(t_1-\tau)\tilde{w}^{\delta r}(t_2-\tau)\nu_3 d\tau;$$

$$\bar{s}(\omega)=\begin{bmatrix}s^{pp}(\omega) & s^{pq}(\omega)\\ s^{qp}(\omega) & s^{qq}(\omega)\end{bmatrix}=\Phi(i\omega)\bar{\nu}\Phi(i\omega)^*, \quad (37)$$

$$s^{\delta r}(\omega)=|\Phi^{\delta r}(i\omega)|^2\nu_3. \quad (38)$$

Here, a star denotes complex conjugation, and

$$\bar{m}_t=\begin{bmatrix}m_t^p\\ m_t^q\end{bmatrix}, \quad \bar{m}_0=\begin{bmatrix}m_0^p\\ m_0^q\end{bmatrix}, \quad (39)$$

$$\bar{K}_0=\begin{bmatrix}D_0^p & K_0^{pq}\\ K_0^{pq} & D_0^q\end{bmatrix}, \quad \bar{\nu}=\begin{bmatrix}\nu_1 & 0\\ 0 & \nu_2\end{bmatrix},$$

$$\alpha_0=\begin{bmatrix}\mathcal{P}_{10}+\mathcal{P}_{11}\cos\omega_* t+\mathcal{P}_{12}\cos 2\omega_* t\\ \mathcal{Q}_{10}+\mathcal{Q}_{11}\cos\omega_* t+\mathcal{Q}_{12}\cos 2\omega_* t\end{bmatrix}, \quad (40)$$

$$\alpha_0'(t)=\mathcal{R}_{10}+\mathcal{R}_{11}\cos\omega_* t+\mathcal{R}_{12}\cos 2\omega_* t. \quad (41)$$

In addition, the quantities $\Phi(i\omega)$, $\tilde{w}(t-\tau)$, $w(t-\tau)$ and $\Phi^{\delta r}(i\omega)$, $\tilde{w}^{\delta r}(t-\tau)$, $w^{\delta r}(t-\tau)$ in (33)–(39) denote the transfer functions, weighting functions, and fundamental solutions corresponding to the linear equations (7). According to [14, 15], these are determined by the formulas

$$\Phi(i\omega)=-(\alpha-i\omega I_2)^{-1} \quad (42)$$

$$=-\frac{1}{\Delta(\omega)}\begin{bmatrix}-(D_2+i\omega) & -N_*\\ N_* & -(D_1+i\omega)\end{bmatrix},$$

$$\alpha=\begin{bmatrix}-D_1 & -N_*\\ N_* & D_2\end{bmatrix}, \quad I_2=\begin{bmatrix}1 & 0\\ 0 & 1\end{bmatrix};$$

$$\Phi^{\delta r}(i\omega)=(D_3+i\omega)^{-1}; \quad (43)$$

$$\Delta(\omega)=\omega_c^2-\omega^2+2\varepsilon i\omega,$$
$$\omega_c^2=N_*^2+D_1D_2\approx N_*^2, \quad 2\varepsilon=D_1+D_2;$$

$$w(t-\tau)=\begin{bmatrix}w^{pp}(t-\tau) & w^{pq}(t-\tau)\\ w^{pq}(t-\tau) & w^{qq}(t-\tau)\end{bmatrix}, \quad (44)$$
$$\tilde{w}(t-\tau)=w(t-\tau)\mathbf{1}(t-\tau),$$

$$w^{pp}(t-\tau)=e^{-1/2(D_1+D_2)(t-\tau)}$$
$$\times\left[\frac{D_2-D_1}{2N_*}\sin N_*(t-\tau)+\cos N_*(t-\tau)\right],$$

$$w^{qq}(t-\tau)=e^{-1/2(D_1+D_2)(t-\tau)}$$
$$\times\left[-\frac{D_2-D_1}{2N_*}\sin N_*(t-\tau)+\cos N_*(t-\tau)\right],$$

$$w^{pq}(t-\tau)=w^{qp}(t-\tau) \quad (45)$$
$$=-e^{-1/2(D_1+D_2)(t-\tau)}\sin N_*(t-\tau);$$

where the elements $w(t-\tau)$ have been written with accuracy to within squared terms and derivatives of the $D_{1,2}N_*^{-1}$, $\mathbf{1}(t-\tau)$ is a unit step function, and

$$w^{\delta r}(t-\tau)=e^{-D_3(t-\tau)}, \quad (46)$$
$$\tilde{w}^{\delta r}(t-\tau)=e^{-D_3(t-\tau)}\mathbf{1}(t-\tau).$$

With $D_{1,2}N_*^{-1}\ll 1$ and constant ν_1, ν_2, and ν_3, formulas (31), (32), (37), and (38) take the form

$$D^p=\frac{2D_1\nu_2-(D_2-D_1)\nu_1}{2D_1(D_1+D_2)}, \quad (47)$$

$$D^q=\frac{2D_2\nu_1+(D_2-D_1)\nu_2}{2D_1(D_1+D_2)}, \quad (48)$$

$$K^{pq}=\frac{\nu_1D_2-\nu_2D_1}{N_*(D_1+D_2)}, \quad (49)$$

$$D^{\delta r}=\frac{\nu_3}{2D_3}, \quad (50)$$

$$s^{pp}(\omega)=\Delta_1^{-2}(\omega)[\nu_1(D_2^2+\omega^2)+\nu_2N_*^2]; \quad (51)$$

$$s^{qq}(\omega)=\Delta_1^{-2}(\omega)[\nu_1N_*^2+\nu_2(D_1^2+\omega^2)]; \quad (52)$$

$$s^{pq}(\omega)=\Delta_1^{-2}(\omega)N_*[-\nu_1(D_2+i\omega) \quad (53)$$
$$+\nu_2(D_1-i\omega)]=\overline{s^{qp}(\omega)};$$

$$s^{\delta r}(\omega)=\Delta_2^{-2}(\omega)\nu_3, \quad \Delta_2^2(\omega)=D_3^2+\omega^2, \quad (54)$$

where

$$\Delta_1^2(\omega)=(N_*^2+D_1D_2-\omega^2)^2+\omega^2(D_1+D_2)^2$$
$$\approx(N_*^2-\omega^2)^2+\omega^2(D_1+D_2)^2.$$

Equations (24) and (28)–(32) lie at the basis of the algorithm for analytical modeling and analysis of the spectral–correlational characteristics of fluctuations of the Earth's motion (see Section 6).

5. LINEAR AND LINEARIZED KINETIC MODELS FOR THE FLUCTUATIONS

We now turn to more subtle probability characteristics: the one- and multi-dimensional distributions. Such characteristics are important for estimating the significance of outliers and level intersections.

Let us first consider the kinetic equations (12) in application to (7) in our approximate (linear) theory, neglecting terms containing $u_{4,8}$ in (7). Then,

Eq. (12) for the one-dimensional characteristic functions of the variables $[p_t q_t]^T$ and δr_t

$$g_1(\lambda_1, \lambda_2; t) = E \exp\{i\lambda_1 p_t + i\lambda_2 q_t\}, \quad (55)$$

$$g_1^{\delta r}(\lambda'; t) = E \exp\{i\lambda' \delta r_t\} \quad (56)$$

takes the form

$$\frac{\partial g_1}{\partial t} = \lambda^T \alpha \frac{\partial g_1}{\partial \lambda} + \left[i\lambda^T \alpha_0(t) - \frac{1}{2}\lambda^T \bar{\nu}(t)\lambda \right] g_1, \quad (57)$$

$$\frac{\partial g_1^{\delta r}}{\partial t} = -\lambda' D_3 \frac{\partial g_1^{\delta r}}{\partial \lambda'} + \left[i\lambda' \alpha_0'(t) - \frac{1}{2}\lambda'^T \nu_3(t) \right] g_1^{\delta r}, \quad (58)$$

where $\lambda = [\lambda_1 \lambda_2]^T$; $\alpha_0(t)$, $\alpha_0'(t)$, and α are defined in (40) and (41); and $b = I_2$.

We assume that the initial distributions in p_0, q_0, and δr_0 are Gaussian:

$$g_0(\lambda) = \exp\left\{ i\lambda^T \bar{m}_0 - \frac{1}{2}\lambda^T \bar{K}_0 \lambda \right\}, \quad (59)$$

$$g_0^{\delta r}(\lambda') = \exp\left\{ i\lambda' m_0^{\delta r} - \frac{1}{2}\lambda'^2 D_0^{\delta r} \right\}. \quad (60)$$

Then, using (57) and (58), in accordance with [14, 15], we have the following implicit formulas for the Gaussian one-dimensional characteristic functions:

$$g_1(\lambda; t) = \exp\left\{ i\lambda^T \left[w(t-t_0)\bar{m}_0 + \int_{t_0}^{t} w(t-\tau)\alpha_0(\tau)d\tau \right] - \frac{1}{2}\lambda^T \times \left[w(t-t_0)\bar{K}_0 w(t-t_0)^T + \int_{t_0}^{t} w(t-\tau)\bar{\nu}(\tau)w(t-\tau)^T d\tau \right] \lambda \right\}; \quad (61)$$

$$g_1^{\delta r}(\lambda'; t) = \exp\left\{ i\lambda' \left[m_0^{\delta r} e^{-D_3(t-t_0)} + \int_{t_0}^{t} e^{-D_3(t-\tau)} \alpha_0'(\tau)d\tau \right] - \frac{1}{2}\lambda'^2 \left[D_0^{\delta r} e^{-2D_3(t-t_0)} + \int_{t_0}^{t} e^{-2D_3(t-\tau)} \nu_3(\tau)d\tau \right] \right\}. \quad (62)$$

The two-dimensional characteristic functions

$$g_{t_1 t_2}(\bar{\lambda}_1, \bar{\lambda}_2) = E \exp\left\{ i\bar{\lambda}_1^T [p_{t_1} q_{t_1}]^T + i\bar{\lambda}_2^T [p_{t_2} q_{t_2}]^T \right\}, \quad (63)$$

$$\bar{\lambda}_1 = [\lambda_{11}\lambda_{12}]^T, \quad \bar{\lambda}_2 = [\lambda_{21}\lambda_{22}]^T,$$

$$g_{t_1 t_2}^{\delta r}(\lambda_1', \lambda_2') = E \exp\{ i\lambda_1' \delta r_{t_1} + i\lambda_2' \delta r_{t_2} \} \quad (64)$$

satisfy equations of the form (57) and (58). According to [14, 15], we have the following implicit formulas for Gaussian initial distributions and $t_1 < t_2$:

$$g_{t_1 t_2}(\bar{\lambda}_1, \bar{\lambda}_2) = \exp\left\{ i \sum_{l=1}^{2} \bar{\lambda}_l^T \times \left[w(t_l - t_0)\bar{m}_0 + \int_{t_0}^{t_l} w(t_l - \tau)\alpha_0 d\tau \right] - \frac{1}{2} \sum_{l,h=1}^{2} \bar{\lambda}_l^T \left[w(t_l - t_0)\bar{K}_0 w(t_h - t_0)^T + \int_{t_0}^{\min(t_l, t_h)} w(t_l - \tau)\bar{\nu}(\tau)w(t_h - \tau)^T d\tau \right] \lambda_h \right\}; \quad (65)$$

$$g_{t_1 t_2}^{\delta r}(\lambda_1', \lambda_2') = \exp\left\{ i \sum_{l=1}^{2} \lambda_l'^T \times \left[m_0^{\delta r} e^{-D_3(t_l - t_0)} + \int_{t_0}^{t_l} e^{-D_3(t_l - \tau)} \alpha_0(\tau)d\tau \right] - \frac{1}{2} \sum_{l,h=1}^{2} \lambda_l' \left[D_0^r e^{-D_3(t_l + t_h - 2t_0)} + \int_{t_0}^{\min(t_l, t_h)} \nu_3(\tau) e^{-D_3(t_l + t_h - 2\tau)} d\tau \right] \lambda_h' \right\}. \quad (66)$$

Expressions for the multi-dimensional characteristic functions for $n > 2$ can be written analogously.

The partial-differential equations (57) and (58) lie at the basis of the differential, linear, one-dimensional, kinetic models with Gaussian white noise. Equations (60), (61), (65), and (66) underlie the finite, linear, one- and two-dimensional Gaussian kinetic models for the case of Gaussian white noise and Gaussian initial distributions of p_{t_0}, q_{t_0}, and δr_{t_0}.

We now turn to the nonlinear theory. Linearized kinetic models for nonlinear fluctuations can be obtained by statistically linearizing the nonlinear functions in (7) and applying the methods of the theory of linear stochastic systems [14, 15]. This leads to expressions (24) and (28)–(30) for the mathematical expectations and correlational characteristics appearing in (19) and (22).

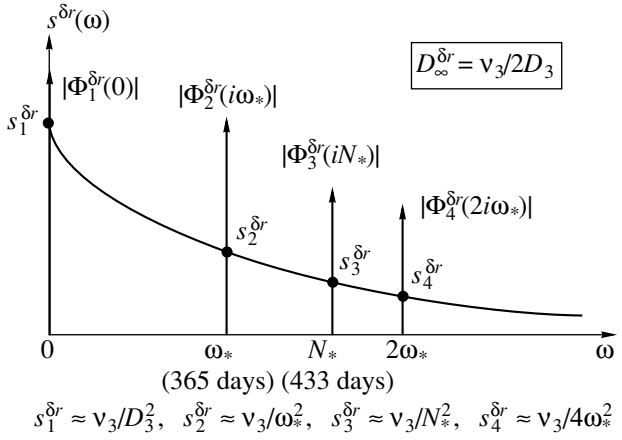

Fig. 1.

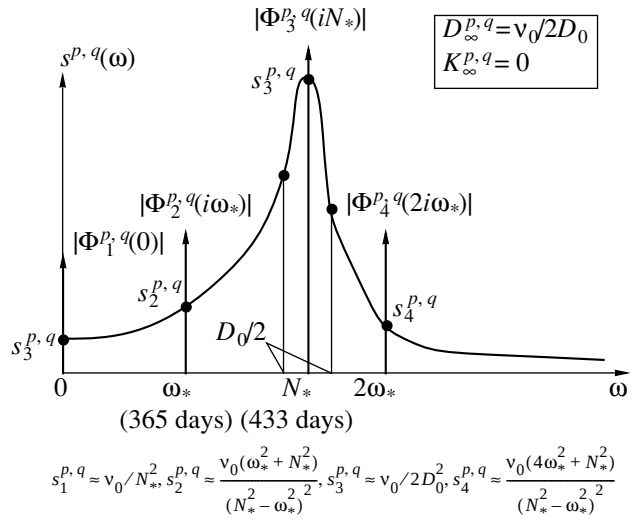

Fig. 2.

Thus, we use the linearized, Gaussian, stochastic differential equations (24) and (25) for the statistical modeling. For analytical modeling in the nonstationary case, we use the deterministic equations (24) and (28)–(30), also applying formulas (31) and (32) in the stationary case (see Section 6).

6. ANALYSIS, MODELING, AND DISCUSSION OF RESULTS

Dynamical spectral–correlational and kinetic models for fluctuations of the Earth's motion (Sections 2–5) provide basic information about the fundamental problem of the statistical dynamics of the Earth's rotation [16].

Figures 1 and 2 show the stationary amplitudes of the mathematical expectations $|\Phi^{p,q,\delta r}(i\omega)|$ at frequencies ω_*, N_*, and $2\omega_*$, together with the spectral densities $s^{p,q,\delta r}(\omega)$ and dispersions and covariations $D_\infty^{p,q,\delta r}$ obtained for the linear theory [formulas (33)–(53)] with white-noise intensities $\nu_1 = \nu_2 = \nu_0$, $\nu_3 > \nu_0$ and specific coefficients for the moments of the dissipative forces $D_1 = D_2 = D_0$, $D_3 > D_0$. The covariation functions have the form

$$k^{p,q}(\tau) = D_\infty^{p,q} e^{-D_0|\tau|} \cos N_*\tau, \qquad (67)$$

$$k^{\delta r}(\tau) = D_\infty^{\delta r} e^{-D_3|\tau|}. \qquad (68)$$

According to [4, 5], various estimates of the relaxation time D_0^{-1} yield values between 10 and 100 years. The level of the mean square deviations $\sqrt{D_\infty^{p,q}}$ will be $(2–4) \times 10^{-2''}$.

Taking into account nonlinear terms with the coefficients $u_{4,8} \sim 10^{-8}$ at the frequency N_* via the analytical modeling yields corrections of 2% (in the mathematical expectation), 6% (in the second moments), and 10% (in the spectral density). These estimates were obtained via statistical modeling.

In addition to analyses of the accuracy of the theory, (33)–(53) can be applied to measurements to identify both the basis parameters of the input model (1)–(3) (N_*, $D_{1,2,3}$) and the parameters $\mathbf{u}$, which are important for estimating trends.

The results of our statistical analyses indicate that spectral–correlational models based on the linear theory can provide sufficient accuracy on time intervals of three to five years. The kinetic models in the Gaussian approximation are fully based on the spectral–correlational characteristics.

7. CONCLUSIONS

Dynamical, Gaussian, linear and nonlinear, spectral–correlational models for fluctuations in the motion of the Earth can be applied to identify basis dynamical parameters using real measurements and analyze their accuracy [1–5]. The models not only preserve the qualitative properties of the fluctuations of the Earth's motion but also describe them with sufficient accuracy on intervals of three to five years.

The Gaussian, spectral–correlational and two-dimensional, kinetic models lie at the basis of standard methods for reducing measurements collected for studies of the statistical dynamics of the Earth's rotation.

Kinetic models for second-order fluctuations of the Earth's motion enable the refinement of spectral characteristics and the characteristics of level intersections and trends. High-order kinetic models are required to study higher-order extrema. In addition, the kinetic characteristics can be used to estimate the errors in the spectral-analysis methods applied in [1–3]. Such models form the basis of nonstandard

methods for reducing measurements in studies of statistical dynamics of the Earth's rotation.

Software developed at the Institute of Informatics Problems of the Russian Academy of Sciences in 2000–2003 enables the realization on a PC of analytical, statistical, and combined modeling of regular and fluctuational motions of the Earth in both stationary and nonstationary regimes.

ACKNOWLEDGMENTS

The authors thanks V.I. Sinitsyn, Yu.V. Chumin, V.V. Belousov, and È.R. Korepanov for their considerable work in creating the programs used for this analysis. This work was supported by the Russian Foundation for Basic Research (project nos. 01-02-17250 and 01-01-00758).

REFERENCES

1. L. V. Rykhlova, G. S. Kurbasova, and T. A. Taidakova, Astron. Zh. **67**, 151 (1990) [Sov. Astron. **34**, 79 (1990)].
2. L. V. Rykhlova, G. S. Kurbasova, and M. N. Rybalova, Nauchn. Inform. Inst. Astron. Akad. Nauk SSSR **69**, 3 (1991).
3. L. V. Rykhlova and G. S. Kurbasova, Astron. Zh. **75**, 632 (1998) [Astron. Rep. **42**, 558 (1998)].
4. M. Arato, *Linear Stochastic Systems with Constant Coefficients* (Springer, Berlin, 1982; Nauka, Moscow, 1989).
5. N. S. Sidorenkov, *Physics of Earth Rotation Instabilities*(Nauka, Moscow, 2002), p. 384 [in Russian].
6. Yu. G. Markov and I. N. Sinitsyn, Dokl. Akad. Nauk **385**, 189 (2002) [Dokl. Phys. **47**, 531 (2002)].
7. Yu. G. Markov and I. N. Sinitsyn, Dokl. Akad. Nauk **387**, 482 (2002) [Dokl. Phys. **47**, 867 (2002)].
8. Yu. G. Markov and I. N. Sinitsyn, Astron. Zh. **80**, 186 (2003) [Astron. Rep. **47**, 161 (2003)].
9. Yu. G. Markov and I. N. Sinitsyn, Dokl. Akad. Nauk **390**, 343 (2003).
10. Yu. G. Markov and I. N. Sinitsyn, Dokl. Akad. Nauk **391**, 194 (2003).
11. W. Munk and G. MacDonald, *The Rotation of the Earth* (Cambridge, 1960; Mir, Moscow, 1964), p. 384.
12. L. D. Akunenko, S. A. Kumakshev, and Yu. G. Markov, Dokl. Akad. Nauk **382**, 199 (2002) [Dokl. Phys. **47**, 78 (2002)].
13. L. D. Akunenko, S. A. Kumakshev, Yu. G. Markov, and L. V. Rykhlova, Astron. Zh. **79**, 952 (2002) [Astron. Rep. **46**, 858 (2002)].
14. V. S. Pugachev and I. N. Sinitsyn, *Stochastic Differential Systems. Analysis and Filtration*, 2nd ed. (Nauka, Moscow, 1990), p. 632 [in Russian].
15. V. S. Pugachev and I. N. Sinitsyn, *Theory of Stochastic Systems* (Logos, Moscow, 2000) [in Russian].
16. I. N. Sinitsyn, Yu. G. Markov, V. I. Sinitsyn, *et al.*, in *Proceedings of Internation School–Seminar on Automatization and Computerization in Science and Technology, ACS'2002*, http://www.elicsnet.ru.

Translated by D. Gabuzda

Astronomy Reports, Vol. 48, No. 2, 2004, pp. 81–88. Translated from Astronomicheskiĭ Zhurnal, Vol. 81, No. 2, 2004, pp. 99–107.

Seyfert Nuclei as Sources of Ultrahigh-Energy Cosmic Rays

A. V. Uryson

Lebedev Physical Institute, Leninskiĭ pr. 53, Moscow, Russia

Received September 28, 2002; in final form, August 8, 2003

Abstract—Particles can be accelerated to ultrahigh energies $E \approx 10^{21}$ eV in moderate Seyfert nuclei. This acceleration occurs in shock fronts in relativistic jets. The maximum energy and chemical composition of the accelerated particles depend on the magnetic field in the jet, which is not well known; fields in the range $\sim$5–1000 G are considered in the model. The highest energies of $E \approx 10^{21}$ eV are acquired by Fe nuclei when the field in the jet is $B \approx 16$ G. When $B \sim$ (5–40) G, nuclei with $Z < 10$ are accelerated to $E \leq 10^{20}$ eV, while nuclei with $Z \geq 10$ acquire energies $E \geq 2 \times 10^{20}$ eV. Only particles with $Z \geq 23$ acquire energies $E \geq 10^{20}$ eV when $B \sim 1000$ G. Protons are accelerated to $E < 4 \times 10^{19}$ eV, and do not fall into the range of energies of interest for any magnetic field B. The particles lose a negligible amount of their energy in interactions with infrared photons in the accretion disk; losses in the thick gas–dust torus are also negligible if the luminosity of the galaxy is $L \leq 10^{46}$ erg/s and the angle between the normal to the galactic plane and the line of sight is sufficiently small, i.e., if the axial ratio of the galactic disk is comparatively high. The particles do not lose energy to curvature radiation if their deviations from the jet axis do not exceed 0.03–0.04 pc at distances from the center of $R \approx 40$–50 pc. Synchrotron losses are small, since the magnetic field frozen in the galactic wind at $R \leq 40$–50 pc is directed (as in the jet) primarily in the direction of motion. If the model considered is valid, the detected cosmic-ray protons could be either fragments of Seyfert nuclei or be accelerated in other sources. The jet magnetic fields can be estimated both from direct astronomical observations and from the energy spectrum and chemical composition of cosmic rays. © *2004 MAIK "Nauka/Interperiodica"*.

1. INTRODUCTION

The hypothesis that active galactic nuclei (AGNs) are sources of cosmic rays is not new and was widely discussed in the 1980s [1]. We have returned to the idea that cosmic rays are accelerated in the nuclei of active galaxies after the direct identification of AGNs as possible sources of cosmic rays with energies $E > 4 \times 10^{19}$ eV [2–6], which was carried out as follows. Various objects located within 100 Mpc of our Galaxy and lying within the 1-σ, 2-σ, and 3-σ error regions for the arrival direction of the particles were analyzed. This means of selecting potential sources was dictated by two factors. First, particles arriving from very large distances would unavoidably lose energy in photon–pion reactions with background radiation [7–9]. Second, the actual coordinates of the particle arrival direction are located within the 3-σ region with a probability of 99.8%, but within the 1-σ region with a probability of only 66.8% [10]. The shower statistics included showers detected at the AGASA, Fly's Eye, Havera Park, and Yakutsk installations [11–14], for which errors in the arrival direction are published. The errors in the Yakutsk showers were calculated in our paper [3], and the errors for the Havera Park showers were presented in [15]. Of these showers, 11 have energies $E > 10^{20}$ eV.

We considered X-ray (as the most powerful) pulsars from the list [16], radio galaxies from the catalogs [17, 18], and AGNs from the catalog [19] as possible sources. For each of these types of objects, we calculated the probability that their coordinates were in the 3-σ region for a shower by chance. The probabilities for chance coincidence proved to be fairly low for moderate Seyfert nuclei with redshifts $z \leq 0.0092$ ($P \approx 3.20\sigma$) and for BL Lac objects ($P \approx 3.15\sigma$; σ is the parameter of the Gaussian probability distribution). According to probability theory, values $P > 3\sigma$ indicate that the corresponding objects are not located in the search field by chance. The probabilities of chance coincidence for the remaining objects considered were $P < 3\sigma$, testifying that they most likely lie in the search field by chance. The value of P depends strongly on the choice of the search area: probabilities of chance coincidence for the 2-σ region surrounding the shower are several orders of magnitude lower than those for the 3-σ region.

Specific models for the acceleration of cosmic rays in active galaxies were proposed in [20, 21]. In the model of [20], the magnetic field in an accretion disk surrounding a supermassive black hole evolves as a consequence of differential rotation of plasma with frozen-in magnetic field. As a result, there is an ex-

1063-7729/04/4802-0081$26.00

plosive (more rapid than exponential) growth in the electric field in some sections of the disk. Particles can be ejected from the flow of plasma in regions of low plasma density at the surface of the disk and can be accelerated by this strong electric field. The acceleration continues until the particles leave the region of explosive electric-field growth or until the growth in the field begins to slow. Numerical computations of the trajectories of individual particles show that particles in a disk with particle density $\sim 10^{16}$ cm^{-3} around a black hole with mass $\sim 10^7 M_\odot$ can be accelerated to energies of $\sim 10^{21}$ eV. The accelerated particles lose some of their energy to synchrotron radiation and the formation of pairs in reactions with photons. Synchrotron losses will be negligible if the particle velocities are aligned with the magnetic field. (Acceleration mechanisms that can operate in the case of other orientations of the particle velocities include acceleration in harmonic fields: if a particle is trapped between the crests of a wave and the magnetic field has a component perpendicular to the particle velocity, the particle will be accelerated [22, 23].) Losses to pair formation depend on the density distribution of the photons. In addition, in the case of collisions between particles and photons, these losses depend on the angle between the directions of motion of the particle and photon. It is therefore possible that some of the accelerated particles could leave the source galaxy virtually without any loss in their energy.

In the model of [21], the particle acceleration occurs in the electric field induced near a supermassive black hole with mass $\sim 10^9 M_\odot$ in periods of low activity of the black hole, when the accretion is diminished. The model is based on two main assumptions. The first is that the magnetic field of the black hole can be as high as $\sim 2 \times 10^{10}$ G, in contrast to the value $\sim 10^4$ G derived in [24] and the limit derived in [25], $B^2 \sim 8\pi\rho$, where ρ is the density of matter in the accretion disk. Second, it is assumed that there is a region with a very low plasma density in quiescent states of the black-hole activity, in which a very strong induced electric field cannot be compensated by the volume charge of the plasma. Regions in which such very strong electric fields can exist are located near the magnetic poles and rotational axis of the black hole. Particles can be accelerated to energies $10^{18} Z$ GeV in these fields. The accelerated particles lose energy in interactions with photons in the disk and via curvature radiation. In quiescent phases, losses to direct pair production and losses in photon reactions are negligible. The particle energy can be decreased to $10^{12} Z$ GeV due to curvature radiation, and the maximum proton energy is accordingly 10^{21} eV.

In both models, the particle acceleration occurs in the presence of extremely strong electric fields. The maximum particle energies $\sim 10^{21}$ eV coincide with the maximum energies detected for cosmic rays [12].

The model of [20] predicts sporadic flares of radiation associated with the ejection of accelerated particles, while the model of [21] predicts a flux of accelerated particles from the galactic nucleus. The moderate Seyfert galaxies that have been identified as possible sources of cosmic rays emit low radio and X-ray fluxes and do not display the characteristic features predicted by these models. In addition, it is not known whether there exist in these galaxies the conditions required to accelerate particles in the proposed scenarios. We have proposed another model for the acceleration of cosmic rays that supposes that various conditions can exist in the cosmic-ray sources, with various acceleration mechanisms being realized. Our model does not predict any specific features of the source radiation apart from the acceleration of particles to energies of $E \approx 10^{21}$ eV.

In sources of cosmic rays, particles are not only accelerated to ultrahigh energies, but also leave the acceleration region without appreciable energy losses. Sections 2–4 present our analysis of data for AGNs and demonstrate that the conditions required for the acceleration and free escape of particles exist in moderate Seyfert galaxies. Section 5 presents estimates of the energy of galactic sources based on the ultrahigh energy cosmic-ray spectrum observed at the Earth. In the Conclusions, we discuss other models for the origin of cosmic rays and the characteristics of cosmic rays predicted by them.

2. CONDITIONS IN ACTIVE GALACTIC NUCLEI

The nuclear activity of AGNs is most likely due to the existence of a supermassive black hole with a mass of $M \approx 10^9 M_\odot$ and an associated accretion disk at the center of the galaxy. The accreting material is provided by gas from stellar winds and supernova explosions surrounding the nucleus, stellar remnants that are disrupted by tidal forces near the black hole, and entire stars that are captured by the hole. The thickness of the accretion disk appears to be ~ 1 pc [26]. Models in which the disk thickness is $\sim 10^{16}$ cm have also been discussed in the literature [27]. The accretion disks in AGNs can apparently be either optically thin or optically thick [26, 28]. Two jets of material flowing out from the inner accretion disk emerge along the rotational axis. Jets of both ordinary and electron–positron plasma and fluxes of electromagnetic radiation have all been considered in the literature; the jet material can be ejected either in the form of individual "blobs" of plasma or as a

continuous flow [28]. The material ejected from the inner regions of the disk flows through the disk along two funnel-like channels formed along the rotational axis.

The ejected particles interact with material in the funnel walls and with their radiation. As a result of pp and $p\gamma$ interactions, electron–positron pairs or pions are born, which decay into positrons and photons, so that an electromagnetic cascade is generated inside the torus, giving rise to collimated beams of gamma radiation [27–30], providing an explanation for the gamma-ray emission of AGNs.

The conditions under which plasma from the disk and funnel walls does not fall into the channel of the funnel are considered in [31]: this is hindered by a magnetic field of $\sim 10^4$ G oriented parallel to the rotational axis of the black hole. (As a result, the electric field inside the funnel cannot be short-circuited by the volume charge of the plasma, analogous to the model of [21], and particles are accelerated inside the funnel by this field.)

The central region of the galaxy is surrounded by a geometrically and optically thick dusty torus that radiates in the infrared; the thickness of this torus can reach ~ 100 pc [32]. Models in which the inner walls of the torus are constantly bombarded by radiation, leading to the liberation of torus material that then falls into the jet, are considered in the literature (see [33] and references therein).

As is clear from this brief summary of various models, disk material can either be contained in the jet from the beginning or fall into the jet at some point. We will assume that the jets contain plasma from the accretion disk.

Different types of AGNs differ in various ways, including the power of their radiation in various bands, the ratio of the radio luminosity to the luminosity of the accretion disk (radio "loudness" or radio "quietness"), and the strength of the jets. Radio images show that radio galaxies have jets extending to tens or hundreds of kiloparsecs [34, 35], while the lengths of the jets in Seyfert nuclei are ~ 1–10 pc [36–40]. Seyfert galaxies are usually considered to be radio-quiet objects (although it is possible that this is not the case for all types of Seyferts [41]).

How can we explain the moderate jets and radio-quiet nature of Seyfert galaxies? Unified schemes for AGNs are discussed in the literature, in which observed differences in properties are due, for example, to differences in the accretion conditions (the mass of accreted gas and the accretion rate) [42], the orientation of the AGN relative to the observer [26], the mass of the central black hole [43], etc. In addition, various authors have explained the radio-loud/radio-quiet dichotomy in various ways. It is possible that radio loudness is correlated with the spin of the central black hole: in radio-loud objects, the spin is close to its maximum value, while the spin is low in radio-quiet objects [44]. Falcke *et al.* [33] propose a unified model for AGNs in which the different properties of radio-quiet and radio-loud objects, and also of FRI and FRII galaxies, are associated with different geometries for a torus surrounding the central black hole: the opening angle of the funnel is appreciably broader for radio-quiet objects and Seyferts than it is for radio-loud objects. As a consequence, the jets in radio-quiet objects and Seyfert galaxies are more poorly collimated and weaker and interact less with the torus (therefore, the production of electron–positron pairs in the funnel is negligible, so that these nuclei emit weakly in gamma rays). It is proposed in [45–47] that, in the vicinity of the central black holes of radio-quiet objects, there are stellar cores with fairly large masses and colliding hot gas flows, in which the jets are disrupted (by $\sim 90\%$) within ~ 1–3 pc of the nucleus.

Our model supposes that moderate Seyfert galaxies have relativistic jets.

A cocoon of perturbed jet material forms around the jet as it propagates [48]. Shock waves are excited in the jet and cocoon as a consequence of the nonlinear development of instabilities at the jet surface, collisions with dense clouds, and velocity fluctuations [28, 49, 50]. Relativistic particles can be accelerated to ultrahigh energies in the fronts of shocks with regular magnetic field (see the reviews [51, 52] and references therein).

We suppose that cosmic rays are accelerated in moderate Seyfert nuclei in the fronts of shock waves in the jet. The magnetic-field strength in the jets is not known. Only various estimates are available: the field in the magnetosphere of a black hole is expected to be $\sim 10^4$ G [24, 25, 42], though the estimates of [21] suggest it could reach $\sim 10^{11}$ G; the fields at distances $\ll 1$ pc from the black hole could be $\sim 10^3$ G [53]; jet fields of ~ 0.01 G and ~ 100 G are considered in [54]; the field in the funnel along which the jets propagate is estimated to be $\ll 700$ G [27]. In our model, the field strength in the jet is an unknown. We obtain an estimate of the field based on the conditions for maximum acceleration of cosmic rays in shock fronts in the jet.

What chemical compositions are possible for the accelerated cosmic rays? Since we assume that the jet contains material from the accretion disk, the composition of the cosmic rays should reflect that of the disk. The chemical composition of AGNs was investigated in [55] and a number of works referenced in [55]. We will assume that both protons and nuclei are present in the jet.

3. ACCELERATION OF COSMIC RAYS IN SEYFERT NUCLEI

The main assumptions of our model are the following. In most Seyfert galaxies, relativistic jets form in the vicinity of a massive central black hole. (It is possible that they are disrupted at distances of 1–3 pc inside a massive stellar core.) The transverse cross section in the central region of the jet is $S = 3 \times 10^{31}$ cm^2, and the jet Lorentz factor is $\gamma = 10$ [45]. Both protons and nuclei are present in the jets. The jet magnetic field is treated as an unknown, and we will obtain an estimate of the field based on the conditions for maximum acceleration of cosmic rays in shock fronts in the jet.

The jet field is parallel to the jet axis, the shocks are also parallel, and particles are accelerated to energies

$$E_j \approx Ze\beta_j B R_j \text{ erg} \quad (1)$$

when they scatter off inhomogeneities in the magnetic field due to turbulence, where Ze is the charge of the particle, β_j is the ratio of the jet velocity to the velocity of light, B is the magnetic field in a hot spot in the jet, and R_j is its transverse size [56]. For the jet parameters presented above, the velocity and transverse size of the jet will be $\beta_j \approx 0.99$ and $R_j \approx 3 \times 10^{15}$ cm and the maximum particle energy will be

$$E_j \approx 1.9 \times 10^{18} ZB \text{ eV}. \quad (2)$$

In the hot-spot magnetic field, the particle simultaneously is accelerated and loses energy to synchrotron radiation. We will assume that, under these conditions, the particle can accumulate the maximum energy if it loses less than half its acquired energy to synchrotron radiation over the acceleration time T_a. In other words, we assume that the acceleration time T_a does not exceed the time T_s over which the particle energy decreases by a factor of two: $T_a \leq T_s$. The acceleration time is equal to [52]

$$T_a \approx l/(\beta_s^2 c), \quad (3)$$

where l is the diffusion mean free path (in the vicinity of a shock, this will be equal to the Larmor radius of the particle, $l \approx r_L$) and β_s is the ratio of the velocity of the shock to the velocity of light. The Larmor radius of a particle is [1] $r_L \approx E/(300ZB)$, where r_L is in cm, the energy E is in eV, and the magnetic field B is in Gauss. The time T_s is equal to [57]

$$T_s \approx 3.2 \times 10^{18}/B_\perp^2 (A/Z)^3 1/Z(Mc^2/E), \quad (4)$$

where $B_\perp$ is the field component perpendicular to the particle's velocity, A is the atomic number of the particle, $M = Am_p$ is the mass of the particle, and m_p is the proton mass. Assuming $T_a \approx T_s$ and $E = E_{\max} \approx 1/2E_j$, we obtain from (2)–(4) the field strength for which the particle is accelerated to the maximum energy,

$$B_{CR} = (3.5 \times 10^2)^{2/3} Z^{-1/3}, \quad (5)$$

and the values of this maximum energy for nuclei ($A/Z \approx 2$):

$$E_{\max A} \approx 6.6 \times 10^{20} (Z/B)^{1/2} \text{ eV}, \quad (6)$$

and for protons:

$$E_{\max p} \approx 1.65 \times 10^{20} B^{-1/2} \text{ eV}. \quad (7)$$

(These same formulas were obtained in a somewhat different way in our paper [58].) If the field is $B \sim$ (5–40) G, nuclei with $Z \geq 10$ acquire energies $E \geq 2 \times 10^{20}$ eV, while lighter nuclei are accelerated only to energies $E \leq 10^{20}$ eV: for protons, $B_p \approx 19.6$ G and $E_{\max p} \approx 3.7 \times 10^{19}$ eV; for He nuclei, $B_{\text{He}} \approx 39.5$ G and $E_{\max \text{He}} \approx 1.5 \times 10^{20}$ eV; and for Fe nuclei, $B_{\text{Fe}} \approx 16$ G and $E_{\max \text{Fe}} \approx 8 \times 10^{20}$ eV. In a field of $B \sim 100$ G, particles with $Z > 2$ are accelerated to energies $E \geq 10^{20}$ eV. In a field of $B \sim 1000$ G, only heavy particles with $Z \geq 23$ acquire energies $E \geq 10^{20}$ eV.

The particles acquire such energies over distances of $R \approx T_a c$ from the base of the jet. Taking the B fields from above, we find that this distance is $R_{\text{He}} \approx 6 \times 10^{15}$ cm$\approx 20R_g$ for He nuclei and $R_{\text{Fe}} \approx 3 \times 10^{15}$ cm $\approx 10R_g$ for Fe nuclei, where R_g is the gravitational radius of a black hole with a mass of $10^9 M_\odot$. In a field of $B \approx 1000$ G, particles with $Z = 23$ are accelerated to $E = 10^{20}$ eV over a distance of $R \approx 0.1R_g$.

Formulas (5)–(7) and these numerical estimates were obtained for a jet radius of $R_j \approx 3 \times 10^{15}$ cm. In a jet with radius kR_j, the maximum particle energy changes by only a factor of $k^{1/3}$. Therefore, these estimates are valid for jets with cross sections in the range $\sim 5 \times 10^{29}$–10^{33} cm^2.

Thus, protons are accelerated to $E < 4 \times 10^{19}$ eV, and do not fall into the energy range of interest for any values of B. Therefore, if this model is correct, cosmic-ray protons with energies $E > 4 \times 10^{19}$ eV were not accelerated in Seyfert nuclei. They are fragments of nuclei, or were accelerated in other sources (such as BL Lac objects). Further, the magnetic fields in jets can be estimated not only based on astronomical observations but also based on the energy spectrum and chemical composition of cosmic rays.

4. ESCAPE OF THE PARTICLES FROM THEIR SOURCES

Accelerated particles that have left the hot spot do not interact with the leading wave excited in the flow

of hot gas by the jet, since this wave propagates more slowly than the jet due to the fact that the density of the gas is lower than that of the jet [50]. The particles lose energy in photon–pion reactions with infrared photons and to synchrotron and curvature radiation. Let us first consider photonic losses.

4.1. Energy Losses of the Particles in Interactions with Photons

During interactions of the particles with photons, the main energy losses occur in photon–pion reactions, $p+\gamma \to p(n)+\pi$, and in direct pair-production reactions, $p+\gamma \to p+e^+ +e$. In the case of nuclei with masses A, photon–pion reactions give rise to the formation of m nucleons and n pions, $A+\gamma \to A'+mN+n\pi$. In addition, photosplitting of the nuclei can occur: $A'+\gamma \to A+mN$. The threshold energy (in the center of mass system) for direct pair production is 1 MeV and for photon–pion production is 145 MeV, so that the former reactions dominate at particle energies $E \le 2.1\times 10^{18}$ eV, while the latter dominate at energies $E \ge 3\times 10^{19}$ eV [1]. The pions produced in photoreactions decay via the paths $\pi^{\pm} \to \mu^{\pm}+\nu$, $\mu^{\pm} \to e^{\pm}+\nu+\nu$, $\pi^0 \to 2\gamma$, and the electrons and photons that are produced in these decays can initiate cascades, leading to an increase in the radiation density and additional energy losses by the accelerated particles.

Photonic losses are greatest in regions with high photon densities, such as the funnel of the accretion disk and the central region of the galaxy surrounded by the geometrically and optically thick dusty torus radiating infrared photons (the thickness of the torus can reach $\sim$100 pc) [32]. The infrared radiation is absorbed and reprocessed by clouds inside the torus. Energy losses in the funnel have been studied in [31, 59], where it was shown that the particles lose only a negligible fraction of their energy in direct pair-production reactions if the radiation has a hard spectrum (as is the case for AGNs). Further, losses can be appreciable in photon–pion reactions, in which case collimated beams of gamma radiation form due to the development of cascades. Photonic losses are negligibly small in accretion disks with optical depths $\tau \le 1$ [21, 56]. (Consequently, collimated beams of gamma radiation do not form in such disks.)

The passage of particles through the gas–dust torus is considered in [56]. The particles lose only an insignificant fraction of their energy in interactions with radiation rescattered in the torus if the luminosity of the galaxy is $L < 10^{46}$ erg/s.

In addition, a particle can lose energy in interactions with radiation emitted in the jet. The emission of such radiation is considered in [33]. Cascades can develop in the jets due to their interaction with the walls of the gas–dust torus. This enhances the radiation density in the jet, leading to additional energy losses by the accelerated particles. However, in Seyfert galaxies, the interaction of the jets with the torus walls is insignificant, so that no cascades develop. For this reason, these AGNs radiate only weakly in gamma rays [33].

An accelerated particle will not intersect the dust torus if it travels at an angle i to the normal to the galactic plane such that $\tan i < r/h$, where r is the inner radius of the torus and h is its thickness, i.e., if the galactic plane is tilted at a relatively small angle to the observer. The angle i is characterized by the ratio of the galactic semiaxes: $\cos i = e_2/e_1$ (if $e_2/e_1 = 0.6$, $i = 55^0$) [60]. Therefore, the ratio e_2/e_1 should be comparatively large for galactic sources of cosmic rays.

As a result of interactions of the particles with infrared photons, electromagnetic cascades develop, giving rise to X-ray radiation along with collimated beams of gamma rays [61]. Therefore, AGNs in which particles were first accelerated and then lost energy are probably X-ray sources.

For these reasons, if the energy losses of the accelerated particles within the funnel and dust torus are small, nuclei that are possible sources of cosmic rays will have modest fluxes at X-ray and gamma-ray energies and will not give rise to collimated beams of gamma rays.

4.2. Energy Losses in Magnetic Fields

Synchrotron losses in the flow of gas are insignificant, since the field in these flows is directed (as in the jet) predominantly along the direction of motion. The curvature losses for a particle with charge Z are [62]

$$-dE/dt = 2/3(Ze)^2 c(E/Mc^2)^4(\rho_c)^{-2}, \quad (8)$$

where ρ_c is the radius of curvature of the field line. Hence, the particle energy halves over a time

$$T_{curv} = 7/2(Mc^2)^8 E^{-3}(Ze)^{-2}\rho_c^2\, c^{-1}. \quad (9)$$

The particle propagates along the field line a distance R_{line}. Particles with energy $E_{\max}$ travel this distance over a time

$$t \approx R_{line}/c \approx 4.6\times 10^9 \text{ s}. \quad (10)$$

The curvature losses will be small if the particle loses no more than half its energy $E_{\max}$ as it moves along the field line:

$$T_{curv} > t. \quad (11)$$

We find the distance R_{line} as follows. The accelerated particle freely leaves the galaxy, having reached regions where the field has decreased enough that the

Larmor radius of the particle becomes roughly $r_L \geq 5$ kpc [63]. (Here, we have taken the characteristic dimensions of the spiral galaxies that are the host galaxies of most Seyferts to be the same as those of our Galaxy.) For ultrarelativistic particles, the Larmor radius is equal to [1] $r_L \approx E/(300ZB)$ (the energy E is measured in eV, the field B in Gauss, and r_L in cm), and, for particles with various Z values and energy $E = E_{\max}$, the condition $r_L \geq 5$ kpc is fulfilled when the field is $B \leq 10^{-5}$ G. Taking the magnetic field to decrease with distance as $B \sim R^{-3}$ [64], and the field at $R \sim 1$ pc to be $B \sim 1$ G [53], we obtain $R_{line} \approx 46$ pc. The curvature radius of the field lines in a dipole magnetic field is $\rho_c = 4R^2/3a$, where R and a are the distances from the center and from the axis of the dipole [21]. Based on this information and (9)–(11), we can estimate the maximum deviation from the jet axis of a particle with energy $E = E_{\max}$ that has traveled a distance $R \approx 46$ pc with small curvature losses: for protons, $a_p \approx 0.01$ pc; for He nuclei, $a_{\rm He} \approx 0.03$ pc; and for Fe nuclei, $a_{\rm Fe} \approx 0.04$ pc.

Let us determine the fraction of accelerated particles that leave the source without significant curvature losses. For such particles, the deviation from the jet axis will be

$$\theta \leq a/R_{line} = 6.5 \times 10^{-4}. \qquad (12)$$

In the wave system, the particles are scattered isotropically. Therefore, the fraction of particles in which we are interested can be found as follows. The angle θ^* between the velocity vector and jet axis in the wave system is related to the angle θ by the expression [65]

$$\tan\theta = (1-\beta^2)^{1/2}(\beta + \cos\theta^*)^{-1}\sin\theta^* \qquad (13)$$
$$= 0.14\sin\theta^*(0.99 + \cos\theta^*)$$

with $\beta \approx 0.99$. For angles $\theta < 0.02$, $\sin\theta^* \approx \theta^*$, $\cos\theta^* \approx 1$ and $\theta \approx 0.07\theta^*$. Hence, $\theta^* \approx 0.01$, and the fraction of particles deviating from the axis by angles (12) is $\eta = 0.01/\pi \approx 3 \times 10^{-3}$; i.e., roughly one in 300 of the accelerated particles leave the source without curvature losses.

We considered the propagation of the particles in the magnetic fields of intergalactic space and in our Galaxy in [58].

5. ESTIMATES OF THE ENERGY OF GALACTIC COSMIC-RAY SOURCES

Thus, based on the flux of cosmic rays measured at the Earth, we can estimate the observed luminosities in ultrahigh energy (UHE) cosmic rays for galactic cosmic-ray sources. This luminosity $L_{\rm UHECR}$ is equal to

$$L_{\rm UHECR} = \int_E^\infty F_g(E)EdE, \qquad (14)$$

where $F_g(E) = KE^{-\gamma}$ is the differential particle-generation spectrum in a Seyfert galaxy. If the spectrum of high-energy cosmic rays is only weakly distorted by interactions in intergalactic space (this is possible if the sources are located within $R \sim 50$ Mpc of the Earth), the particle-generation spectrum in the source $F_g(E)$ and the observed cosmic-ray spectrum $I(E)$ for $E > 5 \times 10^{19}$ eV will have the same form, and $F_g(E) = KE^{-\gamma}$ with $\gamma \geq 3.1$. The intensity of cosmic rays with energy E in the Universe is [1]

$$I(E) = (c/4\pi)F_g(E)n_{Sy}T_{CR}, \qquad (15)$$

where $n_{Sy} = 2 \times 10^{-77}$ cm^{-3} is the density of Seyfert galaxies and T_{CR} is the age of the UHE cosmic rays. Since the distances from which the cosmic rays can arrive without interacting with the background radiation are $R \sim 50$ Mpc, the ages are $T_{CR} = R/c \approx 1.7 \times 10^8$ yr. According to measurements made using various installations [66], the spectrum $I(E)$ at $E > 5 \times 10^{19}$ eV is $I(E) \approx 10^{-39}$–10^{-40} (cm^2 s sr eV)$^{-1}$. We obtain from (14) and (15) the observed luminosity of the galactic sources in cosmic rays with $E > 5 \times 10^{19}$ eV, $L_{\rm UHECR} \approx 10^{41}$–$10^{42}$ erg/s ($\gamma \approx 3.1$). The real luminosity is higher than the observed value by a factor of $1/\eta$ and is $L_{\rm UHECR,eff} \approx 3 \times 10^{43}$–$3 \times 10^{44}$ erg/s. (Note that, if the mass of the black hole is $M \approx 10^9 M_\odot$ and all its energy Mc^2 is spent on accelerating UHE cosmic rays at the power found above, the energy of the black hole is depleted over 10^{13}–10^{14} yr, much longer than the age of the Universe, $T_{Mg} \approx 1.3 \times 10^{10}$ yr.)

6. CONCLUSIONS

We have shown that particles can be accelerated to ultrahigh energies $E \approx 10^{21}$ eV in the nuclei of moderate Seyfert galaxies. In our model, the acceleration takes place in shock fronts in relativistic jets in these objects. Jets in Seyfert nuclei have been studied in references listed in Section 2. We adopted the jet parameters presented in [45] for our estimates. We have assumed that the jets contain material from the accretion disk, so that both protons and nuclei are present in the jets. The maximum energy and chemical composition of the accelerated particles depend on the magnetic field in the jet, which is not well known, and so was treated as an unknown parameter in the model. We considered fields in the range ~5–1000 G. The highest energy $E \approx 8 \times 10^{20}$ eV is acquired by Fe nuclei when the field in the jet is $B \approx 16$ G. When

the field is $B \sim (5–40)$ G, nuclei with $Z \geq 10$ acquire energies $E \geq 2 \times 10^{20}$ eV, while lighter nuclei are accelerated to energies $E \leq 10^{20}$ eV. In a field of $B \sim 1000$ G, only particles with $Z \geq 23$ acquire energies $E \geq 10^{20}$ eV. Protons are accelerated only to $E < 4 \times 10^{19}$ eV and do not fall into the energy range of interest for any value of B. The estimates we have obtained are valid for relativistic jets with cross sections of $\sim 5 \times 10^{29}–10^{33}$ cm^2. The particle acceleration occurs over distances $\sim (0.1–10)R_g$.

The accelerated particles leave the source galaxy without significant energy losses under the following conditions. First, the particles do not lose energy in photon–pion reactions in the accretion disk if its optical depth is $\tau \leq 1$ [21, 31, 56, 59]. Second, losses in the thick gas–dust torus are insignificant if the galaxy luminosity is $L < 10^{46}$ erg/s [56] and the angle between the normal to the galactic plane and the line of sight is sufficiently small, i.e., if the axial ratio of the galactic disk is comparatively high. Third, particles do not lose energy to curvature radiation if their deviations from the jet axis do not exceed $a \leq 0.03–0.04$ pc at distances $R \sim 40–50$ pc. Synchrotron losses are small if the magnetic field frozen in the galactic wind at $R \leq 40–50$ pc is oriented (as in the jet) predominantly along the direction of motion.

The galaxies that are potential sources of cosmic rays should radiate only modest fluxes of X rays and should not emit collimated beams of gamma rays. The power spent by the nucleus on the acceleration of UHE cosmic rays is $3 \times 10^{43}–3 \times 10^{44}$ erg/s. (For this estimate, we have assumed that the measured cosmic-ray spectrum at $E > 5 \times 10^{19}$ eV is [66] $I(E) \approx 10^{-39}–10^{-40}$ (cm^2 s st eV)$^{-1}$.) If the entire energy of a black hole with a mass of $M \approx 10^9 M_\odot$ were spent on accelerating cosmic rays to ultrahigh energies at this rate, the energy would be depleted after $10^{13}–10^{14}$ yrs, much longer than the age of the Universe, $T_{Mg} \approx 1.3 \times 10^{10}$ yr.

The general requirements for the sources of cosmic rays that follow from classical electrodynamics have been studied in [51, 67]. These requirements are satisfied by AGNs.

Other possible mechanisms for producing UHE cosmic rays are discussed in the literature—in the evolution of topological defects [68], in decays of relict super-heavy particles of cold dark matter [69], in gamma-ray bursts [70], etc. What do these models predict? If the first model is correct, most cosmic rays with energies $E \approx 10^{21}$ eV should be gamma rays. In the model of [69], there should be an appreciable ($\sim 20\%$) excess of UHE cosmic rays from the Galactic center. Only UHE protons are produced in gamma-ray bursts. Our model predicts that UHE cosmic rays should be nuclei (nuclear fragments), with no excess cosmic rays from the Galactic center.

If our model is correct, detected protons with energies $E > 4 \times 10^{19}$ eV are either fragments of nuclei or were accelerated in other sources (such as BL Lac objects). The jet magnetic fields can be estimated not only based on astronomical observations but also based on the energy spectrum and chemical composition of the cosmic rays.

Our model can be verified using measurements of the spectrum and composition of UHE cosmic rays. Such measurements will be carried out using AGASA, as well as using future giant installations such as HiRes, Pierre Auger, Telescope Array, satellite instruments (see references in the reviews [71, 72]) and the ShAL-1000 installation [73].

ACKNOWLEDGMENTS

I am grateful to E.Ya. Vil'koviskiĭ, V.A. Dogel', A.V. Zasov, Ya.N. Istomin, and O.K. Sil'chenko for discussions of the model.

REFERENCES

1. V. S. Berezinskiĭ, S. V. Bulanov, V. L. Ginzburg, *et al.*, in *Astrophysics of Cosmic Rays*, Ed. by V. L. Ginzburg (Nauka, Moscow, 1990) [in Russian].
2. A. V. Uryson, Pis'ma Zh. Éksp. Teor. Fiz. **64**, 71 (1996) [JETP Lett. **64**, 77 (1996)].
3. A. V. Uryson, Zh. Éksp. Teor. Fiz. **116**, 1121 (1999) [JETP **89**, 597 (1999)].
4. A. V. Uryson, Astron. Astrophys. Trans. **20**, 347 (2001).
5. A. V. Uryson, Astron. Zh. **78**, 686 (2001) [Astron. Rep. **45**, 591 (2001)].
6. A. V. Uryson, Astron. Astrophys. Trans. **22** (6) (2003); astro-ph/0310520 (2003).
7. K. Greisen, Phys. Rev. Lett. **16**, 748 (1966).
8. G. C. Zatsipin and V. A. Kuz'min, Pis'ma Zh. Éksp. Teor. Fiz. **4**, 114 (1966).
9. F. W. Stecker, Phys. Rev. Lett. **21**, 1016 (1968).
10. G. L. Squires, *Practical Physics* (McGraw-Hill, New York, 1968; Mir, Moscow, 1971).
11. M. Takeda, N. Hayashida, K. Honda, *et al.*, Astrophys. J. **522**, 225 (1999).
12. D. Bird, S. C. Corbato, H. Y. Dai, *et al.*, Astrophys. J. **441**, 144 (1995).
13. A. Watson, in *Particle and Nuclear Astrophysics and Cosmology in the Next Millenium*, Ed. by E. W. Kolb and R. D. Peccei (World Sci., Singapore, 1995), p. 126.
14. B. N. Afanasiev, M. N. Dyakonov, V. P. Egorova, *et al.*, in *Extremely High Energy Cosmic Rays: Astrophysics and Future Observatories*, Ed. by M. Nagano (Inst. Cosmic-Ray Research, Tokyo, 1996), p. 32.
15. G. R. Farrar and P. L. Biermann, Phys. Rev. Lett. **81**, 3579 (1998).
16. S. B. Popov, http://xray.sai.msu.su/~polar/ (2001).

17. H. Spinrad, S. Djorgovski, J. Marr, *et al.*, Publ. Astron. Soc. Pac. **97**, 932 (1985).
18. H. Kuhr, A. Witzel, and I. I. K. Pauliny-Toth, Astron. Astrophys., Suppl. Ser. **45**, 367 (1981).
19. M. P. Veron-Cetty and P. Veron, Astron. Astrophys. **374**, 92 (2001); http://dbsrv.gsfc.nasa.gov/heasarc_veron98.
20. C. A. Haswell, T. Tajima, and J.-I. Sakai, Astrophys. J. **401**, 495 (1992).
21. N. S. Kardashev, Mon. Not. R. Astron. Soc. **276**, 515 (1995).
22. R. Z. Sagdeev and V. U. Shapiro, Pis'ma Zh. Éksp. Teor. Fiz. **17**, 389 (1973) [JETP Lett. **17**, 279 (1973)].
23. T. Katsouleas and J. M. Dawson, Phys. Rev. Lett. **51**, 392 (1983).
24. G. B. Field and R. D. Rogers, Astrophys. J. **403**, 94 (1993).
25. J. H. Krolik, Astrophys. J. **515**, L73 (1999).
26. R. Antonucci, Ann. Rev. Astron. Astrophys. **31**, 473 (1993).
27. W. Bednarek, Astrophys. J. **402**, L29 (1993).
28. M. C. Begelman, R. D. Blandford, and M. J. Rees, Rev. Mod. Phys. **56**, 255 (1984).
29. K. Mannheim and P. L. Biermann, Astron. Astrophys. **253**, L21 (1992).
30. M. Sikora, M. C. Begelman, and M. J. Rees, Astrophys. J. **421**, 153 (1994).
31. W. Bednarek and J. G. Kirk, Astron. Astrophys. **294**, 366 (1995).
32. E. A. Pier and J. H. Krolik, Astrophys. J. **418**, 673 (1993).
33. H. Falcke, Gopal-Krishna, and P. L. Biermann, Astron. Astrophys. **298**, 395 (1995).
34. B. L. Fanaroff and J. M. Riley, Mon. Not. R. Astron. Soc. **167**, 31 (1974).
35. A. H. Bridle and R. A. Perley, Ann. Rev. Astron. Astrophys. **22**, 319 (1984).
36. C. Xu, M. Livio, and S. Baum, Astron. J. **118**, 1169 (1999).
37. N. M. Nagar, A. S. Wilson, and H. Falcke, Astrophys. J. **559**, L87 (2001).
38. A. Thean, A. Pedlar, M. J. Kukula, *et al.*, Mon. Not. R. Astron. Soc. **314**, 573 (2000).
39. H. Falcke, N. M. Nagar, A. S. Wilson, *et al.*, Astrophys. J. **542**, 197 (2000).
40. J. S. Ulvestad and L. C. Ho, Astrophys. J. **562**, L133 (2002).
41. L. S. Ho and C. Y. Peng, Astrophys. J. **555**, 650 (2001).
42. M. J. Rees, Ann. Rev. Astron. Astrophys. **22**, 471 (1984).
43. G. Ghisellini and A. Celotti, Astron. Astrophys. **379**, L1 (2001).
44. R. Moderski, M. Sikora, and J.-P. Lasota, Mon. Not. R. Astron. Soc. **301**, 142 (1998).
45. E. Ya. Vil'koviskiĭ and O. G. Karpov, Pis'ma Astron. Zh. **22**, 168 (1996) [Astron. Lett. **22**, 148 (1996)].
46. E. Y. Vilkoviskij, S. N. Efimov, O. G. Karpova, *et al.*, Mon. Not. R. Astron. Soc. **309**, 80 (1999).
47. E. Y. Vilkoviskij and B. Cherny, Astron. Astrophys. **387**, 804 (2002); astro-ph/0203226.
48. M. C. Begelman and D. F. Cioffi, Astrophys. J. **345**, L21 (1989).
49. R. Blandford and D. Eichler, Phys. Rep. **154**, 1 (1987).
50. S. K. Chakrabarti, Mon. Not. R. Astron. Soc. **235**, 33 (1988).
51. A. M. Hillas, Ann. Rev. Astron. Astrophys. **22**, 425 (1984).
52. C. J. Cesarsky, Nucl. Phys. B (Proc. Suppl.) **28**, 51 (1992).
53. M. J. Rees, Mon. Not. R. Astron. Soc. **228**, 47 (1987).
54. M. Sikora, G. Madejski, R. Moderski, *et al.*, Astrophys. J. **484**, 108 (1997).
55. D. Alloin, R. Barvainis, and S. Guilloteau, Astrophys. J. **528**, L81 (2000).
56. C. A. Norman, D. B. Melrose, and A. Achterberg, Astrophys. J. **454**, 60 (1995).
57. V. L. Ginzburg and S. I. Syrovatskii, *The Origin of Cosmic Rays* (MacMillan, New York, 1964).
58. A. V. Uryson, Pis'ma Astron. Zh. **27**, 901 (2001) [Astron. Lett. **27**, 775 (2001)].
59. M. Sikora, J. G. Kirk, M. C. Begelman, and P. Schneider, Astrophys. J. **320**, L81 (1987).
60. R. Simcoe, K. K. McLeod, J. Schachter, and M. Elvis, Astrophys. J. **489**, 615 (1997).
61. F. W. Stecker, C. Done, M. H. Salamon, and P. Sommers, Phys. Rev. Lett. **66**, 2697 (1991).
62. V. V. Zheleznyakov, *Radiation in Astrophysical Plasmas* (Yanus-K, Moscow, 1997) [in Russian].
63. D. N. Pochepkin, V. S. Ptuskin, S. I. Rogovaya, and V. N. Zirakashvili, in *Proc. 24th Int. Cosmic Ray Conf., Rome* (1995), Vol. 3, p. 136.
64. E. Ya. Vyl'koviskiĭ, private communication.
65. L. D. Landau and E. M. Lifshits, *Field Theory* (Nauka, Moscow, 1990) [in Russian].
66. A. Watson, in *Extremely High Energy Cosmic Rays: Astrophysics and Future Observatories*, Ed. by M. Nagano (Inst. Cosmic-Ray Research, Tokyo, 1996), p. 362.
67. F. Aharonian, A. A. Belyanin, E. V. Derishev, *et al.*, Phys. Rev. D **66**, 023005 (2002).
68. V. Berezinsky and A. Vilenkin, Phys. Rev. Lett. **79**, 5202 (1997).
69. V. A. Kuz'min and V. A. Rybakov, Yad. Fiz. **61**, 1122 (1998).
70. T. Totani, Astrophys. J. **502**, L13 (1998).
71. M. Nagano and A. A. Watson, Rev. Mod. Phys. **72**, 689 (2000).
72. V. A. Tsarev and V. A. Chechin, Dokl. Akad. Nauk **383**, 486 (2002) [Dokl. Phys. **47**, 275 (2002)].
73. Y. A. Fomin, N. N. Kalmykov, G. B. Christiansen, *et al.*, in *Proc. 26th Int. Cosmic Ray Conf., Salt Lake City* (1999), Vol. 1, p. 526.

Translated by D. Gabuzda

Astronomy Reports, Vol. 48, No. 2, 2004, pp. 89–102. Translated from Astronomicheskiĭ Zhurnal, Vol. 81, No. 2, 2004, pp. 108–123.

Masses of X-ray Pulsars in Binary Systems with OB Supergiants

M. K. Abubekerov[1], É. A. Antokhina[2], and A. M. Cherepashchuk[1,2]

[1] *Moscow State University, Vorob'evy gory, Moscow, 119992 Russia*

[2] *Sternberg Astronomical Institute, Universitetskiĭ pr. 13, Moscow, 119992 Russia*

Received June 15, 2003; in final form, August 8, 2003

Abstract—We describe the results of a statistical approach to analyzing the combined radial-velocity curves of X-ray binaries with OB supergiants in a Roche model, both with and without allowance for the anisotropy of the stellar wind. We present new mass estimates for the X-ray pulsars in the close binary systems Cen X-3, LMC X-4, SMC X-1, 4U 1538-52, and Vela X-1. © *2004 MAIK "Nauka/Interperiodica".*

1. INTRODUCTION

Neutron stars are a natural product of the evolution of stars with masses in excess of 10 $M_\odot$. They were predicted theoretically by Landau [1] in the early 1930s, and the first radio pulsar was found in the center of the Crab nebula in the early 1960s. At the beginning of the 1970s—an epoch of active programs in near-Earth space exploration—the "Uhuru" satellite discovered objects with periodic X-ray variability [2] (X-ray pulsars), later identified with neutron stars in binary systems.

Thousands of compact X-ray sources have now been discovered in our Galaxy and other nearby galaxies. Most of these are close binary systems, in which the optical component supplies matter to the neutron star. Accretion with subrelativistic velocities onto the compact component's surface releases immense amounts of X-ray energy with luminosities of the order of 10^{36}–10^{39} erg/s [3–7]. From the point of view of the equation of state of the superdense matter, the key characteristic of an X-ray pulsar is its mass. The theory predicts two stable modes for neutron stars, based on a "soft" equation of state, with $M_{\max} \simeq 1.4\ M_\odot$, and a "hard" equation of state, with $M_{\max} \simeq 1.8\ M_\odot$ [8–12]. The question of whether or not we should adopt the hard equation of state for neutron stars remains unanswered. Among known X-ray pulsars, only Vela X-1 has a mass close to 1.8 $M_\odot$ [13]. Studies of X-ray binaries have been carried out for more than 30 years. Extensive spectroscopic observations have been accumulated which not only enable but also demand for their interpretation a more accurate allowance for effects resulting from the closeness of the components. A point-mass model approximating the optical component as a source of electromagnetic radiation with infinitesimal size is not adequate for analysis of the rich observational data that are now available and cannot be used to correctly estimate the masses of the X-ray pulsars in binary systems. This is especially true for systems with OB supergiants.

In X-ray binaries with OB supergiants, the optical star nearly fills its critical Roche lobe, which determines the limiting equilibrium figure in a rotating reference frame fixed to the binary. Therefore, the shape of the optical component deviates from a sphere, and the velocity field at the stellar surface becomes strongly nonuniform. The surface of the star that is turned toward the X-ray pulsar is heated by the pulsar's radiation, and the nonuniform gravitational acceleration on the companion leads to anisotropy of the stellar wind. All these factors distort the radial-velocity curve of the optical star. The distortions of the radial-velocity curve due to the effects of outflow and the stellar wind in close binaries with OB supergiants are comparable to the orbital velocity. These facts show the necessity of proper fitting of close-binary radial-velocity curves in a Roche model taking into account the anisotropy of the stellar wind [14].

2. DESCRIPTION OF THE ROCHE MODEL

The radial-velocity curves of X-ray binaries are usually analyzed using models with two point masses, though it is not appropriate to approximate the stars in most close binaries as point masses moving in Keplerian orbits for the following reasons.

1. Due to tidal deformation, the optical component is ellipsoidal or pear-shaped due to the gravitational action of the relativistic companion, leading to strongly nonuniform surface temperatures (gravitational darkening). For mass ratios $q = m_x/m_v < 1$ (with m_x and m_v being the masses of the optical and X-ray components), the binary centers of mass

1063-7729/04/4802-0089$26.00

are inside the body of the optical star, leading to significant distortion of the radial-velocity curve.

2. X-ray heating of the side of the optical star facing the relativistic component results in a nonuniform temperature distribution over the stellar surface.

3. It is important for early-type stars in close binaries that the cores of strong absorption lines formed in the outermost atmospheric layers, at the base of the stellar wind, experience radial Doppler shifts. These shifts are due to the regular outflow of the stellar-wind plasma with velocities of the order of the sound speed, $V_s \sim T^{1/2}$. The temperature and local gravitational acceleration vary strongly at the surface of the tidally deformed star, leading to appreciable distortion of the optical component's radial-velocity curve. For early-type stars, the velocity of the stellar wind at its base becomes comparable to the orbital velocity of the optical component, of the order of 10–20 km/s.

For these reasons, the radial-velocity curves of X-ray binaries with OB supergiants should be analyzed using Roche models. We applied our algorithm for synthesizing light curves, radial-velocity curves, and absorption-line profiles, described in detail in [15, 16], to analyze observations of massive close X-ray binaries. We describe the optical star using a Roche model, treating its companion as a point X-ray source. We briefly summarize the main principles of our algorithm below.

The optical star and point relativistic object with masses of m_v and m_x move in elliptical orbits about their common center of mass. The inclination of the binary orbit to the plane of the sky is i. In general, the star's axial rotation is not assumed to be synchronous with the orbital motion. The star's shape coincides with an equipotential surface of the Roche model [16, 17]. The size of the star is determined by the filling coefficient for the critical Roche lobe, $\mu = R/R^*$, where R and R^* are the polar radii for partial and complete filling of the critical Roche lobe at the orbit periastron. The star's tidally distorted surface is subdivided into thousands of mass elements, with the emergent radiation computed for each of them, after which the contributions of the various areas are added taking into account the visibility of each area element at various phases of the orbital period. The computed radiation fluxes from each area element include the effects of gravitational darkening, heating of the stellar surface by the radiation from the companion (the "reflection" effect), and limb darkening. The absorption line profile and line equivalent width for each visible area with its temperature T and local gravitational acceleration g were calculated using the tables of Kurucz [18] for the Balmer lines and an interpolation procedure. We add the local profiles over the stellar surface after first normalizing to the continuum for each area, taking into account the Doppler effect to obtain the total profile for the star at the corresponding phase of the orbital period. The theoretical total profile is subsequently used to determine the star's radial velocity and derive the radial-velocity curve over the course of the orbital period (for more details, see [15]).

The input parameters of the algorithm used to compute the radial-velocity curve of an X-ray binary in the Roche model are collected in Table 1.

3. COMPARISON OF THE THEORETICAL RADIAL-VELOCITY CURVES IN THE ROCHE AND POINT-MASS MODELS

Our main goal was to refine available estimates of the masses of X-ray pulsars in close binaries. Before analyzing the observations, we carried out test computations to compare the theoretical radial-velocity curves in the Roche and point-mass models. We computed the radial-velocity curves using the Hγ line for a hypothetical X-ray system with parameters (Table 1) close to those of the studied systems: Cen X-3, LMC X-4, SMC X-1, Vela X-1, and 4U 1538–52 (Table 2).

To identify the influence of reflection effects on the radial-velocity curves, we computed them in the Roche model for low and high incoming X-ray fluxes, $k_x = 0.05$ and $k_x = 1.4$. The computations of the radial-velocity curves from the Hγ lines demonstrate that the semiamplitude of the curves decreases in the presence of stronger X-ray heating; a similar result was obtained earlier [15]. We can explain this by the fact that, in the case of a stronger X-ray flux incident on the star and stronger heating of the surface facing the companion, the contribution of the light from the star's "nose" to the combined luminosity increases. The areas on the nose contribute more strongly to the star's mean radial velocity. The velocities of such areas are lower than the star's center-of-mass velocity, and so the mean velocity of the star decreases.

The difference of the star's radial-velocity curve from the curve for its center of mass increases from phase 0.0 to phase 0.5 as the star moves along its orbit and its heated surface turns toward the observer. At phase 0.0, the star is in front of the X-ray source. The difference between the star's radial-velocity curves in the Roche and point-mass models should increase with decreasing $q = m_x/m_v$.

Figure 1a compares the theoretical radial-velocity curves of a system (for its parameters, see Table 1) in the Roche and point-mass models. Curves are plotted for the Hγ line and for the case of low heating, $k_x = 0.05$. The semiamplitude of the curve is lower in the Roche model, and the semiamplitudes of the radial-velocity curves can be the same only when the

Table 1. Numerical parameters used to synthesize an X-ray binary radial-velocity curve in the Roche model

Relativistic component's mass	m_x, $M_\odot$	1.35
Optical component's mass	m_v, $M_\odot$	20
Period	P, days	4
Eccentricity	e	0
Longitude of periastron of the optical component	ω, degrees	0
Radial velocity of the system's center of mass	V_γ, km/s	0
Orbital inclination	i, degrees	80
Roche-lobe filling coefficient for the optical component at periastron	μ	0.99
Rotational asynchronism coefficient	f	0.95
Effective temperature of the optical component	T_{eff}, K	30000
Gravitational darkening coefficient	β	0.25
Ratio of the relativistic component's X-ray luminosity to the optical component's bolometric luminosity	$k_x = L_x/L_v$	0.05 и 1.4
Coefficient for reprocessing of the X-ray radiation	A	0.5
Limb-darkening coefficient	u	0.3

Table 2. Observed characteristics of X-ray binaries with OB supergiants (from the literature [13, 19, 20])

Name	Spectral type	T_{eff}, K	P, days	e	i, degrees	μ	f	K_x, km/s
Cen X-3	O(6-9) II-III	35000	2.0871390	<0.0008	83^{+3}_{-3}	$0.995^{+0.005}_{-0.005}$	$0.95^{+0.27}_{-0.25}$	414.1 ± 0.9
LMC X-4	O7 III-V	35000	1.40839	<0.01	63^{+3}_{-3}	~ 1.0	$0.65^{+0.23}_{-0.19}$	400.6
SMC X-1	B0.5Ia	25000	3.89229118	<0.00004	65^{+5}_{-5}	$0.97^{+0.03}_{-0.03}$	$0.95^{+0.34}_{-0.27}$	301.5 ± 4
Vela X-1	B0.5Ibeq	25000	8.964368	0.0898	73^{+3}_{-3}	$0.95^{+0.04}_{-0.04}$	$0.69^{+0.09}_{-0.08}$	278.1 ± 0.3
4U 1538−52	B0Iabe	25000	3.72844	0.08	60^{+5}_{-5}	$0.95^{+0.04}_{-0.04}$	$0.94^{+0.32}_{-0.25}$	309.0 ± 11

The orbital inclination i was derived from the duration of the X-ray eclipse (see, e.g., [20]). The values of e and K_x were derived from the X-ray pulsar's radial-velocity curve.

mass of the relativistic component is increased from 1.35 $M_\odot$ to 1.45 $M_\odot$. To obtain equal semiamplitudes for phase 0.25, the mass of the X-ray pulsar must be increased to 1.55 $M_\odot$. For stronger heating, $k_x = 1.4$, with the remaining parameters unchanged, equal semiamplitudes in the Roche and point-mass models require that the X-ray pulsar's mass be increased to 1.65 $M_\odot$.

Thus, all other conditions being the same, the use of the Roche model leads to an increase in the mass of the relativistic component by ∼7–20% compared to the mass obtained in the point-mass model. This suggests that using the more realistic close-binary model to analyze the radial-velocity curves should enable us to determine whether the masses of the neutron stars in X-ray binaries with OB supergiants exceed the masses of radio pulsars, which are equal, on average, to 1.35 ± 0.04 $M_\odot$ [21].

4. OBSERVATIONAL MATERIAL

Five eclipsing X-ray binaries with OB supergiants have been discovered to date (Table 2). During the last 30 years, extensive observational material has been accumulated for these systems, making it possible to test hypotheses using statistical methods. It is not possible to correctly take into consideration the components' mutual influence with the widely used

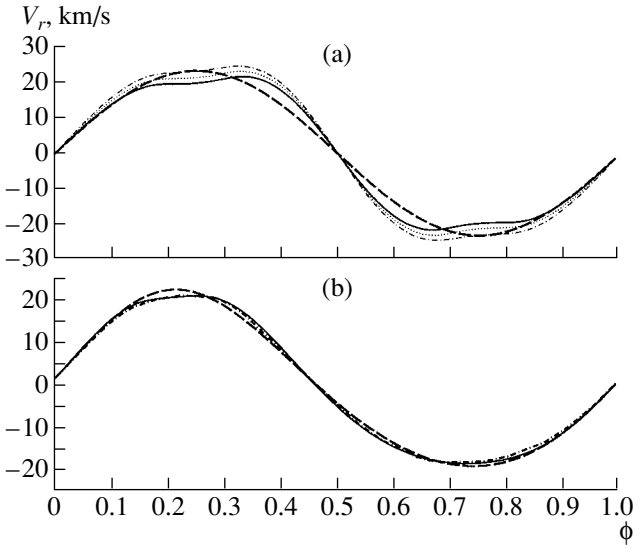

Fig. 1. (a) Theoretical radial-velocity curves of the optical star in a hypothetical X-ray close binary (for its parameters, see Table 1). The curves are derived from the Hγ line. The dashed curve corresponds to the optical star in a point-mass model with $m_x = 1.35\ M_\odot$, and the solid curve, to a Roche model with $m_x = 1.35\ M_\odot$; the dotted curve corresponds to $m_x = 1.45\ M_\odot$, and the dot–dash curve, to $m_x = 1.55\ M_\odot$. (b) Comparison of the theoretical radial-velocity curves of a star in the Roche model based on the Hγ line (solid curve) and the HeI 4471 Å line (dot–dash curve). The parameters are close to those of Vela X-1 ($m_v = 23\ M_\odot$, $m_x = 1.8\ M_\odot$, $P_{orb} = 8.96$ days, $e = 0.0898$, $\omega = 332.59°$, $i = 73°$, $\mu = 0.99$, $f = 0.69$, $T = 25\,000$ K, $\beta = 0.25$, $k_x = 0.05$, $A = 0.5$, $u = 0.38$). The dashed curve is the radial-velocity curve for the optical star's center of mass.

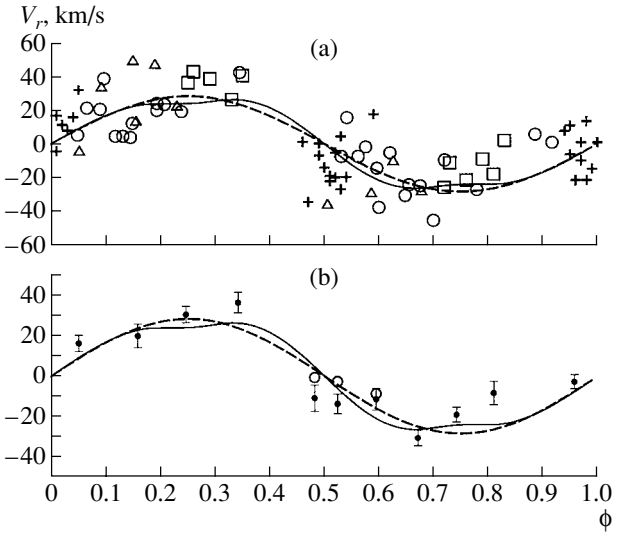

Fig. 2. (a) Master observed radial-velocity curve for the close X-ray binary Cen X-3 (triangles show spectroscopic data for 1976 from [22]; circles, data for 1978 from [23]; crosses, data for 1990 from [24]; and squares, data for 1997 from [24]). For comparison, the theoretical radial-velocity curves are shown for the Roche model (solid curve) and point-mass model (dashed curve), with $m_x = 1.22\ M_\odot$ corresponding to the minimum residual for the Roche model computed using method 2. The parameters are collected in Table 3. (b) Radial velocities averaged within phase intervals (filled circles are the mean radial velocities for the phase bins, and open circles, the radial velocities corrected for the normalized anisotropy function of the optical star's wind). The theoretical radial-velocity curves for the Roche model (solid curve) and point-mass model (dashed curve) with $m_x = 1.22\ M_\odot$ are shown for comparison.

Monte Carlo method in the framework of the point-mass model. For the reasons indicated above, earlier estimates of the masses of X-ray pulsars must be refined and revised using the Roche model.

We constructed a master radial-velocity curve for each of the systems. We describe the spectroscopic data used for each radial-velocity curve below. The center of the X-ray eclipse was taken as the zero phase for all the systems.

Cen X-3. The system consists of an O giant (O(6–9)II–III), with mass 17–18 $M_\odot$ and the X-ray pulsar, and has an orbital period of 2.0871390 days. The orbital eccentricity derived from timing of the X-ray pulses is very low ($e < 0.0008$ [13]), and we have assumed a circular orbit.

We used data from [22–24] acquired in 1976–1997 to construct the master radial-velocity curve (Fig. 2a). The data of [23] were corrected only for the close binary's γ velocity. The corrections for the velocity of the stellar wind were already introduced by the authors when combining the mean observed radial velocities derived from the shifts of the HeI 4471 Å, HeI 5875 Å absorption lines and the hydrogen Balmer lines. The line shifts in [22, 24] were derived relative to the spectrum averaged over all phases, so that the γ velocity was taken into account in the method itself. The mean radial velocities presented in [22] were derived from the HeI 4471 Å, HeII 4541 Å absorption lines and the hydrogen Balmer lines. Of the radial velocities from [24], we used only those measured for the Hγ line. A total of 79 data points were available to us, distributed approximately uniformly in phase. We used these data to construct a master radial-velocity curve for the Cen X-3 system from the Hβ, Hγ, Hδ, HeI 4471 Å, and HeI 5875 Å absorption lines. Our test computations demonstrated that the theoretical radial-velocity curves for the Roche model based on Hγ and other lines (Hβ, Hδ, HeI 4471 Å) coincided, all other parameters being the same (Fig. 1b; see also the text below). Thus, we used the theoretical radial-velocity curves for the Hγ line when fitting the master

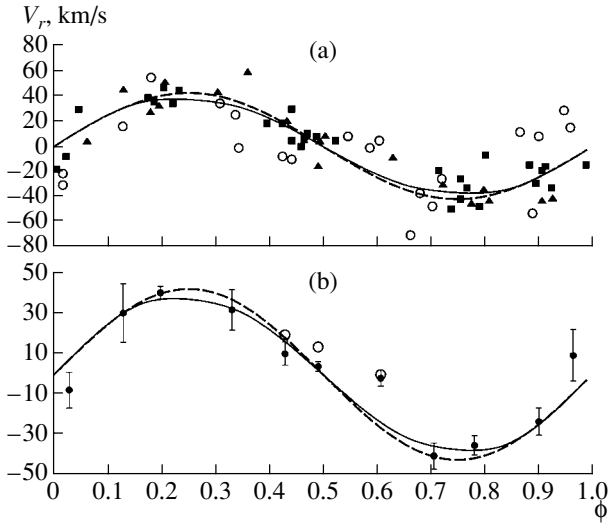

Fig. 3. (a) Master observed radial-velocity curve for the close X-ray binary LMC X-4 (filled triangles show spectroscopic data for 1975 from [25]; circles and filled squares show spectroscopic data for 1982 from [26] acquired with 2.5-m and 4-m telescopes). For comparison, theoretical radial-velocity curves are shown for the Roche model (solid curve) and point-mass model (dashed curve), with $m_x = 1.63\ M_\odot$ corresponding to the minimum residual for the Roche model computed using method 2. The parameters are collected in Table 3. (b) Radial velocities averaged within phase intervals (filled circles are the mean radial velocities for the phase bins, and open circles, the radial velocities corrected for the normalized anisotropy function of the optical star's wind). For comparison, theoretical radial-velocity curves are shown for the Roche model (solid curve) and point-mass model (dashed curve) with $m_x = 1.63\ M_\odot$.

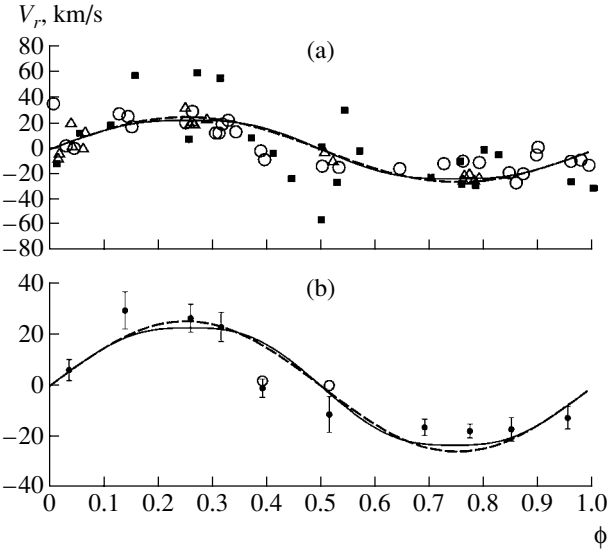

Fig. 4. (a) Master observed radial-velocity curve for the close X-ray binary SMC X-1 (filled squares show spectroscopic data for 1973 from [27]; open circles, spectroscopic data for 1976 from [28]; and open triangles, spectroscopic data for 1989 from [29]). For comparison, theoretical radial-velocity curves are shown for the Roche model (solid curve) and point-mass model (dashed curve), with $m_x = 1.48\ M_\odot$ corresponding to the minimum residual for the Roche model computed using method 2. The parameters are collected in Table 3. (b) Radial velocities averaged within phase intervals (filled circles are the mean radial velocities for the phase bins, and open circles, the radial velocities corrected for the normalized anisotropy function of the optical star's wind). For comparison, theoretical radial-velocity curves are shown for the Roche model (solid curve) and point-mass model (dashed curve) with $m_x = 1.48\ M_\odot$.

radial-velocity curves for Cen X-3, as well as for the other close binaries. The system's γ velocity derived using the spectroscopic data of [23] is 39 km/s.

LMC X-4. The system consists of the X-ray pulsar and an optical star of spectral type O7III–V with a mass of 14–15 $M_\odot$. The eccentricity is very low ($e < 0.01$), and we assumed the orbit to be circular. The orbital period derived from studies of the X-ray pulsar is 1.40839 days.

We used the data of [25, 26] acquired in 1975–1982 to plot the master light curve (Fig. 3a). The earlier observational data presented in [25] were already used in [26]. Thus, we used the newest spectroscopic data of [26]. The radial velocities were derived from the hydrogen absorption lines. Prior to being included in the master radial-velocity curves, the data were corrected for the γ velocity in [26]. The system's γ velocity derived using the spectroscopic data of [26] is 275 km/s.

SMC X-1. The system contains an optical component of spectral type B0.5Ia with a mass of about 17–18 $M_\odot$ and the X-ray pulsar. Its orbital period is 3.89229118 days.

The mean radial-velocity curve (Fig. 4a) was constructed using the data of [27–29]. The mean radial velocities measured from the HeI and SiIV absorption lines and the hydrogen Balmer lines are presented in [27]. The radial velocities determined by Hutchings *et al.* [28] were based on the mean of the shifts of the hydrogen Balmer lines and the HeI, SiIV, and NIII absorption lines in the blue (3900–4000 Å). The radial velocities in [29] were computed using a cross-correlation method based on the entire spectrum from 4000 to 4395 Å relative to the spectrum of the B3V standard star HR 1174, which has a similar spectral type.

Before plotting the mean curve, we corrected the spectroscopic data of [27–29] for the γ velocity. We computed the γ velocity by minimizing the sum of squared deviations between the radial velocities that were observed and synthesized in the Roche model

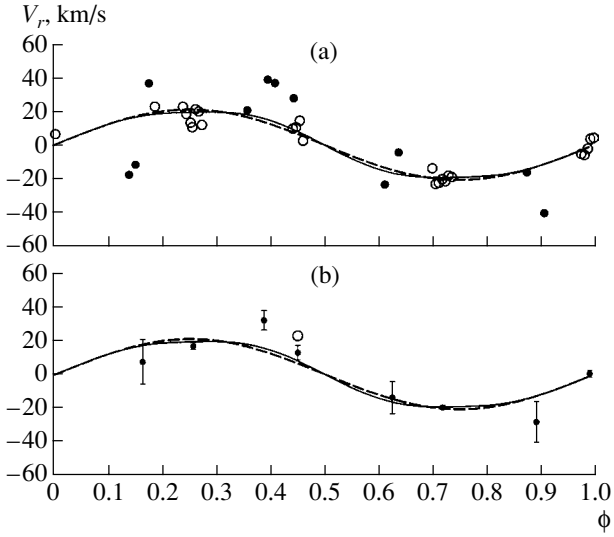

Fig. 5. (a) Master observed radial-velocity curve for the close X-ray binary 4U 1538−52 (filled circles are the spectroscopic data for 1978 of [31], and open circles, the spectroscopic data for 1991 of [32]). For comparison, the theoretical radial-velocity curves are shown for the Roche model (solid curve) and point-mass model (dashed curve), with $m_x = 1.18\,M_\odot$ corresponding to the minimum residual in the Roche model computed using method 2. The parameters are collected in Table 3. (b) The radial velocities averaged within phase intervals (filled circles are the mean radial velocities for the phase bins, and open circles, the radial velocities corrected for the normalized anisotropy function of the optical star's wind). For comparison, the theoretical radial velocity curves are shown for the Roche model (solid curve) and point-mass model (dashed curve) with $m_x = 1.18\,M_\odot$.

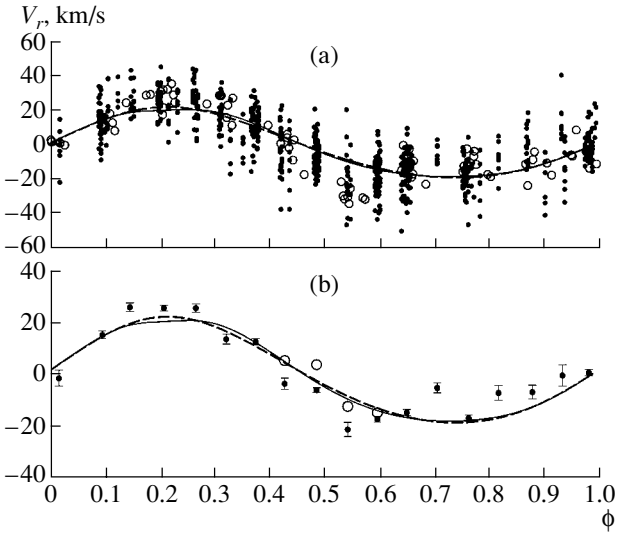

Fig. 6. (a): Master observed radial-velocity curve for the close X-ray binary Vela X-1 (filled circles are the spectroscopic data for 1973 of [33], and open circles, the spectroscopic data for 1995−1996 of [34]). For comparison, the theoretical radial-velocity curves are shown for the Roche model (solid curve) and point-mass model (dashed curve), with $m_x = 1.93\,M_\odot$ corresponding to the minimum residual in the Roche model computed using method 2. The parameters are collected in Table 3. (b) The radial velocities averaged within phase intervals (filled circles are the mean radial velocities for the phase bins, and open circles, the radial velocities corrected for the normalized anisotropy function of the optical star's wind). For comparison, the theoretical radial-velocity curves are shown for the Roche model (solid curve) and point-mass model (dashed curve) with $m_x = 1.93\,M_\odot$.

for the same phase. The γ velocity enters the algorithm used to synthesize the radial-velocity curves additively, so that the condition that the areas of the radial-velocity curve above and below the γ velocity be equal was fulfilled automatically. The γ velocities derived from the spectroscopic data of [27−29] were 173.0, 181.0, and 172.7 km/s.

4U 1538-52. This system consists of the X-ray pulsar and a B0Iabe supergiant with a mass of 17−18 $M_\odot$. The system's orbital period is 3.72844 days. The eccentricity derived from timing of the X-ray pulses is 0.07 ± 0.09 [30]. Due to the large uncertainty of this value, we assumed zero eccentricity.

The master radial-velocity curve (Fig. 5a) is based on the spectroscopic data of [31, 32]. Radial velocities derived from the Hβ, Hγ, HeI 4921 Å, and HeI 4471 Å absorption lines are presented in [31]. The radial velocities in [32] were computed via the cross-correlation method using the spectroscopic standard HD 133955 and HeI absorption lines in the range 6290−6710 Å . These data are in good agreement. We corrected the data from [31, 32] for the close binary's γ velocity. We derived the γ velocities −168.5 and −146.7 km/s using the spectroscopic data of [31, 32], respectively. In this case, the large negative value of the γ velocity may reflect radial expansion of the line-formation region near the base of the stellar wind.

Vela X-1. This system contains a B0.5Ibeq supergiant with a mass of 24−25 $M_\odot$ and the X-ray pulsar. The components are in an elliptical orbit with $e \simeq 0.0898$, and we adopted this eccentricity. The system's orbital period is 8.964368 days.

The observational material for this system is very rich. We used only the radial velocities of [33, 34] for the hydrogen Balmer lines to construct the master radial-velocity curve (Fig. 6a). As a result, data for 1973 and 1995−1996 were included in the master curve; these demonstrated good agreement despite the long time interval separating them.

The Balmer absorption lines from [33] derived from the absolute shifts of the cores of the H_2−H_{10} absorption lines relative to their laboratory wavelengths indicated increasing stellar-wind velocities with decreasing line number in the series—a Balmer progression [35, 36]. This effect is due to the negative

temperature gradient in the star's photosphere, resulting in a dependence of the observed stellar-wind velocity on the excitation potential of the absorption line used to measure this velocity. Thus, the Hβ absorption line is formed in higher and, consequently cooler, layers of the stellar photosphere, so that the stellar-wind velocity derived from this line is higher than the stellar-wind velocity measured from Balmer absorption lines with higher numbers.

According to the data of [37], the γ velocity derived from the Hβ line and HeI, NIII, and SiIV ion lines is -3.5 ± 0.8 km/s. The shifts of the lines' cores relative to their laboratory wavelength are due not only to the γ velocity but also to the velocity of the stellar wind at its base. If the system's γ velocity is much lower than this stellar-wind velocity, it is not possible to determine it from the shifts of the H_2–H_{10} lines due to the strong stellar wind from the OB supergiant. For example, according to the spectroscopy of [33], the radial velocities derived from the H_2, H_3, H_5, and H_6 lines are -29.0, -15.5, -14.0, and -8.5 km/s, respectively. It is evident from these results that the velocity associated with the wind outflow is much higher than the systematic velocity of the center of mass, the latter being -3.5 ± 0.8 km/s [37]. For this reason, we do not present a γ velocity for Vela X-1. The radial velocities derived using the H_2–H_{10} lines from [33] were corrected for the systematic radial velocity (the velocities of the center-of-mass motion and of the stellar wind at its base) individually for each line before including them in the master radial-velocity curve.

The spectral cross-correlation method used in [34] to compute the radial velocities made it unnecessary for us to introduce any further corrections for either the velocity of the stellar wind at its base or the γ velocity.

We can see from the above discussion that the radial velocities we used to fit the observational data were derived from both the hydrogen and HeI absorption lines. Therefore, as was mentioned above, we carried out test computations to check the agreement between the theoretical radial-velocity curves based on the Hγ and HeI 4471 Å lines (Fig. 1b). The radial velocities for the HeI 4471 Å line were computed using a new version of our algorithm for the synthesis of theoretical absorption-line profiles and of the radial-velocity curves for close X-ray binaries [38]. In contrast to the earlier algorithm, which is described in the cited paper and uses the Balmer profiles from the tables of Kurucz [18] for the local profiles, the new algorithm computes the local profiles for area elements on the stellar surface after constructing the model atmosphere irradiated by the external X-rays. Since the X-ray heating is not strong for most of the binaries studied here, we deemed it to be admissible to synthesize the theoretical radial-velocity curves using our earlier algorithm, which requires far fewer computer resources. The theoretical radial-velocity curves for the Hγ and HeI 4471 Å lines shown in Fig. 1b demonstrate good agreement, and, as was already mentioned, we used the theoretical radial-velocity curves based on the Hγ line for our analysis of the master set of observational data for the Balmer lines and HeI absorption lines.

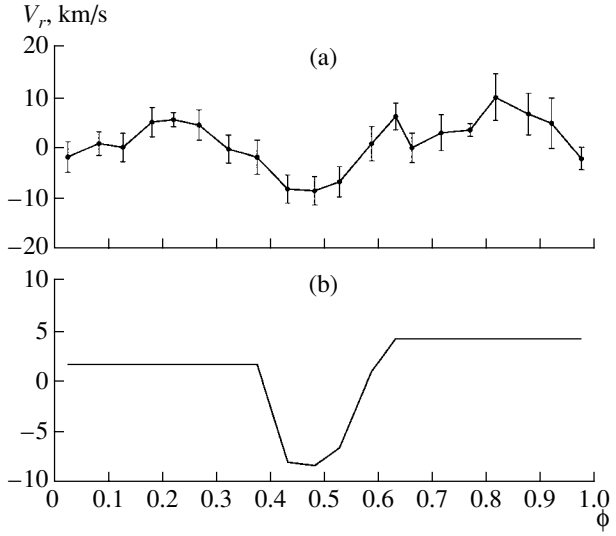

Fig. 7. (a) Anisotropy function of the stellar wind. (b) Same after normalization.

5. THE EFFECT OF ANISOTROPY OF THE STELLAR WIND IN THE ATMOSPHERE OF THE OB STAR

Early-type stars posses high mass-loss rates, up to 10^{-7}–$10^{-5}\dot{M}_\odot$/year. The outflow velocity in the zone in which the absorption lines are formed can be as high as ∼10–20 km/s, and, thus, becomes comparable to the orbital velocity of the OB giant in the system.

The isotropy of the stellar wind in a close binary is disrupted by the gravitational action of the compact object. The optical star is already in a nonuniform gravitational field. The wind velocity near the Lagrangian point L_1 increases; this is observed (Figs. 2a, 3a, 4a, 5a, 6a) as an excess negative radial velocity (toward the observer) at phase 0.5, when the X-ray source is in front of the OB star.

This strongly hinders correct interpretation of the radial-velocity curve for close binaries with early-type optical components. The anisotropy of the stellar wind is a source of errors when searching for a system's spectroscopic orbital elements [14], and

this anisotropy must likewise be taken into account when fitting the radial-velocity curve of the optical component of a close binary. Bearing in mind the difficulties of constructing theoretical models for an anisotropic wind from a distorted star, we approached this problem empirically.

Before fitting the radial-velocity curves of the systems, we calculated the phase dependences of the differences $V_{obs} - V_{teor}$ for each system (with the exception of 4U 1538–52, due to the low number of data points and their nonuniform distribution in orbital phase); V_{obs} is the observed radial velocity for a given orbital phase and V_{teor} is the theoretical value in the Roche model without taking into account the wind. Jumping somewhat ahead, we note that we used the mass of the relativistic object computed using the second method (i.e., not taking into account the radial velocities observed at phases from 0.4 to 0.6) when computing V_{teor}. Such mass estimates for X-ray pulsars are most reliable.

The resulting radial-velocity deviations for all four systems were combined and averaged within phase bins with a width of 0.05. Since the structure of the spectroscopic data for Vela X-1 was such that radial velocities derived from the H_2–H_{10} absorption lines fell at the same phase, we first averaged these within each orbital phase. We adopted the mean velocity from all the absorption lines for V_{obs} (i.e., from H_2–H_{10}) at a given epoch. Unaveraged data were used for the other systems.

The mean curve of the radial-velocity deviations, $V_{obs} - V_{teor}$, for the four systems is presented in Fig. 7a. We will call this relation the stellar-wind anisotropy function. The relation in Fig. 7a clearly demonstrates an excess negative radial velocity (toward the observer) at phases from 0.4 to 0.6, when the nose of the star is turned toward the observer. This result is in qualitative agreement with the physics of anisotropic stellar-wind outflows.

The use of the stellar-wind anisotropy function to correct the observed radial velocities is justified by the fact that it is essentially an empirical relation. We normalized the relation for this purpose. The $V_{obs} - V_{teor}$ residuals were averaged for the phase intervals 0–0.4 and 0.6–1.0. The resulting mean values, 1.79 and 4.32 km/s, were adopted as the zero points for correcting the observed radial velocities in the phase intervals 0.0–0.5 and 0.5–1.0, respectively. The normalized empirical stellar-wind anisotropy function is shown in Fig. 7b.

6. INTERPRETATION OF THE RADIAL-VELOCITY CURVES

Our aim was to determine the mass of the X-ray pulsars from the master radial-velocity curves in the Roche model, taking into account the anisotropy of the stellar wind from the OB star.

We applied a simple method with an exhaustive parameter search and found multiple solutions varying the desired parameter. In our case, the unknown was m_x and the mass of the compact object in the close X-ray binary was varied during the solutions, with all other parameters of the close binary being fixed. The values of these fixed parameters were derived from analyses of the photometric light curves, X-ray eclipse data, and timing of the X-ray pulses. The close-binary parameters used to synthesize the radial-velocity curves are presented in Table 3.

It is often very difficult to measure the true radial velocity of the optical star. Complex processes on the surface of the supergiant and in gaseous structures in the system can lead to both systematic and random deviations. We were faced with the question of how to best take into account the systematic errors. In addition to the effect of anisotropy in the optical star's wind, tidal gravitational waves on the stellar surface could be a source of systematic errors if the orbit is elliptical. The recent study [40] demonstrated that there was no correlation between the orbital phase and the phase of the gravitational tidal waves. Consequently, tidal waves on the optical star's surface are a source of random errors and can be reduced by averaging the data from many nights of observations.

In addition to gravitational–tidal perturbations of the OB supergiant's surface, additional absorption and photoionization effects [41] in the complex gaseous structures in the close binary can be sources of random errors in the observed radial velocities.

To reduce the influence of random errors due to various effects, we averaged the radial velocities within phase intervals. Our subsequent analysis of the radial-velocity curves was based on these mean observed radial velocities. The averaged radial-velocity curves for the program binaries are presented in Figs. 2b, 3b, 4b, 5b, and 6b.

We tested various hypotheses using the Fisher ratio test, which takes into account the most complete information on the averaged data. We describe our adaptation of the Fisher ratio test for the analysis of the radial-velocity curves below. Let $\bar{V}_j^{obs}$ be the observed mean radial velocity for the phase interval centered at phase $\bar{\phi}_j$; V_j^{teor}, the theoretical radial velocity value at this phase; and σ_j, the rms deviation of $\bar{V}_j^{obs}$ from the radial velocities observed in the given phase interval centered at $\bar{\phi}_j$. Let M be the number of the phase intervals, and n_j, the number of radial

Table 3. Numerical parameters used to synthesize the radial-velocity curves of the close X-ray binaries in the Roche model

Parameters	Cen X-3	LMC X-4	SMC X-1	4U 1538–52	Vela X-1
P, days	2.0871390	1.40839	3.89229118	3.72844	8.964368
e	0.0	0.0	0.0	0.0	0.0898
ω, deg*	0.0	0.0	0.0	0.0	332.59
i, deg	82	65	65	65	73
μ**	0.99	0.99	0.97	0.95	0.95 и 0.99
f	0.95	0.65	0.95	0.94	0.69
T_{eff}, K	35000	35000	25000	25000	25000
β	0.25	0.25	0.25	0.25	0.25
k_x	0.05	1.4	0.25	0.0025	0.003
A	0.5	0.5	0.5	0.5	0.5
u***	0.30	0.30	0.38	0.38	0.38
K_x, km/s	414.1	400.6	301.5	309.0	278.1

* The longitude of the periastron of the optical component is given.
** The value for Vela X-1 corresponds to the orbit periastron.
*** Data of [39].

velocities averaged in a given phase interval. We can calculate the residual as follows:

$$\Delta(m_x) = \frac{\sum\limits_{j=1}^{M}(n_j-1)}{M} \frac{\sum\limits_{j=1}^{M} n_j(V_j^{teor} - \bar{V}_j^{obs})^2}{\sum\limits_{j=1}^{M} n_j(n_j-1)\sigma_j^2}. \quad (1)$$

The variable $\Delta(m_x)$ will be distributed according to a Fisher law, $F_{M,\sum\limits_{j=1}^{M}(n_j-1),\alpha}$ [42]. Let us adopt the significance level α. The confidence set for the desired parameter, m_x, will then consist of the values satisfying the condition

$$\Delta(m_x) \le F_{M,\sum\limits_{j=1}^{M}(n_j-1),\alpha}.$$

We solved the inverse problem using the Roche and point-mass models. The latter was used only to reveal disagreements between the results for the two models. We analyzed the mean radial-velocity curves for each system using three methods.

Method 1. Using all the mean observed radial velocities, with no correction for anisotropy of the stellar wind.

Method 2. Rejecting mean observed radial velocities at phases 0.4–0.6 that are most strongly distorted by the effects of the stellar-wind anisotropy.

Method 3. Using the mean radial velocities at phases 0.4–0.6 corrected for the stellar-wind anisotropy function.

Let us consider the details of our procedures for determining the compact object's mass using the first system, Cen X-3, as an example.

Cen X-3. The mean radial-velocity curve for Cen X-3 had 79 data points. Despite the fact that the points were uniformly distributed in orbital phase (Fig. 2a), we can identify close groups of points with similar orbital phases. In the case of Cen X-3, we isolated 11 such groups, within which we averaged the observed radial velocities. The radial velocities averaged within the phase bins are shown in Fig. 2b.

The mean radial velocities show the strongest deviations from the standard curve at phases 0.4–0.6. The supergiant's excess negative radial velocity at these phases is due to the anisotropy of the stellar wind.

Recall that we determined the unknown m_x by carrying out an exhaustive search among its possible values. In the process, we varied the mass of the relativistic component so that the semiamplitude of its radial-velocity curve remained unchanged, $K_x =$ 414.1 km/s [43]. For more detail on the method used to compute the optical component's mass by running through possible masses for the relativistic component, see the Appendix. The remaining binary parameters (Table 3) were fixed.

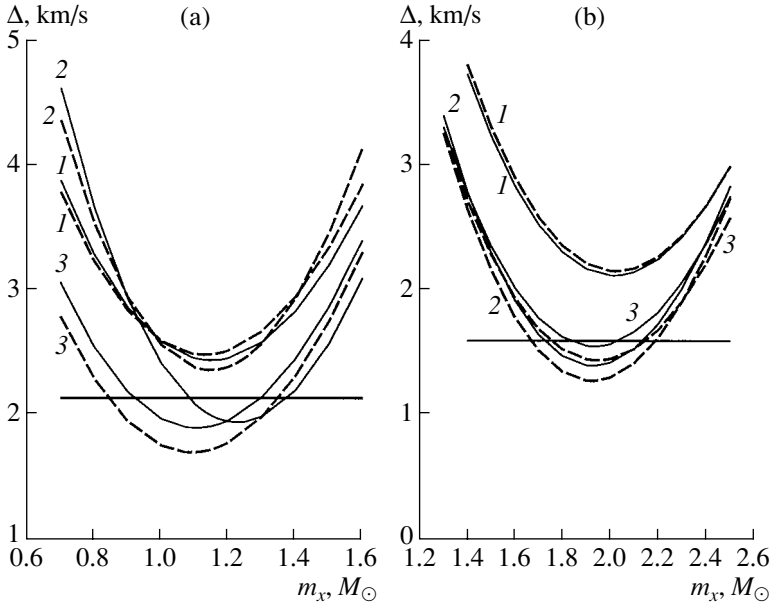

Fig. 8. Deviations of the observed mean radial-velocity curves for (a) Cen X-3 and (b) Vela X-1 from the synthetic curves in the Roche model (solid curve) and point-mass model (dashed curve) obtained using methods 1, 2, and 3. The method used to derive the residuals is indicated by a number near the curve. The horizontal lines correspond to the critical levels in the Fisher ratio test, $\Delta_{8,47} = 2.14$ (a) and $\Delta_{18,782} = 1.605$ (b), for a significance level of 5%.

The residual yielded by analyzing the observed radial velocities using method 1 is shown in Fig. 8a. The significance level adopted for the computations was 5%. We can see in this figure that the model without allowance for the wind anisotropy must be rejected at this significance level. The m_x value corresponding to the minimum residual is presented in Table 4.

Interpretation of the radial-velocity curve is hindered by the strong deviation of the data points from their computed positions near phase 0.5. This does not fit into the Roche model with an isotropic stellar wind. We therefore excluded in the next stage observed radial velocities at phases 0.4–0.6 during the computations, and our analysis of the fitted curves did not take them into account (method 2). The behavior of the residuals is shown in Fig. 8a. We can see that the point-mass model must be rejected according to the Fisher test, whereas the Roche model, which is more adequate for describing the physics of processes in close binaries, is acceptable. We accordingly adopt the Roche model, not because it is necessarily correct, but because there is no reason to reject it (see the review [44] for details).

The mass of the X-ray pulsar corresponding to the minimum residual in the Roche model is 1.63 $M_\odot$. The minimum residual for the point-mass model is reached for 1.47 $M_\odot$. This large a discrepancy can be explained by the difference in the shapes of the synthetic curves for the Roche and point-mass models (Fig. 1a). The barycenter of the system is inside the body of the optical star ($q < 1$), so that some fraction of the optical star's emitting surface is moving in the same direction as the relativistic component. This leads to a lower amplitude of the synthesized radial-velocity curve in the Roche model, all the other parameters being the same, and, hence, to a higher mass for the relativistic object.

In the computations with method 3, we corrected the mean radial velocities at phases 0.4–0.6 for the mean normalized wind anisotropy function. This correction makes the deviation between the synthetic and observed radial velocity values much smaller (Fig. 2b). The differences between the theoretical and corrected observed radial-velocity curves are presented in Fig. 8a. We can see that, in this case, the Fisher ratio test indicates both the Roche and point-mass models to be acceptable.

The resulting masses, along with the masses of the X-ray pulsars in the other systems, are collected in Table 4.

LMC X-4. The master radial-velocity curve contains about 70 data points (Fig. 3a); the averaged master radial-velocity curve is presented in Fig. 3b. The mean velocities in the phase bins were formed using from three to ten points. These mean observed velocities are in good agreement with the theoretical values.

The residuals obtained for the Roche and point-mass models using methods 1 and 2 indicate that both models are acceptable according to the Fisher

Table 4. Masses of X-ray pulsars in the close binaries with supergiants derived from fitting the mean observed radial-velocity curves in the Roche and point-mass models (the confidence interval is given for the 95% confidence level)

Name	Roche model			Point-mass model		
	Method 1	Method 2	Method 3	Method 1	Method 2	Method 3
Cen X-3	1.14	$1.22^{+0.15}_{-0.14}$	$1.10^{+0.05}_{-0.05}$	1.12	1.14	$1.09^{+0.18}_{-0.18}$
LMC X-4	$1.55^{+0.29}_{-0.27}$	$1.63^{+0.42}_{-0.47}$	1.60	$1.40^{+0.30}_{-0.29}$	$1.47^{+0.47}_{-0.43}$	$1.43^{+0.08}_{-0.05}$
SMC X-1	$1.40^{+0.33}_{-0.29}$	$1.48^{+0.47}_{-0.42}$	$1.40^{+0.49}_{-0.45}$	$1.30^{+0.33}_{-0.31}$	$1.36^{+0.41}_{-0.39}$	$1.30^{+0.49}_{-0.45}$
4U 1538−52	$1.21^{+0.28}_{-0.26}$	$1.18^{+0.29}_{-0.27}$	1.26	1.16	$1.13^{+0.11}_{-0.11}$	1.21
Vela X-1 ($\mu = 0.95$)*	2.02	$1.93^{+0.25}_{-0.24}$	$1.94^{+0.08}_{-0.10}$	2.02	$1.92^{+0.30}_{-0.28}$	$1.94^{+0.21}_{-0.18}$
Vela X-1 ($\mu = 0.99$)*	2.02	$1.93^{+0.19}_{-0.21}$	1.94	2.02	$1.92^{+0.30}_{-0.28}$	$1.94^{+0.21}_{-0.18}$

* The confidence interval is given for the error of the mean artificially increased twofold.

test. Because of the initial good agreement of the mean observed and theoretical radial velocities, the residual increases when the observed radial-velocity curve is analyzed using method 3. The increase in the difference between the theoretical and observed radial velocities is quite apparent in Fig. 3b. When the observed mean radial-velocity curve is analyzed using method 3, the point-mass model is rejected by the Fisher test, whereas the Roche model is acceptable. The resulting masses and confidence intervals are presented in Table 4.

SMC X-1. The mean curve contained 70 data points (Fig. 3a). The averaged radial velocities are presented in Fig. 4b; the observed radial velocities at phases 0.40 and 0.51 deviate fairly strongly from the theoretical values.

The analysis of the mean observed radial-velocity curves using any of the three methods indicates that both the Roche and point-mass models are acceptable according to the Fisher ratio test. Correction of the mean observed radial velocities at phases 0.40 and 0.51 reduces the disagreement between the synthetic and observed radial velocities (Fig. 4b); i.e., the residuals obtained using method 3 are lower than those for method 1. This is reflected in the broader confidence interval for the X-ray pulsar masses satisfying the Fisher test at the 95% confidence level for method 3 compared to method 1 (Table 4).

4U 1538−52. The master radial-velocity curve contains 36 data points (Fig. 5a); the values averaged within each group are presented in Fig. 5b. Because of the sparseness of the spectroscopic data, the averaging in some phase intervals was based on radial velocities measured on a single night, making it impossible to reduce the influence of random errors. This could be the origin of the excess positive velocity at phase 0.45.

When analyzing the mean observed radial velocities using method 1, the Roche model passes the Fisher ratio test, whereas the point-mass model is rejected. With the radial velocity at phase 0.45 excluded (model 2), both the Roche and point-mass models pass the Fisher test. Since an excess positive radial velocity is observed at phase 0.45, the correction for the normalized stellar-wind anisotropy function only increases the discrepancy between the mean observed and theoretical radial velocities. Thus, the increased residual yielded by method 3 results in both models being rejected by the Fisher test. The resulting masses and confidence intervals are presented in Table 4.

Vela X-1. The master radial-velocity curve included 782 data points subdivided into 18 groups (Fig. 6a). The values averaged within each group are shown in Fig. 6b. Each phase bin used for the averaging contains many (28 to 82) data points, leading to low standard deviations. Thus, the residuals obtained using method 1, method 2, and method 3 are 8.59, 6.00, and 6.59, respectively, with the quantiles being 1.69, 1.605, and 1.69. The low uncertainties in the averaged data impose stringent requirements on the models, so that even the Roche model with the stellar-wind anisotropy taken into account is rejected by the Fisher test, testifying to the complexity of the physics of the absorption-line-formation processes.

Artificially increasing the standard deviations, σ_j, by a factor of 1.5 reduced the residuals for method 2 to 1.92, whereas the critical level for the Fisher ratio test with a 5% significance level is 1.605. The difference between the critical level for the Fisher test with the 5% significance level and the residuals derived using the other methods using $1.5\sigma_j$ are even higher. When the standard deviations, σ_j, in (1) were artificially doubled, the models for methods 2 and 3 were deemed acceptable by the Fisher test. The model for method 1 is rejected even after doubling the standard

deviations and analyzing the full, uncorrected radial-velocity curve.

The above findings indicate that the Roche model is not adequate to the high-accuracy radial-velocity curve of the optical star in the Vela X-1 system, making the mass of the X-ray pulsar, m_x, derived for this system relatively uncertain.

Because of the large uncertainty in the Roche-lobe filling coefficient, μ, we carried out computations for $\mu = 0.95$ and 0.99, keeping the remaining conditions the same (this corresponds to two lines in Table 4). The deviation of the mean observed radial-velocity curve from the synthetic curve for the Roche model is much lower for $\mu = 0.95$ than for $\mu = 0.99$, which is reflected in a wider confidence interval for the better fit (Table 4). However, the mass of the X-ray pulsar derived from the residual minimum remains the same for the two cases. We conclude that the radial-velocity curve is insensitive to relatively small variations of the Roche-lobe filling coefficient.

Figure 8b shows the behavior of the residuals (for $\mu = 0.95$) found using each of the methods. Table 4 presents the X-ray pulsar masses corresponding to the minimum residuals for models rejected by the Fisher ratio test. It is not possible to derive confidence intervals in these cases.

7. CONCLUSIONS

This paper has presented estimates of the masses of X-ray pulsars that are most adequate to the entire set of observational data for X-ray binaries with OB supergiants. In contrast to earlier studies, we have considered not only the semiamplitude of the radial-velocity curve but also its overall shape.

Our investigation demonstrates that a pure Roche model is insufficient for analyzing the radial-velocity curves of X-ray close binaries with early-type optical stars. This model is often rejected by the Fisher ratio test due to the presence of an excess negative radial velocity near phase 0.5. In a number of cases, only taking into account the wind anisotropy makes it possible to accept the model based on the Fisher test, thereby enabling us to obtain reliable estimates of the neutron-star masses in the X-ray binaries and their confidence intervals.

This study has yielded masses of the X-ray pulsars derived in the Roche model, with the stellar-wind anisotropy taken into account empirically. This model is much more realistic than earlier models based on point masses in Keplerian orbits. Note that the mass estimates for X-ray pulsars in binaries with supergiants obtained in the point-mass models of [13] are in good agreement with our own determinations using the same model with two point masses.

Let us now consider the X-ray pulsar mass estimates for the Roche model. They are systematically higher than the masses derived in the point-mass model, by on average $\sim 10\%$ (Table 4). Our test computations for the SMC X-1 system demonstrated that the systematic excess of the X-ray pulsar masses obtained for the Roche model did not depend on the orbital inclination i (see the Appendix). Thus, we conclude that the X-ray pulsar masses were systematically too low (by 5–10%) in all earlier studies based on point-mass models.

The masses of the X-ray pulsars in LMC X-4 and SMC X-1, $1.63^{+0.42}_{-0.47}\ M_\odot$ and $1.48^{+0.47}_{-0.42}\ M_\odot$, respectively, are somewhat higher than the standard mass for a neutron star, $1.35 \pm 0.04\ M_\odot$ [21], though they can be reconciled with a mass of $1.35 M_\odot$ within our confidence intervals. It is difficult to explain the excess of the X-ray pulsar masses over the standard value as being due to the accumulation of accreted matter from an accretion disk onto the neutron star's surface. A mass of about $0.01\ M_\odot$ could settle onto the pulsar's surface over the optical component's life time during the stage when the Roche lobe is close to being filled, $\sim 10^5$ years, if the mass-loss rate of the optical star is 10^{-7}–$10^{-6}\dot{M}_\odot$/year, taking into account the size of the close binary and the relativistic star's gravitational capture radius.

The X-ray pulsar masses in the Cen X-3, LMC X-4, SMC X-1, and 4U 1538–52 systems derived using the most reliable method, in the Roche model excluding the mean radial velocities near phase 0.5, are $1.22^{+0.15}_{-0.14}\ M_\odot$, $1.63^{+0.42}_{-0.47}\ M_\odot$, $1.48^{+0.47}_{-0.42}\ M_\odot$, and $1.18^{+0.29}_{-0.27}\ M_\odot$, respectively. The mean of the four X-ray pulsar masses is $1.37 \pm 0.15\ M_\odot$ at the 95% confidence level (the mass of the pulsar in the Vela X-1 system was not used for the average due to its anomalously high value). This mean X-ray pulsar mass agrees with the standard radio pulsar mass, $1.35 \pm 0.04\ M_\odot$, within the errors [21].

Our test computations in the Roche model for various orbital inclinations, i, demonstrated the validity of the relation $m_x \sim \sin^{-3} i$ (see the Appendix for more details). Thus, the X-ray pulsar masses derived in the Roche model can easily be recalculated if their orbital inclinations are refined.

An important result of this study is the mass estimate for the compact object in the Vela X-1 X-ray binary. The earlier estimate was $1.86^{+0.32}_{-0.32}\ M_\odot$ at the 95% significance level [34], considerably in excess of the standard value, $1.35 \pm 0.04\ M_\odot$. Our analysis of the radial-velocity curve in the Roche model taking into account the wind anisotropy slightly increased the mass of the X-ray pulsar in this system, to $1.93^{+0.19}_{-0.21}\ M_\odot$ at the 95% confidence level. Note

Table 5. Masses of the SMC X-1 pulsar derived using the Roche and point-mass model for various orbital inclinations (confidence intervals are given for the 95% confidence level)

Orbital inclination	Roche model			Point-mass model		
	Method 1	Method 2	Method 3	Method 1	Method 2	Method 3
$i = 65°$	$1.40^{+0.33}_{-0.29}$	$1.48^{+0.33}_{-0.29}$	$1.40^{+0.49}_{-0.45}$	$1.30^{+0.33}_{-0.31}$	$1.36^{+0.41}_{-0.39}$	$1.30^{+0.49}_{-0.45}$
$i = 75°$ (case A)	$1.15^{+0.27}_{-0.24}$	$1.22^{+0.37}_{-0.36}$	$1.15^{+0.40}_{-0.37}$	$1.08^{+0.27}_{-0.25}$	$1.12^{+0.35}_{-0.31}$	$1.43^{+0.41}_{-0.38}$
$i = 75°$ (case B)	1.156	1.223	1.156	1.074	1.123	1.074
$i = 85°$ (case A)	$1.05^{+0.24}_{-0.22}$	$1.11^{+0.34}_{-0.32}$	$1.05^{+0.37}_{-0.33}$	$0.98^{+0.24}_{-0.24}$	$1.02^{+0.32}_{-0.28}$	$0.98^{+0.38}_{-0.33}$
$i = 85°$ (case B)	1.054	1.114	1.054	0.978	1.024	0.978

again that our Roche model for the Vela X-1 system was rejected by the Fisher ratio test, so that the X-ray pulsar's mass, 1.93 $M_\odot$, cannot be considered very trustworthy. A "hard" equation of state must be used to explain the existence of neutron stars with masses this high. Studies in this direction are very promising.

ACKNOWLEDGMENTS

This study was supported by the Russian Foundation for Basic Research (project code 02-02-17524) and a grant from the program "Leading Scientific Schools of Russia." We thank V.V. Shimanskiĭ for helpful advice.

APPENDIX

When solving the inverse problem, we varied the mass of the X-ray pulsar, m_x, so that the semiamplitude of its radial-velocity curve, K_x, remained unchanged, since this parameter is known to high accuracy from X-ray timing data (Table 2). To keep K_x constant as the mass of the relativistic component, m_x, varied, we had to vary the mass of the optical star, m_v, as well. We used the classical formulas to relate the mass of the optical component, m_v, to each value of the X-ray pulsar's mass, m_x:

$$m_x \sin^3 i = 1.038 \times 10^{-7} P(1-e^2)^{3/2} \times K_v(K_x + K_v)^2, \quad (2)$$

$$m_v \sin^3 i = 1.038 \times 10^{-7} P(1-e^2)^{3/2} \times K_x(K_v + K_x)^2. \quad (3)$$

The point-object model is quite applicable to the X-ray pulsar, justifying the use of (2). The value of K_v it gives for fixed m_x and i characterizes the true velocity of the optical star's center of mass. Due to the various reasons mentioned above (the pear-like shape of the stars, anisotropic winds, heating effects, etc.), the observed K_v can differ from the value of K_v found from (2). Substituting the true K_v derived from (2) into (3), we find the mass of the optical star, m_v, for the specified value of i. In this manner, relating the mass of the optical component to that of the relativistic component, we can keep the semiamplitude of the relativistic component's radial-velocity curve, K_x, constant. Note also that (3) contains only a quadratic dependence on K_v, whereas the dependence on K_x is cubic. This is reflected in the fact that varying m_x by a factor of 2.7 leads to a change in the optical component's mass by only a factor of 1.14.

In the model with two point masses, the masses of the optical star, m_v, and of the X-ray pulsar, m_x, depend on the orbital inclination, i, as $m_v \sim \sin^{-3} i$ and $m_x \sim \sin^{-3} i$. We should check if the relation $m_x \sim \sin^{-3} i$ is valid when the X-ray pulsar's mass is determined using the Roche model for the optical star from the minimum difference between the observed mean radial-velocity curve and the curve synthesized in the Roche model.

For this purpose, we also analyzed the mean radial-velocity curve of the SMC X-1 system in the Roche model using the three methods for orbital inclinations of 75° and 85°. The result is presented in Table 5, where it is called "case A." Having the mass obtained earlier in the Roche model for an orbital inclination of 65° (Table 4), we recalculated this mass for the orbital inclinations 75° and 85° according to the formulas

$$m_x(75°) = m_x(65°)\frac{\sin^3 65°}{\sin^3 75°}, \quad (4)$$

$$m_x(85°) = m_x(65°)\frac{\sin^3 65°}{\sin^3 85°}, \quad (5)$$

where $m_x(65°)$, $m_x(75°)$, and $m_x(85°)$ are the masses of the X-ray pulsar for orbital inclinations of 65°, 75°, and 85°. The results are presented in Table 5, where they are called "case B." We can see that the masses m_x derived from the minimum residual in the Roche model for the orbital inclinations 75° and 85°

(case A) are very close to the masses m_x obtained using (4) and (5) (case B). Thus, the masses m_x derived in the Roche model for the optical star (Table 4) can easily be recalculated using the formula $m_x \sim \sin^{-3} i$ if the orbital inclination, i, is refined.

REFERENCES

1. L. D. Landau, Phys. Z. Sowjetunion **1**, 285 (1932).
2. W. Forman *et al.*, Astrophys. J., Suppl. Ser. **38**, 357 (1978).
3. Ya. B. Zel'dovich, Dokl. Akad. Nauk SSSR **155**, 67 (1964).
4. E. E. Salpeter, Astrophys. J. **140**, 796 (1964).
5. N. I. Shakura and R. A. Sunyaev, Astron. Astrophys. **24**, 337 (1973).
6. J. E. Pringle and M. J. Rees, Astron. Astrophys. **21**, 1 (1972).
7. I. D. Novikov and K. S. Thorne, in *Black Holes*, Ed. by C. De Witt and B. S. De Witt (Gordon and Breach, London, 1973), p. 343.
8. S. L. Shapiro and S. A. Teukolsky, *Black Holes, White Dwarfs, and Neutrons Stars: The Physics of Compact Objects* (Wiley, New York, 1983).
9. W. D. Arnett and R. L. Bowers, Astrophys. J., Suppl. Ser. **33**, 415 (1977).
10. B. Datta, Fundam. Cosmic Phys. **12**, 151 (1988).
11. R. Stock, Nature **337**, 319 (1989).
12. G. E. Brown and H. A. Bethe, Astrophys. J. **423**, 659 (1994).
13. M. H. van Kerkwijk, J. van Paradijs, and E. J. Zuiderwijk, Astron. Astrophys. **303**, 497 (1995).
14. M. Milgrom, Astron. Astrophys. **70**, 763 (1978).
15. E. A. Antokhina and A. M. Cherepashchuk, Astron. Zh. **71**, 420 (1994) [Astron. Rep. **38**, 367 (1994)].
16. E. A. Antokhina, Astron. Zh. **73**, 532 (1996) [Astron. Rep. **40**, 483 (1996)].
17. R. E. Wilson, Astrophys. J. **234**, 1054 (1979).
18. R. L. Kurucz, Astrophys. J., Suppl. Ser. **40**, 1 (1979).
19. A. M. Cherepashchuk, N. A. Katysheva, Khruzina, and C. Yu. Shugarov, *Highly Evolved Close Binary Stars: Catalog* (Netherland Gordon and Breach Sci. Publ., 1996), Vol. 1, Part 1, p. 82.
20. A. V. Goncharskiĭ, S. Yu. Romanov, and A. M. Cherepashchuk, *Finite-Parametric Inverse Astrophysical Problems* (Mosk. Gos. Univ., Moscow, 1991), p. 105 [in Russian].
21. S. E. Thorsett and D. Chakrabarty, Astrophys. J. **512**, 288 (1999).
22. M. Mouchet, S. A. Ilovaisky, and C. Chevalier, Astron. Astrophys. **90**, 113 (1980).
23. J. B. Hutchings, A. P. Cowley, and D. Crampton, Astrophys. J. **229**, 1079 (1979).
24. C. D. T. Ash, A. P. Reynolds, P. Roche, *et al.*, Mon. Not. R. Astron. Soc. **307**, 357 (1999).
25. J. B. Hutchings, D. Crampton, and A. P. Cowley, Astrophys. J. **225**, 548 (1978).
26. R. L. Kelley, J. G. Jernigan, A. Levine, *et al.*, Astrophys. J. **264**, 568 (1983).
27. P. S. Osmer and W. A. Hiltner, Astrophys. J. **217**, 186 (1977).
28. J. B. Hutchings, D. Crampton, A. P. Cowley, and P. S. Osmer, Astrophys. J. **217**, 186 (1977).
29. A. P. Reynolds, R. W. Hilditch, S. A. Bell, and G. Hill, Mon. Not. R. Astron. Soc. **261**, 337 (1993).
30. K. Makishima, K. Koyama, S. Hayakawa, and F. Nagase, Astrophys. J. **314**, 619 (1987).
31. D. Crampton, J. B. Hutchings, and A. P. Cowley, Astrophys. J. **225**, L63 (1978).
32. A. P. Reynolds, S. A. Bell, and R. W. Hilditch, Mon. Not. R. Astron. Soc. **256**, 631 (1992).
33. J. van Paradijs, E. J. Zuiderwijk, R. J. Takens, and G. Hammerschlag-Hensberge, Astrophys. J., Suppl. Ser. **30**, 195 (1977).
34. O. Barziv, L. Kaper, M. H. van Kerkwijk, *et al.*, Astron. Astrophys. **377**, 925 (2001).
35. J. B. Hutchings, Astrophys. J. **235**, 413 (1980).
36. D. Crampton, J. B. Hutchings, and A. P. Cowley, Astrophys. J. **299**, 839 (1985).
37. J. B. Hutchings, Astrophys. J. **192**, 685 (1974).
38. E. A. Antokhina, A. M. Cherepashchuk, and V. V. Shimanskiĭ, Izv. Ross. Akad. Nauk, Ser. Fiz. **67**, 293 (2003).
39. A. A. Rubashevskiĭ, Astron. Zh. **68**, 799 (1991) [Sov. Astron. **35**, 626 (1991)].
40. H. Quantrell, A. J. Norton, T. D. C. Ash, *et al.*, Astron. Astrophys. (2003, in press).
41. L. Kaper, G. Hammerschlag-Hensberge, and E. J. Zuiderwijk, Astron. Astrophys. **289**, 846 (1994).
42. D. J. Hudson, *Statistics. Lectures on Elementary Statistics and Probability Theory* (Geneva, 1964; Mir, Moscow, 1970).
43. F. Nagase, R. H. D. Corbet, C. S. R. Day, *et al.*, Astrophys. J. **396**, L147 (1992).
44. A. M. Cherepashchuk, Astron. Zh. **70**, 1157 (1993) [Astron. Rep. **37**, 585 (1993)].

Translated by N. Samus'